Universiteit Antwerpen

Faculteit Wetenschappen
Departement Fysica

Improving the Accuracy of Transverse Momentum Dependent Parton Branching Methods for Collider Physics

Thesis submitted for the degree of

Doctor of Science: Physics

at the

University of Antwerp

to be defended by

Aron Mees van Kampen

Promotors:
Prof. Dr. Francesco Hautmann
Prof. Dr. Pierre Van Mechelen

Antwerp, 2024

Jury members

Universiteit Antwerpen	Prof. Dr. Sandra Van Aert	(Chair)
	Prof. Dr. Francesco Hautmann	(Promotor)
	Prof. Dr. Pierre Van Mechelen	(Promotor)
	Prof. Dr. Paul Scheunders	(Committee Member)
Université Libre de Bruxelles	Prof. Dr. Laurent Favart	(External Examiner)
Universität Graz	Dr. Simon Plätzer	(External Examiner)

Abstract

This thesis presents several studies on calculations for high-energy proton-proton collisions using the Parton Branching (PB) method for the evolution of transverse momentum dependent parton distribution functions (TMDs). The PB method allows to perform both inclusive and exclusive calculations of collision final states by means of Monte Carlo techniques. Evolution of TMDs in the PB method allows for the resummation of soft gluons by the Sudakov form factor. The implementation of PB TMDs in the TMDLIB library and the implementation of the backward PB Sudakov form factor in the CASCADE3 Monte Carlo event generator allows for the calculation of a wide variety of particle collision processes in a wide kinematic range.

We examine the PB method, focusing on the Sudakov form factor and the soft-gluon resolution scale. By extending the emission phase space with longitudinal splitting fractions z approaching one, we achieve accurate perturbative resummation and a non-perturbative contribution to the evolution. A dynamical resolution scale separates resolvable and non-resolvable phase space regions, acting as a boundary between these perturbative and non-perturbative domains. We show that PB evolution with next-to-leading order (NLO) splitting functions achieves next-to-leading logarithmic (NLL) accuracy in soft-gluon resummation. The implementation of the physical (or effective) soft-gluon coupling enhances Sudakov resummation towards next-to-next-to-leading logarithmic (NNLL) accuracy. Application to the transverse momentum spectrum of the Z-boson in the Drell-Yan (DY) process shows the effect of implementing the physical coupling. Non-perturbative contributions of the Sudakov are illustrated through the extraction of the Collins-Soper (CS) kernel. These extractions highlight the influence of both the emission phase space and the scale of the strong coupling in TMD evolution on the large b behavior of the CS kernel.

Combining higher order matrix element calculations with PB TMDs and TMD shower is done through matching and merging techniques. Azimuthal correlations of high transverse momentum jets in di-jet production and boson-jet production are calculated using PB TMDs matched to NLO matrix elements. QCD predictions for final states with multiple jets in hadron collisions make use of multi-jet merging methods. These methods consistently combine the contributions from hard scattering matrix elements with different parton multiplicities and parton showers. Calculations of jet transverse momentum and jet multiplicity distributions, as well as highly non-trivial jet event shapes, are performed with the recently developed TMD merging method. We investigate theoretical predictions for Z-boson plus jets production using multi-jet merging algorithms. Our analysis focuses on the differential jet rates (DJRs) and their discontinuities, which allows us to develop a method for quantitatively analyzing the merging algorithm and its dependence on the merging scale by varying invariant di-lepton masses.

ii

Samenvatting

Dit proefschrift presenteert verschillende studies over berekeningen voor hoog-energetische proton-proton botsingen met behulp van de Parton Branching (PB) methode voor de evolutie van transversale impulsafhankelijke parton distributies (TMDs). De PB-methode maakt het mogelijk om zowel inclusieve als exclusieve berekeningen van eindtoestanden van deeltjesbotsingen uit te voeren met Monte Carlo-technieken. De evolutie van TMDs in de PB-methode maakt de hersommatie van laag energetische gluonen door gebruik te maken van de Sudakov-vormfactor. De implementatie van PB TMDs in de TMDʟɪʙ bibliotheek en de implementatie van de achterwaartse PB Sudakov vormfactor in de Cᴀsᴄᴀᴅᴇ3 Monte Carlo event generator maakt het mogelijk om een grote variëteit aan deeltjesbotsingsprocessen te berekenen in een breed kinematisch bereik.

We onderzoeken de PB-methode, waarbij we ons richten op de Sudakov-vormfactor en de soft-gluon resolutieschaal. Door de faseruimte van emissies uit te breiden met longitudinale splitsingsfracties z die de waarde één benaderen, bereiken we nauwkeurige perturbatieve hersommatie en een niet-perturbatieve bijdrage aan de evolutie. Een dynamische resolutieschaal scheidt "resolvable" en "non-resolvable" gebieden uit de faseruimte en vormt daarmee de grens tussen perturbatieve en niet-perturbatieve domeinen. We laten zien dat PB evolutie met "next-to-leading order" (NLO) splitsings-functies "next-to-leading" logaritmische (NLL) nauwkeurigheid bereikt in soft-gluon hersommatie. De implementatie van de fysische (of effectieve) soft-gluon koppeling verbetert de Sudakov hersommatie naar "next-to-next-to-leading" logaritmische (NNLL) nauwkeurigheid. Toepassing op het transversale impuls spectrum van het Z-boson in het Drell-Yan (DY) proces toont het effect van de implementatie van de fysische koppeling. Niet-perturbatieve bijdragen van de Sudakov worden geïllustreerd door de extractie van de Collins-Soper (CS) kernel. Deze extracties benadrukken de invloed van zowel de faseruimte als de schaal van de sterke koppeling in TMD-evolutie op het gedrag van de CS kernel bij grote b waarden.

Het combineren van hogere orde matrixelementberekeningen met PB TMDs en een TMD shower wordt gedaan door matching- en mergingtechnieken. Azimuthale correlaties van jets met hoog transversaal impuls in di-jet productie en boson-jet productie worden berekend aan de hand van PB TMDs die gematcht worden met NLO-matrixelementen. QCD voorspellingen voor eindtoestanden met meerdere jets in hadronbotsingen maken gebruik van multi-jet "merging" technieken. Deze methoden combineren consistent de bijdragen van matrixelementen met verschillende partonmultipliciteiten en "parton showers". Berekeningen van transversaal impuls van jets en jet multipliciteiten, evenals zeer niet-triviale jet "event shapes", worden uitgevoerd met de recent ontwikkelde "TMD merging" methode. We onderzoeken theoretische voorspellingen voor de productie van Z-bosonen met jets met behulp van algoritmen voor multi-jet merging. Onze analyse richt zich op "differential jet rates" (DJRs) en hun discontinuïteiten, waarmee we een methode hebben kunnen ontwikkelen voor het kwantitatief analyseren van het merging algoritme en de afhankelijkheid van de merging schaal door invariante di-leptonmassa's te variëren.

iv

Acknowledgements

The PhD program has come to an end and I would like to thank all people that have helped me through it in one way or another.

First I owe my gratitude to Francesco Hautmann for giving me this opportunity to work together for four years. Your knowledge and level understanding of many aspects of QCD and high-energy physics is incredibly large which helped me understanding and interpreting our own results and work from others. Due to many of your ideas, the projects I have been working on have been established.

Many thanks to Ola Lelek, for sharing expertise on Parton Branching, for reading parts of my thesis and especially for the good conversations and happy days at the office. Thanks a lot to Lissa Keersmaekers for being such a good and nice colleague during almost my entire PhD. This thesis would honestly not have reached the current level without you, my dear colleagues Lissa and Ola.

Thanks very much Pierre Van Mechelen for inspiring me to go studying physics about ten years ago and continue to work in your research group five years ago. Your patience and critical eye have helped me a great deal with writing the thesis. Also your concern with the group and well being of its members I respect and appreciate very much.

Thanks to all other people I have been working with, who teached me a lot. Especially thanks to Armando Bermudez Martinez, from whom I learned about TMD merging and the technicalities related to it. I am very grateful to Leif Lönnblad and Stefan Prestel for having me in Lund, Sweden, for a short studentship where I've learned about event generators, parton showers and Pythia in particular. Thank you Pieter Taels for helping me to understand the underlying theories better and for reading and correcting some chapters of my thesis drafts. Many thanks to Thomas Van Laer for joining the project on the merging of pure jet events and for reading and commenting on some of my thesis chapters. We've had many interesting discussions and Thomas' questions made me think and understand more on certain topics. Thank you Mikel Mendizabal for our discussions in Antwerp and Hamburg on CSS, PB and for fun times. Thank you Hannes Jung, for providing much code, information and setting up collaborations.

I want to acknowledge some people from our research group that were important to me as well. Sarah for your great organizing skills allowing me to go to conferences and making sure my administration was in order, I also really enjoyed our chats at the campus. Thanks to my (more than) colleagues Kamiel, Tomas, Hans, Simon, Safura, Yamiel, Maja, Max for enjoyable conversations during lunch, coffee breaks and our famous Friday night beers which only happened during the lockdowns (disclaimer: this was an online event).

The whole journey I would not have managed to finalize without the mental support of my family. Thank you so much, my dear parents, grandparents and sweet sister, for supporting me at any time, unconditionally.

In addition to the content support, I'm very grateful for my close friends who have stand beside me during the past four years despite suffering from hearing my complaints and struggles. The fun things we do together kept me going and motivated.

Contents

Introduction

Progress in the experimental investigation of fundamental interactions at high-energy particle colliders strongly depends on the possibility to carry out realistic event simulations via Monte Carlo (MC) event generators. Many research groups are currently devoting significant efforts to increase the accuracy of analytical and numerical calculations in high-energy physics. This is needed for a relevant comparison of highly accurate experimental measurements with theoretical studies. In this respect, the aim of the whole particle physics community is to increase the precision of the Standard Model (SM) and find physics Beyond-the-Standard-Model (BSM). This forms a crucial input to the current European Strategy Update for Particle Physics [1]. It will also be essential to increase the accuracy for designing and executing forthcoming experimental initiatives like the High-Luminosity Large Hadron Collider (HL-LHC) [2], the proposed forward physics facility [3] and hadron-electron facility [4] at the HL-LHC, the Electron Ion Collider (EIC) [5], and the Future Circular Collider (FCC) [6].

A key component of event generators is provided by parton branching algorithms which describe the radiative processes of quarks and gluons ("partons") occurring in high-energy collisions, based on Quantum Chromodynamics (QCD) [7–9], the gauge field theory of strong interactions. Multiple quark and gluon radiation are associated to any scattering process that involves hadrons. This radiation gives rise to the "parton showers" which accompany any high-energy collision, and contributes to the "jets" of hadronic particles which appear in the final states of hard scattering processes and can be measured by the detectors of high-energy experiments.

Parton branching algorithms go back to the ideas of the pioneering works of the 1980s [10–15], and are based on the dominance of quanta of the quark and gluon fields radiated at small angles ("collinear" radiation) and small energies ("soft" radiation). Multiple soft and collinear radiation gives rise to a hierarchy of logarithmically-enhanced contributions in QCD perturbation theory. In order to achieve reliable high-energy event simulations, such contributions need to be taken into account to all orders in the strong-interaction coupling α_s via "resummation" procedures. A large body of work is being currently devoted to improving the logarithmic accuracy of parton showers and exploring the associated theoretical systematic uncertainties [16–26].

While most of the above works focus on soft and collinear radiation dominating the final-state parton showers, important contributions to advancing the accuracy of parton showers also come from more complete treatments of the initial-state radiation and initial-state hadron structure. The main subject of this thesis is the study of such initial-state effects, and their inclusion in parton branching approaches.

The thesis moves from the observation that accurate treatments of initial-state dynamics require taking into account hadron structure and parton radiation using methods that

go beyond collinear approximations [27–31]. To do this, the key idea is to introduce transverse momentum dependent (TMD), or unintegrated, distributions of partons in the initial state [32, 33]. Recent reviews of TMD distributions are given in [34, 35], and recent steps towards TMD branching methods are taken in [36–39]. The thesis builds on these works, and carries out original work (partly already submitted for publication, partly about to be submitted for publication) in the following three inter-connected streams:

i) development of the TMD Parton Branching approach in its perturbative and non-perturbative components. This includes the investigation of the logarithmic accuracy of the branching algorithm, the study of dynamical constraints on the parton radiation such as soft-gluon angular ordering, the determination of TMD distributions and the non-perturbative Sudakov evolution kernel.

ii) construction of a TMD parton shower MC event generator. This requires several different components: input TMD distributions and their evolution, initial-state showering algorithm, final-state showering and hadronization, generation of hard scattering matrix elements at leading order (LO) and next-to-leading order (NLO) in perturbation theory, combination of hard scattering matrix elements with TMD distributions and showers via procedures of "matching" and "merging".

iii) application of the computational framework thus developed to make theoretical predictions for production processes and observables of interest at the Large Hadron Collider (LHC). This concentrates on production of a) Z-boson + jets, and b) multi-jets. The main focus is on transverse momentum spectra of Z-bosons and jets; jet multiplicity distributions; differential jet rates (DJR); azimuthal correlations of jet-jet and boson-jet final states.

The structure of the thesis' chapters is as follows. Chapters 1, 2 and 3 are review chapters; Chapters 4, 5 and 6 cover topics described above under stream i); Chapter 7 is devoted to the MC event generator in stream ii); Chapters 8 and 9 treat the subset of applications in stream iii) which are carried out via "matching" techniques; Chapters 10, 11 and 12 treat the subset of applications in stream iii) which are carried out via "merging" techniques.

More precisely, the thesis starts with a brief overview of QCD as a gauge theory of strong interactions (Chapter 1), and of key concepts in the application of QCD to physics at high-energy colliders (Chapter 2). It then reviews the Parton Branching (PB) formulation [38, 39] of the QCD evolution of TMD distributions (Chapter 3). This formulation involves evolution kernels which are theoretically calculable (Sudakov form factors and splitting functions) and input distributions which are to be determined from fits to experimental data. On top of that, angular phase-space constraints ensure consistent TMDs, independent on the resolution scale [39]. The next three chapters of the thesis are devoted to analyzing the various elements of this approach. First, we briefly describe a web-based C++ library of fits and parameterizations of TMD distributions, TMDLIB2 (Chapter 4). This is based on the publication [40]. We also review the published PB-TMD sets [37, 38] that are available in this library for wide applications. TMDLIB2 updates and extends the early library TMDLIB (version 1) and corresponding plotting tool TMDplotter [41]. The subsequent calculations presented in the thesis all rely on the parton distributions accessible from the TMDLIB2 library.

Next, we investigate the dynamical phase-space constraints which enter the PB TMD

evolution, in particular, the soft-gluon angular ordering. This leads us to studying dynamical, i.e. branching-scale dependent, soft-gluon resolution scales (Chapter 5). This study is based on the publication [42]. This study also allows us to perform a comparison of PB TMD results with results from two widely-used approaches in the literature: the coherent branching approach of [10, 43] (CMW) and the single-emission approach of [44–47] (KMRW). Further, using the notion of dynamical soft-gluon resolution scales thus explored, we investigate the perturbative and non-perturbative components of the PB TMD Sudakov form factor (Chapter 6). This investigation will be reported in a forthcoming publication [48]. Here we study analytically the PB logarithmic accuracy at leading logarithmic (LL), next-to-leading logarithmic (NLL) and next-to-next-to-leading logarithmic (NNLL) levels, and perform a comparison of PB TMD results with results from the widely-used Collins-Soper-Sterman (CSS) approach [49, 50]. We also present numerical results on the non-perturbative Sudakov effects embodied in the Collins-Soper (CS) kernel.

We then move on to describe the MC event generator CASCADE3 (Chapter 7), an MC generator based on the PB TMD formalism discussed in the previous chapters. This is based on the publication [51], part of the original work performed during the thesis. This MC generator evolves from the earlier generators [52–54]. We give a self-contained description of the physics picture underlying the MC program, in particular introducing the backward Sudakov form factor for the TMD initial-state showering. We also provide a concise account of all the other components of the program.

The final five chapters of the thesis describe applications of the TMD branching formalism and of its MC implementation. These applications can be subdivided into two sets, according to the method used to combine the TMD shower with hard scattering matrix elements. In the first set of applications, we perform a "matching" of NLO matrix elements, computed from the MADGRAPH5_AMC@NLO [55] event generator, with TMD distributions and showers, following the approach proposed in [36] for the Z-boson transverse momentum spectrum. We apply this NLO matching approach to di-jet production (Chapter 8) and to Z + jet production (Chapter 9). These studies are part of the original work done during the thesis and are reported in the publications [56] (on di-jets) and [57] (on Z + jet). We investigate in particular distributions on the correlation in azimuthal angle $\Delta\phi$ between the two jets and between the Z boson and the jet. Focusing on the back-to-back configurations $\Delta\phi \to \pi$, and scanning the kinematical region of transverse momenta from around 100 GeV all the way up to about 1 TeV, we discuss the possibility to use the azimuthal correlations as detailed experimental probes of TMD dynamics. Such measurements will become feasible in the forthcoming high-luminosity phase of the LHC.

In the second set of applications, we perform original "multi-jet merging" calculations, using the TMD multi-jet merging method [58, 59]. We start by briefly reviewing this method and the results that were already published in Refs. [58, 59] for Z + jets production (Chapter 10). Then we study the production of pure QCD jets (Chapter 11). This original work is to be submitted for publication [60]. We compute predictions based on the TMD merging for multi-jet observables including transverse momenta, multiplicities and event shapes such as thrust, aplanarity, the C-parameter and a few others. We present a phenomenological comparison with experimental measurements which have recently become available from the ATLAS experiment at the LHC.

Finally, we continue the exploration of multi-jet merging techniques by performing a study, for the first time, of Z-boson + jets production at varying vector boson invariant masses (Chapter 12), from about 60 GeV to about 800 GeV. This is original work, in progress and about to be submitted for publication [61]. The key idea is to extend the merging technique by introducing a "sliding" merging scale parameter, namely, a merging scale which varies with the hard scale of the process set by the vector boson invariant mass. We present the analysis of the differential jet rates (DJR) associated to $Z +$ jets in a wide range of invariant masses; based on this, we discuss the mass dependence of the jet merging scale. This investigation is topical, as measurements of $Z +$ jets scanning the invariant mass kinematical region have been presented by the CMS experiment at the LHC, and will be continued in the upcoming LHC runs.

1

QCD as a gauge field theory of the strong interaction

This chapter is devoted to provide a compact description of Quantum Chromodynamics (QCD) as the $SU(3)$ gauge field theory describing one of the four fundamental interactions of nature: the strong interaction. The concepts that are introduced in this chapter serve as basic building blocks of QCD and the work of this thesis. Chapter 2 is a natural continuation of this chapter and concentrates on high energy proton-proton (pp) collisions.

1.1 Symmetries of gauge field theories

The Standard Model (SM) of elementary particle physics consists of quantum gauge field theories obeying the following Lie group structure:

$$SU(3) \times SU(2) \times U(1), \tag{1.1}$$

where $SU(n)$ stands for special unitary group of order n. Three out of the four fundamental interactions in physics are described by gauge theories: the strong nuclear interaction, the weak nuclear interaction and the electromagnetic interaction. Quantum electrodynamics (QED) is the abelian gauge field theory of $U(1)$ that describes the interactions among electrically charged particles through photon exchange. $SU(2)$ is the symmetry group of the weak interaction governed by massive W and Z bosons. The underlying symmetries of the strong interaction, describing the behavior of quarks and gluons, are determined by the symmetries of the group $SU(3)$ and its Lie algebra, which contains the generators of the group's transformations.

Mechanisms of these fundamental interactions find their origin in gauge symmetry. The invariance of a Lagrangian $\mathcal{L}$ under gauge transformations, i.e. *gauge invariance*, is an important ingredient to construct the quantum gauge field theories of the SM. Gauge transformations can be interpreted as rotations of internal space. If θ^a is a phase angle and T^a is a generator of the Lie algebra, a local gauge transformation of a field $\psi(x)$ can be written as:

$$\psi(x) \rightarrow G(x)\psi(x) = e^{i\theta^a(x)T^a}\psi(x). \tag{1.2}$$

Equation (1.2) is a local gauge transformation, i.e. the phase is x-dependent. In order to construct a general and physical relevant theory, local gauge invariance is a strong principle and serves as the symmetry of the gauge field theories for the fundamental interactions.

The number of generators T^a, which are represented by $n \times n$ dimensional matrices, is equal to the dimension of the Lie algebra. The commutation relation between two generators is a binary operation that reveals the symmetry of a group which in general writes [62]:

$$\left[T^a, T^b\right] = i f^{abc} T^c,\tag{1.3}$$

where f^{abc} stand for the fully antisymmetric structure constants of the Lie algebra. Groups of order one are *abelian*, i.e. the generators commute. Generators of groups with an order larger than 1 have anti-commuting generators and are *non-abelian*.

A classical Lagrangian density of the form $\mathcal{L}(\psi, \partial\psi)$ is not invariant under local gauge transformations, because the transformation of the field ψ is represented as follows:

$$\partial^\mu (G\psi) = (\partial^\mu G)\psi + G(\partial^\mu \psi).\tag{1.4}$$

The term that contains the derivative of the gauge transformation G destroys the invariance of the Lagrangian under these transformations. This is solved by replacing the partial derivative by a covariant derivative:

$$D_\mu = \partial_\mu - i g A_\mu^a T^a,\tag{1.5}$$

which leads to a gauge invariant Lagrangian $\mathcal{L}(\psi, A_\mu^a)$. A_μ^a are the gauge boson fields representing particles with integer spin that are subject to Bose-Einstein statistics. There are as many fields A^a as there are generators T^a. The fields ψ represent the fermions of the theory that are subject to Fermi-Dirac statistics. Terms $D_\mu \psi$ in the Lagrangian imply that the vector boson fields A_μ^a interact with the scalar fermion fields ψ.

A gauge transformation of the gauge boson fields in the limit of small angles ($\theta^a \ll 1$) differs for abelian and non-abelian groups. In the non-abelian case a gauge invariant transformation of A_μ^a is of the form

$$A_\mu^a \rightarrow A_\mu^a + \frac{1}{g}\partial_\mu \theta^a - f^{abc}\theta^b A_\mu^c,\tag{1.6}$$

where the last term is the anti-symmetric part inherent to non-abelian gauge theories. The second term is equal to the gauge transformation of fields in electromagnetism (then θ represents the scalar potential and g the electric charge e). The coupling strength of the strong interaction is $\alpha_s = g^2/4\pi$.

We limit the scope of this chapter to focus only on $SU(3)$, the symmetry group of QCD, which has eight generators T^a that are the independent anti-Hermitian 3×3 Gell-Mann matrices. The gauge vector boson fields correspond to gluons, which are the mediator particles of the strong interaction. Charges are intrinsic properties of the elementary particles of the fundamental interactions. The strong interaction is governed by *color* charge. Quarks are color charged particles that are excitations of the fermion fields of QCD. They are associated with the fundamental representation of the $SU(3)$ group because they carry one of the three fundamental colors: red, green or blue. Gluons are

associated with the adjoint representation of SU(3), since they are superposition color-anticolor states. The color charge of both quarks and gluons leads to multiple types of fermion-boson, boson-boson interactions.

1.2 The QCD Lagrangian

Field strength tensors in a non-abelian gauge theory contain (derivatives of) multiple gauge fields, the gluon fields A_μ^a in the case of QCD. This non-abelian field strength tensor is written as

$$F_{\mu\nu}^a = \partial_\mu A_\nu^a - \partial_\nu A_\mu^a + g f^{abc} A_\mu^b A_\nu^c. \tag{1.7}$$

From the gauge symmetry group properties, the gauge invariant Yang-Mills Lagrangian density is constructed from Dirac fields ψ and field strength tensor products as:

$$\mathcal{L}_{\text{YM}}(\psi, A^a) = \sum_f \bar{\psi}_f \left(i\slashed{D} - m_f \right) \psi_f - \frac{1}{4} F_{\mu\nu}^a F^{\mu\nu a}, \tag{1.8}$$

where the covariant derivative $\slashed{D} = \gamma^\mu D_\mu$ and γ^μ are the Dirac matrices. The index f in Eq. (1.8) is a flavor index and the sum runs over all six quark fields (up, down, strange, charm, bottom and top). The masses of the quarks are represented by m_f. The Dirac fields ψ in QCD have three color components and correspond to quarks.

The Yang-Mills Lagrangian is common for any non-abelian gauge field theory. It contains terms with products of fields that represent particle interactions. Products of ψ with A_μ^a represent quark-gluon interactions and quadratic terms in A_μ^a represent gluon self-interactions. A detailed calculation of the interaction terms can be found in Ref. [63].

The use of the Yang-Mills Lagrangian of Eq. (1.8) leads to non-physical behavior, because for longitudinal fields ($A^\mu \sim ck^\mu$) the propagation amplitude diverges. In order to define a physical propagator for the gauge field, the Fadeev-Popov method [64] is used to "fix the gauge". The consequence of gauge fixing in a non-abelian theory is the necessity of introducing new, unphysical, so-called "ghost" fields c. With that, the full Lagrangian density of QCD becomes:

$$\mathcal{L}_{\text{QCD}} = \sum_f \bar{\psi}_f (i\slashed{D} - m_f)\psi_f - \frac{1}{4} F_{\mu\nu}^a F^{\mu\nu a} - \frac{1}{2\xi} (\partial_\mu A^\mu)^2 - \bar{c}^a \partial_\mu D_{ac}^\mu c^c, \tag{1.9}$$

where ξ is the gauge parameter from gauge fixing and D_{ac}^μ is the covariant derivative in the adjoint representation:

$$D_{ac}^\mu = \partial^\mu \delta_{ac} + g f_{abc} A^{\mu b}. \tag{1.10}$$

From the Lagrangian in Eq. (1.9), the *Feynman rules* of QCD can be determined. With these, all possible Feynman-diagrams that include strong interactions can be drawn and the transition probability matrix elements can be calculated perturbatively. The Feynman rules contain all possible vertices and the propagators of the color charged fields. These follow directly from the Lagrangian which can be subdivided in a propagation/free term and an interaction term: $\mathcal{L} = \mathcal{L}_{\text{free}} + \mathcal{L}_{\text{interacting}}$. The vertices are the factors from the interacting part of the Lagrangian where multiple (more than two) fields are present in each term. The propagators are related to the factors from the free Lagrangian that

only contain terms that are quadratic in the fields. A more detailed description of the calculation of vertices and propagators can be found in Ref. [63].

In Tab. 1.1, all the propagators and vertices of strongly interacting particles are given. These rules are however not sufficient for a full theory of the strong interaction because they lead to divergences in the case of loop diagrams. Ultraviolet (UV) divergences arise due to large momenta that can circulate in these loops. Another limit in which the calculation of Feynman-diagrams is not sufficient is when initial- or final-state particles, represented by legs in the diagrams, radiate soft (with low energy) or collinear (at small angle) particles. These emissions lead to infrared (IR) divergences that are dealt with in Chapter 2. In the next section, we will deal with UV divergences by discussing the renormalization of the theory.

1.3   Renormalization of a gauge field theory

Diagrams that contain loops have UV divergent probability amplitudes. The key idea behind renormalization is that the divergences that arise are absorbed into a redefinition of physical parameters of the theory. A theory is renormalizable if a finite number of quantities is needed to absorb all infinities. QCD is proven to be a renormalizable theory [65].

The procedure of renormalization consists of three steps: 1) regularization of the divergent amplitudes, 2) rescaling all physical parameters and fields, and 3) computing all the finite physical quantities.

1.3.1   Structure of renormalization

Dimensional regularization   This is the most commonly used regularization method, because it preserves the physical symmetries like gauge- and Lorentz invariance. The key idea of dimensional regularization is to calculate the momentum space integral ($\int d^4k/(2\pi)^4$) of a probability amplitude in general for d dimensions. For less than $d = 4$ dimensions, the UV divergence disappears and the integral is calculable analytically. By applying $d = 4 - 2\epsilon$ (with $\epsilon \ll 1$), the UV divergence is translated to a pole in $1/\epsilon$. This reduction of dimensions goes along with the introduction of a mass-scale parameter: the renormalization scale μ_R. The integration over d^4k transforms as

$$\frac{d^4k}{(2\pi)^4} \to (\mu_R^2)^\epsilon \frac{d^{4-2\epsilon}k}{(2\pi)^{4-2\epsilon}}. \tag{1.11}$$

Rescaling   In the rescaling procedure, a bare observable G_0 is written as the product of a renormalization constant Z and a renormalized observable G:

$$G_0(p_i, \alpha_0) = ZG(p_i, \alpha, \mu_R), \tag{1.12}$$

with $Z = 1 + \delta$ and δ representing the *counterterms* which contain the divergences that come from the $1/\epsilon$ pole. α_0 is the bare coupling strength of the gauge theory, α is the

---
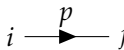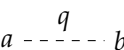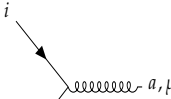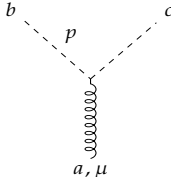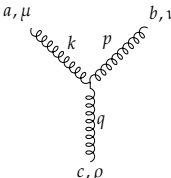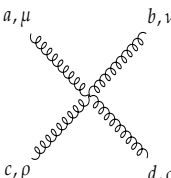
QCD Feynman Rules

Quark propagator	$i \xrightarrow{\ p\ } j$	$= \dfrac{i\delta^{ij}(\slashed{p} + m)}{p^2 - m^2 + i\epsilon}$
Gluon propagator	$a, \mu \ \overset{k}{\text{\textcurrency}} \ b, \nu$	$= \dfrac{i\delta^{ab}}{k^2 + i\epsilon} \left[g^{\mu\nu} - (1-\xi)\dfrac{k^\mu k^\nu}{k^2} \right]$
Ghost propagator	$a \ \text{-----} \ b$ q	$= \dfrac{i\delta^{ab}}{q^2 + i\epsilon}$
Quark-gluon vertex		$= -ig\gamma^\mu T_{ij}{}^a$
Ghost vertex		$= gf^{abc}p^\mu$
Triple gluon vertex		$= \begin{aligned} gf^{abc}\,(g^{\mu\nu}(k-p)^\rho &+ g^{\nu\rho}(p-q)^\mu \\ &+ g^{\rho\mu}(q-k)^\nu) \end{aligned}$
Quartic gluon vertex		$= -ig^2 \left[\begin{array}{l} f^{abe}f^{cde}\,(g^{\mu\nu}g^{\rho\sigma} - g^{\mu\rho}g^{\nu\sigma}) \\ + f^{ace}f^{bde}\,(g^{\mu\rho}g^{\nu\sigma} - g^{\mu\nu}g^{\rho\sigma}) \\ + f^{ade}f^{bce}\,(g^{\mu\rho}g^{\sigma\nu} - g^{\mu\sigma}g^{\rho\nu}) \end{array} \right]$

Table 1.1: Feynman rules for color charged particles [63]. Quarks are straight lines, gluons are wavy lines and ghost particles are dashed lines. Flavor indices are denoted by i or j and color indices by $\{\mu, \nu, \rho, \sigma\}$. The four-momenta of the particles are written along the lines with Roman letters $\{k, p, q\}$. In vertices, the four-momenta point inwards. The Minkowski metric is $g^{\mu\nu} = \text{diag}(1, -1, -1, -1)$.

renormalized coupling strength (the strong coupling α_s in QCD) and p_i are all momenta that are involved. All fields and parameters of the theory should be rescaled so that relations among the renormalization constants Z_i can be constructed.

Calculation of physical parameters   By calculating all the renormalization constants Z, all renormalized fields and parameters can be extracted from the bare quantities and the probability amplitudes become finite.

1.3.2   Renormalization group

The renormalization procedure implies that all the parameters of the quantum field theory become scale-dependent. The QCD Lagrangian does however not contain any dependence on the renormalization scale μ_R. Therefore, physical quantities should not depend on the choice of this scale. This insight leads to continuously generated transformations that leave the Lagrangian invariant. Together these are referred to as the renormalization group (RG). It does, however, not have the mathematical structure of a group. This section gives a brief overview of the RG, for more details we refer the reader to Chapter 2 of Ref. [7] or Chapter 12 of Ref. [63].

With the condition that a bare physical quantity (denoted by G_0) is independent of the renormalization scale μ_R, one can describe the μ_R-dependence of the parameters in the theory. The renormalization group equation (RGE) is:

$$\frac{dG_0}{d\ln\mu_R^2} = 0. \tag{1.13}$$

With the relation between the renormalized and bare quantities given in Eq. (1.12) this becomes

$$\frac{1}{Z}\frac{d(ZG)}{d\ln\mu_R^2} = \frac{\partial G}{\partial\ln\mu_R^2} + \frac{\partial G}{\partial\alpha_s}\frac{\partial\alpha_s}{\partial\ln\mu_R^2} + G\frac{\partial\ln Z}{\partial\ln\mu_R^2} = 0. \tag{1.14}$$

The QCD β-function and *anomalous dimension* γ are defined as coefficients of the RG equation as:

$$\beta(\alpha_s) \equiv \frac{\partial\alpha_s}{\partial\ln\mu_R^2}, \qquad\qquad \gamma(\alpha_s) \equiv \frac{\partial\ln Z}{\partial\ln\mu_R^2}. \tag{1.15}$$

The beta function characterizes how the coupling constant changes with the energy scale. A non-zero QCD β-function thus implies that the coupling strength α_s is dependent on the scale μ_R. The exact form of the strong coupling $\alpha_s(\mu_R)$ is derived in the next section.

Anomalous dimensions describe how fields and operators scale under renormalization. The physical observable G can be measured at a physical scale $\mu_R = Q$. To solve the RG equation (1.14), insert the definitions of the beta function and anomalous dimension from Eq. (1.15) and rescale the parameters by Q changing $G(p_i, \alpha_s, \mu_R)$ into $G(x_i, \alpha_s, t)$ with $x_i = p_i/Q$ and $t = \ln(Q^2/\mu_R^2)$ to yield

$$\left[-\frac{\partial}{\partial t} + \beta(\alpha_s)\frac{\partial}{\partial\alpha_s} + \gamma(\alpha_s)\right]G(x_i, \alpha_s, t) = 0, \tag{1.16}$$

which is the *Callan-Symanzik equation* [63]. It defines the evolution of an observable G in scale t in relation with the running coupling and the anomalous dimension. The dependence on x_i is not important for further derivations and is left out in the following notation. The partial differential equation can be solved with a boundary condition. The value of an observable G is known at the scale of the measurement where $t = 0$, this defines the boundary condition that is $G(0, \alpha_s(t))$.

$$G(t, \alpha_s) = G(0, \alpha_s(t)) \exp \left\{ \int_0^t dt' \gamma(\alpha_s(t')) \right\}. \tag{1.17}$$

This structure of evolution explains the *breaking of scale invariance*. Physical quantities, eg. the coupling strength, quark masses and structure functions (describing the content of hadrons), depend on the probing scale Q^2. The exponential factor in Eq. (1.17) is a "resummation" factor that resums logarithms of the form $\ln(Q^2/\mu_R^2)$.

The renormalization group serves to derive the running of the QCD coupling α_s and the concept of asymptotic freedom. These are discussed in the next section.

1.4 The running strong coupling

In gauge field theories the coupling strength is scale- (μ_R-) dependent as a consequence of the regularization procedure. This is referred to as a "running coupling". Both α (the coupling strength of QED) and α_s (the coupling strength of QCD) are running. At the Z boson mass $m_Z \simeq 91.2$ GeV, the electromagnetic coupling is $\alpha(m_Z) \sim 1/128$ and the strong coupling is $\alpha_s(m_Z) \sim 0.12$. When these parameters are smaller than 1, they are well suited for perturbation theory in which quantities are expressed as power series expansions in α or α_s. However, the need to truncate the perturbation series and calculate the lowest order coefficients causes systematic uncertainties. In general, leading order (LO) α_s calculations give a good qualitative idea of observables, next-to-leading order (NLO) α_s^2 calculations give a more quantitative picture and next-to-next-to-leading order (NNLO) calculations α_s^3 lead to very high precision results.

The QCD coupling constant $\alpha_s(\mu_R)$ decreases as the energy (μ_R) increases, whereas the QED coupling constant $\alpha(\mu_R)$ increases towards high energies. Collider processes unavoidably include interactions at low energy scales, which complicates QCD calculations for collider processes compared to QED calculations.

The exact dependence of α_s on μ_R can be expressed in terms of the QCD β-function given in (1.15), which can be written as a series expansion:

$$\begin{aligned} \beta(\alpha_s) &= -\alpha_s^2 \sum_{n=0}^{\infty} \beta_n \alpha_s{}^n \\ &= -\beta_0 \alpha_s^2 - \beta_1 \alpha_s^3 - \beta_2 \alpha_s^4 + O(\alpha_s^5). \end{aligned} \tag{1.18}$$

The determination of the coefficients β_n of the RG β-function requires the calculation of loop diagrams to order $(n + 1)$ to obtain the renormalization constants Z_i.

The first coefficient of the β-function is

$$\beta_0 = \frac{1}{12\pi}(11C_A - 4T_R N_f), \tag{1.19}$$

where C_A is the Casimir invariant in the adjoint (A) representation (with dimensionality $n = N_c$), which is equivalent to the number of colors N_c. T_R is the trace invariant (in the fundamental representation) and N_f is the number of quark flavours. Color factors are calculated with color algebra which uses the symmetries of the SU(3) group. With this, and using $N_c = 3$ as the number of colors, the following values are obtained: $T_R = 1/2$, $N_f = 6$, $C_A = 3$ and $C_F = (N_c^2 - 1)/2N_c = 4/3$ [66, 67]. C_F represents the Casimir invariant in the fundamental representation.

The RGE on the left side of Eq. (1.15) can approximately be written by truncating Eq. (1.18):

$$\frac{\partial \alpha_s}{\partial \ln \mu^2} \approx -\beta_0 \alpha_s^2 \tag{1.20}$$

when α_s is sufficiently small. Solving this differential equation yields an expression for the running coupling $\alpha_s(\mu)$ at first order (one-loop α_s):

$$\alpha_s(\mu) = \frac{\alpha_s(\mu_0)}{1 + \beta_0 \alpha_s(\mu_0) \ln(\mu^2/\mu_0^2)}. \tag{1.21}$$

For QCD, β_0 is negative, such that:

$$\alpha_s(\mu) < \alpha_s(\mu_0), \qquad \text{for } \mu > \mu_0. \tag{1.22}$$

This phenomenon is called *asymptotic freedom* implying that *partons*, the collective name for quarks and gluons as the constituents of hadrons, are "free" particles at high energies. At low energies, α_s diverges. In that regime, color charged particles are strongly coupled. This phenomenon is called *confinement*. A detailed description on asymptotic freedom and confinement can be found in Ref. [7].

The decrease of the coupling strength with the energy can be physically related to virtual emissions of gluons and quarks that respectively screen and anti-screen the color charge. The first term of the β-function given in (1.19) represents the anti-screening due to gluon loops and the second term represents the screening due to quark/anti-quark pairs. Eventually the anti-screening effect dominates.

QCD gives an expression of α_s in relation to a scale μ but does not give absolute values. The value of α_s needs to be measured experimentally. It can be measured through various processes; measurements from many experiments are averaged by the Particle Data Group and shown in Fig. 1.1. For reference, the value of the coupling is usually given at the mass of the Z boson (m_Z).

The expression in Eq. (1.21) contains a singularity at a fixed scale Λ_{QCD}, the QCD parameter. It takes the value $\Lambda_{QCD} \simeq 200$ MeV $\simeq 1$ fm^{-1}. In case of $\mu \gg \Lambda_{QCD}$, the strong coupling $\alpha_s \ll 1$ and quantities depending on μ can be calculated with perturbation theory. Effects at scales near the QCD scale are non-perturbative. The renormalization group approach in this regime is not sufficient. In this regime partons are confined into hadrons and not behaving as free particles. Hadrons are (non-elementary) particles that are still not fully understood because of the non-perturbative dynamics of the hadronic constituents. Non-perturbative models for hadronization or lattice QCD provide acceptable results describing the formation of hadrons.
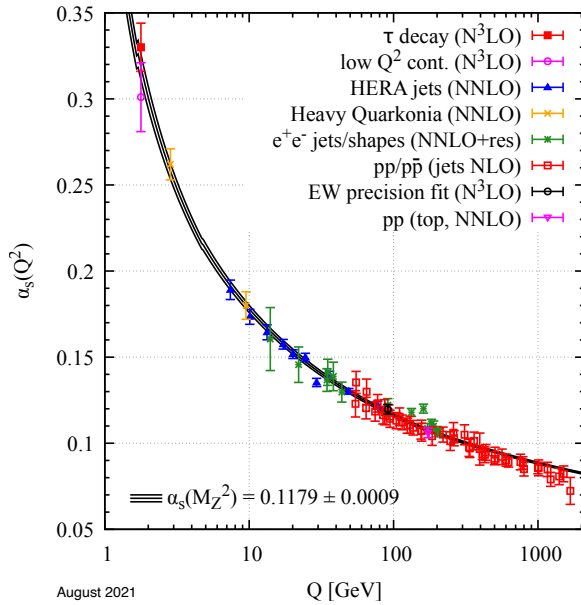
Figure 1.1: Extractions of α_s from various physical observables [68].

1.5   Summary

From this brief chapter where we introduced basic ingredients from QCD serving the subsequent chapters, here are the important messages:

- QCD is a non-abelian gauge field theory. From its Lagrangian, the fundamental interactions among color charged particles, quarks and gluons, can be derived. Not only do the fermions (quarks) interact via a boson (gluon), there are also boson self-interactions which make the theory more complex than QED.

- QCD is a renormalizable theory. The renormalization of fields introduces the dependence on a renormalization scale μ_R. Renormalization group equations are derived from independence on μ_R.

- The QCD coupling α_s runs. The coupling strength is large at low energy scales and small at high energies.

- The QCD scale Λ_{QCD} is a fundamental energy scale of QCD where $\alpha_s \rightarrow \infty$.

Application of QCD to particle collision processes

In this chapter, we introduce the concepts in QCD that allow us to make calculations for particle collision processes at high energies. The previous chapter has indicated why calculations in QCD are complicated; since the coupling strength α_s grows towards small scales, we can not purely rely on perturbation theory. In physical experiments, non-perturbative, hadronic elements are present. Factorization of the cross section and evolution of parton densities allow to combine non-perturbative input with perturbatively calculable objects. We derive these principles in section 2.2 starting from the deep inelastic scattering (DIS) process.

2.1 Introduction

Electron-hadron collisions are well-suited for examining hadron structure and studying parton distribution functions. The study of electron-proton scattering took place already in the 1950s at low energies of the order of 0.1 GeV [69]. Interactions at these energies primarily result in elastic scatterings. Observation of hadron substructure requires higher center-of-mass energies such that the interaction becomes inelastic and causing the electron to break the proton apart. At very high momentum exchanges, the interaction is "deep". Deep inelastic electron-proton scattering (DIS) is a widely studied process both theoretically as well as experimentally. The HERA (Hadron-Elektron-Ring-Anlage) collider at the Deutsches Elektronen-Synchrotron (DESY) in Hamburg has been an important facility for studies to hadronic structure by colliding electrons and protons at a center-of-mass energy $\sqrt{s}$ = 320 GeV. Accurate calculations of the DIS cross section σ require a formalism to combine the perturbatively calculable high energetic interactions and the non-perturbative and soft hadronic interactions. The *collinear factorization* theorem has been very successful in combining the soft and hard dynamics. This is the topic of section 2.2, where the concepts of factorization of the cross section and evolution of parton distribution functions are introduced. These concepts are crucial to perform calculations of strong interaction processes at high energies.

At the Large Hadron Collider (LHC), two beams of protons are accelerated and brought to collisions. The interacting partons exchange a large momentum Q which can cause

the production of heavy particles, e.g. electroweak gauge bosons, Higgs bosons, top quarks or other Standard Model (SM) particles or particles Beyond the SM (BSM). The possibility to go to very high energies in proton-proton collisions lead to the discovery of the Higgs boson in 2012 [70, 71]. Increasing the accuracy of theoretical predictions of LHC processes requires to go beyond the collinear factorization theorem that was introduced for DIS. For example, the transverse momentum spectrum of the Z boson in Drell-Yan (DY) production, the topic of section 2.4, cannot be described well by collinear factorization. This can be overcome by numerical simulations of parton radiation that are taken by Monte Carlo event generators, which are briefly explained in section 2.3. A formal and analytical calculation of the DY p_T spectrum is obtained by including transverse momentum in the factorization theorem, explained in section 2.5.

2.2   Deep-inelastic electron-hadron scattering

Consider the inclusive process of electron-hadron scattering $e^-(k) + h(P) \rightarrow e^-(k') + X$, as illustrated in Fig. 2.1. Here, h represents the incoming hadron carrying momentum P and e is the incoming electron carrying momentum k. Any hadronic final state resulting from the scattered parton and the remnant of the hadron is denoted by X. The hard scattering interaction is defined by the exchange of a virtual photon γ^* with four-momentum q between the electron and a constituent of the hadron, a *parton*. The scattering is considered "deep" when the squared momentum exchange $q^\mu q_\mu$ is large.
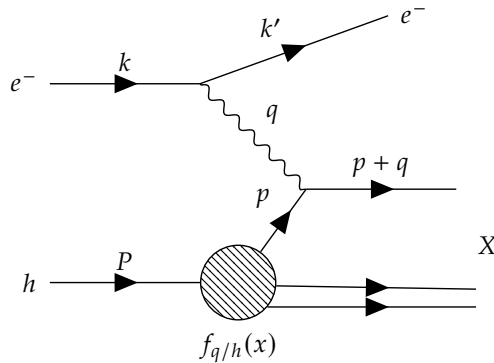
Figure 2.1: Deep inelastic scattering with $p = xP$ the initial longitudinal parton momentum, $Q^2 = -q^2$ the photon virtuality, k the initial and k' the final electron momentum and $f_{q/h}(x)$ the probability distribution function of partons in the hadron.

There are two degrees of freedom in DIS, assuming fixed center-of-mass energy $s = (P + k)^2$. A convenient option for parametrization of the kinematical degrees of freedom includes virtuality Q^2 and Bjorken x:

$$Q^2 \equiv -q^\mu q_\mu, \tag{2.1}$$

$$x = \frac{Q^2}{2P \cdot q}. \tag{2.2}$$

When Q^2 is large, the interaction of the photon with a parton occurs in a short time and

at short distance. The photon travels a distance of $\Delta x_\gamma \sim 1/\sqrt{Q^2} \ll 1$ fm, significantly smaller than the size of a hadron. The partonic hard scattering event is calculable perturbatively and is an *infrared safe* factor, which means that it is generally not sensitive to the long time dynamics in the hadron. Dynamics at lower energies than Q^2 need to be considered as well due to the presence of multiple partons in the incoming hadron.

As seen from the photon in the infinite momentum frame, where the hadron has a large velocity ($v \approx c$) anti-parallel to the direction of the photon, the hadron is Lorentz-contracted in longitudinal direction. Interactions among partons occur time-dilated in this frame, making them quasi-free particles with respect to the photon which interacts with only one parton out of the hadron. In particular, when $Q^2 \gg \Lambda^2_{QCD}$, the probability for multiple partons interacting with the photon is small[1]. This high resolution of the photon ensures that dynamics in the proton and the hard scattering do not interfere, forming the foundation for the factorization theorem. The dynamics of the hard interaction are completely decoupled from the hadronic dynamics. At the lowest order calculation, in which color charge emissions are not taken into account, the factorized DIS cross section is equivalent to that of the *parton model* (PM) [72, 73] where it is factorized in a partonic matrix element for the interaction of the photon with one parton $\sigma_{\gamma i}$ and a hadronic function $f_{i/h}$ that represents the non-perturbative input of dynamics in the hadron:

$$\sigma_{\gamma h}(x, Q^2) = \sum_i \sigma_{\gamma i}(x, Q^2) f_{i/h}(x), \tag{2.3}$$

where $f_{i/h}(x)$ describes the probability of finding a parton with flavor i and momentum fraction x in hadron h, which is referred to as the *parton distribution function* (PDF) or parton density. PDFs are long-distance, hadronic functions that cannot be calculated from first principles with perturbation theory. They need to be extracted from experimental data.

Eq. (2.3) is not a formulation of the cross section that takes into account QCD. For this, higher order diagrams need to be included. QCD radiative corrections, terms with α_s^n ($n \geq 1$), are essential for a correct description of the DIS process at high energies. The PM, that considers the constituents of the proton to be point-like particles, does not include these corrections and does not provide a description of the breaking of scale invariance of the parton density $f_{i/h}$. In the next subsection, we exploit structure functions of QCD that allow for a factorized formulation and a definition of PDFs.

2.2.1 Structure functions and parton distribution functions

The leading order DIS process is calculated purely with QED. Higher order corrections from QCD require the inclusion of the transition probability of a hadron h into any hadronic final state X. For this, hadronic structure functions F_i ($i \in \{1, 2\}$) are included in the cross section as

$$\frac{d\sigma_{\gamma h}}{dx dQ^2} = \frac{4\pi\alpha^2}{xQ^4} \left((1 - y + \frac{y^2}{2})F_2(x, Q^2) - \frac{y^2}{2}F_L(x, Q^2) \right), \tag{2.4}$$

---

[1]The photon-parton interaction probability is suppressed by a factor of Λ^2_{QCD}/Q^2.

where $y = \frac{q \cdot p}{k \cdot p}$ is the inelasticity that describes the fraction of energy lost by the incident lepton in the proton's rest frame and $F_L = F_2 - 2xF_1$ is the longitudinal structure function [7]. In the PM the structure functions "scale", i.e. they do not depend on the energy scale Q^2, and F_2 is equal to the PDF multiplied with the electric charge of the quark (e_i) squared:

$$F_{2,PM}(x) = 2xF_{1,PM}(x) = \sum_i e_i^2 f_{i/h}(x). \tag{2.5}$$

The first equality also holds beyond the parton model and is known as the *Callan-Gross relation*, which is equivalent to $F_L(x) = 0$.

The transition to a QCD description requires a quantum field theory approach in which higher order corrections (powers of α_s) are taken into account. As seen in Chapter 1, renormalization of observable quantities in QCD breaks the scale invariance. Therefore, the structure functions become scale (Q) dependent.
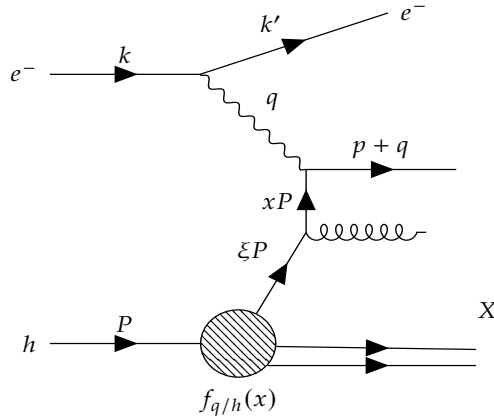
Figure 2.2: The DIS process including first order QCD radiation.

The structure functions need to be regularized in order to remove ultraviolet (UV) and infrared (IR) divergences. UV divergences are dealt with by renormalization. IR divergences arise from *collinear*, i.e. small angle, parton emissions in the higher order corrections. The collinear divergent part can be separated, i.e. *factorized*, from the finite part, coming from wide-angle emissions, by introducing a *factorization scale* μ_F. The structure functions and cross section cannot depend on this scale. The regularized structure function F_k is a convolution of a PDF (the soft, IR sensitive part) and an hard, IR safe function C:

$$F_k(x, Q^2) = \sum_i \int_x^1 d\xi\, C_k^i \left(\frac{x}{\xi}, \frac{Q^2}{\mu_F^2}, \frac{\mu_F^2}{\mu_R^2}, \alpha_s(\mu_R^2) \right) f_{i/h}\left(\xi, \mu_F^2, \alpha_s(\mu_R^2) \right) + \mathcal{O}\left(\frac{\Lambda_{QCD}^2}{Q^2} \right), \tag{2.6}$$

with $k = \{2, L\}$ and ξ the longitudinal momentum fraction of the incoming parton before splitting. The C function is calculable in perturbation theory. With the scale choice $\mu^2 \equiv \mu_R^2 = \mu_F^2$, which we apply throughout the rest of this chapter, the series expansion of the C-function can be written as:

$$C_k^i \left(\frac{x}{\xi}, \frac{Q^2}{\mu^2}, \alpha_s(\mu^2) \right) = \sum_{n=0}^{\infty} \left(\frac{\alpha_s(\mu^2)}{2\pi} \right)^n C_k^{i\,(n)} \left(\frac{x}{\xi}, \frac{Q^2}{\mu^2} \right). \tag{2.7}$$

Truncation of the series expansion of C after the first term corresponds to the PM since $C_k^{i\,(0)}(x/\xi) = e_i\delta(1 - x/\xi)$. There is an arbitrariness to the higher order coefficients of this function because the finite, non-divergent terms can be put either to C or to f. A specific choice of distributing the finite terms (i.e. not logarithmically divergent) in the expansion of Eq. (2.7) is characterized by the *factorization scheme*.

A Mellin transformation[2] [74] converts the convolution of Eq. (2.6) into a normal product containing the Mellin moments (indicated by index N) of each function. This is convenient to derive expressions for the μ dependence of the separate functions. The structure functions' Mellin moments are written as:

$$F_{k,N}(Q^2) = \sum_i C_{k,N}^i\left(\frac{Q^2}{\mu^2}, \alpha_s(\mu^2)\right) f_{i/h,N}(\mu^2). \tag{2.8}$$

The μ dependence of PDFs and structure functions implies the breaking of scale invariance as discussed in Sec. 1.3.2. PDFs are however universal objects, i.e. independent on the process. Structure functions are observable quantities and form the backbone of the fitting procedure of PDFs. DIS serves well for extraction of structure functions. Other types of collisions involving hadrons can also allow for fits of PDFs to data.

2.2.2 DGLAP evolution of parton distributions

The renormalization group equation given in Eq. (1.13) applies to observable quantities like structure functions. Together with the factorized form of the structure function as given in Eq. (2.8), leaving the parton flavor indices out, the RGE can be schematically written as:

$$\mu^2\frac{d}{d\mu^2}F_{k,N}(Q^2) = \frac{d}{d\ln\mu^2}\left[C_{k,N}\left(\frac{Q^2}{\mu^2}, \alpha_s(\mu^2)\right) f_N(\mu^2)\right] = 0. \tag{2.9}$$

The solution of this equation is a Callan-Symanzik equation for the hard function C and one for the parton densities f (leaving out the Mellin index N for simplicity):

$$-\frac{1}{C}\frac{dC}{d\ln\mu^2} = \frac{1}{f}\frac{df}{d\ln\mu^2} = \gamma(\alpha_s(\mu^2)), \tag{2.10}$$

with γ the perturbatively calculable *anomalous dimension* that has the series expansion:

$$\gamma(\alpha_s) = \sum_{n=1}^{\infty} b_n\alpha_s^n. \tag{2.11}$$

Equations (2.10) are not ordinary differential equations though, because the terms C and f also depend on physical scales Q and m. Integrating the last equality in Eq. (2.10) over $\ln\mu^2$ from low scale μ_0 up to high scale Q yields:

$$f(Q^2) = f(\mu_0^2)\exp\left\{\int_{\mu_0^2}^{Q^2}\frac{d\mu'^2}{\mu'^2}\gamma\left(\alpha_s(\mu'^2)\right)\right\}. \tag{2.12}$$

---

[2]A Mellin transformation of any function $f(x, \mu)$ is defined as: $f_N(\mu) = \int_0^1 dx\, x^{N-1}f(x, \mu)$

Logarithmic scaling violation of parton distribution functions arises here as described in Chapter 1. The scaling is broken via the anomalous dimension $\gamma(\alpha_s)$. The integration over μ' has the interpretation of evolution of a hadron from a low scale μ_0 up to a high scale μ (usually taken to be the hard scale Q). This exponential factor resums large logarithmic factors of the form $\alpha_s^n \ln^n(Q^2/\mu_0^2)$ that become large when μ_0 is small compared to Q (i.e. evolution over a large energy range):

$$\exp\left\{\int_{\mu_0^2}^{Q^2} \frac{d\mu'^2}{\mu'^2}\gamma(\alpha_s(\mu'^2))\right\} \simeq \exp\left\{b_1\alpha_s\ln\frac{Q^2}{\mu_0^2}\right\} \tag{2.13}$$

$$= \sum_{n=1}^{\infty}\frac{1}{n!}(b_1\alpha_s)^n\ln^n\left(\frac{Q^2}{\mu_0^2}\right);$$

where we applied the first order term of the expansion given in Eq. (2.11). This is renormalization group (RG) resummation of large logarithms, for hard scattering scales much larger than the hadronic scale $Q^2 \gg \mu_0^2 \simeq 1\,\mathrm{GeV}$, to all orders in the strong coupling.

Equations (2.10) can be rewritten in more detail by reintroducing the flavor indices. The anomalous dimension is then represented as matrix kernel where the diagonal elements are kernels for evolution with flavor conservation and non-diagonal elements represent the possibility of flavor changes. The evolution equations of PDFs are then written as:

$$\frac{d}{d\ln\mu^2}f_a(\mu) = \gamma_{ab}(\alpha_s(\mu))f_b(\mu). \tag{2.14}$$

The result is brought to coordinate space through the inverse Mellin transformation. The anomalous dimension in coordinate space is written as P_{ab}:

$$\gamma_{ab,N}(\alpha_s) = \int_0^1 dz\, z^{N-1}P_{ab}(\alpha_s, z), \tag{2.15}$$

where $P_{ab}(\alpha_s, z)$ are known as the *Altarelli-Parisi splitting functions* [75]. These are perturbatively calculable functions in powers of α_s:

$$P_{ab}(\alpha_s, z) = \sum_{n=1}^{\infty}\left(\frac{\alpha_s}{2\pi}\right)^n P_{ab}^{(n-1)}(z). \tag{2.16}$$

The interpretation of the functions $P_{ab}(z)$ as splitting functions becomes clear later as they are the kernels for evolution equations of parton densities, see Eq. (2.18). The leading order splitting functions $P_{ab}^{(0)}$ give probabilities for single parton emissions such as the one depicted in Fig. 2.3 where parton b with longitudinal momentum fraction x_b emits a parton c with momentum fraction $x_c = x_b - x_a = x_b(1-z)$ and continues as parton a with momentum fraction $x_a = zx_b$. The branching is fully determined by values of x_b and the splitting variable z. The four leading order (LO) splitting diagrams with corresponding splitting functions are given in Tab. 2.1.

The Altarelli-Parisi splitting functions are known up to N⁴LO [76] with which high levels of precision can be reached in calculations. The *plus-prescription* inside the splitting functions is a quantum field theoretical consequence of the cancellation of infrared singularities. It is defined as

$$\int_0^1 dz\,\varphi(z)g(z)_+ = \int_0^1 dz\,[\varphi(z) - \varphi(1)]\,g(z), \tag{2.17}$$
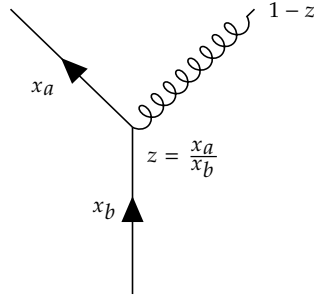
Figure 2.3: Parton branching of a quark into a quark by radiating a gluon. Labels represent the longitudinal momentum fractions x and splitting variable z
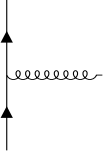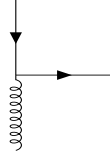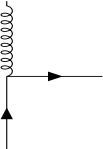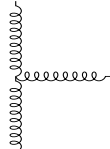
Splitting functions $P_{ab}^{(0)}$			
$P_{qq}^{(0)}$:	$= C_F \left(\dfrac{1+z^2}{1-z} \right)_+$	$P_{qg}^{(0)}$:	$= T_R \left(z^2 + (1-z)^2 \right)$
$P_{gq}^{(0)}$:	$= C_F \dfrac{1+(1-z)^2}{z}$	$P_{gg}^{(0)}$:	$= \begin{aligned} &2C_A \left\{ \left(\tfrac{1}{1-z} \right)_+ - z + \tfrac{1-z}{z} \right\} \\ &+ \left(\tfrac{11}{6} C_A - \tfrac{2}{3} T_R N_f \right) \delta(1-z) \end{aligned}$

Table 2.1: LO splitting functions for processes $q \to qg$, $g \to q\bar{q}$, $q \to gq$ and $g \to gg$ in the limit of massless partons.

obeying the property $\int_0^1 dz [g(z)]_+ = 0$.

The inverse Mellin transformation of Eq. (2.14) to x-space results in the Dokshitzer-Gribov-Lipatov-Altarelli-Parisi (DGLAP) evolution equations [75, 77, 78]

$$\frac{\partial f_a(x, \mu^2)}{\partial \ln \mu^2} = \sum_b \int_x^1 \frac{dz}{z} \, P_{ab} \left(\alpha_s(\mu^2), z \right) \, f_b \left(\frac{x}{z}, \mu^2 \right). \tag{2.18}$$

Because of this equation, the splitting functions usually get referred to as "DGLAP splitting functions". These integral-differential equations of Eq. (2.18) can be solved iteratively. Such a step-by-step solution has the interpretation of a parton emission cascade from a low scale up to a high scale, i.e. an evolution in μ. Chapter 3 provides a detailed explanation of this *parton branching* approach where we move beyond solving these "collinear" PDFs and include a transverse momentum dependence to the parton densities. In formulating the iterative solution, it is critical to address the IR divergences that are still present. A solution for $f_a(x, \mu^2)$ corresponds to the forward evolution of the PDF from μ_0 to a larger scale μ. This enables the calculation of observables using the

factorization theorem, as it allows for determination of the PDFs at any scale. The concept of parton branching is the foundation for numerical simulations of collinear emissions in particle collision events. Monte Carlo event generators are used to simulate such events. The next section provides a brief explanation of the purposes and operations of these programs.

With the physical picture of partons that carry a longitudinal momentum fraction x of the proton, a QCD momentum sum rule is formulated. The ansatz to derive this is that all the partons together carry the full momentum of the proton. In other words, the sum of momentum fractions over all partons, weighted with the parton distribution functions, equals one:

$$\int_0^1 dx\, x \sum_i f_i(x, \mu^2) = 1. \tag{2.19}$$

This is known as the QCD momentum sum rule. From this, a momentum sum rule for the DGLAP splitting functions can be derived [7]:

$$\sum_a \int_0^1 dz\, z\, P_{ab}(\alpha_{\mathrm{s}}(\mu^2), z) = 0. \tag{2.20}$$

2.3   Monte Carlo event generators

This section is dedicated to introduce the concept of Monte Carlo (MC) event generators that are based on the collinear factorization theorem and the DGLAP equations which were explained in the previous section. This section is based largely on the extensive review paper [79].

2.3.1   What is a Monte Carlo event generator?

An accurate description of final states and observables of particle collision processes involving hadrons, e.g. the production of hadronic jets or di-lepton systems, cannot in general be achieved by simply combining hard scattering calculations with collinear parton densities. Parton radiation causes broadening of jets and changes the transverse momentum spectrum of lepton pairs (see sections 2.4 and 2.5). In the 1980s it was realized that the DGLAP evolution equations can be used to simulate such parton radiation cascades, see Refs. [10–15]. The DGLAP equations are used to construct so-called "parton showers" simulating soft (at large z) and collinear (at small angles) emissions, which are used in numerical programs to connect the perturbatively calculable hard scattering cross sections with the small-scale, non-perturbative process of hadron formation.

The goal of a parton shower Monte Carlo event generator (MCEG) is to mimic factorization and perform numerical calculations for a wide variety of processes and over a broad kinematic region by sampling the relevant phase space. These programs generate large numbers of collision events, each of which may contain a large number of final state particles. For accurate calculations, all possible kinematic final state configurations must be accounted for, resulting in many degrees of freedom. The Monte Carlo method [80],

which relies on the generation of random numbers to solve problems, is the most optimal approach for filling and integrating over these multidimensional spaces. Distributions can be sampled by this method generating e.g. phase space points, branching scales, or parton flavors. The process of generating an "event record" containing information about initial, intermediate and final state particles is repeated many times. This generation process involves several steps, which are briefly described below. The final collection of events is sometimes referred to as "pseudo-data", since it can be analyzed identically to data from measurements. Throughout this work, we analyze generated and processed events in to format of HepMC [81] files using the Rɪᴠᴇᴛ3 [82, 83] tool.

The relative accuracy of the calculation improves inversely with the square of the number of event samples: $\sigma_{MC} = 1/\sqrt{N}$, where N is the number of events. The setup of MCEGs allows to only fill phase space regions of interest based on the experimental limits to optimize the statistical uncertainty.

2.3.2 Sub-processes of high energy collision events

We briefly comment on the fundamental sub-processes that are simulated in MCEGs, starting with the process at the hardest scale and moving down to hadronization, which occurs at the lowest scales.

Hard sub-process. MCEGs are built around the hard sub-process. The hard interaction, with a probability given by the "matrix element" (ME), can be generated exclusively. In the matrix element generation, the kinematics of the process is set by sampling the momenta of the particles entering the hard interaction according to PDFs. The total integrated cross section σ is calculated and should not be changed by any of the other sub-processes. The other elements of the program must also preserve the energy and total momentum of the events set in this initial step. For LO matrix element calculations, only the shape of the distributions is reliable. The overall normalization is usually poor in LO calculations due to large corrections of higher order contributions. To compare LO MC predictions with data, so-called K factors are included to normalize the distribution. The pursuit of higher accuracy often requires the inclusion of higher orders in the calculation, such as next-to-leading order (NLO) corrections, which require the inclusion of both real and virtual diagrams and the cancellation of UV and IR divergences. Ultraviolet divergences are treated by renormalization, as in Chapter 1. Infrared divergences require careful treatment, since both real and virtual diagrams contain IR divergences that cancel each other out according to the Bloch-Nordsieck [84] and Kinoshita-Lee-Nauenberg [85, 86] theorems, but they affect phase spaces of different dimensions[3]. Methods to regulate the IR divergences fall into two categories: phase space slicing methods and infrared subtraction methods. The ᴍᴄ@ɴʟᴏ method is an example of the latter category, which is implemented in the Mᴀᴅ Gʀᴀᴘʜ5_ᴀᴍᴄ@ɴʟᴏ [55] program.

Parton showers & jets. Moving backward in time and backwards in energy scale starting from the hard interaction, color and electrically charged particles radiate at the legs of the hard process (i.e. incoming and outgoing lines of the Feynman diagram). These emitters are off-shell and radiate in a space-like fashion. Space-like emissions only occur in *initial*

---

[3]Virtual emissions leave the *n*-particle phase space unchanged whereas real emissions produce a phase space of $n + 1$ particles.

state radiation (ISR), which originates from partons that will enter the hard process. When moving forward in time and backward in energy scale starting from the hard interaction, the emitters are on-shell and emit in a time-like manner. Time-like emissions occur in both ISR as well as *final state radiation* (FSR). A parton shower (PS) simulates soft and collinear emissions of partons. The leading-order Altarelli-Parisi splitting functions in Tab. 2.1 provide the emission rates. The concept of "unitarity" specifies that the total probability of emission and no-emission adds up to one and enables the creation of a no-branching probability. The algorithm behind showers operates as a Markovian process, where the subsequent emissions are uncorrelated [87, 88].

The particles emitted from showers can collapse into the proton remnant or they can form collimated particle cones, known as *jets*. Analytically describing jets is challenging as they contain numerous (soft) partons, but MC programs that include parton showers allow relatively simple calculations of jet observables. Jet clustering algorithms (reviewed in Ref. [89]) guarantee that the calculations remain *collinear and infrared safe*. That is: "for any partonic configuration, replacing any parton with a collinear set of partons with the same total momentum or adding any number of infinitely soft partons in any directions, should produce the identical result" [79]. These algorithms cluster the final state partons into jets using a set of conditions on relative distances and energies between partons in order to belong to a certain jet. Multiple algorithms exist for jet clustering, such as the frequently used k_T algorithm [90–92] and anti-k_T algorithm [93].

Multi-parton interactions. In addition to the partons involved in the hard sub-process, other partons can interact on softer scales and contribute to the so-called *underlying event*. Partons from the same protons that did not participate in the hard interaction may interact, leading to what is known as "multiple partonic interactions" (MPI). Convincing evidence demonstrating the existence of MPI and the importance of MPI modeling is presented through the calculation of the charged particle density with and without an MPI model (referring to Fig. 8 in Ref. [79]). The original model, published in Ref. [94], remains the foundation of numerous models concerning multiple parton scattering processes.

Hadronization. The transition from free, color-charged partons to bound, color-neutral hadronic final states, known as "hadronization", occurs at low energy scales due to a large coupling and confinement. It takes place below the radiation scales in parton showers, in a region where interactions become non-perturbative. Hadronization of final state partons is necessary to achieve realistic hadronic jets. For analyses, events at partonic level can provide already substantial information on observable quantities, such as the transverse momenta of jets or di-lepton pairs.

Besides the listed processes, additional models are typically implemented, such as those for the treatment of proton remnants, other types of underlying event interactions, decays of unstable particles, hadron decay, and primordial/intrinsic transverse momentum.

2.3.3   Matching and merging

Parton emissions can be generated in two seemingly indistinguishable ways: one involves an extra outgoing line in the Feynman diagram (calculated with the ME), and the other requires an additional parton shower emission. Parton showers are built from collinear and soft approximations, implying that the hardest emissions in an event should originate from matrix element calculations. This is enforced by imposing an upper limit on the

starting evolution scale of parton showers. In case of the lowest order process given by the tree-level diagram, the "Born process", this is equal to the hard scattering scale. However, when higher order contributions in the hard process are present, there is not a clearly defined starting scale for the shower. It is important to exercise caution when combining the shower to the hard scattering events.

Simply running parton showers over matrix elements that include higher orders is problematic due to two issues. Firstly, matrix element calculations are "inclusive", providing a probability for at least n final state partons, while a parton shower is "exclusive", providing a probability for exactly n final state partons. Secondly, there is a risk of double counting, i.e. overpopulating certain regions of the phase space, or missing phase space regions by naively combining the two calculations. *Matching* and *merging* procedures address these concerns. Essentially, both include higher orders in α_s where matching procedures combine parton showers with fixed order calculations, and merging procedures allow for a combination of multiple orders α_s^n and generally larger final state parton multiplicities. Matching algorithms are designed to conserve the total cross section when higher orders of α_s are fully integrated in the matrix element, which includes virtual emissions. Matching NLO MEs to parton showers can be done with e.g. the well-established MC@NLO method [95–98], the POWHEG method [99, 100] or more recent methods in Refs [101–103]. These methods have demonstrated high efficacy and are widely employed in the literature. Multi-jet merging approaches combine different fixed-order multiplicities while avoiding double counting of emissions and allowing the parton shower to generate "soft jets" only. Examples of LO merging procedures are MLM [104–106], CKKW [107] or extended versions of CKKW with angular-ordered or truncated showers [108, 109]. Examples of NLO merging algorithms are FxFx [110], MiNLO [111] or others such as those in Refs. [112–115].

2.3.4 General purpose MC event generators

Parton shower Monte Carlo event generators are valuable programs for conducting phenomenology, experimental analyses, and theoretical studies. The number of generators has been extensive over the past forty years, but today there are three prominent, multi-purpose event generators with unique implementations of the essential elements described above. The PYTHIA [116, 117], HERWIG (Hadron Emission Reactions With Interfering Gluons) [118–120] and SHERPA (Simulation of High-Energy Reactions of PArticles) [121, 122] programs offer a wide range of event generation possibilities and user-friendly setups for setting the choice of preference. These three complex generators specialize in calculating accurately the soft processes that accompany the hard process.

While all of these programs have the ability to generate hard scattering events, with some even capable of NLO calculations, specific programs like POWHEG [100] or MADGRAPH [55, 123] or AMEGIC++ [124] focus more on the computation of Feynman-diagram amplitudes. The resulting output from these programs can be easily transferred to parton shower programs through the Les Houches Event (LHE) file format [125]. MCEGs that were mentioned in this section incorporate collinear PDFs. The new work presented in this thesis concerns with the development of transverse momentum dependent parton distributions and the application in Monte Carlo event generation. The following sections motivate the need for parton distribution functions and a factorization theorem that depend on transverse momenta.

2.4   The Drell-Yan process

The collinear factorization framework outlined in section 2.2 does not always work. There
are observables that require different treatment, like the transverse momentum of lepton
pairs produced in hadron-hadron collisions. Large logarithms appear at all orders in the
strong coupling, destroying the convergence of the perturbation series.

The process in which a lepton pair is produced by the decay of a virtual photon or a Z
boson at a hard scale Q^2 by collisions of two protons has been named after S. D. Drell
and T. M. Yan. Inclusive Drell-Yan (DY) production are processes of:

$$A + B \rightarrow l^+ + l^- + X \tag{2.21}$$

where A and B are protons and X represents any hadronic final state. Drell and Yan
calculated the differential cross section of this process by using the parton model in
Ref. [126], as:

$$\frac{d\sigma_{\text{PM}}^{(pp\rightarrow l^+l^-+X)}}{dQ^2} = \frac{4\pi\alpha^2}{9sQ^2} \sum_q \int_0^1 dx_a \int_0^1 dx_b \ e_q^2 \ \delta(x_a x_b s - Q^2) f_q(x_a) f_{\bar{q}}(x_b), \tag{2.22}$$

with x_1 and x_2 longitudinal momentum fractions of the quarks q and $\bar{q}$ and $s = (p_A + p_B)^2$. The partonic center-of-mass energy equals $\hat{s} = x_1 x_2 s$ and the δ-function implies
momentum conservation.

The leading order hard interaction, calculated purely with QED, is illustrated by the
tree diagram on the right side of Fig. 2.4. The corresponding Born cross section $\sigma^{(0)} = 4\pi\alpha^2/9sQ^2$ is given by the first factor on the right hand side of Eq. (2.22).
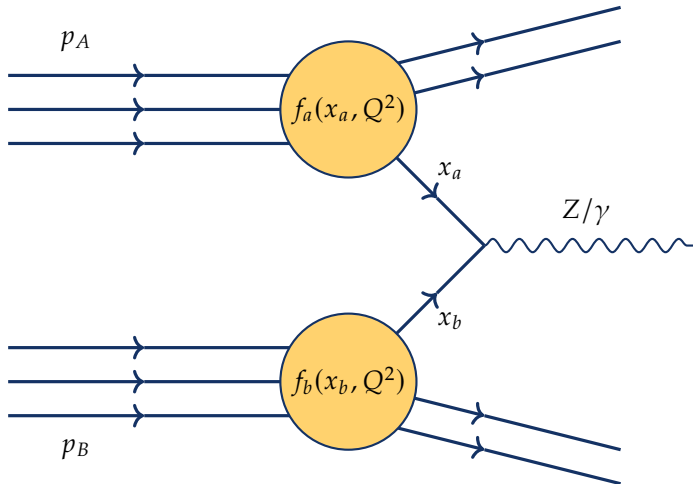
Figure 2.4: Drell-Yan process. The exchanged neutral vector boson has four-momentum
q, interacting partons have longitudinal momenta $x_1 p_A$ and $x_2 p_B$ with p_A and p_B the
momenta of the incoming protons.

A QCD formulation of the DY cross section requires scale dependent PDFs $f_{a/A}(x_a, \mu^2)$,

$f_{b/B}(x_b, \mu^2)$ and a hard factor $H_{ab}(Q^2, \mu^2)$ that includes higher orders in α_s:

$$H_{ab}(Q^2, \mu^2) = \sigma^{(0)}\left(Q^2, \alpha(\mu)\right)\left(1 + \sum_{n=1}^{\infty} H_{ab}^{(n)} \alpha_s^n(\mu)\right), \qquad (2.23)$$

which coincides with the Born cross section at LO. The factorized differential cross section is thus proportional to:

$$\frac{d\sigma_{\text{QCD}}^{(pp \to l^+l^- + X)}}{dQ^2} \sim \sum_{a,b=\{q,\bar{q},g\}} H_{ab}(Q^2, \mu^2) \otimes f_{a/A}(x_a, \mu^2) f_{b/B}(x_b, \mu^2). \qquad (2.24)$$

To describe the transverse momentum (p_T) distribution of the Z boson, one has to go more differential in the cross section and calculate $d\sigma/dQ^2 dy dp_T^2$. This causes problems with the convergence of the series expansion of the perturbative factors in the cross section. Terms with higher powers in the strong coupling do not necessarily converge anymore since they are accompanied by powers of logarithms giving terms of the form $\alpha_s^n \ln^m(Q^2/p_T^2)$. An accurate calculation that takes into account the leading terms can only be achieved by resumming the logarithmically enhanced terms to all orders n.

2.5   Transverse momentum dependent parton densities

Application of collinear factorization resulted in large progress within particle physics. It allows to calculate observables in large kinematic domains and use in data analysis led to discoveries of new particles, decay channels and information on the structure of the proton. However, there are certain kinematic regions where only finite order perturbative (DGLAP) calculations do not work. Emissions of soft gluons that possess very small transverse momentum lead to large logarithms at all orders in the perturbation series in α_s. These series therefore need to be resummed. In deep inelastic scattering and Drell-Yan, the kinematic regions of the phase space where resummation is necessary are respectively the asymptotic high energy region (large s) and the low transverse momentum region (small $q_\perp$).

The DGLAP equations given in Eq. (2.18) are commonly used to construct collinear PDFs $f(x, \mu)$ which depend on longitudinal momentum and the factorization scale. With these functions, one has a one-dimensional picture of the proton. The phase space regions that are logarithmically enhanced by soft gluons require to include the dynamics of partons in the plane transverse to the proton's direction to have a three-dimensional picture of the proton. The transverse momentum dependence of parton distribution functions should thus be uncovered. There are several approaches to do this. Some of these are discussed in detail in Chapters 3, 5 and 6.

2.5.1   Structure functions from DIS

In the case of DIS, the use of collinear factorization is not sufficient to obtain structure functions of the proton in the limit of $\sqrt{s} \to \infty$. For fixed momentum transfer Q they scale

like $1/s$. With the current high energies of colliders and the prospects of future collider energies, more events at low x contribute to the measurements. At small longitudinal momenta, the transverse momentum of the partons becomes relatively more important. Without the inclusion of these degrees of freedom, a fixed order perturbative calculation is not precise as can be seen in Fig. 2.5. The uncertainty bands of these collinear gluon distributions at LO, NLO and NNLO are large and do not overlap. Physically the contributions to the low x regime come from soft gluon emissions which are present at any order in α_s. Terms in the perturbative series expansion of the DIS structure functions are of the form

$$\left[\alpha_s \ln(\sqrt{s}/Q)\right]^k, \tag{2.25}$$

where α_s is considered to be small but the logarithms can become very large in the case of a large center-of-mass energy $\sqrt{s}$. These terms have to be resummed to perform correct perturbative calculations. The resummation of these logarithms is not implied in the DGLAP equations. These types of logarithms are resummed by BFKL (Balitsky-Fadin-Kuraev-Lipatov) [127, 128] types of evolution equations. The CCFM (Catani-Ciafaloni-Fiorani-Marchesini) [129] evolution equations interpolate between BFKL and DGLAP evolution.
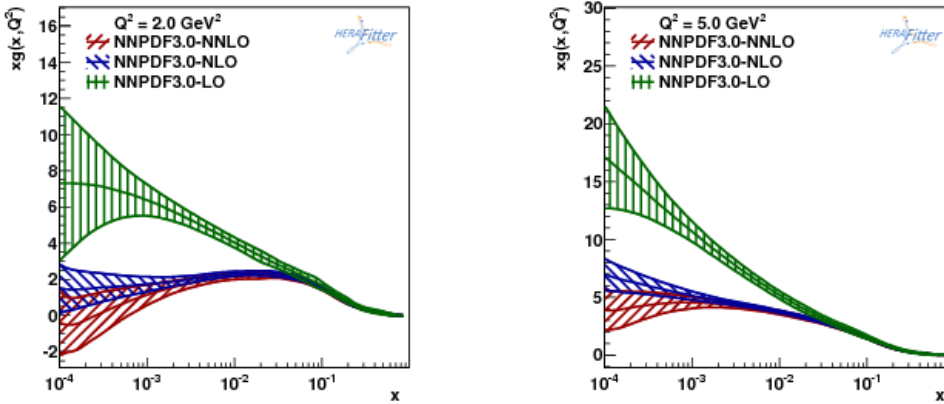
Figure 2.5: The gluon density against longitudinal momentum fraction x for fixed order perturbative calculations at LO, NLO and NNLO. The left plot shows the gluon density at fixed momentum transfer $Q^2 = 2\,\text{GeV}^2$ and the right plot at $Q^2 = 5\,\text{GeV}^2$.[34]

2.5.2   Transverse momentum spectrum from DY

In the case of DY, the transverse momentum (p_T) spectrum of the vector boson or final state di-lepton system is not well described by finite order perturbative calculations of collinear PDFs. This concerns the small p_T region of the spectrum that is sensitive to QCD effects beyond perturbative fixed order associated with soft multi-gluon radiation. In the region of transverse momenta p_T^{ll} small compared to the di-lepton invariant mass m_{ll}, all terms in the perturbative series get possibly enhanced by large logarithms. Reliable theoretical predictions require soft-gluon resummation - also referred to as *Sudakov resummation* - and non-perturbative contributions which can be included by using the TMD theoretical framework. For large p_T, above the peak region, collinear factorization

works fine provided that sufficient higher order diagrams leading to large transverse momentum recoils are taken into account.

In the perturbative series of the transverse momentum spectrum for DY, large logarithms arise for small parton transverse momentum $q_\perp$. The terms in the perturbative series are of the form:

$$\alpha_s^n \ln^m(Q/q_\perp). \tag{2.26}$$

The collection of terms where $n < m \le 2n$ are leading terms [43], but all terms with $n+2 \le m \le 2n$ vanish due to exponentiation [130], leaving terms of the form $\alpha_s^n \ln^{n+1}(Q/q_\perp)$, which are the leading logarithmic (LL) terms. Next-to-leading logarithms (NLL) are terms of the form $\alpha_s^n \ln^n(Q/q_\perp)$ and so on and so forth. A measure of the accuracy of Sudakov resummation is the number of powers of logarithms that are resummed, giving a logarithmic accuracy.

The p_T-spectrum of the Z boson is measured with high precision at the LHC [131–136]. In Fig. 2.6 measurements of the p_T-spectrum at $\sqrt{s}$ = 13 TeV of pp collisions are shown together with theoretical predictions by parton shower event generators. A pure DGLAP calculation, not shown in the figure, is not sufficient to describe the spectrum at small transverse momentum. With the use of MC calculation techniques, shown in the figure, many perturbative orders can be taken into account to obtain results that agree with the measurement also in the high-p_T regime.
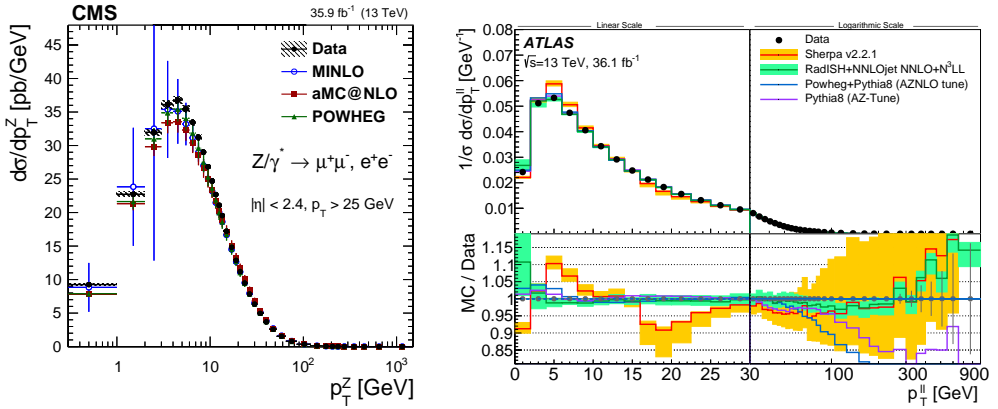
Figure 2.6: Data of measurements of the Z boson p_T-spectrum at $\sqrt{s}$ = 13 TeV by CMS (left) [136] and ATLAS (right) [135] at the LHC and predictions with the parton shower Monte Carlo event generators MINLO, amc@nlo, Powheg, Sherpa and Pythia. The RadISH calculation is based on analytical resummation by CSS.

The accuracy of soft-gluon resummation is determined by the powers of logarithms that are taken into account. The "logarithmic accuracy" of parton shower MCEGs is state-of-the-art research and topic of many groups nowadays [16–26]. The improvement of the logarithmic accuracy of the Parton Branching (PB) method (described in Chapter 3) in terms of the Sudakov form factor that has been implemented in the Cascade3 MC event generator (Chapter 7) is part of the new material in the dissertation and described in Chapter 6.

2.5.3 TMD factorization

With parton shower MCEGs, it is possible to generate transverse momentum using
DGLAP evolution (through splittings of partons). The PDFs that are used in these tools
do however not include this information. More advanced evolution equations that are
able to evolve transverse momentum dependent parton distribution functions (TMDs)
are needed.

Resummation of large logarithms and TMDs are taken into account by the theoretical
framework of transverse momentum dependent (TMD) factorization. Examples of for-
mulations of TMD factorization are the Collins-Soper-Sterman (CSS) formalism [49, 137]
(see Sec. 6.2 for more details) or variants in Soft-Collinear Effective Theory (SCET) [138].

In spite of the many applications of collinear PDFs and the fact that they have been widely
used for analyses in high-energy experiments, TMDs are the subject of intensive studies
and will increasingly contribute to applications in high-energy physics. The factorized
parts of the DY cross section in Eq. (2.24) are integrated over the transverse momentum.
This physically means that the transverse momentum stream is limited; there is no
connection of the transverse momenta from the PDFs to those in the hard scattering
part. In TMD factorization formalisms, both the hard scattering matrix element and
the PDFs are $k_\perp$-dependent, the transverse momentum flows between these parts. An
important step forward in the community of MCEGs is to include TMDs in all elements
of the calculation. The Cascade3 Monte Carlo event generator [51] is developed with this
purpose and is the topic of Chapter 7.

The formalisms that are developed for the high energy and low transverse momentum
regions, such as BFKL, CCFM and CSS (cf. Secs. 2.5.1 and 2.5.2), express the evolution
of TMDs with perturbative kernels (like the splitting functions in DGLAP). It is hard
to apply the equations of these approaches to general collider kinematics because they
only work well for particular observables and in particular kinematic regions. Because
of this, other approaches for the evolution of TMDs have been investigated among which
the Parton Branching method is one approach for TMD evolution, discussed in the next
chapter.

3

PB formulation of TMD evolution

The Parton Branching (PB) method is a recently developed method for the evolution of TMD PDFs [38, 39]. The previous chapters motivated the urge of transverse momentum dependence in the different elements of high energy collision calculations. PB does not focus on an analytical formulation of the differential DY cross section. Instead, the PB method is concerned with QCD evolution equations for collinear PDFs and TMDs and provides a numerical implementation that can be applied to the calculation of any process.

We start in section 3.1 from the DGLAP evolution equations for collinear PDFs where we construct a solution that can be solved iteratively using the Monte Carlo method. This solution has an intuitive interpretation of multiple parton branchings. To achieve this, we introduce a soft-gluon resolution scale, real emission probabilities and the Sudakov form factor. The use of the unitarity picture [7, 11] and the Monte Carlo method provides a means to iteratively solve the integral-differential evolution equations, allowing for the resummation of soft gluon emissions. The introduction of transverse momentum dependence in the evolution equations facilitates the transition to the evolution of TMD PDFs. The implementation of ordering conditions enables to associate evolution variables with the transverse momentum. It was demonstrated in Ref. [38] that the angular ordering condition is crucial to incorporate transverse momentum effects and achieve TMD evolution that is less sensitive to the resolution scale.

3.1   Parton branching

The splitting variable z, as introduced in Chapter 2, represents the ratio of longitudinal momentum fractions of partons in an emission process. In such a process, emitted partons that are indistinguishable from their radiator are either emitted at a small angle, referred to as "collinear" branchings, or carry a very small fraction of the radiator's energy, referred to as "soft" branchings. The latter have a splitting variable z that is close to 1. These soft types of branchings are referred to as *non-resolvable*. The complementary region of the non-resolvable part of the phase space is the *resolvable* phase space region, where the final state partons are distinguishable. A physical interpretation of non-resolvable partons is related to the expression of the evolution scale in terms of physical parameters. At large scales μ, the resolution is higher, implying that more soft branchings are resolved. The

scale μ gets an interpretation by ordering the branchings according to a kinematical parameter, as described in subsection 3.2.1. The resolvable and non-resolvable regions are separated by an infrared (IR) resolution scale z_M. The region where $z > z_M$ is the non-resolvable region and $z < z_M$ the resolvable region of the branching phase space. In this section we apply this concept to the DGLAP evolution equations and express the evolution equations in terms of resolvable emission probabilities.

The splitting functions P_{ab} contain IR divergences and singularities that are associated with particular types of non-resolvable or virtual emissions. Loop diagrams, i.e. virtual emissions, which do not cause any change in longitudinal momentum, are included in the splitting functions as terms containing a $\delta(1 - z)$ factor. Gluon emissions can arise at values of z that are close to 1, producing low-energy gluons which are very soft. These emissions occur frequently due to a divergence towards $z \to 1$ in the splitting function. The terms representing these soft-gluon emissions are diagonal in flavor (as a gluon emission does not change quark flavor) and are accompanied by a factor of $1/(1-z)$. The plus-prescription presented in Eq. (2.17) deals with the divergence towards $z \to 1$.

The splitting functions can be decomposed into three terms: real emissions (not singular in z), virtual emissions (at $z = 1$) and soft-gluon emissions (singular towards $z \to 1$). This decomposition is as follows:

$$P_{ab}(\alpha_s(\mu^2), z) = D_{ab}(\alpha_s(\mu^2))\delta(1 - z) + K_{ab}(\alpha_s(\mu^2))\left(\frac{1}{1 - z}\right)_+ + R_{ab}(\alpha_s(\mu^2), z). \qquad (3.1)$$

For a simplification of the notation, in the remainder of this section we define $\alpha_s \equiv \alpha_s(\mu^2)$. Flavor diagonality is expressed through Kronecker delta functions: $D_{ab} = \delta_{ab}d_a$ and $K_{ab} = \delta_{ab}k_a$. All coefficients of the splitting functions are calculable perturbatively by a series expansion in the strong coupling, as given in Eq. (2.16).

$$k_a(\alpha_s) = \sum_{n=1}^{\infty}\left(\frac{\alpha_s}{2\pi}\right)^n k_a^{(n-1)}, \qquad\qquad d_a(\alpha_s) = \sum_{n=1}^{\infty}\left(\frac{\alpha_s}{2\pi}\right)^n d_a^{(n-1)},$$

$$R_{ab}(\alpha_s, z) = \sum_{n=1}^{\infty}\left(\frac{\alpha_s}{2\pi}\right)^n R_{ab}^{(n-1)}(z). \qquad\qquad\qquad\qquad\qquad (3.2)$$

Leading order (LO) and next-to-leading order (NLO) coefficients of these functions are given in Appendix A. The function k_a that is accompanied by the factor $1/(1 - z)_+$ is referred to in the literature as the *cusp anomalous dimension* and is also denoted by $\gamma_K(\alpha_s) = k_a(\alpha_s)$. NLO coefficients of the splitting functions $P_{ab}^{(1)}(z)$ are obtained by calculations of two-loop diagrams. The radiation diagrams at this order possibly contain both quark and gluon radiation causing the occurrence of both C_F and C_A in one coefficient.

Soft gluons radiate more strongly than soft quarks which is reflected by $k_g^{(0)} > k_q^{(0)}$. In general, the emission of gluons is enhanced for small splitting variables $z \to 1$ due to the $1/(1 - z)$ and $\delta(1 - z)$ factors along the flavor diagonal functions, representing gluon emissions, and the fact that $C_A > C_F$.

3.1.1   Regulating the non-resolvable region

We follow the procedure by Ref. [38] to achieve numerically solvable evolution equations. The DGLAP evolution equations (2.18) can be written using the decomposition of the splitting functions given in Eq. (3.1):

$$\frac{\partial \tilde{f}_a(x,\mu^2)}{\partial \ln \mu^2} = \sum_b \int_x^1 dz \left(D_{ab}(\alpha_{\mathrm{s}})\delta(1-z) + \frac{K_{ab}(\alpha_{\mathrm{s}})}{(1-z)_+} + R_{ab}(\alpha_{\mathrm{s}}, z) \right) \tilde{f}_b \left(\frac{x}{z}, \mu^2 \right), \qquad (3.3)$$

where $\tilde{f}(x, \mu^2) = x f(x, \mu^2)$ are momentum-weighted PDFs.

Resolvable and non-resolvable regions can be separated straightforwardly for the R_{ab} term:

$$\frac{\partial \tilde{f}_a(x,\mu^2)}{\partial \ln \mu^2} = \sum_b \int_x^1 dz D_{ab}(\alpha_{\mathrm{s}})\delta(1-z)\tilde{f}_b \left(\frac{x}{z}, \mu^2 \right) + \sum_b \int_x^1 dz \frac{K_{ab}(\alpha_{\mathrm{s}})}{(1-z)_+} \tilde{f}_b \left(\frac{x}{z}, \mu^2 \right) \quad (3.4)$$

$$+ \sum_b \int_x^{z_M} dz R_{ab}(\alpha_{\mathrm{s}}, z)\tilde{f}_b \left(\frac{x}{z}, \mu^2 \right) + \sum_b \int_{z_M}^1 dz R_{ab}(\alpha_{\mathrm{s}}, z)\tilde{f}_b \left(\frac{x}{z}, \mu^2 \right).$$

All divergent terms for $z \to 1$ must be regulated. The term with D_{ab} only contributes at $z = 1$, indicated by the Kronecker delta, representing a virtual branching that does not change the longitudinal momentum of the parton. That leaves the second term on the right-hand side, $K_{ab}/(1-z)_+$. By using the definition of the plus-prescription from Eq. (2.17), we can write this term as follows:

$$\int_x^1 dz \frac{K_{ab}(\alpha_{\mathrm{s}})}{(1-z)_+} \tilde{f}_b \left(\frac{x}{z}, \mu^2 \right) = \int_0^1 dz \frac{K_{ab}(\alpha_{\mathrm{s}})}{(1-z)_+} \Theta(z-x)\tilde{f}_b \left(\frac{x}{z}, \mu^2 \right) \qquad (3.5)$$

$$= \int_0^1 dz \frac{K_{ab}(\alpha_{\mathrm{s}})}{1-z} \left[\Theta(z-x)\tilde{f}_b \left(\frac{x}{z}, \mu^2 \right) - \Theta(1-x)\tilde{f}_b(x, \mu^2) \right]$$

$$= \int_x^1 dz \frac{K_{ab}(\alpha_{\mathrm{s}})}{1-z} \tilde{f}_b \left(\frac{x}{z}, \mu^2 \right) - \int_0^1 dz \frac{K_{ab}(\alpha_{\mathrm{s}})}{1-z} \tilde{f}_b(x, \mu^2).$$

Separating the resolvable and non-resolvable regions using z_M gives

$$\int_x^1 dz \frac{K_{ab}(\alpha_{\mathrm{s}})}{(1-z)_+} \tilde{f}_b \left(\frac{x}{z}, \mu^2 \right) = \int_x^{z_M} dz \frac{K_{ab}(\alpha_{\mathrm{s}})}{1-z} \tilde{f}_b \left(\frac{x}{z}, \mu^2 \right) + \int_{z_M}^1 dz \frac{K_{ab}(\alpha_{\mathrm{s}})}{1-z} \tilde{f}_b \left(\frac{x}{z}, \mu^2 \right) \quad (3.6)$$

$$- \int_0^{z_M} dz \frac{K_{ab}(\alpha_{\mathrm{s}})}{1-z} \tilde{f}_b(x, \mu^2) - \int_{z_M}^1 dz \frac{K_{ab}(\alpha_{\mathrm{s}})}{1-z} \tilde{f}_b(x, \mu^2).$$

The integral over the non-resolvable region (from z_M up to 1) still needs to be regulated. For this, an expansion of the PDF near $z = 1$ as

$$\tilde{f}_b \left(\frac{x}{z}, \mu^2 \right) = \tilde{f}_b(x, \mu^2) + (1-z)\frac{\partial \tilde{f}_b(x, \mu^2)}{\partial \ln x} + O((1-z)^2), \qquad (3.7)$$

can be inserted in the second term on the right-hand side of Eq. (3.6). The integration over z there gives factors $(1-z_M)^n$ at order n which are very small such that higher order terms can be neglected. Eq. (3.6) becomes:

$$\int_x^1 dz \frac{K_{ab}(\alpha_{\mathrm{s}})}{(1-z)_+} \tilde{f}_b \left(\frac{x}{z}, \mu^2 \right) = \int_x^{z_M} dz \frac{K_{ab}(\alpha_{\mathrm{s}})}{1-z} \tilde{f}_b \left(\frac{x}{z}, \mu^2 \right) - \int_0^{z_M} dz \frac{K_{ab}(\alpha_{\mathrm{s}})}{1-z} \tilde{f}_b(x, \mu^2) \quad (3.8)$$

All IR singularities are contained in the K_{ab} and D_{ab} functions, the R_{ab} term does not contain these divergences and is therefore not significantly contributing at large z. By neglecting the last term of Eq. (3.4) and inserting Eq. (3.8) the evolution equations become:

$$\frac{\partial \tilde{f}_a(x, \mu^2)}{\partial \ln \mu^2} = \sum_b \int_x^{z_M} dz \left[\frac{K_{ab}(\alpha_s)}{1-z} + R_{ab}(\alpha_s, z) \right] \tilde{f}_b \left(\frac{x}{z}, \mu^2 \right)$$

$$+ \sum_b \left\{ \int_x^1 dz D_{ab}(\alpha_s) \delta(1-z) - \int_0^{z_M} dz \frac{K_{ab}(\alpha_s)}{1-z} \right\} \tilde{f}_b(x, \mu^2). \qquad (3.9)$$

The first term with integral over z up to z_M describes evolution of real parton emissions. The real-emission splitting functions (referred to as the "unregularized splitting functions" $\hat{P}$ in Ref. [7]) are therefore defined as:

$$P_{ab}^{(R)}(\alpha_s, z) = \frac{K_{ab}(\alpha_s)}{1-z} + R_{ab}(\alpha_s, z). \qquad (3.10)$$

The second term describes virtual and non-resolvable emissions. The second term of Eq. (3.9) describes virtual and non-resolvable emissions; the parton flavor a does not change in this process. A splitting process $b \rightarrow ac$ is described by P_{ab} or equivalently by P_{cb}. We can interchange the flavor indices in the second term of Eq. (3.9) since D_{ab} and K_{ab} are diagonal in flavor, such that the evolution equations become:

$$\frac{\partial \tilde{f}_a(x, \mu^2)}{\partial \ln \mu^2} = \sum_b \int_x^{z_M} dz P_{ab}^{(R)}(\alpha_s, z) \tilde{f}_b \left(\frac{x}{z}, \mu^2 \right) + \qquad (3.11)$$

$$+ \sum_c \left\{ \int_x^1 dz D_{ca}(\alpha_s) \delta(1-z) - \int_0^{z_M} dz \frac{K_{ca}(\alpha_s)}{1-z} \right\} \tilde{f}_a(x, \mu^2).$$

Starting from Eq. (3.11) and subtracting the term $\sum_c \int_0^1 z P_{ca}(\alpha_s, z) dz$, which is zero due to the momentum sum rule (Eq. (2.20)) gives:

$$\frac{\partial \tilde{f}_a(x, \mu^2)}{\partial \ln \mu^2} = \sum_b \int_x^{z_M} dz P_{ab}^{(R)} \tilde{f}_b \left(\frac{x}{z}, \mu^2 \right) + \qquad (3.12)$$

$$+ \sum_c \left\{ \int_x^1 dz D_{ca}(\alpha_s) \delta(1-z) - \int_0^{z_M} dz \frac{K_{ca}(\alpha_s)}{1-z} \right.$$

$$\left. - \int_0^1 dz \, z \left(R_{ca}(\alpha_s, z) + D_{ca}(\alpha_s) \delta(1-z) + \frac{K_{ca}(\alpha_s)}{(1-z)_+} \right) \right\} \tilde{f}_a(x, \mu^2),$$

where the decomposition of the DGLAP splitting functions P_{ab} from Eq. (3.1) was applied. The terms with integrals over D_{ca} in Eq. (3.12) cancel against each other because the first term in the second line is:

$$\int_x^1 dz D_{ca}(\alpha_s) \delta(1-z) = \int_0^1 dz D_{ca}(\alpha_s) \delta(1-z) \Theta(z-x) = D_{ca}(\alpha_s). \qquad (3.13)$$

Once again, the integration of R_{ca} over the non-resolvable region ($z_M < z < 1$) can be

neglected. Regularization of the K term is still needed. One proceeds as follows:

$$\int_0^1 dz\, z\, \frac{K_{ca}(\alpha_s)}{(1-z)_+} = \int_0^1 dz\, z\, \frac{K_{ca}(\alpha_s)}{1-z} - \int_0^1 dz \frac{K_{ca}(\alpha_s)}{1-z} \tag{3.14}$$

$$= \int_0^{z_M} dz\, z\, \frac{K_{ca}(\alpha_s)}{1-z} - \int_0^{z_M} dz \frac{K_{ca}(\alpha_s)}{1-z} + \int_{z_M}^1 dz\, z\, \frac{K_{ca}(\alpha_s)}{1-z} - \int_{z_M}^1 dz \frac{K_{ca}(\alpha_s)}{1-z}.$$

The third term on the right-hand side of the last equality can be written as

$$\int_{z_M}^1 dz\, z\, \frac{K_{ca}(\alpha_s)}{1-z} = \int_{z_M}^1 dz \frac{1+z-1}{1-z} K_{ca}(\alpha_s) = \int_{z_M}^1 dz \frac{K_{ca}(\alpha_s)}{1-z} - \int_{z_M}^1 dz\, K_{ca}(\alpha_s), \tag{3.15}$$

of which the first term cancels with the last term of Eq. (3.14) and the second term is of the order of $(1 - z_M)$ and thus negligible. Only the first two terms of Eq. (3.14) remain. The evolution equations can then be written using another substitution of real-emission splitting functions

$$\frac{\partial \tilde{f}_a(x, \mu^2)}{\partial \ln \mu^2} = \sum_b \int_x^{z_M} dz\, P_{ab}^{(R)} \tilde{f}_b\left(\frac{x}{z}, \mu^2\right) \tag{3.16}$$

$$+ \sum_c \left\{ - \int_0^{z_M} dz\, z\, R_{ca}(\alpha_s, z) - \int_0^{z_M} dz\, z\, \frac{K_{ca}(\alpha_s)}{1-z} \right\} \tilde{f}_a(x, \mu^2).$$

In the last line we recognize again the real-emission splitting functions, with an extra factor of z. The evolution equations then become:

$$\frac{\partial \tilde{f}_a(x, \mu^2)}{\partial \ln \mu^2} = \sum_b \left(\int_x^{z_M} dz\, P_{ab}^{(R)}(\alpha_s, z) \tilde{f}_b\left(\frac{x}{z}, \mu^2\right) - \int_0^{z_M} dz\, z\, P_{ba}^{(R)}(\alpha_s, z) \tilde{f}_a(x, \mu^2) \right). \tag{3.17}$$

3.1.2 Evolution with the Sudakov form factor

The form of Eq. (3.16) is not solvable analytically nor does it have the right structure to be solved with the Monte Carlo techniques [139] because this coupled differential equation depends both on $\tilde{f}_a$ as on $\tilde{f}_b$ and integration limits differ. To be suitable for the MC approach, one makes use of *unitarity* [7, 11] which states that the probability of an emission is complementary to that for no emission in any domain of the evolution variable $\{\mu_0^2, \mu^2\}$. In terms of resolvable and non-resolvable emissions this is translated in the unity of the sum of the probabilities for resolvable branchings ($\mathcal{P}_a$) and for *no* resolvable branchings ($\mathcal{P}_a^{no}$):

$$\mathcal{P}_a(\mu^2, \mu_0^2) + \mathcal{P}_a^{no}(\mu^2, \mu_0^2) = 1. \tag{3.18}$$

In this subsection we first illustrate the general construction and interpretation of a no-branching probability $\mathcal{P}_a^{no}$ in terms of scale $t = \ln \mu^2$. Here, flavor indices and the splitting variable z are left out. Then we give the detailed form of the no-branching probability in Eq. (3.24) that can be implemented in the PB evolution equations.

The probability for a resolvable branching at a scale μ of parton a into parton b by emitting parton c is proportional to splitting functions $P(t)$. This does not represent the

probability for a splitting within a finite interval $\Delta t = t - t_0$. For both *forward* (going up in scale t) and *backward* (going down in scale t) types of evolution, the no-branching probability has to be known over a finite interval of the evolution scale to perform a calculation of the evolution of PDFs. A no-branching probability for identical starting and final scale is equal to one.

The probability for no resolvable branching in an infinitesimal interval dt is

$$\mathcal{P}^{no}(dt) = 1 - dtP, \tag{3.19}$$

where for simplicity we suppose the splitting functions P to not dependent on the scale t. The no-branching probability over a finite scale interval $\{t_0, t\}$ is calculated by subdividing the domain into many (n) infinitesimal subintervals, multiplication of the n no-branching probability factors and taking the limit $n \to \infty$:

$$\mathcal{P}^{no}(\Delta t) = \lim_{n \to \infty} \left(1 - \frac{\Delta t}{n}P\right)^n = \exp\left(-\Delta t P\right), \tag{3.20}$$

where we exponentiated according to the definition $\exp(x) = \lim_{n \to \infty}(1 + x/n)^n$. The splitting functions, governing the probability for a branching, however depend on the scale μ. The no-branching probability therefore can generally be written as:

$$\Delta(\mu^2, \mu_0^2) \equiv \exp\left\{-\int_{\mu_0^2}^{\mu^2} d\ln\mu'^2 P(\mu')\right\}, \tag{3.21}$$

where the argument of the exponent essentially is an average, or effective, splitting probability of evolution in the interval $\{\mu_0, \mu\}$.

The probability for an emission at scale μ, starting from μ_0, is equal to the product of the branching probability $P(\mu)$ and the no-branching probability $\Delta(\mu, \mu_0)$:

$$\mathcal{P}(\mu, \mu_0) = P(\mu) \exp\left\{-\int_{\mu_0^2}^{\mu^2} d\ln\mu'^2 P(\mu')\right\} = P(\mu)\Delta(\mu^2, \mu_0^2), \tag{3.22}$$

from which the following differential equation can be derived:

$$-\frac{d\Delta(t)}{dt} = P(t)\Delta(t). \tag{3.23}$$

It is possible to rewrite the DGLAP evolution equations in terms of Δ by using the property in Eq. (3.23). For this, we have to reintroduce the parton flavor indices and take into account the z-dependence of the splitting functions.

To maintain the exact evolution dynamics as in Eq. (3.17), the *Sudakov form factor* Δ_a for PB is defined as [38]:

$$\Delta_a(z_M, \mu^2, \mu_0^2) = \exp\left\{-\sum_b \int_{\mu_0^2}^{\mu^2} d\ln\mu'^2 \int_0^{z_M} dz\, z\, P_{ba}^{(R)}(\alpha_s(\mu'), z)\right\}, \tag{3.24}$$

which can be interpreted as the probability that a parton a does not emit any resolvable parton (b) during evolution from scale μ_0 up to μ. With this object, the evolution equations

in Eq. (3.17) can be written in terms of real-emission probabilities $P_{ab}^{(R)}$ and Sudakov form factors $\Delta_a(\mu^2)$ as

$$\frac{\partial}{\partial \ln \mu^2}\left(\frac{\tilde{f}_a(x,\mu^2)}{\Delta_a(\mu^2)}\right) = \frac{1}{\Delta_a(\mu^2)}\sum_b \int_x^{z_M} dz P_{ab}^{(R)}(\alpha_s(\mu^2),z)\tilde{f}_b\left(\frac{x}{z},\mu^2\right). \qquad (3.25)$$

This form of the evolution equation is solvable iteratively, as explained in section 3.1.3.

The Sudakov form factor is a resummation factor, like that in the renormalization of α_s (see Eq. (1.17)) or for evolution of PDFs (see Eq. (2.13)). In this way, the non-resolvable region of the branching phase space and multiple soft-gluon emissions are taken into account by exponentiation.

For results that are described in Chapters 5 and 6 it is convenient to rewrite the Sudakov form factor and perform the integration of z. The momentum sum rule for splitting functions (Eq. (2.20)) and the decomposition of the splitting functions (Eq. (3.1)) are useful identities to rewrite the argument of the Sudakov form factor. The momentum sum rule can be written as:

$$0 = \sum_a \int_0^1 dz\, z\, P_{ab}(\alpha_s,z) = \sum_a \left\{\int_0^{z_M} dz\, z\, P_{ab}(\alpha_s,z) + \int_{z_M}^1 dz\, z\, P_{ba}(\alpha_s,z)\right\} \qquad (3.26)$$
$$= \sum_a \int_0^{z_M} dz\, z\, \left[R_{ab}(\alpha_s,z) + \frac{\delta_{ab}k_a(\alpha_s)}{1-z}\right] - \int_0^{z_M} dz\frac{k_a(\alpha_s)}{1-z}$$
$$+ \sum_a \int_{z_M}^1 dz\, z\, R_{ab}(\alpha_s,z) + \int_{z_M}^1 dz\frac{z-1}{1-z}k_a(\alpha_s) + d_a(\alpha_s)\, .$$

The terms with integrals $\int_{z_M}^1 dz$ can be neglected because of their small integration region and their opposite signs. The first term of Eq. (3.26) contains the real emission splitting functions, causing the following identity to be true:

$$\sum_a \int_0^{z_M} dz\, z\, P_{ab}^{(R)}(\alpha_s) \simeq \int_0^{z_M} dz\frac{k_a(\alpha_s)}{1-z} - d_a(\alpha_s). \qquad (3.27)$$

Note that this is only fully valid when the argument of the strong coupling does not depend on the splitting variable z. The Sudakov form factor can then approximately be written as

$$\Delta_a(z_M,\mu^2,\mu_0^2) \simeq \exp\left\{-\int_{\mu_0^2}^{\mu^2}\frac{d\mu'^2}{\mu'^2}\left(\int_0^{z_M}\frac{k_a(\alpha_s)}{1-z}dz - d_a(\alpha_s)\right)\right\}. \qquad (3.28)$$

To simplify the notation, Sudakov form factors are usually written only with their upper limit argument: $\Delta(\mu^2) \equiv \Delta(\mu^2,\mu_0^2)$.

3.1.3   Evolution with multiple emissions

The integral-differential equation (3.25) can be solved by integration over $\ln(\mu'^2)$ from μ_0^2 up to μ^2. This results in an integral equation of the Fredholm type (Eq. (32) in Ref. [38]):

$$\tilde{f}_a(x,\mu^2) = \Delta_a(\mu^2)\tilde{f}_a(x,\mu_0^2) + \sum_b \int_{\mu_0^2}^{\mu^2} \frac{d\mu'^2}{\mu'^2} \frac{\Delta_a(\mu^2)}{\Delta_a(\mu'^2)} \int_x^{z_M} dz P_{ab}^{(R)}(\alpha_s(\mu'^2),z)\tilde{f}_b\left(\frac{x}{z},\mu'^2\right).$$

(3.29)

The integrals in this equation are difficult to calculate analytically. Monte Carlo methods are highly effective to solve these. Fredholm type equations can be solved iteratively. Each step in the iteration represents a contribution to the evolution with an additional branching. This also forms the foundation of a parton shower algorithm [140]. A step-by-step iterative solution of Eq. (3.29) is explained below.
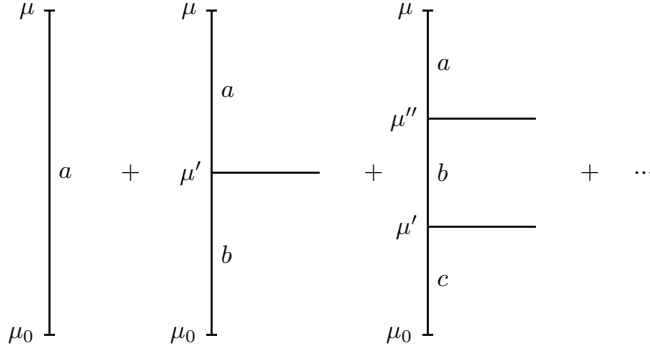
Figure 3.1: Solution of the branching equation by iteration.

The first term $\Delta_a(\mu^2)\tilde{f}_a(x,\mu_0^2)$ represents PDF evolution of a parton with flavor a at a scale μ_0^2 without any resolvable branching, through multiplying with the Sudakov form factor at final evolution scale μ^2. The starting distribution is fit to experimental data or could be constructed with a toy model. The left diagram in Fig. 3.1 illustrates the contribution of this term to the evolution.

The second term on the right-hand side takes into account the contributions from parton splittings at scales between μ_0 and μ. These splittings change the flavor from b to a and the parton's longitudinal momenta from x/z to x. The second iteration is obtained by inserting the first solution into $\tilde{f}_b$ of the second term:

$$\tilde{f}_a^{(1)}(x,\mu^2) = \sum_b \int_{\mu_0^2}^{\mu^2} \frac{d\mu'^2}{\mu'^2} \frac{\Delta_a(\mu^2)}{\Delta_a(\mu'^2)} \int_x^{z_M} dz P_{ab}^{(R)}(\alpha_s(\mu'^2),z)\Delta_b(\mu'^2)\tilde{f}_b\left(\frac{x}{z},\mu_0^2\right).$$

(3.30)

This gives the contribution to evolution of one branching at scale μ' (shown in the middle diagram of Fig. 3.1).

Inserting the second solution on the right-hand side of Eq. (3.30) into $\tilde{f}_b$ in Eq. (3.29) yields the contribution of two branchings to the evolution, as illustrated in Fig. 3.1. The

expression would be

$$\tilde{f}_a^{(2)}(x,\mu^2) = \sum_b \int_{\mu_0^2}^{\mu^2} \frac{d\mu''^2}{\mu''^2} \frac{\Delta_a(\mu^2)}{\Delta_a(\mu''^2)} \int_x^{z_M} dz_2 P_{ab}^{(R)}\left(\alpha_s(\mu''^2),z_2\right) \times \qquad (3.31)$$

$$\times \sum_c \int_{\mu_0^2}^{\mu''^2} \frac{d\mu'^2}{\mu'^2} \frac{\Delta_b(\mu''^2)}{\Delta_b(\mu'^2)} \int_{x/z_2}^{z_M} dz_1 P_{bc}^{(R)}\left(\alpha_s(\mu'^2),z_1\right)\Delta_c(\mu'^2)\tilde{f}_c\left(\frac{x}{z_1 z_2},\mu_0^2\right).$$

Repetition of this procedure infinitely would yield an exact solution:

$$\tilde{f}_a(x,\mu^2) = \sum_{i=0}^{\infty} \tilde{f}_a^{(i)}(x,\mu^2). \qquad (3.32)$$

In practice, Monte Carlo methods simulate this procedure. This begins with selecting a parton with flavor a, at scale μ_j, followed by generating values of μ' and z for a branching, solved through $R = \Delta_a(z_M,\mu_j',\mu_{j+1}')$, where R is a random number between 0 and 1. For each generated branching scale μ' a z value is generated according to the splitting functions (see Eq. (37) in Ref. [38]). A new parton flavor is picked randomly following the splitting functions as well. As μ' increases, the PDF value is ultimately reached at scale μ.

Parton branching methods employ this sequential evolution process and are applicable in both backward evolution of parton showers from high scale μ to lower scale μ_0 as well as forward evolution of the parton densities. However, it should be noted that Eq. (3.29) solely evolves collinear PDFs, i.e. parton densities that do not contain information on the transverse momentum. To advance towards transverse momentum dependent PDFs (TMDs), it is crucial to monitor the transverse momentum of the partons along the evolution procedure and ensure a proper ordering of branchings along the branching cascade.

3.2 PB TMD evolution

When including transverse momentum $(k_\perp)$ dependence to the PDFs, two degrees of freedom $(k_{\perp,x}, k_{\perp,y})$ enter the evolution equations. The evolution equations for TMDs can be written in a general form by starting from Eq. (3.29), changing the evolution variable to a vector $\mu' \rightarrow \boldsymbol{\mu}'_\perp$ (with components $\mu'_{\perp,x}$ and $\mu'_{\perp,y}$) and inserting $k_\perp$-dependence in the parton densities $\tilde{f}_a(x,\mu^2) \rightarrow \widetilde{\mathcal{A}}_a(x,k_\perp,\mu^2)$:

$$\widetilde{\mathcal{A}}_a(x,k_\perp,\mu^2) = \Delta_a(\mu^2,\mu_0^2)\widetilde{\mathcal{A}}_a(x,k_{\perp,0},\mu_0^2) + \sum_b \int \frac{\mathrm{d}^2\boldsymbol{\mu}'_\perp}{\pi\mu'^2}\Theta(\mu^2-\mu'^2)\Theta(\mu'^2-\mu_0^2) \quad (3.33)$$

$$\times \frac{\Delta_a(\mu^2)}{\Delta_a(\mu'^2)} \int_x^{z_M} \mathrm{d}z\, P_{ab}^{(R)}(\alpha_s,z)\widetilde{\mathcal{A}}_b\left(\frac{x}{z},k'_\perp,\mu'^2\right) ,$$

where $\widetilde{\mathcal{A}}_a(x,k_\perp,\mu^2) = x\mathcal{A}_a(x,k_\perp,\mu^2)$ is the momentum-weighted TMD of a parton with flavor a at a longitudinal momentum fraction x of the hadron's momentum and transverse

momentum $k_\perp$ at a scale μ^2. The longitudinal momentum transfer at a branching is z and the momentum scale of the branching is

$$\mu' = |\boldsymbol{\mu}'_\perp| \,. \tag{3.34}$$

In the dynamics of the evolution, it is only this absolute value of the evolution vector that matters. When generating emissions numerically in the iterative solution process, both a size μ' and an (random) angle ϕ need to be generated.

Integration limits on the size of the evolution variable are set by means of Θ-functions. The integral over the absolute value μ' ranges between μ_0 and μ, while the angle of the vector in the transverse plane, ϕ (i.e. the azimuthal angle), represents the other degree of freedom. The factor $1/\pi$ ensures normalization and accounts for the ϕ dependence. The real emission probabilities are unchanged with respect to the collinear case[1].

Integration over the transverse momentum reduces these equations to evolution of integrated TMDs (iTMDs), i.e. collinear distributions:

$$\tilde{f}_a(x, \mu^2) = \int \frac{\mathrm{d}^2 \boldsymbol{k}_\perp}{\pi} \, \widetilde{A}_a(x, \boldsymbol{k}_\perp, \mu^2) \,, \tag{3.35}$$

where the transverse momentum vector contains two degrees of freedom: $|\boldsymbol{k}_\perp|$ and ϕ. The evolution equations for integrated TMDs $\tilde{f}_a$ are given by Eq. (3.29).

Equation (3.33) does not specify how to calculate the transverse momentum of parton a, $k_\perp$, from the transverse momentum of parton b, $k'_\perp$. It also does not specify what should be the scale of the strong coupling. For this, one needs an ordering condition that associates the evolution variable $\boldsymbol{\mu}'_\perp$ with kinematic variables.

3.2.1   Ordering conditions and color coherence

The association of the evolution variable with either the virtuality of the parton or a related parameter results in the ordering of branchings associated with a kinematic variable. With a two-dimensional evolution variable, branchings can be ordered in different ways.

An evolution equation for TMDs is constructed in Ref. [38] similar to that for collinear PDFs. Various ordering conditions were investigated in this first paper on PB TMD evolution. The ordering can affect the following three elements of the evolution dynamics:

1. calculation of the new transverse momentum $k_{\perp a}(z, \mu')$,

2. scale of the running coupling $\alpha_{\mathrm{s}}\left((b(z)\mu')^2\right)$ at a branching,

3. soft-gluon resolution scale $z_M(\mu')$.

---

[1]Recent developments of splitting functions in the case of TMD evolution, so-called "transverse momentum dependent splitting functions", are published in Ref. [141]

These three elements can be included in the TMD evolution equations as parameterizations via functions $a(z)$, $b(z)$ and $z_M(\mu')$ as follows:

$$\widetilde{\mathcal{A}}_a(x, k_\perp, \mu^2) = \Delta_a(\mu^2, \mu_0^2)\widetilde{\mathcal{A}}_a(x, k_{\perp,0}, \mu_0^2) + \sum_b \int \frac{d^2\boldsymbol{\mu}'_\perp}{\pi\mu'^2} \frac{\Delta_a(\mu^2)}{\Delta_a(\mu'^2)}\Theta(\mu^2 - \mu'^2)\Theta(\mu'^2 - \mu_0^2)$$

$$\times \int_x^{z_M(\mu')} dz\, P_{ab}^{(R)}\left(\alpha_s\left(b^2(z)\mu'^2\right), z\right)\widetilde{\mathcal{A}}_b\left(\frac{x}{z}, k_\perp + a(z)\mu', \mu'^2\right), \qquad (3.36)$$

In order to determine the ordering conditions represented by $a(z)$ and $b(z)$, consider the single parton branching of parton b that emits parton c and moves on in the branching cascade as parton a as shown in Fig. 3.2. Partons a, b and c have four-momenta k_a, k_b and k_c that are of the form $k^\mu = (E_k, k^1, k^2, k^z) = (E_k, \boldsymbol{k}_\perp, k^z)$, where $\boldsymbol{k}_\perp = (k^1, k^2)$ and $k_\perp = |\boldsymbol{k}_\perp|$. In light-cone coordinates this is $k = (k^+, k^-, \boldsymbol{k}_\perp)$ where $k^\pm = \frac{1}{\sqrt{2}}(E_k \pm k^z)$. The transverse momentum of parton c is denoted as $\boldsymbol{q}_\perp$.
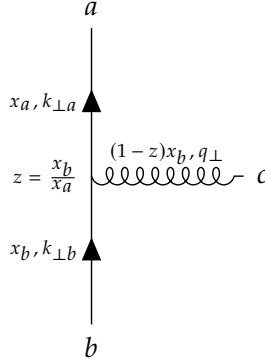
Figure 3.2: Parton branching with longitudinal momentum fractions x_b, $x_a = zx_b$, $x_c = (1 - z)x_b$ and transverse momenta $k_{\perp a}$, $k_{\perp b}$, $q_\perp$.

Conservation of the minus component of the parton momenta gives[2]:

$$\frac{k_b^2 + k_{\perp b}^2}{2k_b^+} = \frac{k_a^2 + k_{\perp a}^2}{2k_a^+} + \frac{k_c^2 + q_\perp^2}{2k_c^+}. \qquad (3.37)$$

The plus components can be easily related through the use of the splitting variable: $k_a^+ = zk_b^+$, $k_c^+ = (1 - z)k_b^+$, such that Eq. (3.37) becomes:

$$k_b^2 + k_{\perp,b}^2 = \frac{k_a^2 + k_{\perp,a}^2}{z} + \frac{k_c^2 + q_\perp^2}{1 - z}. \qquad (3.38)$$

Virtuality and transverse momentum ordering The virtuality and transverse momentum ordering conditions assume a strong ordering in transverse momenta implying that $k_{\perp b}^2 \ll k_{\perp a}^2$ such that $|\boldsymbol{k}_{\perp a}| = -|\boldsymbol{q}_\perp|$. Both the incoming particle b and the emitted particle c are on-shell: $k_b^2 = k_c^2 = 0$, assuming that the partons are massless.

---

[2]An important identity here is: $k^2 = 2k^+k^- - k_\perp^2$.

Association of the evolution scale μ' with the virtuality of parton a ($\mu'^2 = -k_a^2$) defines the virtuality ordering [142]:

$$q_\perp^2 = (1 - z)\mu'^2. \tag{3.39}$$

The assumption $z \to 0$ (valid in the high-energy or small-x limit) defines the transverse momentum ordering (p_T ordering):

$$q_\perp^2 = \mu'^2. \tag{3.40}$$

Angular ordering   Virtuality ordering and transverse momentum ordering are not based on quantum field theory arguments. A theoretical observation that gives an indication for the appropriate ordering condition is the QCD *color coherence* phenomenon [10, 43, 143–145]. Color coherence is the effect of destructive interference between parton emissions within emission cones[3]. In the evolution calculation, only the emissions that do not cancel need to be counted. Therefore, sequential branchings should be ordered according to their (rapidity) angles: $\theta_{i+1} > \theta_i$. This is visualized in Fig. 3.3, where the vertical line represents the evolution of a parton from the proton at a low scale up to the hard scattering at large scale (upper grey zone). An angular ordering of the branchings can be accomplished by use of the rescaled transverse momentum $\bar{q}_\perp$ [147]:

$$\bar{q}_\perp = \frac{|q_\perp|}{1 - z}. \tag{3.41}$$
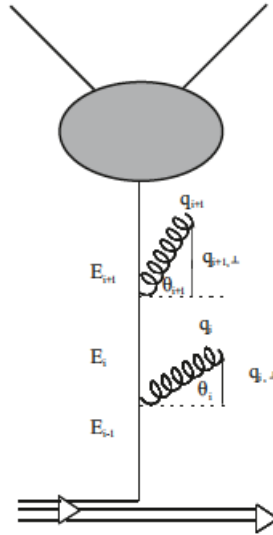
Figure 3.3: Cascade of soft gluons radiated by a parton that evolves up to the hard scattering process. The soft gluons are ordered in their angles so that $\theta_{i+1} > \theta_i$. [142]

---

[3]A similar effect occurs in QED, called the *Chudakov effect* [146].

With angular ordering, emissions are ordered along the branching cascade according to their rescaled transverse momenta: $\bar{q}_{\perp,i+1} > \bar{q}_{\perp,i}$[4]. Association of this with the evolution variable defines the angular ordering condition:

$$q_\perp^2 = (1-z)^2 \mu'^2. \tag{3.42}$$

The expressions for $a(z)$, $b(z)$ and $z_M(\mu')$ in Eq. (3.36) are summarized for all ordering conditions in Tab. 3.1. The soft-gluon resolution scale $z_M(\mu')$ is obtained by rewriting and maximization of the ordering condition for z. In p_T ordering, the evolution scale μ' does not depend on the splitting variable implying a fixed resolution scale z_M. In virtuality and angular ordering, the upper z limit is obtained by the use of a minimum transverse momentum scale $q_\perp^{\min} \equiv q_0$. The physical interpretation of q_0 is that of the minimum emitted transverse momentum at which a parton can be resolved.

Early studies in Refs. [10, 148] have demonstrated that a coherent branching approach requires the strong coupling scale to be the emitted transverse momentum, $q_\perp$, which is achieved by setting $a(z) = b(z)$.

	Transverse momentum $a^2(z)\mu'^2$	IR cut-off z_M	Scale of α_s $b^2(z)\mu'^2$
p_T ordering	$q_\perp^2 = \mu'^2$	$z_M = 1 - \epsilon$	$\alpha_s(\mu'^2)$
Virtuality ordering	$q_\perp^2 = (1-z)\mu'^2$	$z_M(\mu') = 1 - \left(\frac{q_0}{\mu'}\right)^2$	$\alpha_s\left((1-z)\mu'^2\right)$
Angular ordering	$q_\perp^2 = (1-z)^2\mu'^2$	$z_M(\mu') = 1 - \frac{q_0}{\mu'}$	$\alpha_s\left((1-z)^2\mu'^2\right)$

Table 3.1: Ordering conditions of evolution, the soft-gluon resolution scale and scale of the strong coupling. The parameters q_0 and ϵ are constants whereas μ' and z are variable parameters.

In Ref. [38], TMD evolution calculations have been performed for all scenarios of $a(z)$ and $b(z)$ in Eq. (3.36) and with fixed resolution scales $z_M = 1 - \epsilon$ with various values of ϵ. Figure 3.4 shows results of these calculations for gluon TMDs using p_T ordering (left) and angular ordering (right) with different fixed values of ϵ. From the comparison of these two ordering conditions, the conclusion has been made in [38] that with the implementation of angular ordering in the formalism, one obtains stable, quasi z_M-independent TMDs while with p_T ordering this is not the case. For this reason, reliable phenomenological studies require the use of angular ordered evolution of TMDs.

The role of the functions $a(z)$ and $b(z)$ in angular ordering has been analyzed in Refs. [36, 37, 149] for TMD applications to DY processes. We analyze the angular ordered situation $a(z) = b(z) = 1 - z$ in dept in Chapter 5.

---

[4]The CCFM formalism also has an ordering of the evolution in the rescaled transverse momentum, but as $\bar{q}_{i+1} > z\bar{q}_i$
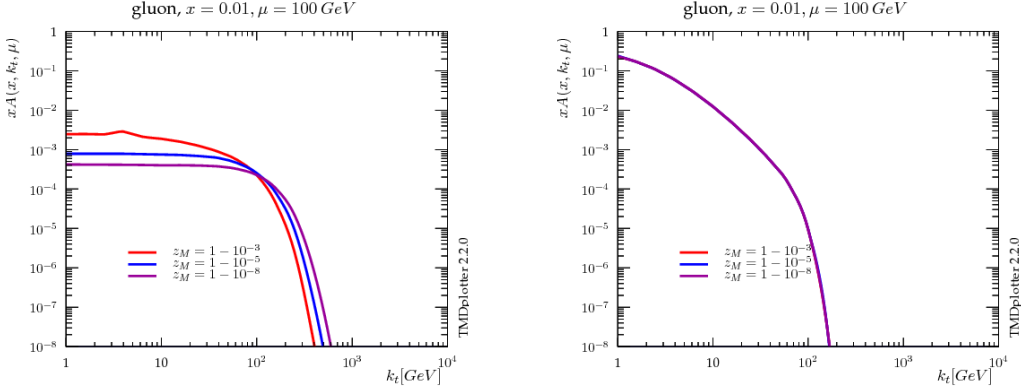
Figure 3.4: TMDs constructed by the PB method using p_T ordering (left plots) and angular ordering (right plots). The two plots are functions of $|k_\perp|$ with fixed $x = 0.01$. Three curves on each plot differ only by values of the resolution scale: $z_M = 1 - 10^{-3}$, $1 - 10^{-5}$ and $1 - 10^{-8}$ which are respectively represented by the red, blue and purple curves. [38]

3.2.2   Dealing with transverse momentum

An essential component of the PB TMD evolution algorithm involves managing transverse momentum recoils by keeping track of the emitted transverse momentum $q_{\perp,i}$ in each step along the branching cascade. The resulting transverse momentum at the final scale is obtained through the vectorial sum of all transverse momentum recoils:

$$\boldsymbol{k_\perp} = k_{\perp,0} - \sum_i \boldsymbol{q_{\perp,i}}. \tag{3.43}$$

The starting distribution $\widetilde{\mathcal{A}}_a(x, k_{\perp,0}, \mu_0^2)$ at scale μ_0^2 is factorized in a collinear PDF at scale μ_0 and a parameterization of intrinsic transverse momentum of partons in a hadron:

$$\widetilde{\mathcal{A}}_a(x, k_{\perp,0}, \mu_0^2) = x f_a(x, \mu_0^2) \cdot \mathcal{I}(k_{\perp,0}) . \tag{3.44}$$

In principle, the function $\mathcal{I}$ can take any form. The PB method parameterizes this by a normalized Gaussian function with a width defined by the q_s parameter that is $q_s^2 = 2\sigma^2$ (with σ the standard deviation of a Gaussian distribution).

$$\mathcal{I}_{\text{Gauss}}(k_{\perp,0}^2, q_s^2) = \frac{1}{\pi q_s^2} \exp\left(-\frac{k_{\perp,0}^2}{q_s^2}\right). \tag{3.45}$$

This element of the PB evolution contains non-perturbative input because of small scales μ_0^2 and a transverse momentum Gaussian curve around $k_{\perp,0}^2 = 0$. In non-perturbative studies presented in Chapter 6 this is one element to take into consideration.

Chapter 4

The TMDlib library and PB-TMD sets

We have seen in Chapter 2 that an important ingredient for the application of QCD factorization theorems to the phenomenology of high-energy colliders is given by transverse momentum dependent parton distribution functions (TMDs).

In this short chapter[1] we describe recently developed software presented in Ref. [40] which provides a common library, TMDLIB2, for such parton distributions. This allows for easy access of commonly used TMDs, and constitutes a platform for studies of the three-dimensional (3D) structure of hadrons.

The chapter is structured as follows. In the introduction, we sketch the current situation regarding PDF libraries and motivate the need for a library that provides TMDs. In Sec. 4.2, we give the main elements of the TMDLIB2 library. As an example of implemented TMDs, we explain properties of the two PB-TMD sets included in TMDLIB2 in Sec. 4.3 since these are important for the subsequent studies of this thesis. Finally, in Sec. 4.4 we describe schematically how TMD uncertainties are included in this program.

4.1 Introduction

The calculation of processes at high energy hadron colliders is based in general on the calculation of a partonic process (matrix element) convoluted with the likelihood to find a parton of specific flavor and momentum fraction at a given scale within the hadrons. If the parton density depends only on the longitudinal momentum fraction x of the hadron's momentum carried by a parton, and the scale μ, the processes are described by collinear factorization with the appropriate evolution of the parton densities (PDFs) given by the DGLAP evolution equations. Such descriptions are successful for sufficiently inclusive processes, like inclusive deep-inelastic lepton-hadron scattering (DIS).

In several less inclusive processes, on the other hand, we have discussed in Chapter 2 that also the transverse momentum of the interacting partons plays an important role, leading to an extension of the collinear factorization theorem to include transverse degrees of freedom. Different factorization theorems for the inclusion of transverse momenta to

---

[1]This work has been published in N.A. Abdulov et al., "*TMDlib2 and TMDplotter: a platform for 3D hadron structure studies*", European Physical Journal C 81 (2021) 8, 752

the parton densities have been developed in the past, leading to transverse momentum dependent (TMD) parton distributions and unintegrated parton distribution functions (uPDFs) [34]. These densities provide a 3D imaging of the hadron structure, extending the one dimensional picture given by PDFs. For semi-inclusive processes, like semi-inclusive DIS (SIDIS), Drell-Yan (DY) production and e^+e^- annihilation, TMD factorization has been formulated by many groups [49, 50, 150–160]. The high-energy (small-x limit) factorization was formulated for heavy flavor and heavy boson production in Refs. [33, 161–166] using gluon uPDFs [167–175].

Since the number of available TMD densities, obtained from parameterizations and fits to experimental data performed by different groups, increases very rapidly, it has been necessary to develop a common platform to access the different TMD sets in a common form. In 2014 the first version of TMDLIB (version 1) and TMDplotter was released [41], which made several TMD sets available to the community. This library has set a common standard for accessing TMD sets, similar to what was available for collinear parton densities in PDFlib [176, 177] and LHAPDF [178]. TMDLIB is a C++ library which provides a framework and an interface to a collection of different uPDF and TMD parameterizations. The next section gives the main features of the TMDLIB2 library.

4.2   The TMDlib framework

The TMDlib library and its new version TMDLIB2 consider momentum weighted TMD parton distributions $x\mathcal{A}_j(x, k_\perp, \mu)$ of flavor j as functions of the parton's light-cone longitudinal momentum fractions x of the hadron's momentum, the parton's transverse momentum $k_\perp$, and the evolution scale μ [34]. Besides, the library also contains integrated TMDs obtained from the integration over $k_\perp$, as follows

$$x\mathcal{A}_{int}(x, \mu) = \int_{k_{\perp,\min}}^{k_{\perp,\max}} dk_\perp^2 \; x\mathcal{A}(x, k_\perp, \mu) \,, \tag{4.1}$$

The tool TMDplotter allows for web-based plotting of distributions implemented in TMDLIB2, together with collinear PDFs as well. In Fig. 4.1 (left), we show an example of the integrated TMDs of the PB-TMD-NLO-HERAI+II-2018-set1 [37], in which the integral between $k_{\perp,\min} = 0.01$ and $k_{\perp,\max} = 100$ GeV is compared with the collinear PDF set HERAPDF2.0 [179]. By construction both sets are identical. However in general Eq. (4.1) does not converge to a collinear PDF. This is shown in the right plot of Fig. 4.1 showing the integrated TMDs of PV17 [180] integrated over in a range where $k_{\perp,\min} = 0.01$ and $k_{\perp,\max} = 100$ GeV with the corresponding collinear distribution MMHT2014 [181].

In TMDLIB2 the densities are defined more generally as momentum weighted distributions $x\mathcal{A}(x, \bar{x}, k_\perp, \mu)$, where $x, \bar{x}$ are the (positive and negative) light-cone longitudinal momentum fractions [46, 182–184].
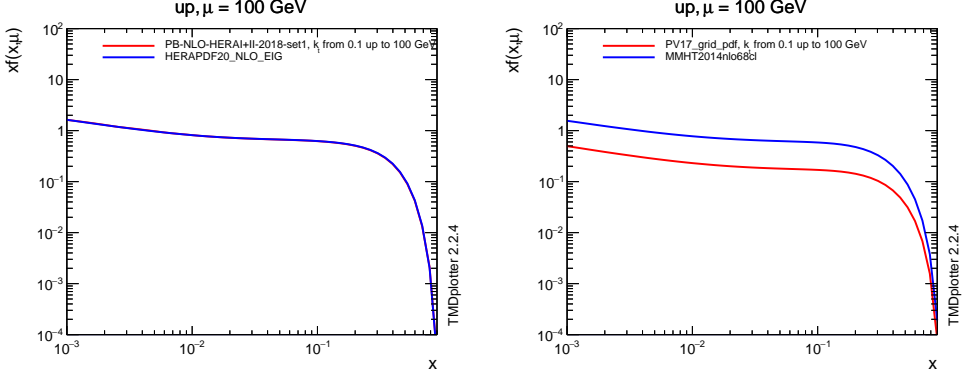
Figure 4.1: Comparison of up-quark distributions, $xf(x, \mu) = x\mathcal{A}_{int}(x, \mu)$ as a function of x at $\mu = 100$ GeV. Left: comparison of the integrated distribution PB-NLO-HERAI+II-2018-set1 [37] with HERAPDF2.0 [179]. Right: comparison of integrated distribution PV17 [180] with MMHT2014 [181].

4.3 PB-TMD sets

In Chapter 3 the PB method was formulated as a way to obtain TMDs for all light flavors over a wide range of x, transverse momentum $k_\perp$, and scale μ essentially by solving NLO RGEs through Sudakov form factors, separating resolvable and non-resolvable branchings via a soft-gluon resolution scale [7, 11] and keeping track of the transverse momenta at each branching. Fits to experimental data of inclusive DIS precision measurements at HERA [179] were presented in Ref. [37] by the `xFitter` [185, 186] framework. With these, two TMD sets PB-TMD-NLO-HERAI+II-2018-set1 and PB-TMD-NLO-HERAI+II-2018-set2 as well as their integrated analogues were obtained. They are evolved up to scale $\mu^2 = Q^2$ with the following dynamics and kinematic constraints:

- The starting distributions $\tilde{f}_a(x, \mu_0^2)$ are taken from fits to DIS measurements from H1 and ZEUS resulting in the PDF HERAPDF2.0 [179].

- The starting evolution scale μ_0^2 is 1.9 GeV^2 for set1 and $\mu_0^2 = 1.4$ GeV^2 for set2.

- Evolution is performed with NLO splitting functions $P_{ab}^{\text{NLO}} = \frac{\alpha_s}{2\pi} P_{ab}^{(0)} + \left(\frac{\alpha_s}{2\pi}\right)^2 P_{ab}^{(1)}$

- In both sets, emitted transverse momentum $q_\perp$ is associated to the evolution variable μ' according to the angular ordering condition: $q_\perp = (1 - z)\mu'$.

- The scale of the strong coupling is treated differently:

  - Set 1 has $\alpha_s(\mu')$

  - Set 2 has $\alpha_s(q_\perp)$.
    For this scenario, an additional constraint to avoid approaching Λ_{QCD} is needed which is obtained by introducing a cut-off $q_{cut} = 1.0$ GeV and applying $\alpha_s(\max(q_\perp^2, q_{cut}^2))$.

- The soft-gluon resolution scale is fixed for both sets at $z_M = 1 - 10^{-5}$.

The integrated distributions are available through LHAPDF [178] and the TMD sets are implemented in TMDLIB2.
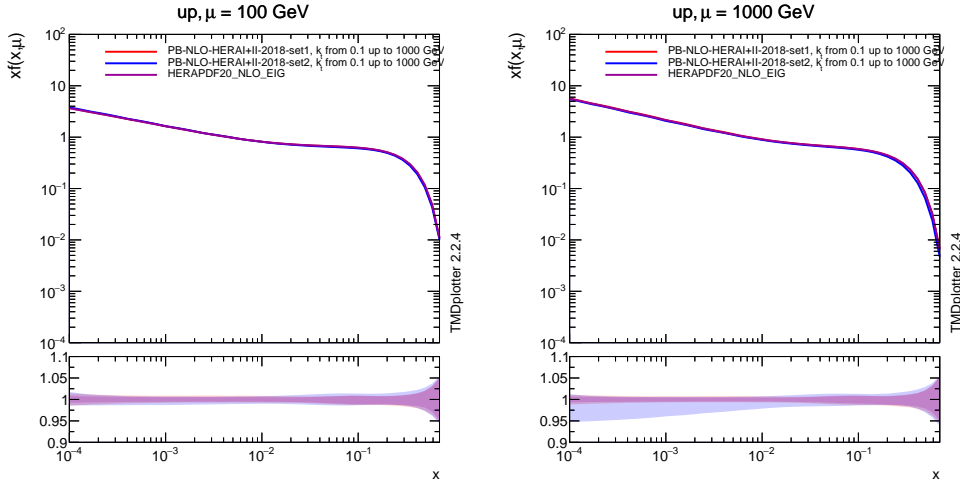
Figure 4.2: Collinear parton density distributions for up quarks (PB-NLO-HERAI+II-2018-set1, PB-NLO-HERAI+II-2018-set2 and HERAPDF2.0) as a function of x at $\mu = 100$ and 1000 GeV. In the lower panel the uncertainties are shown.
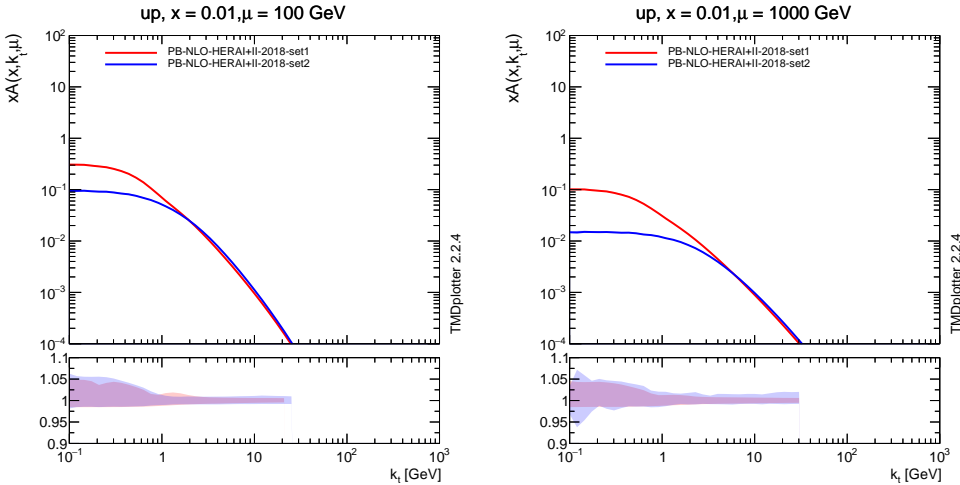
Figure 4.3: TMD parton density distributions for up quarks (PB-TMD-NLO-HERAI+II-2018-set1 and PB-TMD-NLO-HERAI+II-2018-set2) as a function of $k_\perp$ at $\mu = 100$ and 1000 GeV and $x = 0.01$. In the lower panels show the full uncertainty of the TMDs, as obtained from the fits [37].

In Fig. 4.2 (from [56]) the distributions of the collinear densities set1 and set2 are produced with TMDplotter for up-quarks at evolution scales of $\mu = 100$ and 1000 GeV. In Fig. 4.3 (from [56]) TMD distributions for up-quarks at $x = 0.01$ and $\mu = 10$ and 100 GeV are shown, which are also produced with TMDplotter. Differences between set1 and set2 are clearly visible in the small $k_\perp$-region which is affected mainly by the different treatment of α_s.

4.4 Uncertainty TMD sets

The estimation of theoretical uncertainties is an important ingredient for phenomeno-logical applications, and uncertainties from PDFs and TMDs play a central role. The uncertainties of TMDs are estimated usually from the uncertainties of the input parame-ters or parameterization. There are two different methods commonly used: the Hessian method [187] which is applied if the parameter variations are orthogonal or the Monte Carlo method providing Monte Carlo replicas [188, 189]. The specific prescriptions on how to calculate the uncertainties for a given TMD set should be found in the original publication describing the TMDs.
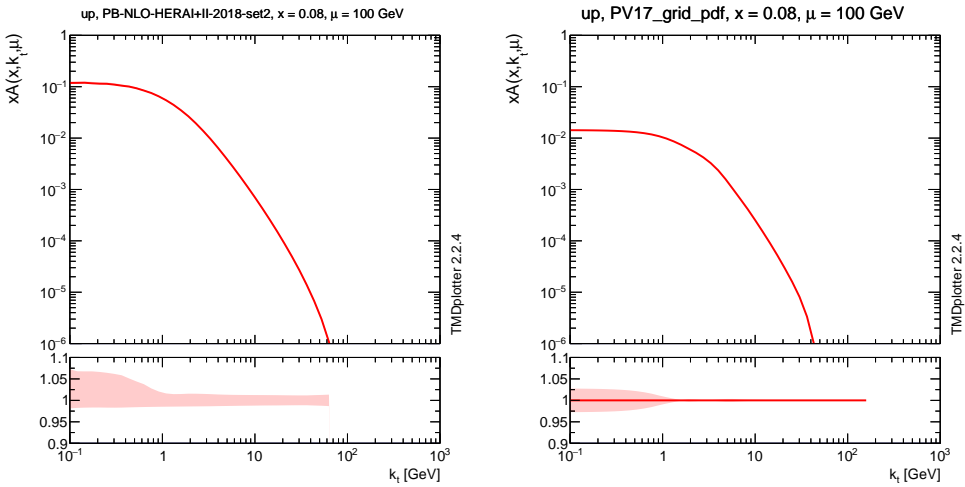
Figure 4.4: Transverse momentum distribution $x\mathcal{A}(x, k_\perp, \mu)$ at $x = 0.08$ and $\mu = 100$ GeV obtained with PB-TMD-NLO-HERAI+II-2018-set2 [37] (left) and PV17 [180] (right).

Examples of TMDs with uncertainty bands are shown in Fig. 4.4 for the PB-TMD-Set2 and the PV17 sets. The parameters of intrinsic $k_\perp$- distribution are part of the fit of PV17, while they are not fitted for the PB sets (see discussion in Ref. [37]).

The uncertainties of the PB-TMD distributions in Sec. 4.3 include both experimental and model uncertainties, as determined in Ref. [37]. In general, it is observed that those uncertainties are small; for $k_\perp > 1$ GeV they are of the order of 2–3 %.

Chapter 5

Dynamical soft-gluon resolution scale in transverse momentum distributions

In Chapter 3 the QCD evolution of TMD distribution functions has been formulated in the PB formalism [38, 39]. In this approach, soft-gluon coherence effects are taken into account by introducing the soft-gluon resolution scale and exploiting the relation between transverse-momentum recoils and branching scales.

The content of the current chapter has been published in Ref. [42][1]. Here we present investigations on the implications of dynamical, i.e. branching-scale dependent, resolution scales. We present both analytical studies and numerical solutions of the PB evolution equations in the presence of dynamical resolution scales. We use this to compare PB with other approaches in the literature, and to analyze predictions for transverse momentum distributions in Z-boson production at the LHC.

5.1 Introduction

Theoretical predictions for precision physics at high-energy hadron colliders such as the LHC require methods for QCD resummations [190] to all orders in the strong coupling. For observables sensitive to Sudakov resummation, TMD parton distributions [34] provide a theoretical framework to both carry out resummed perturbative calculations and incorporate systematically non-perturbative dynamics.

An important point in obtaining TMD distributions by means of the PB method concerns the ordering variables used to perform the branching evolution. Because the transverse momentum generated radiatively in the branching is sensitive to the treatment of the non-resolvable region [191], a supplementary condition is needed to relate the transverse momentum recoil and the scale of the branching. This relation embodies the well-known property of angular ordering presented in Chapter 3, and implies that the soft-gluon resolution scale can be dynamical.

---

[1]This work has been published in F. Hautmann, L. Keersmaekers, A. Lelek and A.M. van Kampen, "Dynamical soft-gluon resolution scale in transverse momentum distributions at the LHC", Nuclear Physics B **949**, (2019) 114795

By means of a mapping between branching scales and transverse momenta using the angular ordering condition, we discuss the resolvable radiation regions and PB evolution equations. We solve these equations with dynamical resolution scale numerically by applying the Monte Carlo solution techniques developed in [39, 192]. We compare the PB results with results from two other approaches: the coherent branching approach of Catani, Marchesini and Webber (CMW) [10, 43] and the single-emission approach of Kimber, Martin, Ryskin and Watt (KMRW) [44–47]. We present an application of our formalism to the Z-boson transverse momentum distribution in Drell-Yan (DY) production [126] at the LHC, and study its sensitivity to dynamical resolution scales at low transverse momenta.

The chapter is organized as follows. In Sec. 5.2 we recapitulate the dynamical soft-gluon resolution scale and describe the resolvable and non-resolvable emission regions of the phase space. In Sec. 5.3 we map branching scales to transverse momenta, and give the corresponding form of PB equations. In Sec. 5.4 we use these results to perform an analytic comparison of the multiple-emission PB and single-emission KMRW approaches. In Sec. 5.5 we solve the PB evolution equation with dynamical resolution scale by numerical methods, and present predictions for the Z-boson transverse momentum spectrum at the LHC. We give conclusions in Sec. 5.6.

5.2   Soft-gluon angular ordering in PB-TMD evolution

In the PB approach, QCD color coherence is accounted for by the association of rescaled transverse momentum recoils with the evolution variable. With that, the emissions are ordered according to their angles by [38]

$$q_\perp^2 = (1-z)^2 \mu'^2 \ . \tag{5.1}$$

This condition implies that $a(z)$ and $b(z)$ in the general TMD evolution equation in Eq. (3.36) take the form of $1-z$, giving:

$$\widetilde{\mathscr{A}}_a(x, k_\perp, \mu^2) = \Delta_a(\mu^2, \mu_0^2)\widetilde{\mathscr{A}}_a(x, k_{\perp,0}, \mu_0^2) + \sum_b \int \frac{d^2\mu'_\perp}{\pi\mu'^2_\perp}\Theta(\mu^2 - \mu'^2_\perp)\Theta(\mu'^2_\perp - \mu_0^2) \quad (5.2)$$

$$\times \int_x^{z_M(\mu')} dz \, \frac{\Delta_a(\mu^2)}{\Delta_a(\mu'^2)} \, P_{ab}^{(R)}\left(\alpha_s\left((1-z)^2\mu'^2\right), z\right) \widetilde{\mathscr{A}}_b\left(\frac{x}{z}, \mathbf{k}_\perp + (1-z)\mathbf{\mu}'_\perp, \mu'^2\right) \ .$$

The scale of the strong coupling is associated to the transverse momentum recoil [10, 37, 43] such that $\alpha_s((1-z)^2\mu'^2) = \alpha_s(q_\perp^2)$ and the Sudakov form factor $\Delta(\mu^2) \equiv \Delta(\mu^2, \mu_0^2)$ equals

$$\Delta_a(\mu^2, \mu_0^2) = \exp\left\{-\sum_b \int_{\mu_0^2}^{\mu^2} \frac{d\mu'^2}{\mu'^2} \int_0^{z_M(\mu')} dz \, z \, P_{ba}^{(R)}\left(\alpha_s\left((1-z)^2\mu'^2\right), z\right)\right\} \ . \tag{5.3}$$

The function $z_M(\mu')$ specifies the soft-gluon resolution scale [39] which separates the region of resolvable branchings ($z < z_M$) from the region of non-resolvable branchings

($z > z_M$), for any given μ'. We have denoted the minimum transverse momentum with which any emitted parton can be resolved by q_0, so that

$$q_\perp > q_0 \ . \tag{5.4}$$

By inserting the angular ordering relation (5.1) into Eq. (5.4), the condition for resolving soft gluons is given by $z < z_M(\mu')$ with [7, 11, 38]

$$z_M(\mu') = 1 - q_0/\mu' \ , \tag{5.5}$$

where the momentum scale q_0 is understood to be $q_0 \simeq \Lambda_{\mathrm{QCD}}$. Here we concentrate on implications of the resolution scale $z_M(\mu')$ in Eq. (5.5).

Evolution of integrated momentum-weighted TMDs $\tilde{f}_a(x, \mu^2)$ (Eq. (3.35)) is obtained by the integrated analogue of Eq. (5.2):

$$\tilde{f}_a(x, \mu^2) = \Delta_a(\mu^2, \mu_0^2)\tilde{f}_a(x, \mu_0^2) + \sum_b \int_{\mu_0^2}^{\mu^2} \frac{d\mu'^2}{\mu'^2} \Theta(\mu^2 - \mu'^2)\Theta(\mu'^2 - \mu_0^2) \tag{5.6}$$

$$\times \int_x^1 dz \Theta\left(1 - \frac{q_0}{\mu'} - z\right) \frac{\Delta_a(\mu^2)}{\Delta_a(\mu'^2)} P_{ab}^{(R)}\left(\alpha_{\mathrm{s}}((1-z)^2\mu'^2), z\right) \tilde{f}_b\left(\frac{x}{z}, \mu'^2\right) \ .$$

It has been shown in Refs. [38, 39] that for $z_M \to 1$ and $\alpha_{\mathrm{s}} \to \alpha_{\mathrm{s}}(\mu'^2)$ these are collinear parton distribution functions satisfying the DGLAP evolution equations [75, 77, 78, 193].[2]

We depict the resolvable region of the phase space by a yellow area in the (μ', z)-plane in Fig. 5.1. The resolvable region is separated from the non-resolvable region by the red curve that represents the dynamical resolution scale $z_M(\mu')$. Fig. 5.1(a) represents the case of contributions to the distribution function with $x \geq 1 - q_0/\mu_0$, while Fig. 5.1(b) represents the case of $x < 1 - q_0/\mu_0$.

Note that the infrared region near the QCD scale Λ_{QCD} is automatically avoided by using the dynamical resolution scale with $q_0 = 1$ GeV.

5.3 Mapping evolution scales to transverse momenta

We next recast the PB evolution for integrated TMDs and separation between resolvable and non-resolvable branchings in terms of longitudinal momentum fractions and transverse momenta. To this end, we exploit the angular ordering relation in Eq. (5.1) to map branching scales on to transverse momenta for the resolvable regions in Fig. 5.1.

Given the minimum transverse momentum q_0 and the lowest scale μ_0 of the evolution, for any x it is useful to distinguish the two cases illustrated in Fig. 5.1, depending on whether a) $\mu_0 \leq q_0/(1 - x)$ or b) $\mu_0 > q_0/(1 - x)$. For any z with $x \leq z \leq 1$, in case a) the emitted transverse momentum spans the interval $q_0 \leq q_\perp \leq \mu(1 - z)$, while in case b) we have $\mu_0(1-z) \leq q_\perp \leq \mu(1-z)$. This results into different forms of the branching equations in the two cases, once they are expressed directly in terms of transverse momenta.

---

[2]The convergence to DGLAP at LO and NLO has been verified numerically in [38] against the evolution program QCDNUM [194] at level of better than 1% over a range of five orders of magnitude both in x and in μ.
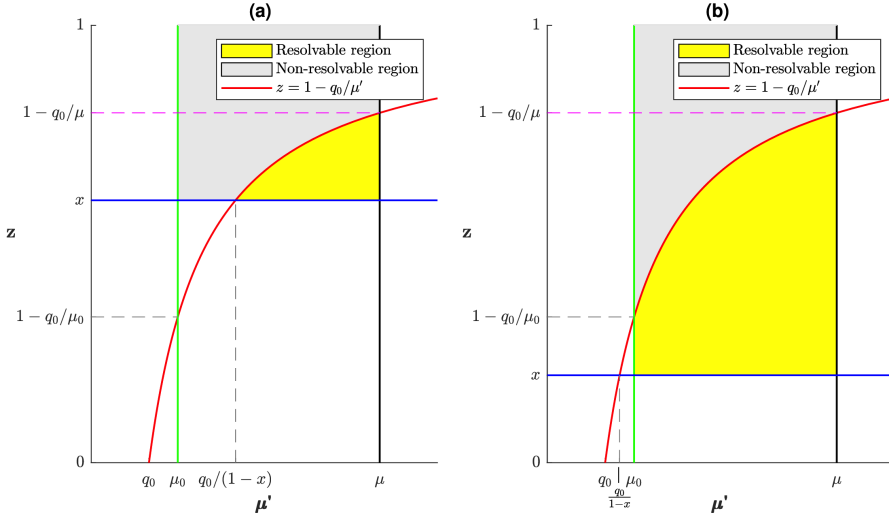
Figure 5.1: The angular ordering condition $z_M(\mu') = 1 - q_0/\mu'$ with the resolvable and non-resolvable emission regions in the (μ', z)-plane: a) the case $1 > x \geq 1 - q_0/\mu_0$; b) the case $1 - q_0/\mu_0 > x > 0$.

5.3.1 Case a) $1 > x \geq 1 - q_0/\mu_0$

For $x \geq 1 - q_0/\mu_0$ the resolvable emission region is mapped to the domain in the $(z, q_\perp)$ plane pictured in Fig. 5.2(a). We change the integration variable from μ' to $q_\perp$ in the integrated form of branching equation (5.6) using the angular ordering relation (5.1). Then Eq. (5.6) can be recast in terms of transverse momenta as

$$\tilde{f}_a(x, \mu^2) = \Delta_a(\mu^2, \mu_0^2)\tilde{f}_a(x, \mu_0^2) + \sum_b \int \frac{dq_\perp^2}{q_\perp^2} \int_x^1 dz \, \Theta(q_\perp^2 - q_0^2) \, \Theta(\mu^2(1-x)^2 - q_\perp^2) \quad (5.7)$$

$$\times \Theta(1 - q_\perp/\mu - z) \, \frac{\Delta_a(\mu^2, \mu_0^2)}{\Delta_a\left(q_\perp^2/(1-z)^2, \mu_0^2\right)} \, P_{ab}^{(R)}(\alpha_s(q_\perp^2), z)\tilde{f}_b\left(\frac{x}{z}, \frac{q_\perp^2}{(1-z)^2}\right) \, .$$

5.3.2 Case b) $1 - q_0/\mu_0 > x > 0$

For $x < 1 - q_0/\mu_0$ the resolvable emission region is mapped to the domain in the $(z, q_\perp)$ plane pictured in Fig. 5.2(b). Performing the same change of integration variable in Eq. (5.6) as in case a) of the previous subsection, we recognize that now a subtraction term arises from the low-$q_\perp$ region, $q_0 < q_\perp < (1-x)\mu_0$, so that Eq. (5.6) is rewritten in
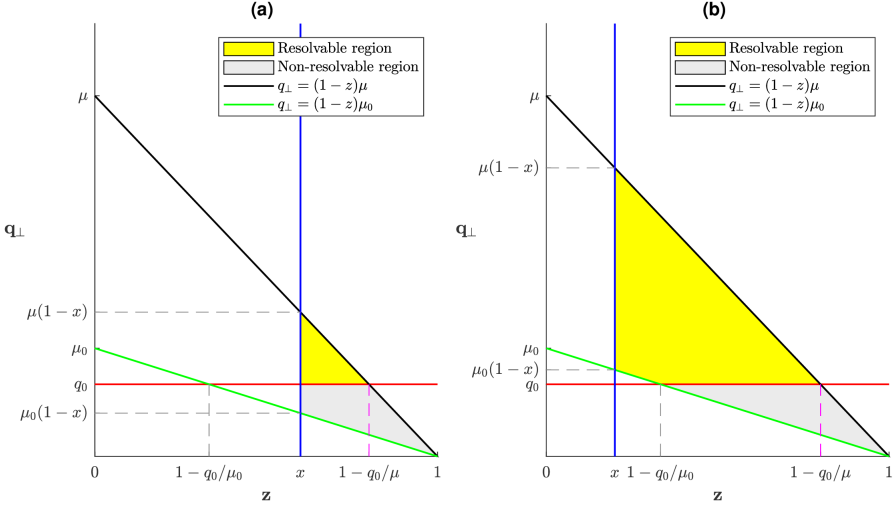
Figure 5.2: Resolvable and non-resolvable emission regions in the $(z, q_\perp)$ plane for evolution in the cases a) $1 > x \geq 1 - q_0/\mu_0$ and b) $1 - q_0/\mu_0 > x > 0$.

terms of transverse momenta as

$$
\begin{aligned}
\tilde{f}_a(x, \mu^2) &= \Delta_a(\mu^2, \mu_0^2)\tilde{f}_a(x, \mu_0^2) + \sum_b \int \frac{dq_\perp^2}{q_\perp^2} \int_x^1 dz \left[\Theta\left(q_\perp^2 - q_0^2\right) \Theta\left(\mu^2(1-x)^2 - q_\perp^2\right) \right. \\
&\quad \times \left. \Theta\left(1 - \frac{q_\perp}{\mu} - z\right) - \Theta\left(q_\perp^2 - q_0^2\right) \Theta\left(\mu_0^2(1-x)^2 - q_\perp^2\right) \Theta\left(1 - \frac{q_\perp}{\mu_0} - z\right) \right] \\
&\quad \times \frac{\Delta_a(\mu^2, \mu_0^2)}{\Delta_a\left(q_\perp^2/(1-z)^2, \mu_0^2\right)} P_{ab}^{(R)}(\alpha_s(q_\perp^2), z)\tilde{f}_b\left(\frac{x}{z}, \frac{q_\perp^2}{(1-z)^2}\right) .
\end{aligned}
\tag{5.8}
$$

We observe that the first term in the square bracket in Eq. (5.8) is a contribution analogous to that in Eq. (5.7), while the second term in the square bracket provides the low-$q_\perp$ subtraction.

Alternatively, the branching kernel in the case $x < 1 - q_0/\mu_0$ can be expressed as a sum of two contributions, corresponding respectively to the $q_\perp < (1-x)\mu_0$ region and $q_\perp > (1-x)\mu_0$ region, as follows:

$$
\begin{aligned}
\tilde{f}_a(x, \mu^2) =&\, \Delta_a(\mu^2, \mu_0^2)\tilde{f}_a(x, \mu_0^2) + \tag{5.9} \\
&+ \sum_b \int \frac{dq_\perp^2}{q_\perp^2} \int_x^1 dz \left[\Theta\left(q_\perp^2 - q_0^2\right) \Theta\left(\mu_0^2(1-x)^2 - q_\perp^2\right) \right. \\
&\times \Theta\left(z + \frac{q_\perp}{\mu_0} - 1\right) \Theta\left(1 - \frac{q_\perp}{\mu} - z\right) + \Theta\left(q_\perp^2 - (1-x)^2\mu_0^2\right) \Theta\left(\mu^2(1-x)^2 - q_\perp^2\right) \\
&\times \left. \Theta\left(1 - \frac{q_\perp}{\mu} - z\right) \right] \frac{\Delta_a(\mu^2, \mu_0^2)}{\Delta_a\left(q_\perp^2/(1-z)^2, \mu_0^2\right)} P_{ab}^{(R)}(\alpha_s(q_\perp^2), z)\tilde{f}_b\left(\frac{x}{z}, \frac{q_\perp^2}{(1-z)^2}\right) .
\end{aligned}
$$

Here the two terms of the sum in the square bracket, given by products of Θ-functions, describe the low-$q_\perp$ and high-$q_\perp$ contributions.

In the next section we will use the form for the branching equations derived above, along with the formulas of Sec. 5.2, to carry out a comparison of the PB method [38, 39] with other existing approaches in the literature. We will analyze in particular different treatments of the QCD parton cascade, in which the transverse momentum is generated either through multiple emissions or through a single emission.

5.4   Multiple-emission versus single-emission approaches

5.4.1   Comparison with the CMW approach

As an approach based on the unitarity picture [7, 11] of parton evolution and angular ordering, the PB method [38, 39] can naturally be compared with the coherent branching approach of Catani-Marchesini-Webber (CMW) [10, 43]. Since Refs. [10, 43] do not construct TMD distributions, we examine branching equations in the PB and CMW approaches at the level of integrated distributions. The evolution equation for PDFs $D(x, Q)$ in scale Q in the CMW coherent branching approach is given by Eq. (42) of Ref. [10] as:

$$\mu \frac{\partial}{\partial \mu} D(x, Q) = \int_x^{1-\epsilon(Q)} \frac{dz}{z} D\left(\frac{x}{z}, Q\right) \hat{P}(z) \frac{\alpha_{\text{s}}(Q(1-z))}{\pi} \tag{5.10}$$
$$- D(x, Q) \int_0^{1-\epsilon(Q)} dz \hat{P}(z) \frac{\alpha_{\text{s}}(Q(1-z))}{\pi} \,,$$

where $\epsilon(Q) = Q_0/Q$ and splitting functions are applied at leading order. This equation corresponds with Eq. (3.17), where the only kernels are real-emission (or unregularized) splitting functions $\hat{P} = P_{ab}^{(R)}$. We observe that at this integrated level, the PB evolution equation (5.6) with a dynamical resolution scale and $\alpha_{\text{s}}(q_\perp^2)$ agrees with that by CMW. In Ref. [10] this branching equation is studied at LO with one-loop splitting kernels and running coupling, while in Ref. [39] (and in the present chapter) it is studied at NLO with two-loop splitting kernels and running coupling.[3]

5.4.2   Comparison with the KMRW approach

The Kimber-Martin-Ryskin-Watt (KMRW) approach [44–47], is designed to construct TMD "unintegrated" parton distributions. In contrast to the PB method, in which the transverse momentum and the branching scale are calculated at each branching, KMRW is a one-step evolution approach: it performs evolution in one scale up to $q_\perp^2$, while the second scale is generated only in the last step of the evolution. The KMRW physical picture is thus quite different from that of PB and CMW. In particular, in KMRW the

---

[3]The treatment in Ref. [39] incorporates in particular the two-loop correction to the coupling which is shown in Ref. [43] to be required to obtain next-to-leading-logarithmic accuracy in the soft-gluon resummation.

transverse momentum is produced as a result of a single emission, while in PB it is built from multiple emissions.

In the KMRW literature, the distinction between the values of the two momentum scales μ_0 and q_0 discussed in Sec. 5.3 is not made. For the purpose of this comparison, therefore, we set $q_0 \approx \mu_0$ in the formulation of Sec. 5.3, and we will thus be using the branching equation valid in case a) of Subsec. 5.3.1, Eq. (5.7).

In the KMRW approach the TMD distribution $\widetilde{D}_a$ is obtained by [44–47]

$$\widetilde{D}_a(x, \mu^2, q_\perp^2) \quad = \quad T_a(\mu^2, q_\perp^2) \sum_b \int_x^{1-C(q_\perp, \mu)} dz P_{ab}^{(R)}\left(\alpha_s(q_\perp^2), z\right) \tilde{f}_b\left(\frac{x}{z}, q_\perp^2\right) \ , \quad (5.11)$$

where the Sudakov form factor is given by

$$T_a(\mu^2, q_\perp^2) = \exp\left\{ -\int_{q_\perp^2}^{\mu^2} \frac{dq_\perp'^2}{q_\perp'^2} \sum_b \int_0^{1-C(q_\perp', \mu)} dz \, z \, P_{ba}^{(R)}\left(\alpha_s(q_\perp'^2), z\right)\right\} \ , \quad (5.12)$$

and the collinear density $\tilde{f}_a(x, \mu^2)$ obeys the evolution equation

$$\tilde{f}_a(x, \mu^2) = \tilde{f}_a(x, \mu_0^2) T_a(\mu^2, \mu_0^2) \quad (5.13)$$
$$+ \int_{\mu_0^2}^{q_{\perp M}^2} \frac{dq_\perp^2}{q_\perp^2} \left(T_a(\mu^2, q_\perp^2) \sum_b \int_x^{1-C(q_\perp, \mu)} dz P_{ab}^{(R)}\left(\alpha_s(q_\perp^2), z\right) \tilde{f}_b\left(\frac{x}{z}, q_\perp^2\right)\right) \ .$$

The phase space parameters $C(q_\perp, \mu)$ and $q_{\perp M}$ in the above formulas are assigned according to two distinct prescriptions [44–47, 195] in the KMRW approach:

$$C(q_\perp, \mu) = q_\perp/\mu \ , \quad q_{\perp M} = \mu(1 - x) \quad \text{for KMRW strong ordering} \quad (5.14)$$

and

$$C(q_\perp, \mu) = q_\perp/(q_\perp + \mu) \ , \quad q_{\perp M} = \mu(1 - x)/x \quad \text{for KMRW angular ordering.} \quad (5.15)$$

Having mapped the PB evolution onto transverse momenta in Sec. 5.3, we are in a position to directly compare the PB and KMRW results. By considering Eq. (5.7) and Eq. (5.13) with KMRW strong ordering conditions (5.14), we recognize that PB and KMRW differ in the momentum scales at which both the Sudakov form factor and the collinear density $\tilde{f}_b$ are evaluated, as KMRW uses transverse momenta whereas PB uses transverse momenta rescaled by $1/(1 - z)$. From Eq. (5.7) and Eq. (5.13) with KMRW angular ordering conditions (5.15), we recognize that in this case PB and KMRW, besides differing in the arguments of Sudakov factor and collinear density, differ also in the phase space regions in longitudinal and transverse momenta that are populated by the radiative processes.

We thus see that, also taking into account the possible prescriptions in Eqs. (5.14) and (5.15), the one-step picture of KMRW leads to different results from the multiple-emission PB picture. In Sec. 5.5 we illustrate the implications of these differences by performing numerical calculations for the TMD distributions that result from evolution in the two approaches, and examining the corresponding predictions for the DY Z-boson transverse momentum spectra at the LHC.

5.4.3   Remark on Sudakov form factors

It is worth noting that the definition of the Sudakov form factor itself plays a different role in the context of the PB approach and the KMRW approach.

In the PB approach the Sudakov form factor $\Delta_a(\mu^2, \mu_0^2)$ has the interpretation of probability for no resolvable branching in a given evolution interval from μ_0 to μ, and fulfills the property

$$\Delta_a(\mu^2, \tilde{\mu}^2)\Delta_a(\tilde{\mu}^2, \mu_0^2) = \Delta_a(\mu^2, \mu_0^2) \tag{5.16}$$

for any evolution scale $\tilde{\mu}$.

For example, for the Sudakov form factor in the angular-ordered evolution we use

$$\Delta_a(\mu^2, \mu_0^2) = \exp\left\{ -\sum_b \int_{\mu_0^2}^{\mu^2} \frac{d\mu'^2}{\mu'^2} \int_0^{1-q_0/\mu'} dz\, z\, P_{ba}^{(R)}\left(\alpha_s((1-z)^2\mu'^2), z\right)\right\}, \tag{5.17}$$

for which Eq. (5.16) is fulfilled. Mapping the argument of the exponent to transverse momenta is performed by means of the angular ordering relation and requires reversing the integrals twice as follows

$$\int_{\mu_0^2}^{\mu^2} \frac{d\mu'^2}{\mu'^2} \int_0^{1-q_0/\mu'} dz = \tag{5.18}$$

$$= \int_0^{1-q_0/\mu_0} dz \int_{\mu_0^2}^{\mu^2} \frac{d\mu'^2}{\mu'^2} \qquad\qquad + \int_{1-q_0/\mu_0}^{1-q_0/\mu} dz \int_{q_0^2/(1-z)^2}^{\mu^2} \frac{d\mu'^2}{\mu'^2}$$

$$= \int_0^{1-q_0/\mu_0} dz \int_{(1-z)^2\mu_0^2}^{(1-z)^2\mu^2} \frac{dq_\perp^2}{q_\perp^2} \qquad\qquad + \int_{1-q_0/\mu_0}^{1-q_0/\mu} dz \int_{q_0^2}^{(1-z)^2\mu^2} \frac{dq_\perp^2}{q_\perp^2}$$

$$= \int_{\mu_0^2}^{\mu^2} \frac{dq_\perp^2}{q_\perp^2} \int_0^{1-q_\perp/\mu} dz \qquad\qquad + \int_{q_0^2}^{\mu_0^2} \frac{dq_\perp^2}{q_\perp^2} \int_{1-q_\perp/\mu_0}^{1-q_\perp/\mu} dz.$$

The integration regions follow from phase space diagrams such as Fig. 5.2(b) with the difference that the lower z limit of the Sudakov form factor is equal to 0. The Sudakov form factor can than be written as:

$$\Delta_a(\mu^2, \mu_0^2) = \exp\left\{ -\sum_b \left[\int_{\mu_0^2}^{\mu^2} \frac{dq_\perp^2}{q_\perp^2} \int_0^{1-q_\perp/\mu} dz + \right.\right. \tag{5.19}$$

$$\left.\left. + \int_{q_0^2}^{\mu_0^2} \frac{dq_\perp^2}{q_\perp^2} \int_{1-q_\perp/\mu_0}^{1-q_\perp/\mu} dz \right] z\, P_{ba}^{(R)}\left(\alpha_s(q_\perp^2), z\right)\right\},$$

for which Eq. (5.16) is still fulfilled. In the case that $\mu_0 = q_0$, the second term of the exponent is zero.

On the other hand, using the KMRW Sudakov of Eq. (5.12), Eq. (5.16) is not fulfilled. Rather, one has

$$T_a(\mu^2, k_\perp^2)T_a(k_\perp^2, \mu_0^2) = \tag{5.20}$$

$$= T_a(\mu^2, \mu_0^2)\exp\left\{ \sum_b \int_{\mu_0^2}^{k_\perp^2} \frac{dq_\perp^2}{q_\perp^2} \int_{1-C(q_\perp, k_\perp)}^{1-C(q_\perp, \mu)} dz\, z\, P_{ba}^{(R)}\left(\alpha_s(q_\perp^2), z\right)\right\}.$$

This implies that, besides the different treatment of radiative processes noted in Subsec. 5.4.2, we observe differences between the single-emission and multiple-emission approaches also in the treatment of the non-resolvable processes. We may expect that the features noted in Subsec. 5.4.2 and in this subsection will lead to different behaviors in transverse momentum distributions both at high transverse momenta and at low transverse momenta.

Effects such as these noted here in Eq. (5.20) and in Ref. [42] in the context of Parton Branching and KMRW, characterized by the breaking of the equality in Eq. (5.16), have been studied in Refs. [196, 197] in the context of analytic resummation.

5.5 Numerical results

We investigate next the numerical implications of the analysis in the previous sections on TMDs, iTMDs and DY spectra.

5.5.1 TMDs from PB and KMRW

In this section we present numerical results for TMD distribution functions from the PB approach with dynamical resolution scale. We perform numerical comparisons with KMRW TMDs. The results are shown as functions of flavor, longitudinal momentum fraction x, transverse momentum $k_\perp$ and evolution scale μ.

KMRW TMD distribution sets have been obtained in [198] according to the KMRW angular ordering prescription (5.15), using the CT10nlo PDF [199] set as a starting collinear distribution and a flat parametrization for $k_\perp < 1$ GeV as an intrinsic $k_\perp$ distribution at starting scale μ_0. These distributions have been included in the TMDlib library [40, 41] described in Chapter 4 under the name MRW-CT10nlo.[4]

To evaluate PB TMDs, we solve numerically Eq. (5.2) with the dynamical resolution scale in Eq. (5.5) where we take $q_0 = 1$ GeV, and $q_\perp$ as the scale of α_s. We use the Monte Carlo solution method developed in [38, 39] and implemented in `uPDFevolv` [192]. Following Eqs. (3.44) and (3.45), we take the intrinsic $k_\perp$ distribution given by a Gaussian at starting scale μ_0 with (flavor-independent and x-independent) width $\sigma = q_s/\sqrt{2}$ where $q_s = 0.5$ GeV. For the purpose of performing comparisons with the KMRW TMD set MRW-CT10nlo, we take the same starting collinear distribution CT10nlo [199].

In addition, we introduce an approximation to the PB framework, which we refer to as "PB last step", which is obtained from PB by taking the same settings as the full PB calculation but restricting the transverse momentum $k_\perp$ to the last emission only. We use the PB-last-step Monte Carlo simulation as a guidance to distinguish effects from single emission and multiple emissions.

---

[4]Strictly speaking, the TMD set MRW-CT10nlo has been obtained using the differential definition of KMRW TMDs (see e.g. [195, 198]). We have performed also studies with KMRW TMDs defined according to the integral definition (as in Eq. (5.11)) and we have verified that our conclusions remain valid.
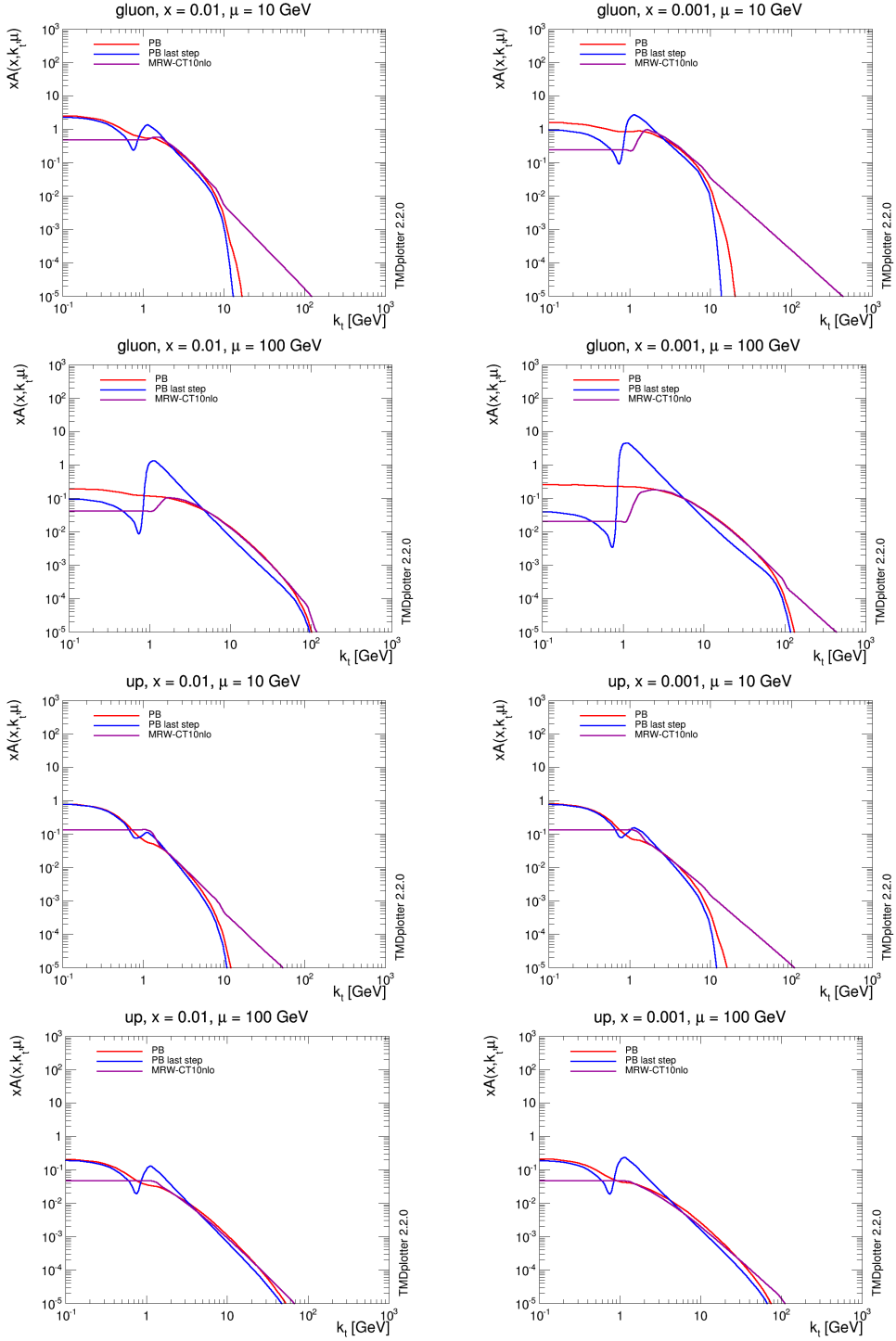
Figure 5.3: Transverse momentum $k_\perp = k_t$ distributions from evolution with PB (in red), PB last step (in blue) and KMRW (in purple) as functions of transverse momentum for gluons and quarks and for different values of longitudinal momentum fraction x and evolution scale μ.

In Fig. 5.3 we show transverse momentum distributions of gluon and up-quark TMDs obtained from PB, MRW-CT10nlo and PB-last-step calculations, at different values of x and μ.[5] We may distinguish three regions of low $k_\perp$, middle $k_\perp$ and high $k_\perp$, characterized by distinct behaviors. Significant numerical differences between PB and KMRW show up especially in the extreme regions $k_\perp \ll \mu$ and $k_\perp \gg \mu$, while in the middle values around $k_\perp \sim \mu$ the two predictions tend to become closer.

In particular, we observe that at low $k_\perp$ the smearing of the intrinsic $k_\perp$ distribution due to evolution gives rise to different behaviors in the single-emission and multiple-emission cases. The kink at low $k_\perp$ in MRW-CT10nlo is a consequence of the single-emission picture, and is not present in the full PB case, where multiple branchings are responsible for generating the transverse momentum.

We also observe that at high $k_\perp$ the MRW-CT10nlo distribution is far harder than PB and PB-last-step. This reflects the different pattern of radiative contributions in KMRW from PB, illustrated in Sec. 5.4. As noted in [198], the treatment of the Sudakov form factor in Eq. (5.12) for $k_\perp^2 > \mu^2$ influences the MRW-CT10nlo high $k_\perp$ tail.

5.5.2 iTMDs from PB and KMRW

In Fig. 5.4 the results of integrating MRW-CT10nlo, PB and PB-last-step TMDs over the transverse momentum $k_\perp$ at a given evolution scale μ are shown as functions of x. Results are shown for integrating TMDs over $k_\perp < \mu$ (Fig. 5.4(left)) and over all $k_\perp$ (Fig. 5.4(right)). For comparison, we also plot CT10nlo distributions at the same μ. In the lower parts of the figure the ratios of integrated TMDs to CT10nlo are plotted. As expected, we observe that none of the distributions integrate to CT10nlo, given that the resolution scale z_M is far from 1, and the scale of the running coupling α_s is $q_\perp$ — see discussion below Eq. (5.6). In the case of integrating over all $k_\perp$ (Fig. 5.4 (right)) we note that MRW-CT10nlo gives rise to a much higher distribution than all other curves, implying that the MRW-CT10nlo high-$k_\perp$ tail has a significant impact at integrated level for most values of x. On the other hand, when integrating over $k_\perp < \mu$ (Fig. 5.4 (left)) the deviation of MRW-CT10nlo from collinear CT10nlo is much smaller than that of PB, which is a further manifestation of the differences between the KMRW and PB physical pictures illustrated in Sec. 5.4.

5.5.3 Z boson p_T spectrum

As explained in Chapter 2, the low-p_T region of the Z boson transverse momentum spectrum is sensitive to soft-gluon resummation and TMD effects. In this section we apply TMDs to the calculation of the DY p_T spectrum by means of the Cascade3 [51] program that is explained in Chapter 7. We obtain predictions for the Z boson distribution based on PB TMDs that include effects of a dynamical soft-gluon resolution scale. We compare them with KMRW results.

Following [37], we use on-shell LO matrix elements (in the format of LHE files [125]) generated by the Pythia8 Monte Carlo event generator [116, 200]. We are only interested

---

[5]The plots in Figs. 5.3-5.4 are obtained using the TMDplotter tool [40, 41] described in Chapter 4.
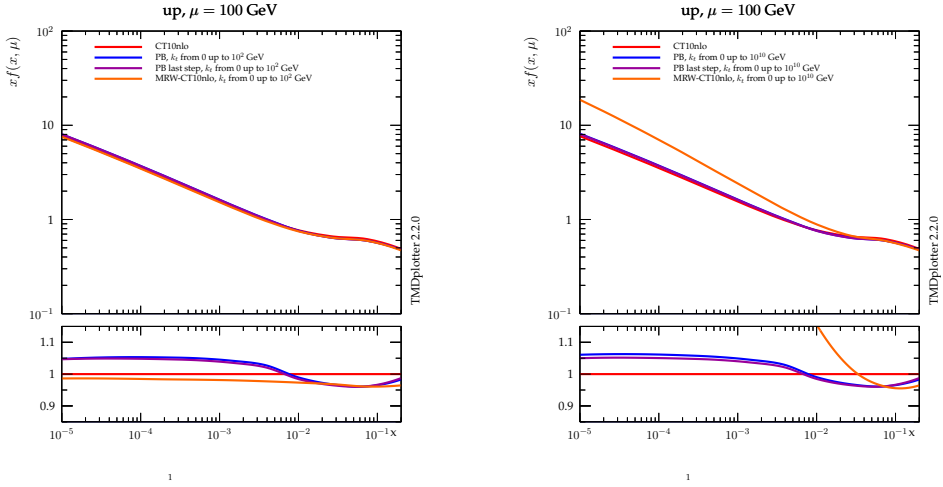
Figure 5.4: The results of integrating TMDs over $k_\perp < \mu$ (left) and over all $k_\perp$ (right) as functions of x.

in the low-p_T region, higher order matrix element contributions are therefore left out for simplicity.

In Fig. 5.5 predictions for the Z boson p_T spectrum at $\sqrt{s} = 8$ TeV are shown using MRW-CT10nlo and PB TMDs, and compared to measurements by ATLAS [131]. We see that the MRW-CT10nlo calculation and PB calculation with dynamical z_M give rise to different shapes in the spectrum both in the region of low p_T around the peak and in the region of high p_T toward the upper end of the transverse momentum range shown. There is an interval of intermediate p_T in which they are less dissimilar. The agreement of the PB calculation with the measurements is good, while MRW-CT10nlo does not describe the high p_T region, and the slope at low p_T.

For reference, we also compare PB predictions with fixed and dynamical z_M shown in Fig. 5.5. Fixed z_M ($z_M = 1 - \epsilon$) predictions are obtained by using the PB-TMD-Set2 of Ref. [37]. We see that the slope of the p_T spectrum is affected by dynamical z_M particularly in the low p_T region. The results indicate that measurements of the Z boson p_T with high resolution in the region $p_\perp \lesssim 5$ - 10 GeV will allow one to probe quantitatively effects of soft-gluon angular ordering and dynamical resolution scales.

We have limited ourselves to showing results for central values of the predictions, because TMD uncertainties in the case of dynamical z_M are not yet available.
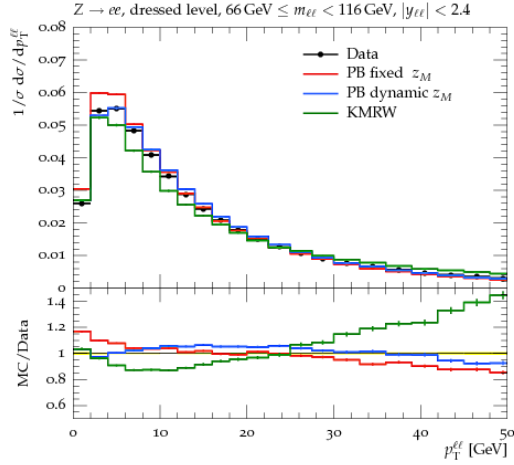
Figure 5.5: Predictions for the Z-boson p_T spectrum obtained with PB and MRW-CT10nlo TMDs compared to the 8 TeV ATLAS measurement [131].

5.6 Conclusion

In this chapter, using the PB method described in Chapter 3 for angular-ordered TMD evolution, we have studied physical implications of the dependence of the soft-gluon resolution parameter on the branching scale. Mapping the phase space of resolvable and non-resolvable emissions from (μ', z) space to $(z, q_\perp)$ space, we have written down the corresponding form of the evolution kernel. We have established the comparison of the PB formulation with other existing formulations, notably the ones known as CMW [10, 43] and KMRW [44–47].

On one hand, we find that the PB formula coincides with CMW at the level of integrated distributions. CMW was originally developed by evaluating splitting kernels at LO, while we evaluate the kernels at NLO. On the other hand, we find significant differences of PB with respect to KMRW, which can be traced back to the fact that PB builds the initial-state transverse momentum from multiple emissions, while KMRW builds it from single emission — the last step in the initial-state evolution cascade. We examined these differences in detail both analytically and numerically. We find that the numerical effects are large in the extreme regions of low $k_\perp$ and high $k_\perp$, but small in the middle $k_\perp$ region.

We apply the results to the evaluation of the DY Z-boson p_T spectrum and comparison with LHC measurements. We compare PB versus KMRW, finding significantly different behaviors in the low-p_T and high-p_T regions. We study the sensitivity of the Z-boson p_T spectrum to effects of the soft-gluon resolution scale, and observe that these could be accessed by detailed measurements fine binning in the region $p_T \lesssim$ 5 - 10 GeV.

Chapter 6

The TMD PB Sudakov form factor in the context of TMD factorization

In this chapter, partially presented in published work[1] and largely identical to a prepared article ready for publication [48], we analyze the structure of the Parton Branching (PB) TMD Sudakov form factor introduced in Chapter 3 and compare it to the Sudakov form factor of the formalism by Collins, Soper and Sterman (CSS) [49, 50].

6.1 Introduction

The PB method [38, 39] is developed for the evolution of TMDs and for application in parton shower Monte Carlo (MC) event generators to enhance numerical precision across a wide kinematic range for all hadronic collider processes and observables. The forward evolution of TMDs leads to precise numerical results in the small-p_T region of the transverse momentum spectrum of the Z boson [36, 57], where both resummation and a non-perturbative model are crucial.

The aim of this study is to analyze and improve the logarithmic accuracy of resummation by the PB evolution, specifically by its Sudakov form factor. This factor is a necessary ingredient for resummation in Monte Carlo approaches. Calculations at next-to-next-to-leading logarithmic (NLL) accuracy by parton shower Monte Carlo calculations as in Refs. [16–26] requires additional steps that are not the focus of this chapter. We concentrate on the resummation by the Sudakov form factor and we do this by first detailing the CSS formalism in section 6.2. Analytical Sudakov resummation following the CSS approach remains one of the main pillars in TMD factorization and QCD. Section 6.3 then presents the major novel concepts of this research. This is original work performed during the doctorate. We discuss the resummation accuracy achieved by the PB method using NLO splitting functions in the evolution. By implementing the physical soft-gluon coupling [202, 203] as an extension of the CMW coupling [43], we improve the logarithmic accuracy up to next-to-next-to-leading logarithmic (NNLL) accuracy in the PB evolution.

---

[1]Part of this chapter has been published in A. Bermudez Martinez, F. Hautmann, L. Keersmaekers, A. Lelek, M. Mendizabal Morentin, S. Taheri Monfared and A. M. van Kampen, "*The Parton Branching Sudakov and its relation to CSS*", Proceedings of Science PoS (EPS-HEP2023) 270 [201]

We also examine the non-perturbative contribution of the PB Sudakov when the soft-gluon resolution scale is close to one. Results from various PB evolution scenarios are evaluated at the level of the transverse momentum spectrum of the Z boson.

Section 6.4 contains results obtained by co-authors of the article. Here we show the effect of different evolution scenarios with and without the non-perturbative PB Sudakov to examine the non-perturbative aspect of the PB method by extraction of the Collins-Soper (CS) kernel [150, 204] through the technique that was established in Ref. [205].

6.2   The CSS formalism for TMD factorization

The aim of Collins, Soper and Sterman in the 1980s was to provide an expression for the Drell-Yan (DY) cross section differential in p_T. Collinear factorization is not suitable to calculate this differential cross section. It requires soft-gluon resummation to obtain an accurate transverse momentum spectrum from analytical calculations (see Sec. 2.5). In this section, we elaborate on the analytical formalism of TMD factorization that includes the resummation of low-p_T enhanced logarithms.

The processes of interest in general are of the form:

$$h_1 + h_2 \rightarrow F(Q^2, y, p_T^2) + X, \qquad (6.1)$$

where F is the final-state of the hard system triggered by colliding hadrons h_1 and h_2 of which the constituent partons c and $\bar{c}$ interact at interaction energy Q, rapidity y and transverse momentum p_T. In general, the inclusive - i.e. for any hadronic final state X - cross section can be separated in two contributions:

$$\frac{d\sigma^F}{dQ^2 dy dp_T^2} = \left[\frac{d\sigma^F}{dQ^2 dy dp_T^2} \right]_{\text{res.}} + \left[\frac{d\sigma^F}{dQ^2 dy dp_T^2} \right]_{\text{fin.}}, \qquad (6.2)$$

where the first term on the right-hand side is dominant for $p_T^2 \ll Q^2$ and the second term contains contributions for $p_T^2 \simeq Q^2$. The second term, also referred to in the literature as "finite term" or "Y-term", can be written as a convolution of a perturbatively calculable hard function with collinear PDFs $f(x, \mu)$ (similar to collinear factorization). Instead, we are interested in the first term on the right-hand side of Eq. (6.2), which contains all logarithmic enhancements due to multiple soft-gluon emissions. These large logarithmic terms are of the form $\alpha_s^n \ln^m(Q^2/p_T^2)$ and are resummed to all powers in the strong coupling.

A TMD factorized cross section has a partonic matrix element $\hat{\sigma}$ and two soft factors that are transverse momentum dependent functions (TMDs) $\mathcal{F}$ which depend on longitudinal momentum fractions (x) and transverse coordinates (b):

$$\left[\frac{d\sigma^F}{dQ^2 dy dp_T^2} \right]_{\text{res.}} \simeq d\hat{\sigma}_{c\bar{c}} \left(\alpha_s(Q^2), \frac{\mu^2}{Q^2} \right) \otimes \mathcal{F}_{c/h_1}(x_a, b; \zeta, \mu) \, \mathcal{F}_{\bar{c}/h_2}(x_b, b; \zeta, \mu), \qquad (6.3)$$

where the $\otimes$-symbol represents integrations over $x_{a,b}$, longitudinal momenta, and b, the *impact parameter*. Partons c and $\bar{c}$ annihilate at the hard interaction scale Q^2.

The TMDs $\mathcal{F}$ depend on two scales, the renormalization scale μ and the rapidity scale ζ, and obey evolution equations [206]:

$$\frac{\partial \ln \mathcal{F}(x, b; \zeta, \mu)}{\partial \ln \sqrt{\zeta}} = \mathcal{D}(b; \mu), \tag{6.4}$$

$$\frac{d \ln \mathcal{F}(x, b; \zeta, \mu)}{d \ln \mu} = \gamma_j(\alpha_\mathrm{s}(\mu)) - \frac{1}{2} \gamma_K(\alpha_\mathrm{s}(\mu)) \ln \frac{\zeta}{\mu^2}, \tag{6.5}$$

where γ_j is the RG coefficient specific to quark with flavor j, γ_K is the *cusp anomalous dimension* (equal to k_a, see Chapter 3) and $\mathcal{D}$ is the CS kernel whose evolution in μ is determined by:

$$\frac{d\mathcal{D}(b; \mu)}{d \ln \mu} = -\gamma_K(\alpha_\mathrm{s}(\mu)). \tag{6.6}$$

In the formalism constructed by Collins, Soper and Sterman, published in 1985 [49], referred to as CSS1, the TMDs can be identified as the product of three objects that contribute to different regions in transverse momentum: collinear PDFs f, coefficient functions C_{ab} and a Sudakov form factor $\sqrt{S}$. More explicitly, the differential cross section is written as:

$$\left[\frac{d\sigma^F}{dQ^2 dy dp_T^2} \right]_{\mathrm{res.}} = \sum_{c,\bar{c}} \sigma_{c\bar{c}}^{(0)F}(Q^2) H_{c\bar{c}}^F \left(\alpha_\mathrm{s}(Q^2), \frac{\mu^2}{Q^2} \right) \int \frac{d^2\boldsymbol{b}}{(2\pi)^2} e^{i\boldsymbol{p_T} \cdot \boldsymbol{b}} S(\boldsymbol{b}, \mu; b_{\max}, \mu_0) \tag{6.7}$$

$$\times \sum_a \int_{x_a}^1 \frac{d\xi_a}{\xi_a} C_{c/a} \left(\frac{x_a}{\xi_a}, \boldsymbol{b}; \mu_0^2, \alpha_\mathrm{s}(\mu_0^2) \right) f_{a/h_1} \left(\xi_a, \mu_0^2 \right)$$

$$\times \sum_b \int_{x_b}^1 \frac{d\xi_b}{\xi_b} C_{\bar{c}/b} \left(\frac{x_b}{\xi_b}, \boldsymbol{b}; \mu_0^2, \alpha_\mathrm{s}(\mu_0^2) \right) f_{b/h_2} \left(\xi_b, \mu_0^2 \right),$$

where a and b are initial partons from the incoming hadrons at scale μ_0. The partonic cross section is written as the product of a Born cross section $\sigma_{c\bar{c}}^{(0)F}(Q^2)$ and higher order function $H_{c\bar{c}}^F$ containing virtual emission diagrams. Real emission contributions are contained in the convolution of C with f functions. Both H and C are perturbatively calculable functions:

$$H_c^F(\alpha_\mathrm{s}) = \sum_{n=0}^\infty \left(\frac{\alpha_\mathrm{s}}{2\pi} \right)^n H_c^{F(n)}, \tag{6.8}$$

$$C_{qa}(\alpha_\mathrm{s}, z) = \delta_{qa} \delta(1 - z) + \sum_{n=1}^\infty \left(\frac{\alpha_\mathrm{s}}{2\pi} \right)^n C_{qa}^{(n)}(z). \tag{6.9}$$

The variables $x_{a,b}$ are longitudinal momentum fractions and $\xi_{a,b}$ are analogues of splitting variables.

The resummed cross section is mainly written in impact parameter (b) space, which is the Fourier conjugate space of the phase space. This is crucial in the CSS formalism to take into account momentum conservation which is expressed through

$$\delta^{(2)}(\boldsymbol{p_T} - \sum_j \boldsymbol{q}_{\perp,j}) = \int \frac{d^2\boldsymbol{b}}{(2\pi)^2} e^{i\boldsymbol{p_T} \cdot \boldsymbol{b}} \prod_j e^{-i\boldsymbol{q}_{\perp,j} \cdot \boldsymbol{b}}, \tag{6.10}$$

where $\boldsymbol{q}_{\perp,j}$ are the transverse momenta of (soft) parton emissions. The product of exponential factors $\exp(-i\boldsymbol{q}_{\perp} \cdot \boldsymbol{b})$ is absorbed in S. The Sudakov form factor deals with multiple soft-gluon emissions.

A visualization of this TMD factorized form of the hadron-hadron cross section by CSS is shown in Fig. 6.1.
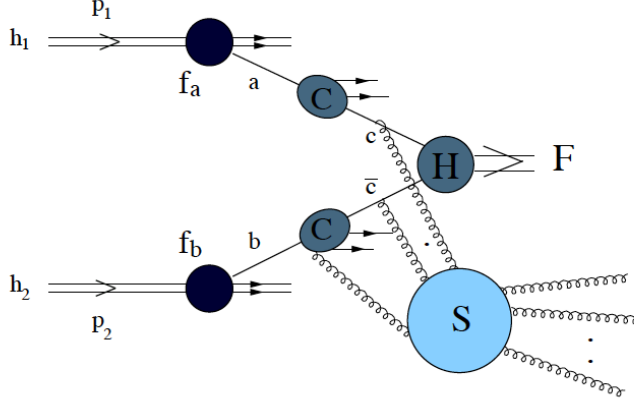
Figure 6.1: TMD factorization by the CSS formalism of two colliding hadrons (h_1 and h_2) leading to a hard process H producing a final state F. Evolution is determined by coefficient functions C and Sudakov form factor S. Fig. from Ref. [207]

Non-perturbative contributions are contained within the PDFs, which are entirely non-perturbative, as well as the Sudakov form factor, which is partially non-perturbative. The Sudakov form factor is a combination of a factor acting at small-b, for resummation (R), and one for large-b, which contains the non-perturbative (NP) contribution:

$$S(b, \mu; b_{\max}, \mu_0) = S^{(R)}(b, \mu) \times S^{(NP)}(b; b_{\max}, \mu_0). \tag{6.11}$$

The scale $b_{\max}$ serves as boundary between perturbative and non-perturbative contributions. The perturbative part is restricted to $b < b_{\max}$ and the non-perturbative part concerns $b > b_{\max}$.

In the original formalism by CSS, the Drell-Yan cross section is calculated by matching perturbative functions $C_{ab}(\alpha_s)$ to collinear PDFs and resumming large logarithms from real emissions by a Sudakov form factor that contains perturbative functions $A_a(\alpha_s)$ and $B_a(\alpha_s)$. In the year 2000, Catani et al. extended this form in Ref. [207] by incorporating the hard functions H in order to define A_a, B_a, and C_{ab} in a process-independent manner. The Sudakov form factor of this first formalism by CSS, which we refer to as CSS1, equals [206]:

$$S^{\text{CSS1}}(b, Q; b_{\max}, Q_0) = \exp\left\{-\int_{\mu_{b_*}^2}^{\mu_Q^2} \frac{\mathrm{d}\mu'^2}{\mu'^2} \left(A_a(\alpha_s)\ln\left(\frac{Q^2}{\mu'^2}\right) + B_a^F(\alpha_s)\right)\right\}$$

$$\times \exp\left(-g_{a/h_1}(x_a, b, b_{\max}) - g_{b/h_2}(x_b, b, b_{\max}) - g_D(b, b_{\max})\ln\frac{Q^2}{Q_0^2}\right), \tag{6.12}$$

where the scales $\mu_{b_*} = C_1/b_*$ (C_1 proportionality constant) and $b_* = b/\sqrt{1 + b^2/b_{\max}^2}$. The b_* variable is introduced to be able to combine perturbative and non-perturbative solutions by the "b_*-prescription" [49, 50]. The scale Q_0 is a fixed reference scale, and μ_Q is calculated as $C_2 Q$, where C_2 can be adjusted to optimize the calculation based on the specific application. Q_0 and Q have a meaning analogous to that of the DGLAP evolution scales μ_0 and μ.

The functions $g_{i/h}$ and g_D are independent of scales Q and μ and converge to zero as b decreases. The $g_{i/h}$'s can be interpreted as analogues of the intrinsic transverse momentum distribution $\mathcal{I}(k_{\perp,0}^2)$ in the PB method (see Eq. (3.44)).

The factors in the cross section that have upper index F, are specific to the process. However, renormalization group transformation mix the H function with C and B functions. These functions within the TMDs can be made process independent by selecting a particular resummation scheme [207]. The PDFs $f_{j/H}$ do not depend on the process as they are universal.

The first exponent with perturbatively calculable functions $A_a(\alpha_s)$ and $B_a(\alpha_s)$ (of which coefficients are given in Appendix B) resum the soft-gluon logarithms $\alpha_s^n \ln^m(Q^2/q_\perp^2)$ to all orders n as described in Chapter 1 and illustrated in Eq. (2.13). The perturbative calculable functions have the following series expansions:

$$A_a(\alpha_s) = \sum_{n=1}^{\infty} \left(\frac{\alpha_s}{2\pi}\right)^n A_a^{(n)}, \qquad B_a(\alpha_s) = \sum_{n=1}^{\infty} \left(\frac{\alpha_s}{2\pi}\right)^n B_a^{(n)}. \qquad (6.13)$$

The logarithmic accuracy is related to the coefficients of these functions that are included in a calculation. Note that the first term in the exponent of Eq. (6.12), which includes $A_a(\alpha_s)$, is accompanied by an additional logarithm. It is therefore referred to as the *double logarithmic* term. The term with $B_a(\alpha_s)$ is referred to as the *single logarithmic* term.

The counting of logarithms is done as described in Sec. 2.5.2[2]. Leading logarithmic (LL) terms in the perturbation series are of the form $\alpha_s^n \ln^{n+1}(Q^2/q_\perp^2)$, next-to-leading logarithmic (NLL) terms are of the form $\alpha_s^n \ln^n(Q^2/q_\perp^2)$, next-to-next-to-leading logarithms (NNLL) have $\alpha_s^n \ln^{n-1}(Q^2/q_\perp^2)$, and so on. LL accuracy is obtained by including the coefficient $A^{(1)}$, NLL accuracy is obtained by $A^{(2)}$ and $B^{(1)}$, NNLL accuracy is obtained by $A^{(3)}$ and $B^{(2)}$, etc. In short, to achieve N^{m}LL accuracy, the coefficients $A^{(m+1)}$ and $B^{(m)}$ are required.

In a more recent version of the TMD factorization approach, referred to as CSS2 [50], the Sudakov form factor is structured differently compared to that in CSS1. The separation of non-perturbative contributions and resummation terms is no longer as distinct. However, CSS2 offers several other advantageous features [206], e.g. new, modified definitions of TMDs in terms of gauge-invariant operator matrix elements. These definitions utilize the exact TMD evolution equations as given in Eqs. (6.4) and (6.5), without power suppressed corrections, resulting in a clearer relation between fits and TMDs. The Sudakov form factor of CSS2 can be written using the functions γ_j, γ_K and $\mathcal{D}$ in manner highly

---

[2]We do not take into account any contributions from C_{ab} coefficients in counting resummed logarithms.

comparable to Eq. (6.12) as

$$S^{\text{CSS2}}(b, Q, b_{\max}, Q_0) = \exp\left\{-\int_{\mu_0^2}^{\mu_Q^2} \frac{d\mu'^2}{\mu'^2}\left(\gamma_K(\alpha_s)\ln\left(\frac{Q^2}{\mu'^2}\right) - \gamma_j(\alpha_s)\right)\right\}$$

$$\times \exp\left(\mathcal{D}(b, \mu_0)\ln\frac{Q^2}{Q_0^2}\right), \tag{6.14}$$

where $\mu_0 = C_2 Q_0$ is a reference scale. The coefficients of functions A and γ_K as well as those from B and γ_j do not correspond at all orders, which is referred to as the *collinear anomaly* found by Becher and Neubert in Ref. [208]. These functions are linked by derivatives of the Collins-Soper (CS) kernel $\mathcal{D}(b, \mu_0)$, proven by Collins and Rogers in Ref. [206]. The CS kernel consists of both perturbative and non-perturbative contributions. By introducing the b_*-notation, the second exponential function of Eq. (6.14), i.e. the non-perturbative Sudakov of CSS2, is

$$\exp\left(\mathcal{D}(b, \mu_0)\ln\frac{Q^2}{Q_0^2}\right) \simeq \exp\left(\mathcal{D}(b_*, \mu_{b_*})\ln\frac{Q^2}{\mu_{b_*}^2}\right) \times \tag{6.15}$$

$$\exp\left\{-g_{a/A}(x_a, b, b_{\max}) - g_{b/B}(x_b, b, b_{\max}) - g_D(b, b_{\max})\ln\frac{Q^2}{Q_0^2}\right\},$$

where the functions $g_{a/A}$ and g_D are identical to those in the CSS1 formalism.

6.3 The PB Sudakov; NNLL resummation and non-perturbative Sudakov

This section is devoted to revealing the logarithmic structure of the PB method that arises from the Sudakov form factor, increasing the logarithmic accuracy of the PB method by introducing the physical soft-gluon coupling α_s^{phys} and analyzing the ultra-soft phase space region treated by the PB Sudakov.

To study the resummation accuracy, we use the PB Sudakov with virtual splitting functions as introduced in Eq. (3.28):

$$\Delta_a(\mu^2, \mu_0^2) = \exp\left\{-\sum_b \int_{\mu_0^2}^{\mu^2} \frac{d\mu'^2}{\mu'^2} \int_0^{z_M} z P_{ba}^{(R)}(\alpha_s, z)dz\right\} \tag{6.16}$$

$$\simeq \exp\left\{-\int_{\mu_0^2}^{\mu^2} \frac{d\mu'^2}{\mu'^2}\left(\int_0^{z_M} k_a(\alpha_s)\frac{1}{1-z}dz - d_a(\alpha_s)\right)\right\}, \tag{6.17}$$

where the last approximation becomes an equality in the case that $z_M = 1$ and the scale of the strong coupling is equal to the branching scale, $\alpha_s(\mu'^2)$. Coefficients of the functions k_a and d_a are given in Appendix A. For the purpose of this study, we investigate different scenarios where the value of z_M and the scale of α_s differ.

When integrating up to $z_M = 1 - \epsilon$ with $\epsilon = 10^{-5}$, as in the PB-TMD sets Set 1 and Set 2 [37, 38], emissions are generated in the non-resolvable region. We separate resolvable from

non-resolvable regions in this Sudakov form factor by using the dynamical resolution scale $z_M^{\text{dyn}} = 1 - q_0/\mu'$, which was introduced and studied in Chapter 5:

$$\Delta_a(\mu^2, \mu_0^2) = \exp\left\{-\int_{\mu_0^2}^{\mu^2} \frac{d\mu'^2}{\mu'^2} \left(\int_0^{1-q_0/\mu'} \frac{k_a(\alpha_s)}{1-z}dz - d_a(\alpha_s)\right)\right\}$$
$$\times \exp\left\{-\int_{\mu_0^2}^{\mu^2} \frac{d\mu'^2}{\mu'^2} \int_{1-q_0/\mu'}^{1-\epsilon} \frac{k_a(\alpha_s)}{1-z}dz\right\} \tag{6.18}$$

This separation is similar to the separation of the resummation and non-perturbative Sudakov by CSS. Instead of regions in impact parameter separated by $b_{\max}$, the separation here is in terms of emitted transverse momenta through the angular ordering relation with a separation scale q_0.

$$\Delta_a(\mu^2, \mu_0^2) = \Delta_a^{(\text{R})}(\mu^2, \mu_0^2, q_0^2) \cdot \Delta_a^{(\text{NP})}(\mu^2, \mu_0^2, \epsilon, q_0^2)\,. \tag{6.19}$$

In the following we show that these two factors of the PB Sudakov have a similar interpretation as the two factors of the CSS Sudakov as given in Eq. (6.11), both analytically and numerically. Moreover, we will improve the logarithmic accuracy that is given by the first factor.

6.3.1 NNLL resummation with the physical soft-gluon coupling

We show that $\Delta_a^{(\text{R})}$ resums logarithmically enhanced terms $\alpha_s^n \ln^m(Q^2/q_\perp^2)$ identically to CSS. For this, we need to map the evolution variable $\mu'_\perp$ to the transverse momenta $q_\perp$ with the angular ordering condition, $q_\perp = (1-z)\mu'_\perp$, similar to the procedure in Chapter 5. This allows us to compare the PB Sudakov directly to that from CSS. The resummation part of the PB Sudakov can then be written as in Eq. (5.19)[3]:

$$\Delta_a^{(\text{R})}(\mu^2, \mu_0^2, q_0^2) = \exp\left\{-\int_{q_0^2}^{\mu^2} \frac{dq_\perp^2}{q_\perp^2} \left(\int_0^{1-q_\perp/\mu} \frac{k_a(\alpha_s)}{1-z}dz - d_a(\alpha_s)\right)\right.$$
$$\left. + \int_{q_0^2}^{\mu_0^2} \frac{dq_\perp^2}{q_\perp^2} \int_0^{1-q_\perp/\mu_0} dz \frac{k_a(\alpha_s)}{1-z}\right\}\,. \tag{6.20}$$

Clearly, the phase space covered by this Sudakov is that where $|q_\perp| > q_0$. The second term in the exponent can be neglected since $\mu_0 \approx q_0 = \mathcal{O}(1\,\text{GeV})$. With $q_\perp^2$ as the scale of α_s, the z-integral can be performed to obtain:

$$\Delta_a^{(\text{R})}(\mu^2, q_0^2) = \exp\left\{-\int_{q_0^2}^{\mu^2} \frac{dq_\perp^2}{q_\perp^2} \left(\frac{1}{2}k_a(\alpha_s)\ln\left(\frac{\mu^2}{q_\perp^2}\right) - d_a(\alpha_s)\right)\right\}\,. \tag{6.21}$$

Note that this structure bears a strong resemblance to the perturbative part of the Sudakov form factor of CSS, i.e. the first exponential factor in Eq. (6.12). For this, we assume that the scales μ_{b_*} and q_0 can be set equal.

---

[3]Note that the integration limits differ because by starting from q_0 in the first term, a subtraction of a phase space element is required, whereas in Chapter 5 an addition was needed.

If the coefficients of the K and D parts of the splitting functions P_{ab} were to agree with the CSS functions A and B respectively, one would gain $N^m LL$ accuracy in PB by including $k^{(m)}$ and $d^{(m-1)}$. The PB-TMD sets have implemented splitting functions with NLO accuracy (in powers of α_s), resulting in negligible sub-leading logarithms.

LL accuracy in PB is obtained by the $k_a^{(0)}$ coefficient of the LO splitting functions since it coincides with $A_a^{(1)}$. The $d_a^{(0)}$ coefficient coincides with $B_a^{(1)}$ providing the single logarithmic term at NLL accuracy[4]. The double logarithmic term at NLL is obtained by the NLO splitting function coefficients, where $k_a^{(1)}$ is equal to $A_a^{(2)}$, sub-leading terms are then included due to presence of the $d_a^{(1)}$ coefficient.

6.3.1.1   NNLL at single logarithmic level

Differences can be found between the single logarithmic terms at NNLL, $B^{(2)}$ and $d^{(1)}$ (App. A & B). We devote attention to the cause of this apparent discrepancy in function values, which turns out to be due to a scheme choice.

The partonic cross section $H_{c\bar{c}}^F$ causes a dependence of the B_a^F function of the CSS formula (6.7) to the process and the resummation scheme [207] through renormalization group transformations. An RGE (for the definition, see Eq. (1.15)) of the hard scattering function can be written generally as:

$$\frac{\partial \ln H_{c\bar{c}}^F(\alpha_s(\mu^2))}{\partial \ln \mu^2} = \beta(\alpha_s)\frac{\partial \ln H_{c\bar{c}}^F(\alpha_s(\mu^2))}{\partial \alpha_s} \equiv \gamma_H(\alpha_s(\mu^2)), \qquad (6.22)$$

which follows from renormalization group invariance of the total cross section. Integration over $\ln \mu^2$ from $\ln \mu_0^2$ up to $\ln Q^2$ gives

$$H_{c\bar{c}}^F(\alpha_s(Q^2)) = \exp\left\{\int_{\mu_0^2}^{Q^2}\frac{d\mu^2}{\mu^2}\gamma_H(\alpha_s(\mu^2))\right\} H_{c\bar{c}}^F(\alpha_s(\mu_0^2)). \qquad (6.23)$$

The argument of the exponent is of the same (logarithmic) structure as the B function. The resummation part of the Sudakov form factor can then schematically be written as:

$$S(b,Q) = \exp\left\{-\int_{1/b^2}^{Q^2}\frac{d\mu'^2}{\mu'^2}\left(A_a(\alpha_s)\ln\left(\frac{Q^2}{\mu'^2}\right) + B_a(\alpha_s) - \gamma_H(\alpha_s(\mu^2))\right)\right\}. \qquad (6.24)$$

The $B_a(\alpha_s)$ function from Eq. (6.12) then shifts like:

$$B_a^S(\alpha_s(\mu^2)) = B_a^{\tilde{S}}(\alpha_s(\mu^2)) - \gamma_H(\alpha_s(\mu^2)). \qquad (6.25)$$

from one certain resummation scheme (S) to another ($\tilde{S}$). Using the perturbative expansions in the strong coupling of the QCD beta-function (Eq. (1.18)) and the hard scattering function (Eq. (6.8)), the relation of coefficients at order α_s^2 can be written explicitly as [207]:

$$B_a^{S(2)} = B_a^{\tilde{S}(2)} + \beta_0 H_a^{S\tilde{S}(1)}. \qquad (6.26)$$

---

[4]Being precise, $d_a^{(0)} = -1/2 B_a^{(1)}$, since a factor of $1/2$ arises due to the presence of two TMDs $\tilde{\mathcal{A}}$ in a cross section calculated with PB, while only one factor of S_a is present in the CSS cross section.

There exists a resummation scheme in which the process dependence is contained entirely in the hard function, $H_a^{S\tilde{S}}$, and the B_a coefficients are universal and equivalent to coefficients of the DGLAP splitting functions, as demonstrated in Ref. [207]. This resummation scheme, where $B_a^{(2)}$ corresponds to $d_a^{(1)}$, is that of the "$\overline{\text{MS}}$ resummation scheme" [207]. CSS applications commonly use the $B_a^{(2)}$ coefficient from the "DY scheme".

A straightforward comparison of the (quark) coefficients $d_q^{(1)}$ and $B_q^{(2)}$ from Appendices A and B respectively gives:

$$B_q^{(2)} - (-2) \cdot d_q^{(1)} = 16 C_F \pi \beta_0 (\zeta_2 - 1). \tag{6.27}$$

The factor -2 on the left-hand side is applied due to differently defined Sudakov form factors of PB (Eq. (6.21)) and CSS (Eq. (6.12)) and the occurrence of two TMDs in the calculation with PB whereas CSS includes one factor of S_a in the cross section.

We observe that the difference between the single logarithmic coefficients at NNLL accuracy is a single factor of the form $\beta_0 \cdot H$, that corresponds to the form of Eq. (6.26).

6.3.1.2   NNLL at double logarithmic level

The NNLO coefficient $A_q^{(3)}$ that contributes to NNLL accuracy does not coincide with the cusp anomalous dimension $k_q^{(2)} = 2 C_F \gamma_K^{(2)}$ (see Eq. (6.28)). This difference cannot be explained by the choice of the resummation scheme, since $A(\alpha_s)$ is a resummation scheme independent function. This difference is due to the collinear anomaly [208]. We note that the difference between the NNLL double logarithmic quark coefficient $A_q^{(3)}$ and the cusp anomalous dimension is contained in the perturbative part of the CS kernel $\mathcal{D}(b, \mu)$ from Eq. (6.15):

$$A_q^{(3)} - k_q^{(2)} = C_F \pi \beta_0 \left[C_A \left(\frac{808}{27} - 28\zeta_3 \right) - \frac{112}{27} N_f \right] \tag{6.28}$$

$$= -\frac{\pi \beta_0}{\alpha_s^2} \mathcal{D}(b\mu = 2e^{-\gamma_E}). \tag{6.29}$$

To arrive at the second equality, we use Eq. (69) from Ref. [206].

NNLL accuracy can be achieved through the *physical soft-gluon coupling* (referred to as the "physical coupling") described in Refs. [202, 203], which extends the CMW coupling that was developed for NLL resummation [43]. The physical soft-gluon coupling is essentially an effective coupling that incorporates effects of multiple soft gluons. We apply the physical coupling:

$$\alpha_s^{\text{phys}} = \alpha_s \left(1 + \sum_{n=1}^{\infty} \mathcal{K}^{(n)} \left(\frac{\alpha_s}{2\pi} \right)^n \right) \tag{6.30}$$

to modify the PB Sudakov and obtain correct higher order Sudakov resummation:

$$\Delta_a(\mu^2, \mu_0^2) = \exp \left\{ -\int_{q_0^2}^{\mu^2} \frac{dq_\perp'^2}{q_\perp'^2} \left(\int_0^{z_M} k_a(\alpha_s^{\text{phys}}) \frac{1}{1-z} dz - d_a(\alpha_s^{\text{phys}}) \right) \right\}. \tag{6.31}$$

The first order coefficient of $\mathcal{K}$ is [202]:

$$\mathcal{K}^{(1)} = C_A \left(\frac{67}{18} - \frac{\pi^2}{6} \right) - \frac{5}{9} N_f \tag{6.32}$$

and the second order coefficient is [202]:

$$\mathcal{K}^{(2)} = C_A^2 \left(\frac{245}{24} - \frac{67}{9}\zeta_2 + \frac{11}{6}\zeta_3 + \frac{11}{5}\zeta_2^2 \right) + C_F N_f \left(-\frac{55}{24} + 2\zeta_3 \right)$$
$$+ C_A N_f \left(-\frac{209}{108} + \frac{10}{9}\zeta_2 - \frac{7}{3}\zeta_3 \right) - \frac{1}{27}N_f^2 + \frac{\pi\beta_0}{2} \left(C_A \left(\frac{808}{27} - 28\zeta_3 \right) - \frac{224}{54}N_f \right). \tag{6.33}$$

By using a combination of DGLAP splitting functions with the physical soft-gluon coupling at appropriate orders we obtain PB predictions without subleading logarithms from the Sudakov form factor.

Pure NNLL We gain NNLL accuracy in the PB Sudakov by the use of NLO splitting functions and including the physical coupling as:

$$\alpha_s^{\text{NNLL}} = \alpha_s \left(1 + \mathcal{K}^{(2)} \left(\frac{\alpha_s}{2\pi} \right)^2 \right). \tag{6.34}$$

The coefficient $\mathcal{K}^{(1)}$ is not included in Eq. (6.34) because it is equal to $k_q^{(1)}$ (being a part of the implemented NLO splitting functions). With that, Eq. (6.21) becomes:

$$\ln \left(\Delta_a^{(\text{NNLL})}(\mu^2, q_0^2) \right) = - \int_{q_0^2}^{\mu^2} \frac{dq_\perp^2}{q_\perp^2} \left(\frac{\alpha_s^{\text{NNLL}}}{2\pi} \right) \left[\ln \frac{\mu^2}{q_\perp^2} \left(k_a^{(0)} + \frac{\alpha_s^{\text{NNLL}}}{2\pi} k_a^{(1)} \right) - d_a^{(0)} - \frac{\alpha_s^{\text{NNLL}}}{2\pi} d_a^{(1)} \right]$$

$$= - \int_{q_0^2}^{\mu^2} \frac{dq_\perp^2}{q_\perp^2} \frac{\alpha_s}{2\pi} \left[\ln \frac{\mu^2}{q_\perp^2} \left(k_a^{(0)} + \frac{\alpha_s}{2\pi} k_a^{(1)} \right) - d_a^{(0)} - \frac{\alpha_s}{2\pi} d_a^{(1)} + \right.$$

$$\left. + \left(\frac{\alpha_s}{2\pi} \right)^2 \mathcal{K}^{(2)} \left(k_a^{(0)} \frac{1}{2} \ln \frac{\mu^2}{q_\perp^2} - d_a^{(0)} \right) \right], \tag{6.35}$$

where $\mathcal{K}^{(2)} \cdot k_a^{(0)} = A_a^{(3)}$.

Pure NLL We have also obtained, for the first time, a pure NLL prediction with PB by combining LO splitting functions with an implementation of the physical coupling truncated at $\mathcal{K}^{(1)}$:

$$\alpha_s^{\text{CMW}} = \alpha_s \left(1 + \mathcal{K}^{(1)} \left(\frac{\alpha_s}{2\pi} \right) \right). \tag{6.36}$$

With that, Eq. (6.21) gives:

$$\ln \left(\Delta_a^{(\text{NLL})}(\mu^2, q_0^2) \right) = - \int_{q_0^2}^{\mu^2} \frac{dq_\perp^2}{q_\perp^2} \left(\frac{\alpha_s^{\text{CMW}}}{2\pi} \right) \left[\frac{1}{2} k_a^{(0)} \ln \frac{\mu^2}{q_\perp^2} - d_a^{(0)} \right] \tag{6.37}$$

$$= - \int_{q_0^2}^{\mu^2} \frac{dq_\perp^2}{q_\perp^2} \left[\frac{\alpha_s}{2\pi} \left(\frac{1}{2} k_a^{(0)} \ln \frac{\mu^2}{q_\perp^2} - d_a^{(0)} \right) + \left(\frac{\alpha_s}{2\pi} \right)^2 \mathcal{K}^{(1)} \left(\frac{1}{2} k_a^{(0)} \ln \frac{\mu^2}{q_\perp^2} - d_a^{(0)} \right) \right],$$

where $\mathcal{K}^{(1)} \cdot k_a^{(0)} = A_a^{(2)}$ and $k_a^{(0)} = 2C_a$ with $C_a = C_F$ for quarks and $C_a = C_A$ for gluons.

6.3.2 The non-perturbative Sudakov of PB

Here we argue that the PB Sudakov given in Eq. (6.31) and maintaining a fixed resolution scale close to one, not only allows for soft-gluon resummation at NNLL precision, but also achieves a non-perturbative description in TMD evolution that surpasses the incorporation of intrinsic transverse momentum.

We consider the very small transverse momentum region, $|q_\perp| < q_0$ where the non-perturbative Sudakov (i.e. the second factor of Eq. (6.19)) governs the emissions[5]:

$$\Delta_a^{(\text{NP})}(\mu^2, \mu_0^2, \epsilon, q_0) = \exp\left\{-\int_{\mu_0^2}^{\mu^2} \frac{d\mu'^2}{\mu'^2} \int_{1-q_0/\mu'}^{1-\epsilon} dz \frac{k_a(\alpha_s)}{1-z}\right\}. \tag{6.38}$$

In this (non-resolvable) region, we set the argument of the strong coupling to q_0^2.

When the running coupling is not dependent on z and μ', the integrals in Eq. (6.38) straightforwardly lead to:

$$\Delta_a^{(\text{NP})}(\mu^2, \mu_0^2, \epsilon, q_0^2) = \exp\left\{-\frac{k_a(\alpha_s)}{2} \ln\left(\frac{\mu^2}{\mu_0^2}\right) \ln\left(\frac{q_0^2}{\epsilon^2 \mu_0 \mu}\right)\right\}. \tag{6.39}$$

Although the Sudakov form factor is significantly influenced by the value of ϵ, it should be noted that the PB TMDs are infrared safe [39] and independent of ϵ because of angular ordering.

An analytical comparison of Eq. (6.39) with the CSS Sudakov form factor in Eqs. (6.12), (6.14) and (6.15) demonstrates that there are corresponding logarithms of μ^2/μ_0^2 (or Q^2/Q_0^2) in the exponent. This observation inspires the study performed in section 6.4 where we extract the CS kernel from the PB approach using both models with and without the non-perturbative Sudakov.

6.3.3 Numerical results

Figure 6.2 depicts the effect of the physical soft-gluon coupling presented in Eq. (6.34) and Eq. (6.35) on the (i)TMDs of gluons and down quarks. This is compared to the standard PB evolution of PB-TMD-set2 with NLO splitting functions and without the physical coupling.

In all curves, the value of the coupling constant α_s is determined by the scale of $q_\perp^2$ and a fixed value of $z_M = 1 - 10^{-5}$ is applied. The starting evolution scale is $\mu_0 = 1.3$ GeV. The Sudakov form factor's separation scale is established by $q_0 = 1.0$ GeV, i.e. for $|q_\perp| < 1.0$ GeV α_s is set to the value $\alpha_s(q_0)$. The investigation comprises three evolution scenarios:

1. NLO: PB evolution of HERAPDF2.0 with NLO splitting functions and 2-loop α_s;

---

[5]The arguments presented in this section apply to both models with standard running coupling α_s and physical coupling α_s^{phys}.

2. NLL: PB evolution of HERAPDFLO with LO splitting functions and 1-loop α_s with the implementation of the CMW coupling through Eq. (6.36);

3. NNLL: PB evolution of HERAPDF2.0 with NLO splitting functions and 2-loop α_s with the implementation of the physical coupling through Eq. (6.34).

In the third scenario, the physical coupling has been included in both the Sudakov form factor and the real emission probabilities to preserve momentum conservation [141]. It is apparent that the disparity between NLL and NLO for both TMDs and iTMDs is considerable, while the discrepancy between NLO and NNLL predictions is only about 2%. This is to be expected, as the NLO calculation includes already the $d^{(1)}$ coefficient that contributes to NNLL resummation. Moreover, in the NLL calculation only LO splitting functions govern the dynamics of resolvable branchings.
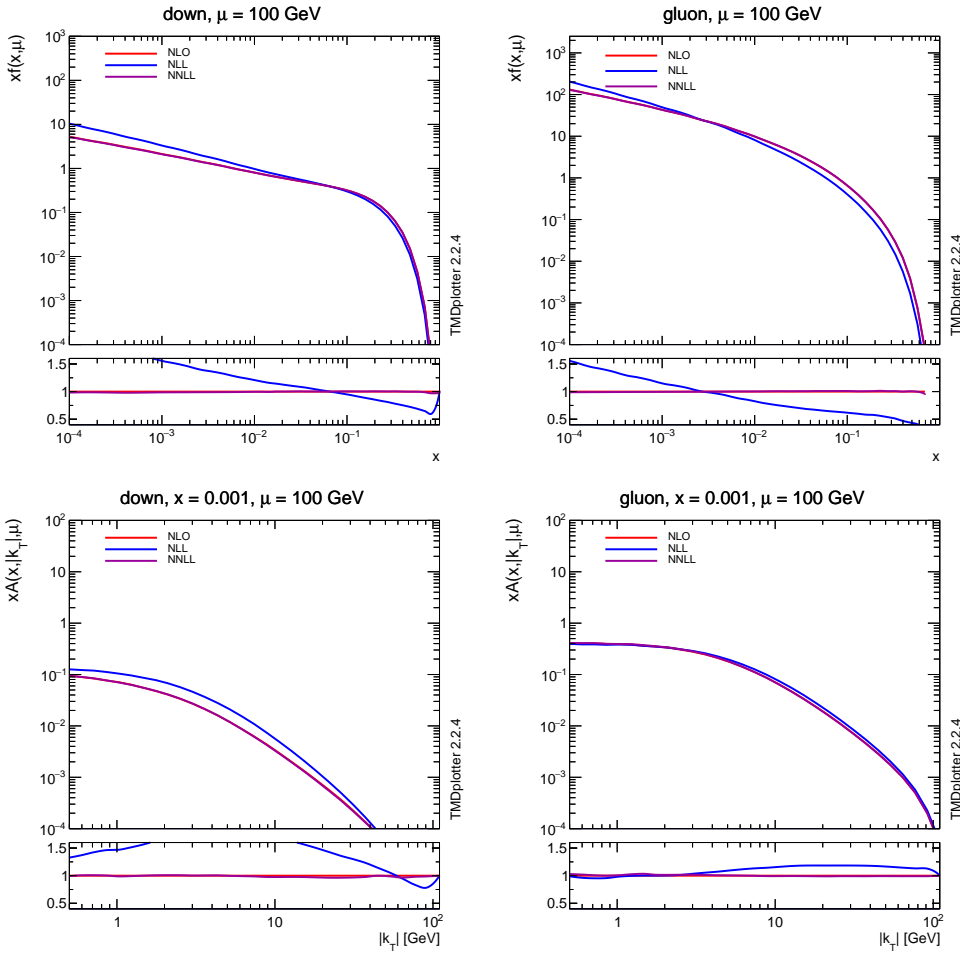
Figure 6.2: iTMDs (top) and TMDs (bottom) for down-quark and gluon at $\mu = 100$ GeV acquired through the PB methodology for different evolution scenarios described in section 6.3.3. The NLO prediction (red curve) serves as the reference for the ratio plots in the bottom panels.

The numerical impact on a given physical parameter by including the physical coupling can be estimated by calculating the transverse momentum spectrum of the Z boson in DY events. Figure 6.3 shows simulations with the three differently obtained TMDs as previously discussed. NLO matrix elements have been generated using MAD-GRAPH5_AMC@NLO [55] with HERWIG6 subtraction terms and the iTMD PB-NLO-2018-set2 [37]. CASCADE3 [51] matches the TMDs of interest to these matrix elements [36] (see Chapters 7, 8 and 9). Also at the physical level, there is a significant difference between the NLL and NLO results while going from NLO to NNLL results again in only a 2% difference.
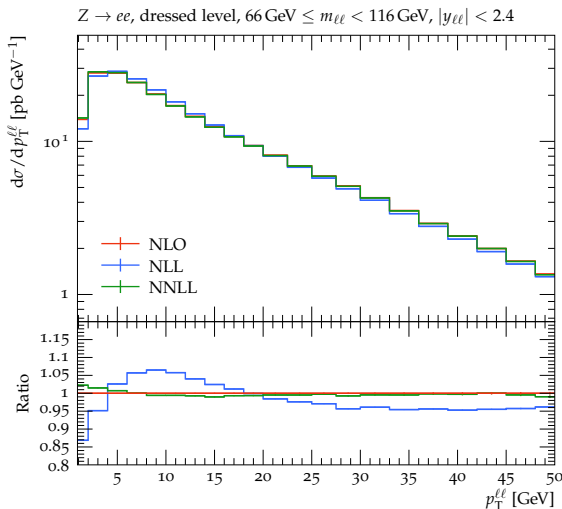
Figure 6.3: Z boson transverse momentum spectrum calculations at $\sqrt{s}$ = 8 TeV obtained at different orders of logarithmic accuracy described in detail in section 6.3.3. The ratios are shown relative to the NLO prediction (in red).

6.4 The Collins Soper kernel of PB

The CS kernel, $\mathcal{D}(b, \mu_0)$ in Eq. (6.14), is a part of the TMD factorization theorem that was introduced in Refs. [150, 204]. Its evolution in μ is determined by the cusp anomalous dimension as given in Eq. (6.6). In Refs. [50, 208–210] it was shown that the CS kernel contains information on the exchange of non-perturbative and soft gluons and that it also determines the evolution of TMD parton distributions. A self-contained definition of the CS kernel was found in Ref. [211], providing the scaling of the kernel through the matrix elements without referring to the TMDs. In Ref. [205], a first direct method to numerically extract the CS kernel from scattering cross sections was provided and applied to the PB approach. In this work, this method was followed to study in detail the behavior of the CS kernel extracted from different PB predictions depending on the evolution details.

6.4.1   TMD models

Four PB models evolved with NLO splitting functions and 2-loop α_s are studied. In all models, the emitted transverse momentum is calculated following the angular ordering relation $q_\perp^2 = (1 - z)^2 \mu'^2$. The models differ in the settings of the soft-gluon resolution scale and scale of the strong coupling. The evolution settings of four models are the following:

1. with $\alpha_s(q_\perp^2)$ and $z_M = 1 - 10^{-5}$, where the intermediate $q_0 = 1.0$ GeV is used for separating the perturbative and non-perturbative regions. In the non-perturbative region, α_s is frozen to $\alpha_s(q_0^2)$;

2. with $\alpha_s(\mu'^2)$ and $z_M = 1 - 10^{-5}$, where the initial evolution scale, $\mu_0 = 1.3$ GeV, is the lowest scale in α_s;

3. with $\alpha_s(q_\perp^2)$ and $z_M = 1 - q_0/\mu'$ with $q_0 = 1.0$ GeV (i.e. there is no non-perturbative Sudakov form factor).

4. with $\alpha_s(q_\perp^2)$ and $z_M = 1 - q_0/\mu'$ with $q_0 = 0.5$ GeV (i.e. there is no non-perturbative Sudakov form factor).

In scenarios 3 and 4, q_0 serves as the lowest emitted transverse momentum as well as the lowest scale of the strong coupling. All parton distributions are obtained with the same starting parametrization (PB-NLO-HERAI+II-2018-set2 [37]), i.e. all the differences between the TMDs come purely from the evolution. Evolution with the first scenario corresponds to that of PB-TMD-NLO-HERAI+II-2018-set2 (denoted by PB-TMD-Set2).

In Fig. 6.4 we show integrated parton distributions (iTMDs) obtained with the PB approach of gluon and down quark flavours for these four different evolution scenarios. In particular, one can see the role of the amount of branchings in the different evolution scenarios.

Changing the scale of α_s from the transverse momentum of the emitted parton $q_\perp^2 = (1 - z)^2 \mu'^2$ to the scale of the branching μ'^2 decreases the amount of branchings if other elements of the evolution are kept the same. This is well reflected in the shape of the iTMDs for the scenarios 1 and 2 in Fig. 6.4 where the red curve corresponds to more branchings than the blue one. That is why the red curve is higher at small and middle x and lower in the very large x region compared to the blue curve. Similarly, altering z_M from a fixed value ~ 1 to a dynamical one decreases the amount of branchings by eliminating the soft radiation if other elements of the evolution are kept the same, which can be seen by comparing the red and purple curves. A larger dynamical resolution scale allows more branchings, which results into the difference between the orange and purple curves. When comparing the orange curve with the purple one, it is evident that the orange curve exhibits a higher number of branchings, arising from both a lower cut in α_s and a higher z_M compared to the purple scenario.

In Fig. 6.5 the transverse momentum distributions obtained with the PB-approach are shown for the same configurations as in Fig. 6.4. The TMDs show very clearly the effect of applying different evolution scenarios, in the whole $k_\perp$ range. The shapes have a natural explanation in PB through the determination of transverse momentum as a vectorial sum
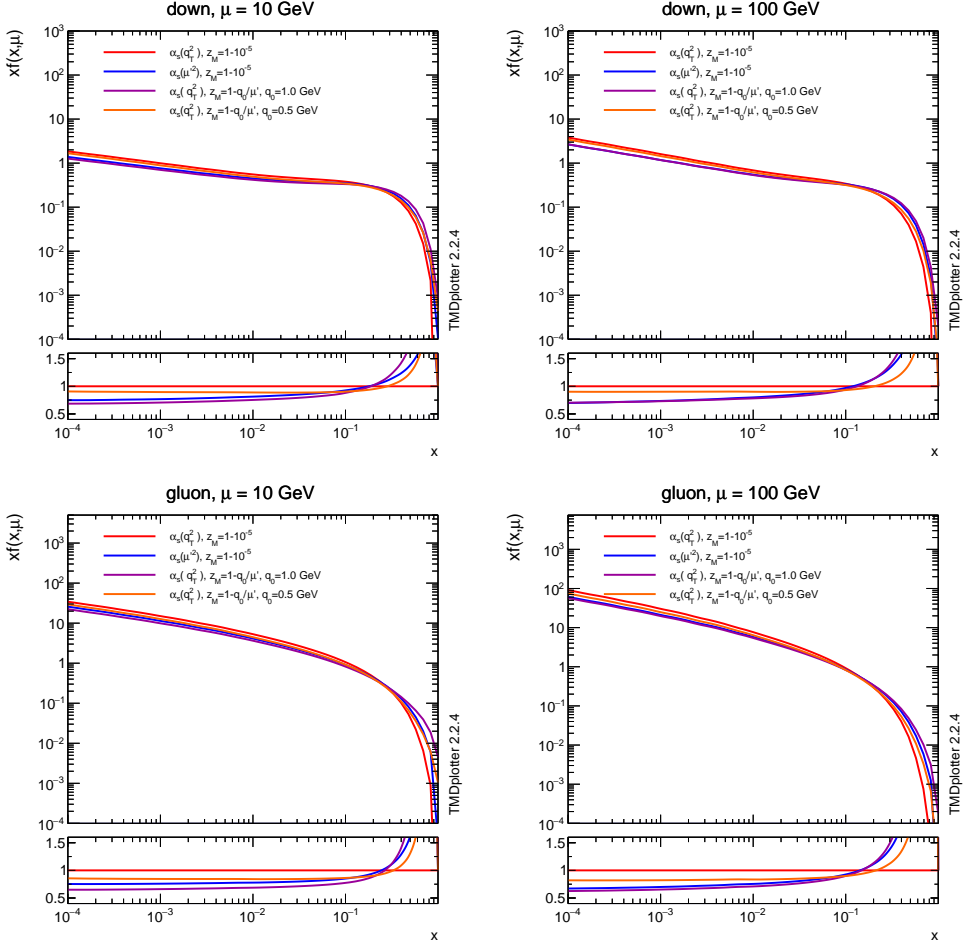
Figure 6.4: Gluon and down-quark iTMDs at $\mu = 10$ GeV (left column) and $\mu = 100$ GeV (right column) obtained from the PB approach for different evolution scenarios with toy models. The red curve serves as the reference for the ratio plots in the bottom panels.

of the intrinsic $k_{\perp,0}$ and all the momenta emitted in the evolution. Other details of the evolution such as the value of z_M and the scale of $\alpha_{\rm s}$ play important roles, which was already observed in the previous chapter.

6.4.2 CS kernel extractions with TMD scenarios

To extract the CS kernel from PB predictions, we use the expression provided in [205]:

$$\mathcal{D}(b, \mu_0) = \frac{\ln(\Sigma_1(b)/\Sigma_2(b)) - \ln Z(Q_1, Q_2) - 2\Delta_R(Q_1, Q_2; \mu_0)}{4\ln(Q_2/Q_1)} - 1. \qquad (6.40)$$

We calculate the DY transverse momentum distributions at different DY masses (Q_1 and Q_2) and adjust the values of the center-of-mass energy $\sqrt{s}$ such that the same ranges
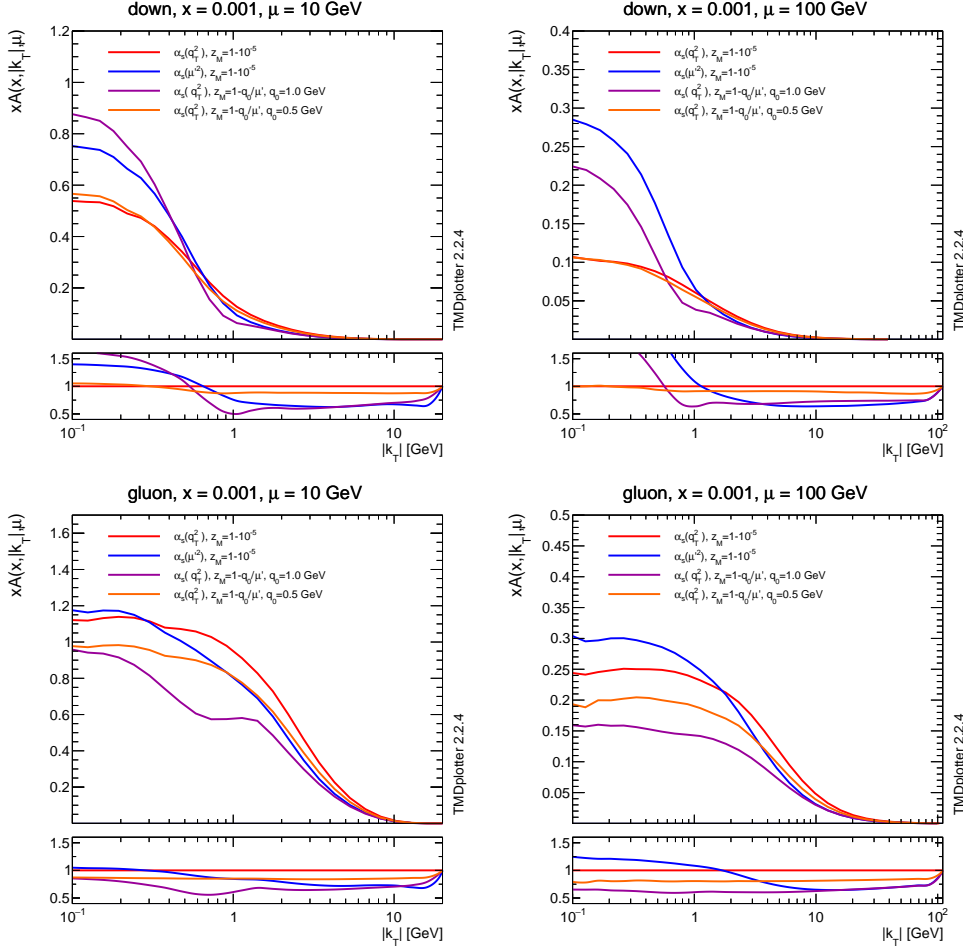
Figure 6.5: TMDs for gluon and down-quarks at $\mu = 10$ GeV (left column) and $\mu = 100$ GeV (right column) obtained from the PB approach for different evolution scenarios.

of longitudinal momentum fractions are probed. Σ_1 and Σ_2 are Hankel transformed transverse momentum distributions of the Z boson and

$$\Delta_R(Q_1, Q_2; \mu_0) = \int_{Q_2}^{Q_1} \frac{d\mu}{\mu} \gamma_j(\mu, Q_1) - 2\ln\frac{Q_1}{Q_2}\int_{\mu_0}^{Q_2} \frac{d\mu}{\mu}\gamma_K(\mu). \tag{6.41}$$

The function Z is given by

$$Z(Q_1, Q_2) = \frac{\alpha_{\text{em}}^2(Q_1)|C_V(Q_1, \mu_{Q_1})|^2}{\alpha_{\text{em}}^2(Q_2)|C_V(Q_2, \mu_{Q_2})|^2} \tag{6.42}$$

where α_{em} is the electromagnetic coupling and C_V is the hard coefficient function. All terms in Eq. (6.40) except Σ_1/Σ_2 are perturbative and known up to up to N^3LO.

We have used the integrated TMD PB-NLO-HERAI-II-2018-set2 from LHAPDF in MAD-GRAPH5_AMC@NLO [55] to generate DY events in pp collisions at NLO with HERWIG6 sub-

traction terms for masses Q = 12, 16, and 20 GeV, at centre-of-mass energies $\sqrt{s}$ = 655.2, 873.6, and 1092 GeV respectively, with a maximum rapidity of $\eta^{ll}_{\max}$ = 4. With these values we ensure that the same region in the longitudinal momentum fraction is probed, as specified in [205]. We have matched NLO matrix elements to TMDs according to the procedure from Ref. [36] using the MC@NLO method and CASCADE3. Discrete Hankel transforms of the obtained distributions give cross section distributions in b-space. The CS kernels for all four models are extracted at a scale μ_0 = 2 GeV employing perturbative terms of Z and Δ_R at N^{3}LO accuracy. They are shown in the top panel of Fig. 6.6. Statistical uncertainties are shown as bands around the curves and obtained from the cross sections using the bootstrap method.
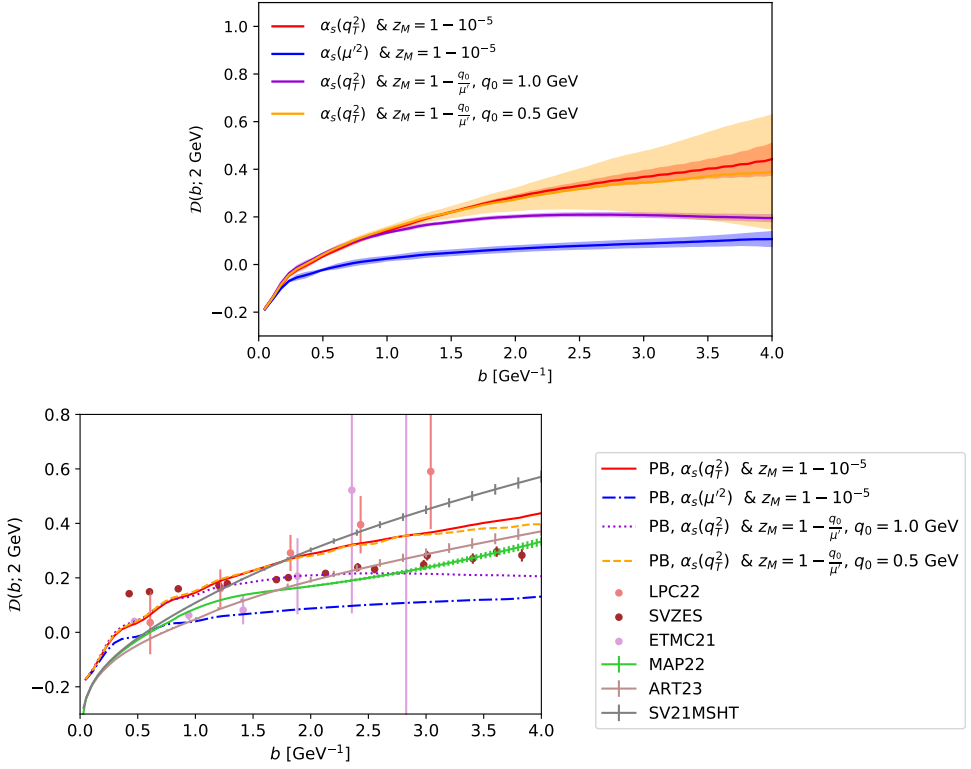
Figure 6.6: Top: Comparison of CS kernels extracted from PB predictions using different dynamical and fixed z_M scenarios and different treatments for the strong coupling. Bottom: Comparison of CS kernels obtained from different PB models and several example extractions obtained in the literature.

The obtained CS kernels are shown on the top panel of Fig. 6.6. They are sensitive to the treatment of radiation: PB-TMD-Set2 (red curve), which uses $\alpha_s(q_\perp)$ and includes the region of $z^{\mathrm{dyn}}_M < z < 1 - \epsilon$, provides a linear behavior in the kernel at large b as was observed in Ref. [205], while with the dynamical resolution scale with q_0 = 1 GeV (purple curve) the behavior in this region seems to be flat. When the minimal resolved emitted transverse momentum is lowered to q_0 = 0.5 GeV (orange curve), there are additional branchings originating from the lower cut in α_s and from the region $1 - 1/\mu' < z < 1 - 0.5/\mu'$ compared to the purple curve, which leads to a significant change in the

large b region. Interestingly, despite having no non-perturbative Sudakov in the sense of Eq. (6.38) (i.e. no very soft gluons but more soft gluons than the model with $q_0 = 1$ GeV), the orange curve becomes close to the red one. The model with $\alpha_s(\mu')$ (blue curve) has a contribution from very soft radiation, yet a smaller amount than PB-TMD-Set2 due to the higher scale in the strong coupling, leading to a much lower slope at large b. Moreover, the scale of the coupling also leads to a different treatment of harder radiation, therefore this model differs from the other models already at small values of b.

The curves extracted from different PB models can be compared with the CS kernel extracted by other methods and groups. In the lower panel of Fig. 6.6 we compare the PB extractions from the top panel to several extractions of other groups which can be found in the literature: phenomenological MAP22 [212], ART23 [213], SV21MSHT [213] and lattice LPC22 [214], SVZES [215] and ETMC21 [216]. The spread of the PB results is quite large and covers a significant fraction of other extractions. The results with flattening behavior at large b are especially interesting since most of the extractions in the literature assume a rising behavior.

6.4.3   CS kernel dependence on intrinsic $k_\perp$

Finally, the impact of the intrinsic transverse momentum on the PB CS kernel is studied. Again four different models applying PB TMD evolution are considered, all with $\alpha_s(q_\perp^2)$, but now varying the width of the Gaussian (the q_s parameter) that represents intrinsic transverse momentum (see Eq. (3.45)):

1. $\alpha_s(q_\perp^2)$, $z_M = 1 - \epsilon$ and $q_s = 0.5$ GeV,

2. $\alpha_s(q_\perp^2)$, $z_M = 1 - \epsilon$ and $q_s = 0.1$ GeV,

3. $\alpha_s(q_\perp^2)$, $z_M = 1 - q_0/\mu'$ and $q_s = 0.5$ GeV,

4. $\alpha_s(q_\perp^2)$, $z_M = 1 - q_0/\mu'$ and $q_s = 0.1$ GeV,

where $q_0 = 1.0$ GeV and $\epsilon = 10^{-5}$. Fig. 6.8 shows the cross sections in momentum(p_T)- and coordinate(b)-space for these different kinematical selections. The choice of q_s influences the results in the cross sections, both in p_T- and b-space. The prediction in the low p_T region is especially sensitive to the intrinsic transverse momentum in the case of a dynamical resolution scale where a kink is visible for the scenario with small q_s, reflecting the shapes of the TMDs (Fig. 6.7) contributing to this region.

We determine the CS kernel for the four PB-TMD cases. The results are shown in Fig. 6.9. We observe no significant dependence on the intrinsic $k_\perp$. This is understood by the parametrization of the starting distribution for TMD evolution by PB (see Eq. (3.44)). The intrinsic transverse momentum currently is a flavor- and x-independent Gaussian function and the intrinsic $k_\perp$ distributions cancel out in the ratio of cross sections in Eq. (6.40).
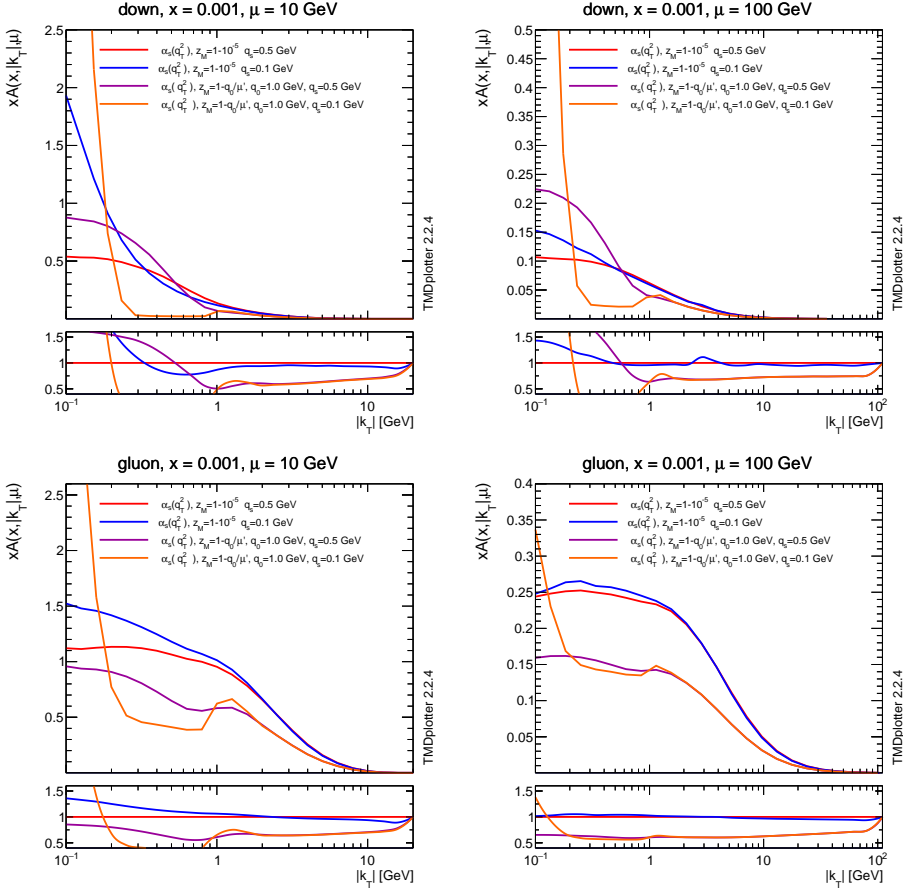
Figure 6.7: The impact of intrinsic k_T variation on TMDs for evolution scenario with $\alpha_s(q_\perp^2)$, $z_M = 1 - 10^{-5}$ and $\alpha_s(q_\perp)^2$, dynamical z_M with $q_0 = 1.0$ GeV.

6.5 Conclusion

In this study, we conducted a comprehensive investigation of the PB Sudakov form factor and resummation by the PB method within the context of TMD factorization.

The PB TMD evolution equation resums Sudakov logarithms. The logarithmic accuracy and comparison with analytic resummation methods by CSS have been discussed extensively. We conclude that previous calculations in the PB TMD approach were performed with leading-logarithmic (LL) and next-to-leading logarithmic (NLL) accuracy and did contain subleading logarithms from next-to-next-to-leading logarithmic (NNLL) accuracy. The subleading logarithms come from the $B^{(2)}$ coefficient that is included in the PB method by incorporating NLO splitting functions (via $d^{(1)}$). However, the form of $B^{(2)}$ found in literature can differ from $d^{(1)}$ because of the resummation scheme dependence of $B(\alpha_s)$. Results by applying NLO splitting functions for TMD evolution in this chapter were labeled by "NLO".
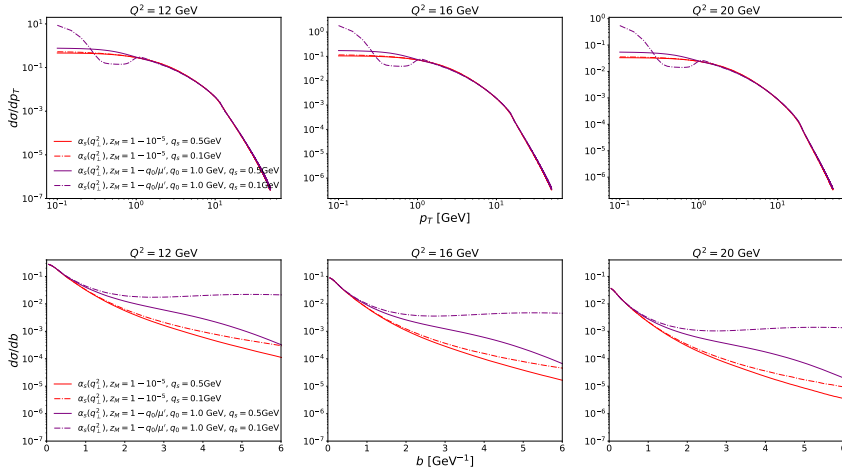
Figure 6.8: The impact of intrinsic transverse momentum on cross sections of the di-lepton pair in momentum and position spaces for models with $\alpha_s(q_\perp)$ with dynamical and fixed z_M scenarios.
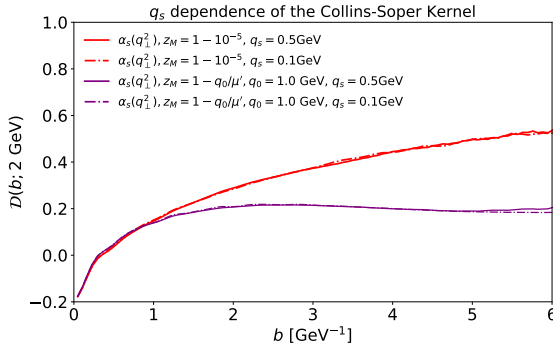
Figure 6.9: Dependence of the CS kernels on the intrinsic transverse momentum, q_s, for evolution with $\alpha_s(q_\perp)$ with dynamical and fixed z_M scenarios.

The logarithmic accuracy gained by the Sudakov form factor can be systematically improved to NNLL by means of an effective soft-gluon coupling, referred to as the "physical coupling". In this way, the double logarithmic NNLL $A^{(3)}$ coefficient is incorporated. We discussed the implications of this new term on parton distributions and the p_T spectrum of the Z boson. We observed that its effect is rather small. This small effect is due to subleading logarithms that are present in an NLO calculation, i.e. this already contains a part of the NNLL resummation accuracy. PB-TMDs including the effective coupling have not been fitted to data and are not yet available in TMDLIB for wide use. To gain NNLL accuracy in parton showers, future work is required to treat recoil effects similarly as done in [17, 21, 22].

Motivated by the soft-gluon resolution scale z_M associated with angular ordering, we introduced an intermediate scale - denoted as z^{dyn} - into the PB Sudakov form factor. This led to the division of the phase space into two distinct regions: $|q_\perp| > q_0$ and $|q_\perp| < q_0$, which we referred to as the perturbative and non-perturbative Sudakov regions,

respectively.

Our observations revealed that the non-perturbative component of the PB factorized Sudakov form factor denoted as $\Delta_a^{(NP)}$, exhibits a logarithmic structure resembling the CS kernel. In the numerical investigations, four PB models that vary in terms of the amount of radiation were explored. The modeling of radiation involves parametrizing α_s using different arguments of the running coupling and freezing it at different scales as well as considering the inclusion or exclusion of $\Delta_a^{(NP)}$ in the calculations. We demonstrated the impact of these different evolution models on parton distributions at both integrated and $k_\perp$-dependent levels.

Encouraged by the observation that $\Delta_a^{(NP)}$ resembles the CS kernel, in the last part of this chapter, the method of [205] was used to extract the CS kernel from four different PB models. From the obtained kernels we conclude that what contributes in PB to the extracted kernel is more than just the Δ_a^{NP}: it is a cumulative effect of many branchings, governed in our models by α_s and z_M. The obtained curves spread over a wide range in $(b, \mathcal{D})$ space, covering other extractions from the literature. We conclude that different modelling of radiation can lead to a very different kernel behavior, including different slopes.

Chapter 7

The CASCADE Monte Carlo event generator

This chapter[1] is dedicated to describing CASCADE3, a Monte Carlo event generator based on transverse momentum dependent (TMD) parton distribution functions, as it is described in Ref. [51]. In this numerical program, hard processes which can be generated externally in collinear factorization with leading order (LO) multileg or next-to-leading order (NLO) parton level generators are treated by including transverse momenta of the initial partons according to TMD densities and applying dedicated TMD parton showers and hadronization. The initial state parton shower is tied to the TMD parton distribution, with all parameters fixed by the TMD distribution itself. Final state parton showering and hadronization models are included as well, creating a tool that can provide calculations of partonic as well as hadronic level events.

We describe the new developments in CASCADE3 for a full PB-TMD parton shower and the matching of TMD parton densities to collinear hard process calculations. The chapter is organized as follows. In the introduction, we motivate the need for a Monte Carlo event generator based on TMDs. In Sec. 7.2, the matching of TMDs to the incoming partons in the case of on-shell matrix element input is explained. Section 7.3 elaborates on the initial state TMD parton shower, which has the dynamics of PB evolution discussed in Chapter 3. Section 7.4 briefly mentions all elements of the program that are important for generating fully showered and hadronized events. On top of the hard process input and initial state radiation, there are input TMD sets, final state radiation, hadronization, scale and TMD uncertainties, and multi-jet merging. With these, the program has all the necessary ingredients for phenomenological analyses of the implied theory. This is the basis for the following chapters, which make extensive use of CASCADE3.

7.1 Introduction

The simulation of processes for high energy hadron colliders has been improved significantly in the past years by automation of NLO calculations and matching of the hard

---

[1]This work has been published in S. Baranov et al., *"CASCADE3 A Monte Carlo event generator based on TMDs"*, European Physical Journal C 81 (2021) 5, 425.

processes to parton shower Monte Carlo event generators which also include a simulation of hadronization. Among those automated tools are the MadGraph5_amc@nlo [55] generator based on the mc@nlo [95–98] method or the Powheg [100] generator for the calculation of the hard process. The results from these packages can then combined with the Herwig [119], Sherpa [121, 122] or Pythia8 [116, 117] packages for parton showering and hadronization. Different jet multiplicities can be combined at the matrix element level and then merged with special procedures, like the MLM [104–106] or CKKW [107] merging for LO processes, the FxFx [110] or MiNLO method [111] for merging at NLO, among others. While the approaches of matching and merging matrix element calculations and parton showers are very successful, the matrix elements are calculated with collinear dynamics and in general purpose MCEGs, only the inclusion of initial state parton showers results in a net transverse momentum of the hard process.

The Cascade3 Monte Carlo event generator covers a large kinematic domain of currently relevant high-energy physics processes by applying the PB method, explained in Chapter 3, and the corresponding PB TMD parton densities [38, 39]. The initial state evolution is fully described and determined by the TMD density for all flavor species, including quarks, gluons and photons at small and large x and any scale μ.

With the current advances in determination of PB TMDs, it is natural to develop a scheme, where the initial parton shower follows as close as possible the TMD parton density and where either collinear (on-shell) or $k_\perp$-dependent (off-shell) hard process calculations can be included at LO or NLO. In order to be flexible and to use the latest developments in automated matrix element calculations of the hard process at higher order in the strong coupling α_s, events available in the LHE file format [125], which contains all the information of the hard process including the color structure, can be further processed for parton shower and hadronization in Cascade3.

7.2   The hard process

The cross section for the scattering process of two hadrons A and B can be written in collinear factorization as a convolution of the partonic cross section of partons a and b, $a + b \rightarrow X$, and the densities $f_{a(b)}(x, \mu)$ of partons a (b) inside the hadrons A (B),

$$\sigma(A + B \rightarrow Y) = \int dx_a \int dx_b \, f_a(x_a, \mu) \, f_b(x_b, \mu) \, \sigma(a + b \rightarrow X), \qquad (7.1)$$

where $x_a(x_b)$ are the fractions of the longitudinal momenta of hadrons A, B carried by the partons $a(b)$, $\sigma(a + b \rightarrow X)$ is the partonic cross section, and μ is the factorization scale of the process. The final state Y contains the partonic final state X and the recoils from the parton evolution and hadron remnants.

In Cascade3 we extend collinear factorization to include transverse momenta in the initial state by adding transverse momentum to incoming partons in an on-shell process. The hard processes in collinear factorization can be calculated by standard automated methods like MadGraph5_amc@nlo [55] for multi-leg processes at LO or NLO accuracy. The matrix element processes are calculated with collinear PDFs, as provided by LHAPDF [178].

Collinear parton densities $f(x, \mu)$ in the factorization formula given in Eq. (7.1) are replaced by TMD densities $\mathcal{A}(x, k_\perp, \mu)$ with $k_\perp$ being the transverse momentum of the interacting parton. Integration over the transverse momenta then gives the total cross section as in Eq. (7.1). However, when the hard process is to be combined with a TMD parton density, these $k_\perp$ integrals of the TMD densities must agree with the collinear ($k_\perp$-integrated) densities; this feature is guaranteed by construction for the PB-TMDs (also available as integrated PDFs in LHAPDF).

In a LO partonic calculation the TMD or the parton shower can be included respecting energy momentum conservation, as described below. In an NLO calculation based on the MC@NLO method [95–98], the contribution from collinear and soft partons is subtracted, as this is added later with the parton shower. For the use with PB TMDs, the Herwig6 [217, 218] subtraction terms are best suited as the angular ordering conditions coincide with those applied in the PB-method (a thorough discussion and numerical demonstration of this are given in Chapter 9).

When transverse momenta of the initial partons from TMDs are to be included to the hard scattering process, which was originally calculated under the assumption of collinear initial partons, care has to be taken that energy and momentum are still conserved. When the initial state partons have transverse momenta, they also acquire virtual masses. The procedure adopted in Cascade3 is the following: for each initial parton, a transverse momentum is assigned according to the TMD density, and the parton-parton system is boosted to its center-of-mass frame and rotated such that only the longitudinal and energy components are non-zero. The energy and longitudinal component of the initial momenta $p_{a,b}$ can be recalculated by taking into account the virtual masses $Q_a^2 = k_{\perp,a}^2$ and $Q_b^2 = k_{\perp,b}^2$, incorporating energy-momentum conservation by conserved quantity $\hat{s}$, assuming massless partons $p_{a,b}^2 = 0$ and exploiting relations between lightcone momentum components, as [219]

$$E_{a,b} = \frac{1}{2\sqrt{\hat{s}}}\left(\hat{s} \pm (Q_b^2 - Q_a^2)\right) \tag{7.2}$$

$$p_{z\,a,b} = \pm \frac{1}{2\sqrt{\hat{s}}}\sqrt{(\hat{s} + Q_a^2 + Q_b^2)^2 - 4Q_a^2 Q_b^2} \tag{7.3}$$

with $\hat{s} = (p_a + p_b)^2$ with $p_a(p_b)$ being the four-momenta of the interacting partons a and b. The partonic system is then rotated and boosted back to the overall center-of-mass system of the colliding particles. By this procedure, the parton-parton mass $\sqrt{\hat{s}}$ is exactly conserved, while the rapidity of the partonic system is approximately restored, depending on the transverse momenta.

In Fig. 7.1 a comparison of the Drell-Yan (DY) mass, transverse momentum and rapidity is shown from an NLO calculation of DY production in pp collisions at $\sqrt{s} = 13$ TeV in the mass range $30 < m_{\rm DY} < 2000$ GeV. The curve labelled NLO(LHE) is the calculation of MadGraph5_amc@nlo with the subtraction terms, the curve NLO(LHE+TMD) is the prediction after the transverse momentum is included according to the procedure described above. In the p_T spectrum one can clearly see the effect of including transverse momenta from the TMD distribution. The DY mass distribution is not changed, and the rapidity distribution is almost exactly reproduced, only at large rapidities small differences are observed.
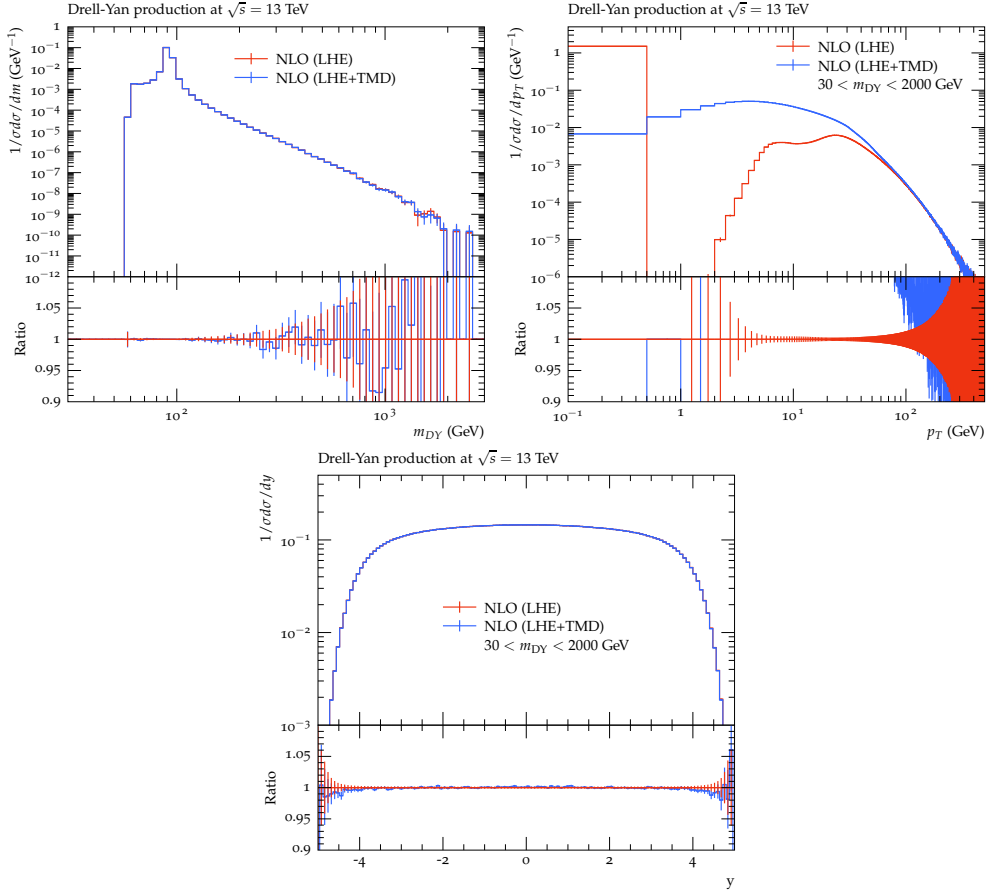
Figure 7.1: Distributions of Drell-Yan mass, transverse momentum and rapidity for $pp \rightarrow \mathrm{DY} + X$ at $\sqrt{s}$ = 13 TeV. The hard process is calculated with MADGRAPH5_AMC@NLO. NLO(LHE) is the prediction including subtraction terms, NLO(LHE+TMD) includes transverse momenta of the interacting partons according to the description in the text.

The transverse momenta $k_\perp$ are generated according to the TMD density $\mathcal{A}(x, k_\perp, \mu)$, at the original longitudinal momentum fraction x and the hard process scale μ. In a LO calculation, the full range of $k_\perp$ is available, but in an NLO calculation via the MC@NLO method a "shower scale", also referred to as "matching scale", defines the boundary between parton shower and real emissions from the matrix element, limiting the transverse momentum $k_\perp$. Technically the factorization scale μ is calculated within CASCADE3 (see parameter lhescale) as it is not directly accessible from the LHE file, while the *shower scale* is given by SCALUP. There are five options for the factorization scale: 1) using SCALUP, the lowest transverse momentum scale in the LHE file, 2) using the centre-of-mass energy of the partonic system $\hat{s}$, 3) using half the scalar sum of all final state parton's transverse momenta squared, 4) using $\hat{s}$ for LO processes and the sum of transverse momenta $q_\perp^2$ of final state partons in case of higher order emissions, 5) using $\hat{s}$ for LO processes and the maximum transverse momentum $q_\perp$ of the emitted parton for higher order events. The limitation of the transverse momenta coming from

the TMD distribution and TMD shower to be smaller than the *shower scale* guarantees that the overlap with real emissions from the matrix element is minimized according to the subtraction of counterterms in the MC@NLO method. The shower scale is also referred to as the "matching scale".

The advantage of using TMDs for the complete process is that the kinematics are fixed, independent of simulating explicitly the radiation history from the parton shower. For inclusive processes, for example inclusive Drell-Yan processes, the details of the hadronic final state generated by a parton shower do not matter, and only the net effect of the transverse momentum distribution is essential. However, for processes which involve jets, the details of the parton shower become also important. The parton shower, as described in Sec. 7.3.2, follows very closely the transverse momentum distribution of the TMD and thus does not change any kinematic distribution after the transverse momenta of the initial partons are included.

All hard processes available in MadGraph5_aMC@NLO can be used in Cascade3. The treatment of multi-jet merging via the recently developed TMD merging method is described in Chapter 10.

Cascade3 also has the ability to treat effects subleading to the leading powers in α_s by using off-shell matrix elements. In this mode, the incoming partons already have non-zero transverse momentum at the level of the hard scattering cross section and the transverse boost is not applied. This is done by setting `lheHasOnShellPartons=0` in the steering card of the program (given in Appendix C).

7.3 Initial state TMD parton shower

The initial state parton shower in Cascade3 that simulates initial state radiation (ISR) follows consistently the parton evolution of the TMDs. By this we mean that the splitting functions P_{ab}, the order and the scale of α_s, as well as kinematic restrictions are identical to both the parton shower and the evolution of the parton densities.

7.3.1 The PB TMD backward Sudakov form factor

The PB method formulates an angular ordered evolution of momentum weighted TMD PDFs (cf. Eq. (3.36) in Chapter 3) that is iteratively solvable by

$$
\tilde{\mathcal{A}}_a(x, k_\perp^2, \mu^2) = \Delta_a(\mu^2)\,\tilde{\mathcal{A}}_a(x, k_\perp^2, \mu_0^2) + \sum_b \int \frac{d\mu'^2}{\mu'^2} \frac{d\phi}{2\pi} \frac{\Delta_a(\mu^2)}{\Delta_a(\mu'^2)} \Theta(\mu^2 - \mu'^2)\,\Theta(\mu'^2 - \mu_0^2)
$$
$$
\times \int_x^{z_M} dz\, P_{ab}^{(R)}\left(\alpha_s((1-z)^2\mu'^2), z\right) \tilde{\mathcal{A}}_b\left(\frac{x}{z}, k_\perp'^2, \mu'^2\right) , \tag{7.4}
$$

where $\mathbf{k}_\perp$ is the transverse momentum vector of the propagating parton after branching (particle a on the right of Fig. 7.2) and $k_\perp = |\mathbf{k}_\perp|$. Furthermore

$$
k_\perp' = |\mathbf{k}_\perp + (1-z)\boldsymbol{\mu}_\perp'| \tag{7.5}
$$

is the transverse momentum of the parton before branching (particle b on the right of Fig. 7.2) with $\boldsymbol{\mu}'_\perp = \mathbf{q_{t,c}}/(1-z)$ the rescaled transverse momentum vector of the emitted parton. The integration over the two-dimensional evolution variable $\boldsymbol{\mu}'_\perp$ in Eq. (7.4) is split in an integral over the absolute value $\mu' = |\boldsymbol{\mu}'_\perp|$ and an integral over the azimuthal angle ϕ between $\mathbf{q_{t,c}}$ and $\mathbf{k}_\perp$.

The argument in α_s is dependent on the evolution variable μ'. For coherent branching [145] this should be the emitted transverse momentum $q_{t,c}$.

The Sudakov form factor is given by (see Eq. 3.24):

$$\Delta_a(\mu^2) = \exp\left(-\sum_b \int_{\mu_0^2}^{\mu^2} \frac{d\mu'^2}{\mu'^2} \int_0^{z_M} dz\, z\, P_{ba}^{(R)}(\alpha_s, z)\right) . \tag{7.6}$$

Dividing Eq. (7.4) by $\Delta_a(\mu^2)$ and differentiating with respect to μ^2 yields the differential expression of the evolution equation which describes the probability of resolving a parton with transverse momentum $\mathbf{k}_\perp'$ and momentum fraction x/z into a parton with momentum fraction x and emitting another parton during a small decrease in μ:

$$\mu^2 \frac{d}{d\mu^2}\left(\frac{\tilde{\mathcal{A}}_a(x, k_\perp^2, \mu^2)}{\Delta_a(\mu^2)}\right) = \sum_b \int_x^{z_M} dz \frac{d\phi}{2\pi} P_{ab}^{(R)}(\alpha_s, z) \frac{\tilde{\mathcal{A}}_b\left(\frac{x}{z}, k_\perp'^2, \mu^2\right)}{\Delta_a(\mu^2)} . \tag{7.7}$$

The normalized probability is then given by

$$\frac{\Delta_a(\mu^2)}{\tilde{\mathcal{A}}_a(x, k_\perp^2, \mu^2)} d\left(\frac{\tilde{\mathcal{A}}_a(x, k_\perp^2, \mu^2)}{\Delta_a(\mu^2)}\right) = \sum_b \frac{d\mu^2}{\mu^2} \int_x^{z_M} dz \frac{d\phi}{2\pi} P_{ab}^{(R)}(\alpha_s, z) \frac{\tilde{\mathcal{A}}_b\left(\frac{x}{z}, k_\perp'^2, \mu^2\right)}{\tilde{\mathcal{A}}_a\left(x, k_\perp^2, \mu^2\right)}. \tag{7.8}$$

This equation can be integrated between μ_{i-1}^2 and μ^2 to give the no-branching probability (Sudakov form factor) for the backward evolution Δ_{bw}:

$$\Delta_{bw}(x, k_\perp^2, \mu^2, \mu_{i-1}^2) \equiv \frac{\Delta_a(\mu^2)}{\Delta_a(\mu_{i-1}^2)} \frac{\tilde{\mathcal{A}}_a(x, k_\perp^2, \mu_{i-1}^2)}{\tilde{\mathcal{A}}_a(x, k_\perp^2, \mu^2)} \tag{7.9}$$

$$= \exp\left\{-\sum_b \int_{\mu_{i-1}^2}^{\mu^2} \frac{d\mu'^2}{\mu'^2} \frac{d\phi}{2\pi} \int_x^{z_M} dz\, P_{ab}^{(R)}(\alpha_s, z) \frac{\tilde{\mathcal{A}}_b\left(x', k_\perp'^2, \mu'^2\right)}{\tilde{\mathcal{A}}_a(x, k_\perp^2, \mu'^2)}\right\},$$

with $x' = x/z$. This Sudakov form factor is very similar to the Sudakov form factor in ordinary parton shower approaches, with the difference that for the PB TMD shower the ratio of PB TMD densities $[\tilde{\mathcal{A}}_b\left(x', k_\perp'^2, \mu'^2\right)]/[\tilde{\mathcal{A}}_a(x, k_\perp^2, \mu'^2)]$ is applied, which includes a dependence on $k_\perp$.

In Eq. (7.9) a relation between the Sudakov form factor Δ_a used in the evolution equation and the Sudakov form factor Δ_{bw} used for the backward evolution of the parton shower is made explicit. A similar relation was also studied in Refs. [220, 221]. In Ref. [220] the z_M limit was identified as a source of systematic uncertainty when using conventional showers with standard collinear PDFs; in the PB approach, especially when using PB-TMD-Set2, the z_M limits of forward and backward TMD evolution coincide. This allows for a consistent formulation of the parton shower with PB TMDs that follows the dynamics of the initial construction of the TMD.

The advantage of utilizing the PB TMD shower is that setting the parameters of the parton shower through TMD distributions allows for associating the parton shower uncertainties with the TMD uncertainties arising from systematic global fits to experimental data.

7.3.2   The initial state TMD shower algorithm

A backward evolution method, as now common in Monte Carlo event generators, is applied for the initial state parton shower. It evolves from the hard scale of the matrix-element process in a backwards manner down to the soft scale of the incoming hadron. However, unlike the conventional parton shower, which generates transverse momenta of the initial state partons during the backward evolution, the transverse momenta of the initial partons of the hard scattering process are fixed by the TMD. The parton shower does not alter the kinematics, and the transverse momenta during the backward cascade adhere to the behavior of the TMD.

The starting value of the evolution scale μ is calculated from the hard scattering process (`lhescale`). In case of on-shell, NLO matrix elements, the transverse momentum of the hardest parton in the parton shower evolution is limited by the *shower-scale*.
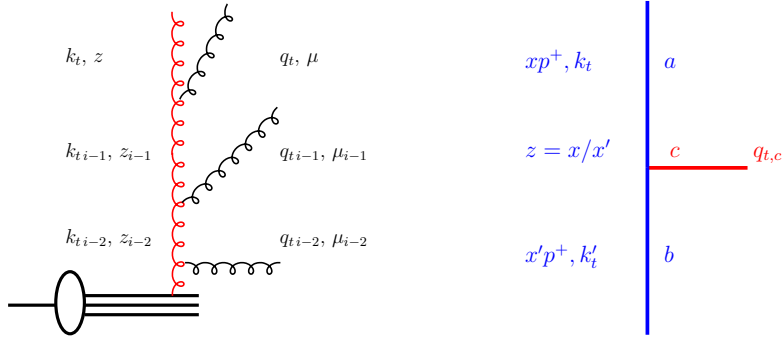
Figure 7.2: Left: Schematic view of a parton branching process. Right: Branching process $b \rightarrow a+c$.

Starting at the hard scale $\mu = \mu_i$, the parton shower algorithm generates a new scale μ_{i-1} at which a resolvable branching occurs (see Fig. 7.2 left). This scale μ_{i-1} is selected from the Sudakov form factor Δ_{bw} as given in Eq. (7.9) (see also [52]). In the parton shower language, the selection of the next branching comes from solving $R = \Delta_{bw}(x, k_\perp, \mu_i, \mu_{i-1})$ for μ_{i-1} using uniformly distributed random numbers R for given x and μ_i. Solving the integrals from Eq. (7.9) numerically for every branching is not efficient, instead the "veto-algorithm" [219, 222] is applied. The splitting variable z_{i-1} for the branching is then obtained from the splitting functions following the standard methods (see Eq. (2.37) in [38]) by:

$$\int_{z_{min}}^{z_{i-1}} dz' P_{ba}^{(R)}(\alpha_s(\mu_{i-1}), z').$$ (7.10)

In the parton shower, we treat resolvable branchings, defined via a cut in $z < z_M$, by real splitting functions $P^{(R)}$, and virtual or non-resolvable branchings, with $z > z_M$, by the Sudakov form factor Δ_{bw}.

The calculation of the transverse momentum $k_\perp$ is sketched in Fig. 7.2 (right). The transverse momentum of the emitted parton $q_{t,c}$ is calculated by applying the angular ordering condition (see Eq. (3.42)):

$$q_{t,c}^2 = (1-z)^2 \mu'^2 .$$ (7.11)

Ordering in μ' is then identical to ordering in the angle Θ of the emitted parton with respect to the beam directions since also $q_{t,c} = (1 - z)E_b \sin \Theta$

Once the transverse momentum of the emitted parton $\mathbf{q_{t,c}}$ is known, the transverse momentum of the propagating parton can be calculated from

$$\mathbf{k_\perp}' = \mathbf{k_\perp} + \mathbf{q_{t,c}} \tag{7.12}$$

with a uniformly distributed azimuthal angle ϕ assumed for the vector components of $\mathbf{k_\perp}$ and $\mathbf{q_{t,c}}$. The generation of the parton momenta is performed in the center-of-mass frame of the collision (in contrast to conventional parton showers, which are generated in different partonic frames).

The whole procedure is iterated until one reaches a scale $\mu_{i-1} < Q_0$, with Q_0 being a cut-off parameter, which can be chosen to be the starting evolution scale of the TMD. It is of advantage to continue the parton shower evolution to lower scales $Q_0 \sim \Lambda_{QCD}$.

The final transverse momentum of the propagating parton $\mathbf{k_\perp}$ is the sum of all transverse momenta $\mathbf{q_{t,c}}$ (see the right figure in Fig. 7.2):

$$\mathbf{k_\perp} = \mathbf{k_{t,0}} - \sum_c \mathbf{q_{t,c}} \ . \tag{7.13}$$

with $\mathbf{k_{t,0}}$ being the intrinsic transverse momentum.

This initial state TMD shower differs significantly from ordinary parton showers because PB TMD distributions are determined from fits to experimental data, which places constraints on fixed-scale inputs to evolution, while in ordinary parton showers instead non-perturbative physics parameters and showering parameters are tuned. No MC tuning is performed in the PB TMD case.

7.4   Main elements of the Monte Carlo program

To conclude this chapter, we provide a brief summary of the building blocks of the CASCADE Monte Carlo program and its functionalities. A detailed technical description of the program, including its installation and operation, is given in Appendix C.

The main elements of the program are the following.

Hard process   See section 7.2.

Initial state parton showers   See section 7.3.

TMD parton densities   All available TMD parton density sets can be accessed through the TMD library TMDLIB [40, 41] (see also Chapter 4). These parton densities can be selected in CASCADE via `PartonDensity` with a value > 100000. For example the TMDs from the Parton Branching method [37] are selected via `PartonDensity=102100 (102200)` for PB-TMD-NLO-HERAI+II-2018-set1 (set2).

Final state parton showers The final state parton shower uses the parton shower routine `PYSHOW` of Pythia. Leptons in the final state, coming for example from Drell-Yan decays, can radiate photons, which are also treated in the final state parton shower. Here the method from `PYADSH` of Pythia is applied, with the scale for the QED shower being fixed at the virtuality of the decaying particle (for example the mass of the Z-boson). The default scale for the QCD final state shower is $\mu^2 = 2 \cdot (m_{1\perp}^2 + m_{2\perp}^2)$ (`ScaleTimeShower=1`), with $m_{1(2)\perp}$ being the transverse mass of the hard parton 1(2). Other choices are possible: $\mu^2 = \hat{s}$ (`ScaleTimeShower=2`) and $\mu^2 = 2 \cdot (m_1^2 + m_2^2)$ (`ScaleTimeShower=3`). In addition a scale factor can be applied: `ScaleFactorFinalShower`$\times \mu^2$ (default: `ScaleFactorFinalShower=1`).

Hadronization The hadronization (fragmentation of the partons in colorless systems) is done exclusively by Pythia. Hadronization (fragmentation) is switched off by `Hadronization = 0` (or `NFRA = 0` for the older steering cards). All parameters of the hadronization model can be changed via the steering cards.

Uncertainties Uncertainties of QCD calculations mainly arise from missing higher order corrections, which are estimated by varying the factorization and renormalization scales up and down by typically a factor of 2. The scale variations are performed when calculating the matrix elements and are stored as additional weights in the LHE file, which are then passed directly via Cascade3 to the HEPMC [81] output file for further processing. The uncertainties coming from the PDFs can also be calculated as additional weight factors during the matrix element calculation. However, when using TMDs, additional uncertainties arise from the transverse momentum distribution of the TMD. The PB-TMDs come with uncertainties from the experimental uncertainties as well as from model uncertainties, as discussed in Ref. [37]. These uncertainties can be treated and applied as additional weight factors with the parameter `Uncertainty_TMD=1`.

Multi-jet merging Showered multi-jet LO matrix element calculations can be merged using the TMD merging prescription [58, 59], which we will discuss in Chapter 10. The merging performance is controlled by the three parameters `Rclus`, `Etclus`, `Etaclmax`. Final-state partons with pseudorapidity η <`Etaclmax` present in the event record after the shower step but before hadronization are passed to the merging machinery if `Imerge = 1`. Partons are clustered using the kt-jet algorithm with a cone radius `Rclus` and matched to the PB evolved matrix element partons if the distance between the parton and the jet is $R < 1.5\times$`Rclus`. The hardness of the reconstructed jets is controlled by its minimum transverse energy `Etclus` (merging scale). The number of light flavor partons is defined by the `NqmaxMerge` parameter. Heavy flavor partons and their corresponding radiation are not passed to the merging algorithm. All jet multiplicities are treated in exclusive mode except for the highest multiplicity `MaxJetsMerge` which is treated in inclusive mode.

Chapter 8

Application of NLO + PB TMD matching to di-jet azimuthal correlations

In Chapter 3 we have discussed the PB TMD formalism, and in Chapter 7 we have described the implementation of PB in the TMD Monte Carlo event generator CASCADE3. In this chapter[1] and the next one we combine the TMD PB evolution with next-to-leading order (NLO) perturbative matrix elements through an appropriate "matching" procedure and apply this to specific processes of interest at the LHC, namely di-jet production (in this chapter) and Z-boson plus jet production (in the next chapter). We focus in particular on final-state azimuthal correlations in the di-jet and boson-jet cases, and illustrate that they provide sensitive probes of TMD dynamics.

Experiments at the LHC carry out accurate measurements of azimuthal correlations $\Delta\phi_{12}$ in multi-jet [223–227] and vector-boson plus jets [228, 229] final states. When two jets, or a boson and a jet, recoil nearly back-to-back, reliable QCD predictions call for soft-gluon resummation (see recent studies of Refs. [230–233] in the di-jet case and Refs. [234–240] in the boson-jet case). This region is probed by TMDs [34, 40, 41] in the initial state.

With the increase in luminosity at the LHC, it becomes possible to explore this region experimentally over a wide kinematic range in the hard scale of the process, set by the leading jet's transverse momentum $p_{T,j1}$, from $p_{T,j1} \approx O(100\,\text{GeV})$ to $p_{T,j1} \approx O(1000\,\text{GeV})$. In particular, at the highest scales the nearly back-to-back region accessible with the experimental angular resolution of about 1 degree is characterized by transverse momentum imbalances of a few ten GeV, which can be investigated by analyzing jets with measurable transverse momenta, reconstructable with experimental techniques. Observables in this kinematic region can be calculated with perturbation theory and require resummation of multiple soft gluons.

The combined study of the leading jet p_T and p_T-imbalance dependence of TMD dynamics is especially important, because the production of colored states near the back-to-back region may be influenced by *factorization-breaking* effects [241–244], due to interferences of gluons emitted in the initial and final state. An indirect strategy to explore the potential impact of these effects is to compare calculations which assume factorization with high-precision measurements. The observations regarding factorization-breaking effects in

---

[1]This work has been published in M. I. Abdulhamid et al., "*Azimuthal correlations of high transverse momentum jets at next-to-leading order in the parton branching method*", European Physical Journal C 82 (2022) 1, 36 [56].

multi-jet and boson-jet production are discussed in Chapter 9. In the boson-jet scenario, the final state is less colored than in the di-jet case, making the comparison between these studies interesting.

In this chapter we explore in detail high-p_T di-jet production and calculate azimuthal correlations, using NLO-matched PB TMD predictions. In Chapter 9 we perform an analogous study for boson-jet azimuthal correlations, based on Ref. [57].

8.1   Introduction

The description of the cross section of high-p_T jets in pp collisions is one of the most important tests of predictions obtained in QCD. Much progress has been achieved by experimental collaborations at the LHC in the description of inclusive jets [245–256] by applying next-to-leading (NLO) [99, 257–259] and next-to-next-to-leading-order (NNLO) calculations [260–263]. In multi-jet production, the azimuthal angle $\Delta\phi_{12}$ between the two highest transverse momentum jets is an inclusive measurement of additional jet radiation. At leading order (LO) in the strong coupling α_s, where only two jets are present, the jets are produced back-to-back, with $\Delta\phi_{12} = \pi$, while a deviation from this back-to-back configuration indicates the presence of additional jets, and only higher-order calculations can describe the observations. The azimuthal correlation between two jets has been measured in $p\bar{p}$ collisions at the Tevatron and at the LHC at center-of-mass energies going from $\sqrt{s} = 1.96$ TeV up to $\sqrt{s} = 13$ TeV by multiple collaborations in e.g. [223–227, 264, 265]. When measurements of azimuthal correlations of di-jets are compared with LO or NLO computations supplemented by parton showers, deviations of 50% are observed in the medium $\Delta\phi_{12}$ region even at NLO (see e.g. [225, 226]), which requires a more detailed understanding. In the $\Delta\phi_{12} \to \pi$ region, deviations of up to 10% are observed [227], significantly larger than the experimental uncertainties.

Since initial state parton radiation moves the jets away from the $\Delta\phi_{12} = \pi$ region, it is appropriate to investigate the implications of TMDs in the description of the $\Delta\phi_{12}$ measurements. Kinematic effects of the initial-state transverse momenta in the interpretation of jet measurements were pointed out in [29, 30]. A calculation based on TMD distributions is found in Ref. [230, 231] and further investigated in [232, 233].

In this chapter, based on Refs. [56, 266, 267], we calculate azimuthal correlations of high-p_T di-jets by applying the PB formulation of TMD evolution together with NLO calculations of the hard scattering process in the MC@NLO [55] framework. We compare the predictions with CMS data from [226, 227]. The chapter is organized as follows. We first describe in Sec. 8.2 how TMDs and TMD parton showers are matched to fixed NLO perturbative calculations. We show predictions using PB-TMDs together with the TMD parton shower of CASCADE3 in Sec. 8.3. We compare these predictions with the one using the PYTHIA8 parton shower [116, 117]. We give conclusions in Sec. 8.4.

8.2 Matching PB TMDs to NLO events

Matching PB TMDs to NLO matrix elements was performed for the first time in Ref. [36] for inclusive Z-boson production by exploiting the MC@NLO method [98]. NLO matching is crucial to avoid double counting of parton emissions (transverse momentum) between the matrix element generator, MADGRAPH5_AMC@NLO [55], and the TMD PDF. The MC@NLO method is a *subtraction method*, where soft and collinear contributions to the NLO cross section are subtracted from the matrix element in the form of *subtraction terms* (also referred to as *counterterms*). In order to produce a physical cross section, this needs to be supplemented by a parton shower or with PB TMD evolution. The subtraction terms therefore depend on the parton shower (or TMD) that is used. In the PB-TMD case provided by CASCADE3, the TMD fills the infrared phase space region. For the PB-TMDs and the PB-TMD parton shower, HERWIG6 [217, 218] subtraction terms are applied to the hard scattering events which is motivated by the angular ordering in the PB evolution[2].

The predictions for multi-jet production at NLO are obtained using the MAD-GRAPH5_AMC@NLO [55] framework. We used MADGRAPH5_AMC@NLO in two different modes: i) the fixed NLO mode, in which only partonic events are produced, without parton shower and hadronization, and ii) the MC@NLO mode, in which infrared subtraction terms are included to avoid double counting of parton emissions between matrix-element and parton-shower calculations.

In the fixed NLO mode, MADGRAPH5_AMC@NLO produces event files with the partonic configuration in LHE format [125] which are then processed through CASCADE3. In this mode, the hard scattering event record is kept without any modification. Processing through CASCADE3 has the significant advantage that a fixed NLO calculation can be obtained making use of all the analyses coded in RIVET [82, 83].

In the MC@NLO mode, subtraction terms are included which depend on the parton shower used. MADGRAPH5_AMC@NLO [55] is used for NLO calculation of di-jet production with the input of integrated NLO PB parton distributions with $\alpha_s(m_Z) = 0.118$. The LHE files including subtraction terms are combined with PB-TMD sets available in TMDLIB2, PB-TMD-NLO-HERAI+II-2018-set1 and PB-TMD-NLO-HERAI+II-2018-set2 (hereafter denoted by PB-TMD-Set1 and PB-TMD-Set2, respectively), through CASCADE3.

The matching scale μ_M, which limits the contribution from PB-TMDs and TMD showers ($\mu_M = $ `SCALUP` included in the LHE file), guarantees that the overlap with real emissions from the matrix element is minimized according to the subtraction of counterterms in the MC@NLO method. The factorization and renormalization scales at matrix element level are set to

$$\mu_{R,F} = \frac{1}{2} \sum_i \sqrt{m_i^2 + q_{\perp,i}^2} \tag{8.1}$$

both in MC@NLO as well as in the PB-TMDs in CASCADE3. The index i runs over all particles in the matrix element final state.

In CASCADE3, as described in detail in Chapter 7, the transverse momentum of the initial state partons is calculated according to the $k_\perp$ distribution provided by the PB-TMD at

---

[2]A comparison of applying PB-TMDs with application of the angular ordered HERWIG6 parton shower on transverse momentum and rapidity spectra is presented in Chapter 9 (Sec. 9.3).

given longitudinal-momentum fraction x and evolution scale μ. This transverse momentum is used for the initial state partons provided by MADGRAPH5_AMC@NLO, and their longitudinal momentum is adjusted such that the mass and the rapidity of the di-jet system is conserved, similar to what has been done in the DY case [268]. The initial state TMD parton shower does not change the kinematics of the hard process, after the $k_\perp$ from the TMD is included. The final state parton shower is obtained with the corresponding method implemented in `Pythia6` [269], by vetoing emissions which do not satisfy angular ordering (`MSTJ(42)=2`).
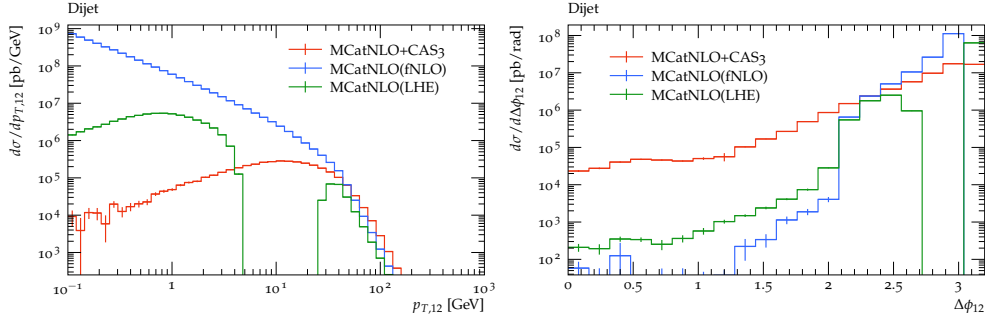

Figure 8.1: Transverse momentum spectrum of the di-jet system $p_{T,12}$ (left) and $\Delta\phi_{12}$ distribution (right). The predictions are shown for fixed NLO (MC@NLO(fNLO)), the (unphysical) LHE level (MC@NLO(LHE)) and after inclusion of PB-TMDs (MC@NLO+CAS3).

In Fig. 8.1 we show results for the transverse momentum distribution of the di-jet system $p_{T,12}$ and the azimuthal correlation $\Delta\phi_{12}$ between the two leading jets as obtained from the calculations at fixed NLO (blue curve), at the level including subtraction terms (LHE level, green curve) and after inclusion of PB-TMDs (red curve). We note the rising cross section of the fixed NLO calculation towards small $p_{T,12}$ (or at large $\Delta\phi_{12}$). This is the region in $p_{T,12}$ and $\Delta\phi_{12}$ where the subtraction terms are relevant and a physical prediction is obtained when PB-TMDs and parton showers are included. The jets are defined with the anti-k_T jet algorithm [93], as implemented in the `FastJet` package [270], with a jet cone resolution parameter of $R = 0.4$ and a leading jet transverse momentum $p_{T,j} > 200$ GeV. The use of jets (instead of partons) is the reason for the tail towards small $\Delta\phi_{12}$ in the MCatNLO(LHE) and MCatNLO(fNLO) calculation.

8.3   Azimuthal correlations in multi-jet production

We apply the framework described in the previous section, based on the matching of PB-TMDs with NLO matrix elements, to describe the measurement of azimuthal correlations $\Delta\phi_{12}$ obtained by CMS at $\sqrt{s} = 13$ TeV [226] and in the back-to-back region [227]. Only leading jets with a transverse momentum of $p_{T,j1} > 200$ GeV are considered. We show distributions of $\Delta\phi_{12}$ for $p_{T,j1} > 200$ GeV as well as for the very high p_T region of $p_{T,j1} > 1000$ GeV , where the jets appear very collimated. We apply the collinear and TMD PDF of Set2, unless explicitly specified different, with running coupling $\alpha_s(m_Z) = 0.118$.

We may estimate the theoretical systematics by considering two kinds of uncertainties:

those that come from variation of the arbitrary scales that appear in the various factors entering the jet cross section, and those that come from the determination of the TMD parton distributions and showers. The former include the renormalization scale in the strong coupling, the factorization scale used in the parton distribution and the matching scale to combine the matrix element and PB TMD. The latter include both experimental and model uncertainties in the TMD extraction.

As regards the scale variations, we present results corresponding to the 7-point scheme variation around the central values for the renormalization and factorization scale. This 7-point scheme involves varying these scales ($\mu_{R,F}$) by a factor of 2 up and down, avoiding the extreme cases of variation {0.5,2} and {2,0.5}. The dependence on the matching scale μ_M has been studied by co-authors who found that the resulting uncertainties are within the band of variation of factorization and renormalization scales.

The experimental and model uncertainties on the determination of the TMD distributions as described in Chapter 4 and Ref. [37] are included as well.

In Fig. 8.2 we show a comparison of the measurement by CMS [226] for different values of $p_{T,j1}$ (denoted in the figures by p_T^{leading}) with the calculation of CASCADE3 (MC@NLO+CAS3) including PB-TMDs, parton shower, and hadronization. The uncertainties from scale variation and TMD determination are shown separately. The central values of the two curves are identical.

Figure 8.2: Azimuthal correlation $\Delta\phi_{12}$ for $200 < p_{T,j1} < 300$ GeV (left) and $1000 < p_{T,j1} < 1200$ GeV (right) as measured by CMS [226] compared with predictions from MC@NLO+CAS3. Scale- and TMD-uncertainties are shown in both plots.

In Fig. 8.3 the measured $\Delta\phi_{12}$ distribution [227] in the back-to-back region ($170^o < \Delta\phi_{12} < 180^o$) is compared with the predictions by CASCADE3. Again, TMD and scale uncertainties are shown separately and central values are identical.

The measurements are described very well in the back-to-back region. The scale uncertainty is significantly larger than the TMD uncertainty, especially in the low $p_{T,j1}$ region. A difference between the measurement and the prediction is observed at small $\Delta\phi_{12}$ due to missing higher orders in the matrix element calculation. Even at high $p_{T,j1} > 1000$ GeV

Figure 8.3: Azimuthal correlation $\Delta\phi_{12}$ in the back-to-back region for $p_{T,j1} > 200$ GeV (left) and $p_{T,j1} > 1000$ GeV (right) as measured by CMS [227] compared with predictions from MC@NLO+CAS3. Scale- and TMD-uncertainties are shown in both plots.

the prediction is in agreement with the measurements (within uncertainties), while only in the highest $\Delta\phi_{12}$ bin ($\Delta\phi_{12} > 179^o$) a deviation of about 10% is observed.

8.3.1   Effect on $\Delta\phi_{12}$ of the scale in the strong coupling

In Figs. 8.4 and 8.5, we compare the predictions using PB-TMD-Set1 with those from PB-TMD-Set2, which differ in their treatment of scale in α_s. Both are compared to measurements as well and the ratio of predictions to this data is shown in the bottom panel. The differences between PB-TMD-Set1 and PB-TMD-Set2 become significant in the back-to-back region, which is sensitive to the low $k_\perp$-region of the TMD. As already observed in the case of Z-boson production in Ref. [36], PB-TMD-Set2 with the transverse momentum as a scale for α_s(which is required from the angular ordering condition) allows a better description of the measurement. It has been explicitly checked that the choice of the collinear parton density function (in contrast to the choice of the TMD densities) does not matter for the $\Delta\phi$ distributions, since they are normalized. The region of low $\Delta\phi_{12}$ in Figs. 8.2 and 8.4 is not well described with an NLO di-jet matrix element calculation supplemented with TMD densities and TMD parton shower because in the low $\Delta\phi_{12}$ region higher-order hard emissions play a significant role. These higher-order hard emissions could for example be merged with PB-TMDs and TMD showers by means of the TMD merging method described in chapter 10 and Ref. [59] in order to describe well the low $\Delta\phi_{12}$ region.

8.3.2   Comparison with PYTHIA8 and study of underlying event

In Fig. 8.6 predictions obtained with MC@NLO+PYTHIA8 are compared with MC@NLO+CAS3. In the calculation of MC@NLO+PYTHIA8, the PYTHIA8 subtraction terms are used and

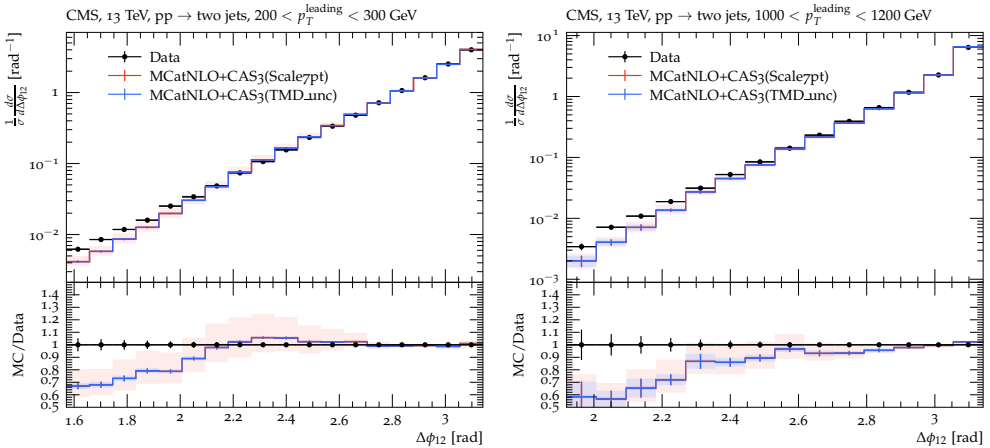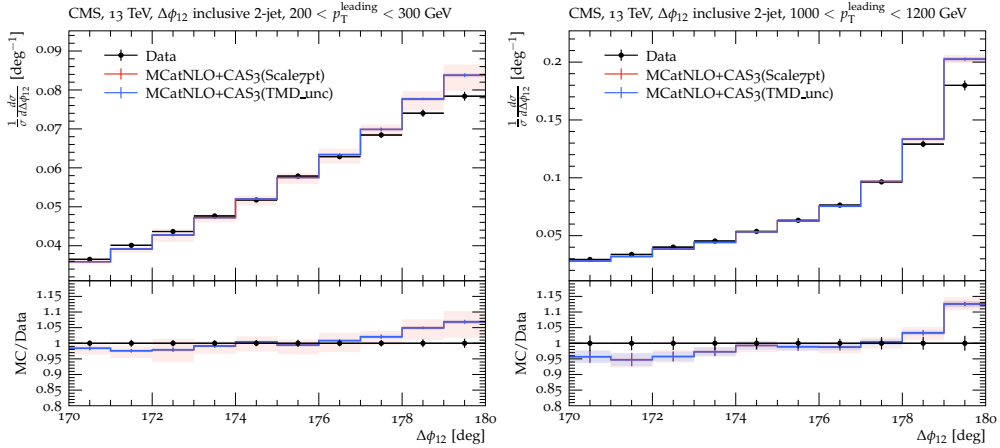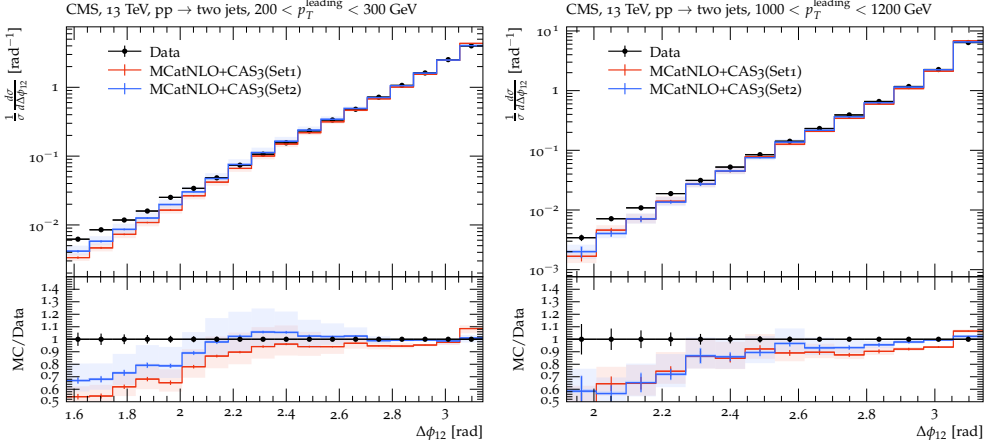*Figure 8.4:* Azimuthal correlation $\Delta\phi_{12}$ for $p_{T,j1} > 200$ GeV (left) and $p_{T,j1} > 1000$ GeV (right) as measured by CMS [226] compared with predictions from MC@NLO+CAS3. Both scale uncertainties as well as TMD uncertainties are shown.
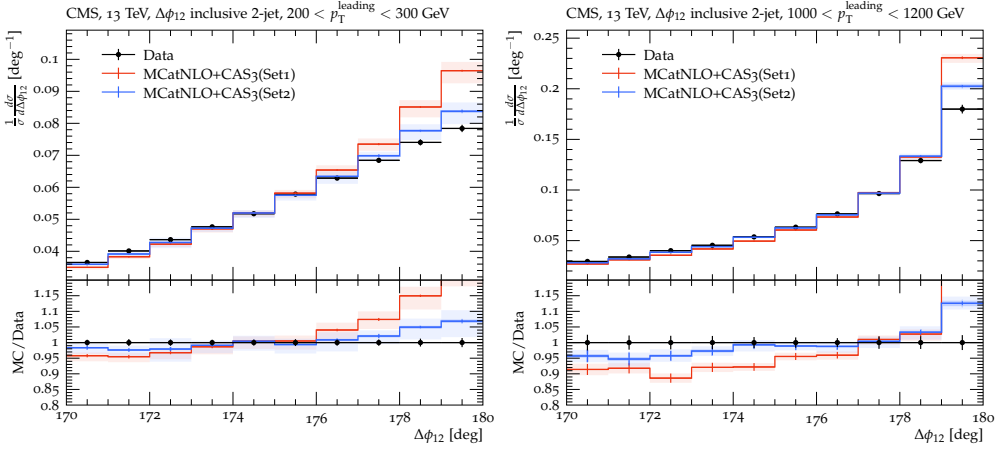
Figure 8.5: Azimuthal correlation $\Delta\phi$ in the back-to-back region for $p_{T,j1} > 200$ GeV (left) and $p_{T,j1} > 1000$ GeV (right) as measured by CMS [227] compared with predictions from MC@NLO+CAS3. Both scale uncertainties as well as TMD uncertainties are shown.

the NNPDF3.0 [271] parton density and tune CUETP8M1 [272] are applied. The uncertainties of the PYTHIA8 prediction are derived by combining the fixed-order scale variation from MC@NLO with renormalization scale variations in the parton shower. We use the method of [273] together with the guidelines of [274] to obtain consistent scale variations where possible. In particular, this means that the renormalization scale variation at fixed order and in the parton shower are fully correlated[3]. The factorization scale variation is only applied at fixed order, as argued in [274]. We observe a significant

---

[3]This also ensures that for fixed-order-dominated observables, the cancellation between the expansion of the shower and the subtraction in MC@NLO also occurs for non-central renormalization scales without significant deformation of the – there fully appropriate – fixed-order uncertainties.

dependence on the matching scale μ_M, the details of matching in case of di-jets needs further investigation.

Fig. 8.6 also shows the contribution from multi-parton interactions in the scenario of a Pythia8 calculation, which is very small for jets with $p_{T,j1} > 200$ GeV. The prediction obtained with mc@nlo+Pythia8 is in all $\Delta\phi_{12}$ regions different from the measurement and mc@nlo+CAS3, illustrating the role of the treatment of parton showers.
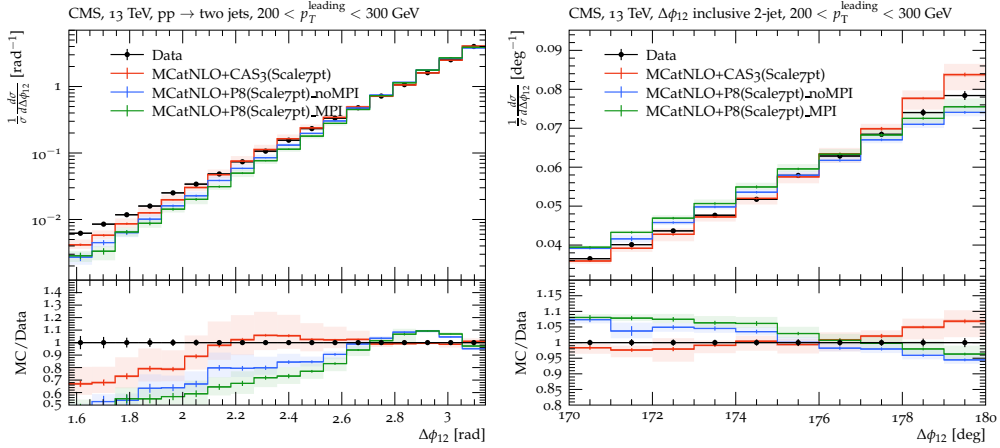
Figure 8.6: Azimuthal correlation $\Delta\phi_{12}$ over a wide range and (left) in the back-to-back region (right) for $p_{T,j1} > 200$ GeV compared with predictions from mc@nlo+Pythia8 and mc@nlo+CAS3. The uncertainties in the mc@nlo+Pythia8 calculation are obtained from scale and associated shower variations, as described in the main text.

8.4 Conclusion

We have investigated the azimuthal correlation of high transverse momentum jets in pp collisions at $\sqrt{s}$ = 13 TeV by applying PB-TMD distributions to NLO calculations via MC@NLO . We use the same PB-TMDs and MC@NLO calculations which have been used for Z production at LHC energies in Ref. [36].

The predictions of MC@NLO+CAS3 obtained with PB-TMD-Set2 distributions [37] and TMD parton shower are in reasonable agreement with the measurements in the larger $\Delta\phi_{12}$ regions. Only in the very high $p_{T,j1}$ region, a deviation from the measurement is observed.

The uncertainties of the predictions are dominated by the scale uncertainties of the matrix element calculations, while the PB-TMD and TMD shower uncertainties are very small, as they are directly coming from the uncertainties of the PB-TMDs. No uncertainties, in addition to those from the PB-TMD, come from the PB-TMD parton shower.

Significant differences are observed between predictions with PB-TMD-Set2, using the transverse momentum as scale in α_s, and PB-TMD-Set1, which uses the evolution scale as an argument in α_s. This observation confirms the importance of consistently handling the soft-gluon coupling in angular ordered parton evolution.

The uncertainties of the predictions are dominated by the scale uncertainties of the matrix element, while uncertainties coming from the PB-TMDs and the corresponding PB-TMD shower are very small. No other uncertainties, in addition to those of the PB-TMD, come from the PB-TMD shower, since it is directly correlated with the PB-TMD density.

We have also investigated predictions using MC@NLO with PYTHIA8 to illustrate the importance of details of the parton shower.

Application of NLO + PB TMD matching to boson-jet azimuthal correlations

In this chapter[1] we continue the exploration of final-state azimuthal correlations which we started in the previous chapter, by applying the same kind of analysis of the previous chapter to the case of Z-boson + jet production. We compare in detail high-p_T di-jet and Z+jet production by applying the PB TMD method [38, 39] matched to NLO matrix elements.

In Chapter 8 the NLO PB TMD predictions have been found to describe well the measurements of di-jet azimuthal correlations [226, 227]. In the present chapter we apply the same method to the calculation of Z+jet production, and present the corresponding predictions. In Z boson production the final state is less colored than in multi-jet production, causing the possible factorization breaking effects to be less strong. It is therefore interesting to compare the results to those from di-jet events. We use the same kinematic region for the high-p_T di-jet and Z+jet production to allow a direct comparison of the angular observables in the two cases.

This chapter is structured as follows. We start by an introduction and motivation of the study of boson-jet azimuthal correlations with TMDs in Sec. 9.1. We then recap the basic elements of the method to match PB-TMDs to NLO matrix elements via MC@NLO+CASCADE3 in Sec. 9.2. A study performed by collaborators on the matching procedure with MC@NLO is presented in Sec. 9.3 where the use of HERWIG6 subtraction terms is defended by comparing results of initial state TMD shower with HERWIG6 showering. In Sec. 9.4 we present results obtained with PB for the Z+jet azimuthal correlations and compare them with the di-jet case. We summarize in Sec. 9.5.

---

[1]This work has been published in H. Yang et al., "*Back-to-back azimuthal correlations in Z+jet events at high transverse momentum in the TMD parton branching method at next-to-leading order*", European Physical Journal C 82 (2022) 8, 755 [57].

9.1   Introduction

The description of jet production in association with a Z boson in hadron-hadron collisions is another important test of predictions obtained in QCD, and provides a relevant background to Higgs boson studies and to new physics searches. The associated Z boson plus jet production has been measured by CDF and D0 in proton-antiproton collisions at a center-of-mass energy $\sqrt{s}$ = 1.96 TeV [275, 276]. At the LHC, the ATLAS and CMS collaborations have published measurements in pp collisions at a center-of-mass energy $\sqrt{s}$ = 7 TeV [277–279], 8 TeV [228] and 13 TeV [229, 280]. Azimuthal correlations between Z bosons and jets have been measured at 8 TeV [228] and 13 TeV [229].

The distribution in the azimuthal angle $\Delta\phi$ between the Z boson and the jet is an especially sensitive observable, probing several aspects of QCD physics. At leading order in the strong coupling α_s, one has $\Delta\phi = \pi$. The smearing of this delta-like distribution is a measure of higher order QCD radiation. In the region near $\Delta\phi = \pi$, this is primarily soft gluon radiation, while in the region of small $\Delta\phi$ it is primarily hard QCD radiation. The large-$\Delta\phi$ region of nearly back-to-back Z boson and jet is influenced by both perturbative and non-perturbative QCD contributions. The relative significance of these contributions depends on the scale of the transverse momentum imbalance between the boson and the jet. Importantly, the resummation of soft multi-gluon emissions in the nearly back-to-back region probes the transverse momenta of the initial state partons, which can be described by transverse momentum dependent (TMD) [34] parton distribution functions (PDFs). Theoretical predictions for Z boson + jet production including soft gluon resummation have recently been given in Refs. [234–240].

All the experimental measurements of boson-jet azimuthal correlations that have been performed so far are in the kinematical range of transverse momenta of the Z boson and the jets of the order $p_T \approx O(100)$ GeV . In this kinematical range, fixed-order perturbative corrections beyond next-to-leading order (NLO) are sizeable, and at small $\Delta\phi$ NLO calculations are usually not sufficient for reliable predictions. For the large-$\Delta\phi$ region of nearly back-to-back Z boson and jet, the boson-jet p_T imbalance scale is of order a few GeV, which is significantly influenced by both perturbative resummation and non-perturbative effects. It is worth noting that all the experimental measurements performed up to now do not cover the large $\Delta\phi$, nearly back-to-back, region with sufficiently fine binning to investigate detailed features of QCD.

With the increase in luminosity at the LHC, it becomes possible to measure Z+jet production in the high p_T range, with $p_T \approx O(1000)$ GeV . We observe again, as in the di-jet scenario, that in this kinematical range the resummation of soft gluons and TMD dynamics in the nearly back-to-back region can be explored in a new regime, characterized by boson-jet p_T imbalance scales on the order of a few ten GeV. The large-$\Delta\phi$ region, involving deviations of the order of the experimental angular resolution of about 1 degree from $\Delta\phi = \pi$, can be investigated by analyzing jets with measurable transverse momenta.

Based on the above observation, in this chapter we propose experimental investigations of back-to-back azimuthal correlations in the $p_T \approx O(1000)$ GeV region, with a systematic scan of the large-$\Delta\phi$ regime from this high p_T region down to $p_T \approx O(100)$ GeV – a regime which is completely unexplored experimentally up to now. We present dedicated phenomenological studies of this $\Delta\phi$ region as a function of p_T, enabling one to explore boson-jet transverse momentum imbalances from a jet scale of several ten GeV down

to the few GeV scale. We use the PB approach to TMD evolution, matched to NLO calculations of Z+jet production with MADGRAPH5_AMC@NLO [55] that has shown to be successful in the scenario of the di-jet $\Delta\phi_{12}$ spectrum (presented in Chapter 8), for the Z boson p_T spectrum at the LHC (in Ref. [36]) and to the Drell-Yan (DY) p_T spectrum at lower fixed-target energies (in Ref. [268]). The investigation of the same method in the Z+jet case is therefore compelling.

Vector boson + jet production is also, as for di-jet production, believed to be sensitive to factorization - breaking [241–244] effects [242] that become important in the case of colored final states. We will see that, in the region of leading transverse momenta of the order $p_T \approx \mathcal{O}(100\,\text{GeV})$, the boson-jet final state is more strongly correlated azimuthally than the jet-jet final state. As the transverse momenta increase above the electroweak symmetry breaking scale, $p_T \approx \mathcal{O}(1000\,\text{GeV})$, this difference is reduced, and the boson-jet and jet-jet become more similarly correlated. We connect this behavior to features of the partonic initial state and final state radiation in the boson-jet and jet-jet cases.

In order to investigate factorization - breaking effects, we propose in Ref. [57] measurements of azimuthal correlations in Z+jet processes scanning the phase space from low transverse momenta $p_T \approx \mathcal{O}(100\,\text{GeV})$ to high transverse momenta $p_T \approx \mathcal{O}(1000\,\text{GeV})$ to systematically compare them to measurements of di-jet azimuthal correlations. A thorough investigation of azimuthal correlations in the back-to-back region in Z+jet events has been performed in Ref. [235], addressing the issue of factorization - breaking.

9.2 Calculation of Z+jet azimuthal correlation with PB-TMDs

In this section, we recap the importance of PB-TMDs in the calculation of DY production and motivate the use of PB-TMD Set 2 in the calculations for Z+jet azimuthal correlations. Then we provide technical details on the matching procedure for calculation of $\Delta\phi_{Zj}$ by processing NLO matrix elements with CASCADE3 using the MC@NLO framework, matching PB TMDs to fixed-NLO.

TMDLIB2, as described in Chapter 4, includes two TMD sets evolved with PB evolution: PB-TMD-NLO-HERAI+II-2018-set1 and PB-TMD-NLO-HERAI+II-2018-set2, hereafter denoted by PB-TMD-Set1 and PB-TMD-Set2 respectively. It has been shown in Refs. [36, 268] that PB-TMD-Set2 provides a better description of experimental measurements for the Z-boson spectrum at low-p_T. Also, it has been shown in Chapter 8 that the transverse momentum scale in the running coupling α_s is important for a good description of data on di-jet angular correlations. Therefore, we concentrate in this chapter on PB-TMD-Set2 only.

In Fig. 9.1 we show the transverse momentum distributions for up quarks and gluons at $x = 0.01$ and $\mu = 100$ and 1000 GeV for PB-TMD-Set2. The $k_\perp$ distribution of gluons is broader than that of quarks, due to gluon self-coupling and the different color factors. In Fig. 9.1 also the uncertainties of the distributions, as obtained from the fit [37], are shown. The differences in the transverse momentum spectra of quarks and gluons will show up in differences in azimuthal correlation distributions.
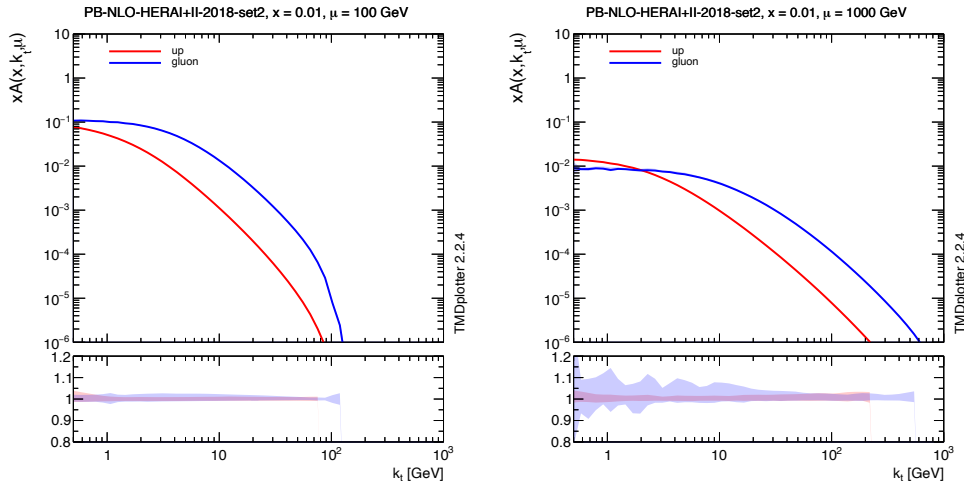
Figure 9.1: Transverse momentum distributions for up quarks (red curve) and gluons (blue curve) from PB-TMD-Set2 at μ = 100 and 1000 GeV and x = 0.01. The lower panels show the full uncertainty of the TMDs, as obtained from the fits [37].

The MC@NLO+CASCADE3 framework to combine PB TMD resummation with fixed-order NLO matrix elements has been developed in [36, 268] and is explained in Chapter 8. The Z+jet process at NLO is calculated with MADGRAPH5_AMC@NLO using the collinear PB-NLO-HERAI+II-2018-set2, as obtained in Ref. [37] applying $\alpha_s(m_Z)$ = 0.118. The matching of NLO matrix elements with PB TMD parton distributions based on Refs. [36, 51, 268] and the extension to di-jet production are described in Chapter 8. Predictions are obtained by processing the MADGRAPH5_AMC@NLO event files in LHE format [125] through CASCADE3 [51] for an inclusion of TMD effects in the initial state and for simulation of the corresponding parton shower (labeled MC@NLO+CAS3 in the following).

Fixed order NLO Z+jet production is calculated in a procedure similar to the one applied for di-jet production (labeled MC@NLO(fNLO)). Fully matched NLO calculations are calculated in the MC@NLO mode, where HERWIG6 [217, 218] subtraction terms are included. The matching scale μ_M limits the contribution from PB-TMDs and TMD showers in these calculations. The use of HERWIG6 subtraction terms together with CASCADE3 is justified in the following section.

Factorization and renormalization scales in PB-TMD-Set2 are set to

$$\mu_{R,F} = \frac{1}{2} \sum_i p_{T,i}, \tag{9.1}$$

where the index i runs over all particles in the matrix element final state. This scale is also used in the PB-TMD parton distribution $\mathcal{A}(x, k_\perp, \mu)$. Scale uncertainties of the predictions are obtained from variations of the scales around the central value in the 7-point scheme.

In Fig. 9.2 we show the distributions of the transverse momentum of the Z+jet system, $p_{T,Zj}$, and the azimuthal correlation in the Z+jet system, $\Delta\phi_{Zj}$, for a fixed NLO calculation, for the full simulation including PB-TMD PDFs and parton showers as well as

for the MC@NLO calculation at the level where subtraction terms are included without addition from parton shower (LHE-level). We require a transverse momentum $p_T > 200$ GeV for the Z boson and define jets with the anti-$k_\perp$ jet-algorithm [93], as implemented in the `FastJet` package [270], with a distance parameter of $R = 0.4$. The effect of including PB-TMD PDFs and parton showers can be clearly seen from the difference to the fixed NLO and LHE-level calculations.

In the low $p_{T,Zj}$ region one can clearly see the expected steeply rising behavior of the fixed NLO prediction. In the $\Delta\phi_{Zj}$ distribution the phase space needed for $\Delta\phi_{Zj} < 2/3\pi$ is not filled by fixed NLO, since at most two jets in addition to the Z boson appear in the fixed NLO calculation. At large $\Delta\phi_{Zj}$, the fixed NLO prediction rises faster than the full calculation including resummation via PB-TMDs and parton showers.
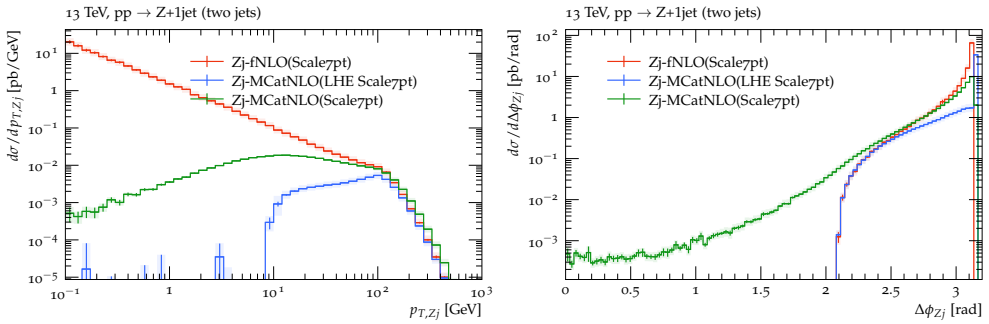
Figure 9.2: Transverse momentum spectrum of the Z+jet-system $p_{T,Zj}$ (left) and $\Delta\phi_{Zj}$ distribution (right). Shown are predictions from fixed NLO (fNLO), the (unphysical) distribution at LHE-level and the full simulation (after inclusion of PB-TMDs and TMD showers, MC@NLO+CAS3).

9.3   Comparison of CASCADE3 and HERWIG6

Matching PB-TMDs to NLO partonic events from MADGRAPH5_AMC@NLO is done by using HERWIG6 (H6) subtraction terms in the matrix elements. In this section, we summarize investigations presented in Ref. [57] about the contribution of the parton shower used in CASCADE3. Predictions obtained with MC@NLO+CAS3 are compared with predictions from MC@NLO+H6, using identical LHE files produced with MADGRAPH5_AMC@NLO for Z boson production. The NLO accuracy of the calculations is preserved by construction, since the use of PB-TMD distributions and TMD shower, as well as the ordinary parton shower, does not change the inclusive cross section. The Z boson is reconstructed from two oppositely charged leptons with $p_T > 20$ GeV in $|\eta| < 2.4$ and di-lepton masses near the Z mass peak. We also show jet observables where jets are clustered with the anti-$k_\perp$ algorithm with distance parameter 0.4 with $p_T > 30$ GeV and $|\eta| < 5$.

In H6, the allowed region of the splitting variable z for a branching $q \rightarrow qg$ in the final state shower is $Q_q/Q < z < 1 - Q_g/Q$ (e.g. A.2.2 in Ref. [96]), with $Q_q = m_q + $ `VQCUT` and $Q_g = m_g + $ `VGCUT`, and m_q, m_g being the quark and gluon effective masses, and `VQCUT`, `VGCUT` the minimum virtuality parameters. Similar cuts are applied for the initial state shower.

First we investigate final state parton showers. We compare transverse momentum distributions of the two leading jets in Z+jet events: the first (highest p_T) jet is part of the lowest order process, while the second (highest p_T) jet is the real correction and therefore subject to subtraction terms (keeping in mind that the highest p_T jet in the NLO calculation can also come from the α_s^2 real emission diagram). In CASCADE3, the Pythia6 final state shower is used (the PB method has not yet been applied for final state radiation), with the angular ordering veto condition. Since final state radiation is independent of parton densities, a direct comparison of MC@NLO+CAS3 and MC@NLO+H6, using the same LHE files, while only simulating final state radiation, is possible.

In Fig. 9.3 we show a comparison of predictions of the transverse momentum distributions of the two leading jets in Z+jet events where only final state radiation has been applied, i.e. no initial state radiation and no hadronization are included. The uncertainty coming from different parameter settings in the H6 final state parton shower is estimated by changing the light quark masses from the default to $m_l = 0.32$ GeV and VQCUT,VGCUT from the default to 0.1(1.5), labelled as $Vc_l(Vc_h)$, respectively.

Figure 9.3: Comparison of predictions obtained with MC@NLO+CAS3 and MC@NLO+H6 for Z+jet obtained with MC@NLO. Shown are predictions using only the final state parton shower. The band of MC@NLO+CAS3 shows the uncertainties obtained from scale variation.

In Fig. 9.4 a comparison is shown for the pseudorapidity η of the first two highest p_T jets. Within the variation of the parameters, the prediction of MC@NLO+CAS3 agrees well with the one of MC@NLO+H6, justifying the application of the Pythia6 final state parton shower algorithm.

Next we include the contribution of PB - TMDs and the PB - TMD parton shower in the initial state (ISR) and compare the predictions with H6 calculations. In Fig. 9.5 we show the transverse momentum of the Z boson, its rapidity distribution and the transverse momentum of the leading reconstructed jet with $p_T > 30$ GeV and $|\eta| < 5$. Here the rapidity y of the Z boson is used, since it is related to the momentum fractions of the initial partons (instead of the pseudorapidity η which is used for jets as it is related to the scattering angle θ). We show a comparison of MC@NLO+CAS3 and MC@NLO+H6 predictions (including the same parameter variations for H6 as for the final state shower). In the region of low transverse momentum of the Z boson the sensitivity to the parameter
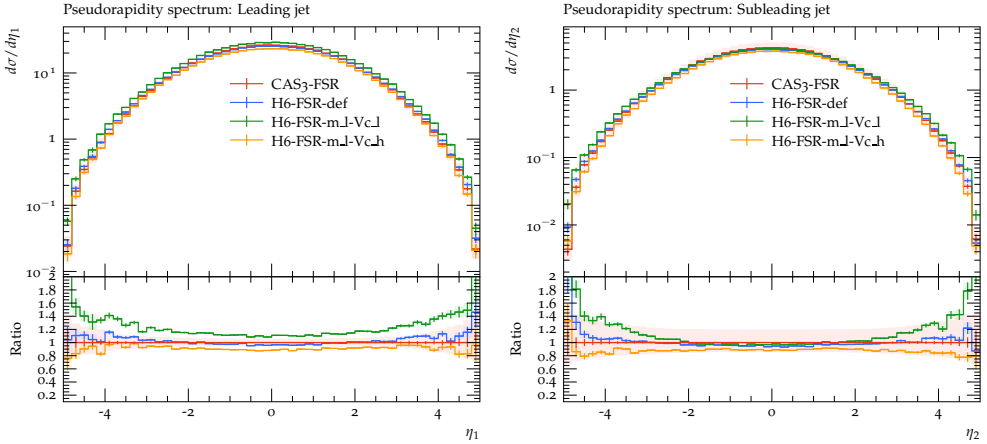
Figure 9.4: Comparison of predictions obtained with MC@NLO+CAS3 and MC@NLO+H6 for Z+jet obtained with MC@NLO. Shown are predictions using only final state parton shower. The band of MC@NLO+CAS3 shows the uncertainties obtained from scale variation (as described in the text).

choice in H6 is largely visible.

Finally, we show Z+jet events with both initial and final state radiation. In Fig. 9.6 we show a comparison of MC@NLO+CAS3 and MC@NLO+H6 predictions (including the same parameter variations for H6 as for the final state shower) for the transverse momentum of the first two highest p_T jets. In Fig. 9.7 the corresponding comparison is shown for the pseudorapidity distributions. The transverse momentum distributions agree well within the uncertainties coming from parameter variations, while for the η-distributions some differences in the very forward/backward regions are seen. However, one can see that a variation of VQCUT, VGCUT has a significant effect especially in the forward/backward region.

In conclusion, we observe agreement between predictions obtained by MC@NLO+CAS3 and MC@NLO+H6 within the band of parton shower parameter variation in H6, confirming the use of H6 subtraction terms in MC@NLO together with PB-TMDs and PB-TMD initial state parton shower, as applied in MC@NLO+CAS3.

9.4 Back-to-back azimuthal correlations in Z+jet and di-jet production

In this section, we present predictions, obtained in the framework described above, for Z+jet and di-jet production. [2] The selection of events follows the one of azimuthal correlations $\Delta\phi_{12}$ in the back-to-back region ($\Delta\phi_{12} \rightarrow \pi$) in di-jet production at $\sqrt{s} =$ 13 TeV as obtained by CMS [227]: jets are reconstructed by FastJet with the anti-$k_\perp$ algorithm [93] with a distance parameter of 0.4 in the rapidity range of $|y| < 2.4$. We

---

[2]A framework based on CCFM evolution [52] was described in [281, 282] for di-jet and vector boson + jet correlations.
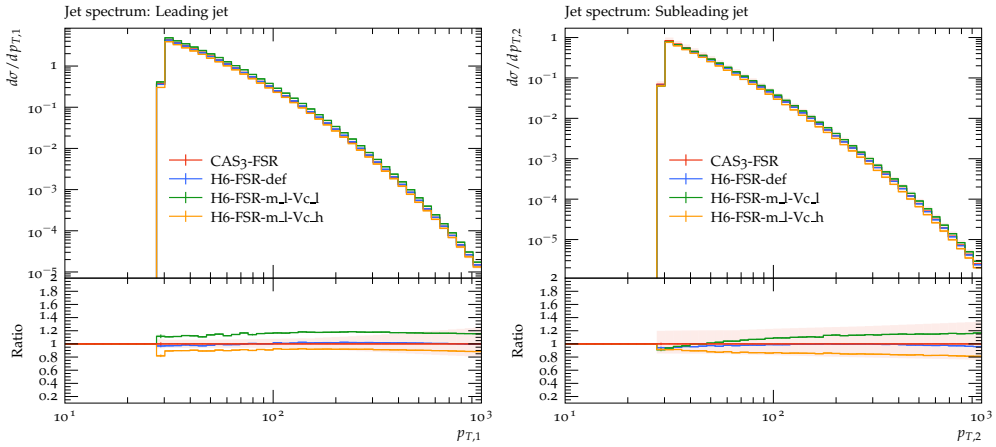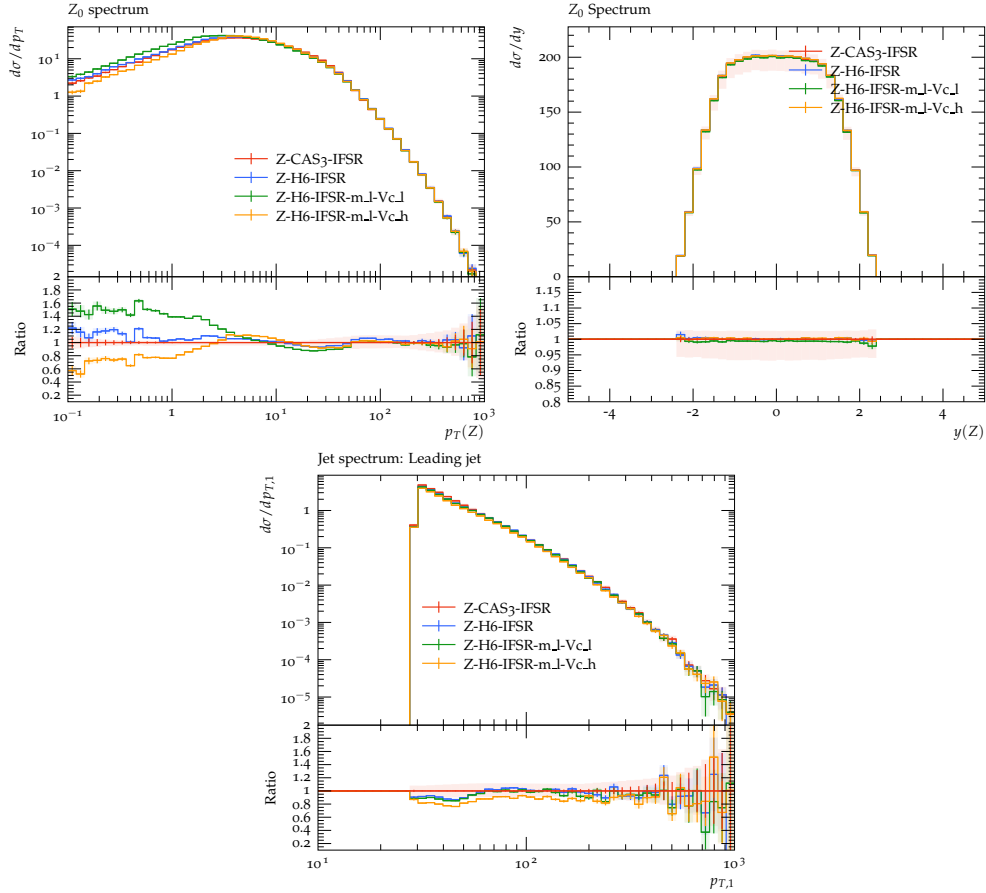
Figure 9.5: Comparison of predictions obtained with MC@NLO+CAS3 and MC@NLO+H6 for Z production obtained with MC@NLO. Shown are predictions using initial state parton shower. The band of MC@NLO+CAS3 shows the uncertainties obtained from scale variation (as described in the text).

require either two jets with $p_{T,j1} > 200$ GeV or a Z boson and a jet as leading or subleading objects with a transverse momentum $p_{T,j1} > 200$ GeV.

We consider distributions of the azimuthal correlation between the Z boson and the leading jet, $\Delta\phi_{Zj}$, for $p_{T,j1} > 200$ GeV as well as for the very high p_T region of $p_{T,j1} > 1000$ GeV. The calculations are performed with MC@NLO+CAS3 using the collinear and TMD parton densities PB-NLO-2018-HERAI+II-set2 and PB-TMD-Set2 with the running coupling $\alpha_s(m_Z) = 0.118$ and the PB-TMD initial state parton shower.

In Fig. 9.8, the prediction for the azimuthal correlations $\Delta\phi_{Zj}$ for Z+jet production in the back-to-back region is shown.[3] In the same figure we show, for comparison, the prediction of azimuthal correlations $\Delta\phi_{12}$ for di-jet production in the same kinematic region, compared to the measurement of multi-jets obtained by CMS [227]. We observe

---

[3]Predictions for the region of small $\Delta\phi$ require including the contribution of higher parton multiplicities via a calculation including multi-jet merging [59].
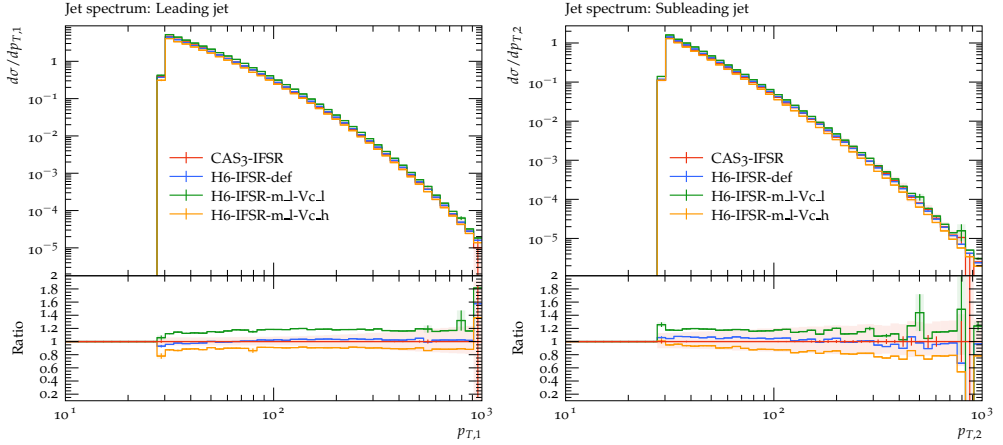
Figure 9.6: Comparison of predictions obtained with MC@NLO+CAS3 and MC@NLO+H6 for Z+jet obtained with MC@NLO. Shown are predictions using initial and final state parton shower. The band of MC@NLO+CAS3 shows the uncertainties obtained from scale variation (as described in the text).
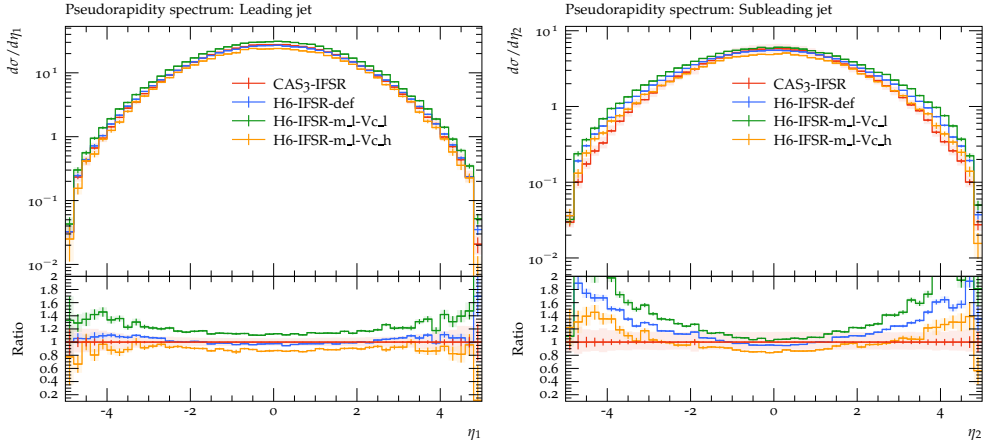
Figure 9.7: Comparison of predictions obtained with MC@NLO+CAS3 and MC@NLO+H6 for Z+jet obtained with MC@NLO. Shown are predictions using initial and final state parton shower. The band of MC@NLO+CAS3 shows the uncertainties obtained from scale variation (as described in the text).

that the distribution of the azimuthal angle $\Delta\phi_{Zj}$ in Z+jet-production for $p_{T,j1}$>200 GeV is more strongly correlated towards π than the distribution of angle $\Delta\phi_{12}$ in di-jet production. This difference is reduced for $p_{T,j1}$> 1000 GeV .

Differences in $\Delta\phi$ between Z+jet and di-jet production can result from the different flavor composition of the initial state and therefore different initial state transverse momenta and initial state parton shower, as well as from differences in final state showering since both processes have a different number of colored final state partons. Effects coming

Figure 9.8: Predictions of the azimuthal correlation $\Delta\phi_{Zj}(\Delta\phi_{12})$ for Z+jet and di-jet processes in the back-to-back region for $p_T^{leading} \equiv p_{T,j1} >$ 200 GeV (left) and $p_T^{leading} \equiv p_{T,j1} >$ 1000 GeV (right) obtained from MC@NLO+CAS3. Shown are the uncertainties obtained from scale variation. The measurements of di-jet correlations as obtained by CMS [227] are shown as data points, for comparison.

from factorization-breaking, interference between initial and final state partons, would depend on the final state structure and the number of colored final state partons. In the following subsections, we discuss separately the initial state and final state effects in the $\Delta\phi$ distributions and show theoretical uncertainties that come from the matching scale.

9.4.1   Contribution from initial state radiation to p_T

We first investigate the role of initial state radiation and the dependence on the transverse momentum distributions coming from the TMDs, which gives a large contribution to the decorrelation in $\Delta\phi$. The $k_\perp$-distribution obtained from a gluon TMD PDF is different from the one of a quark TMD PDF as shown in Fig. 9.1 for $x = 0.01$ and scales of $\mu = 200(1000)$ GeV . In Fig. 9.9 we show the probability of gg, qg and qq initial states (q stands for both quark and antiquark) as a function of the leading jet transverse momentum $p_{T,j1}$ for Z+jet and di-jet production obtained with MC@NLO+CAS3. At high $p_{T,j1} >$ 1000 GeV the qq channel becomes important for both Z+jet and di-jet final states, while at lower $p_{T,j1} >$ 200 GeV the gg channel is dominant in di-jet production, leading to larger decorrelation effects, since gluons radiate more compared to quarks.
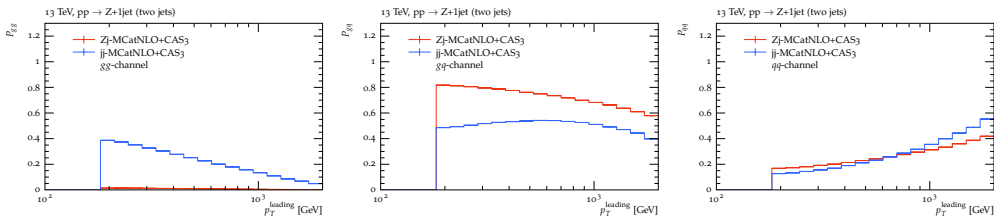
Figure 9.9: The probability of gg, qg and qq initial states in Z+jet and di-jet production as a function of $p_{T,j1}$. The predictions are calculated with MC@NLO+CAS3.

9.4.2 Comparison of final states from Cascade3 and Pythia8

The role of final state radiation in the correlation in $\Delta\phi$ distributions is more difficult to estimate, since the subtraction terms for the NLO matrix element calculation also depend on the structure of the final state parton shower. In order to estimate the effect of final state shower we compare a calculation of the azimuthal correlations in the back-to-back region obtained with mc@nlo+CAS3 with a calculation with mc@nlo+Pythia8 (labeled mc@nlo+P8). Results are shown in Fig. 9.10. For the calculation mc@nlo+P8 we apply the Pythia8 subtraction terms in the MadGraph5_amc@nlo calculation, use the NNPDF3.0 [271] parton density and CUETP8M1 tune [272].
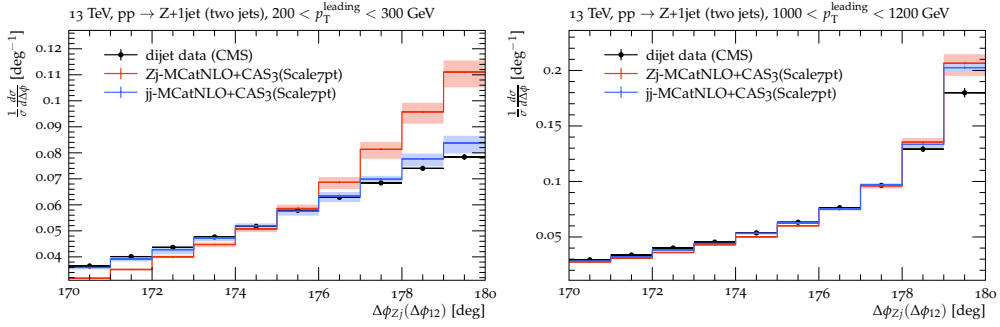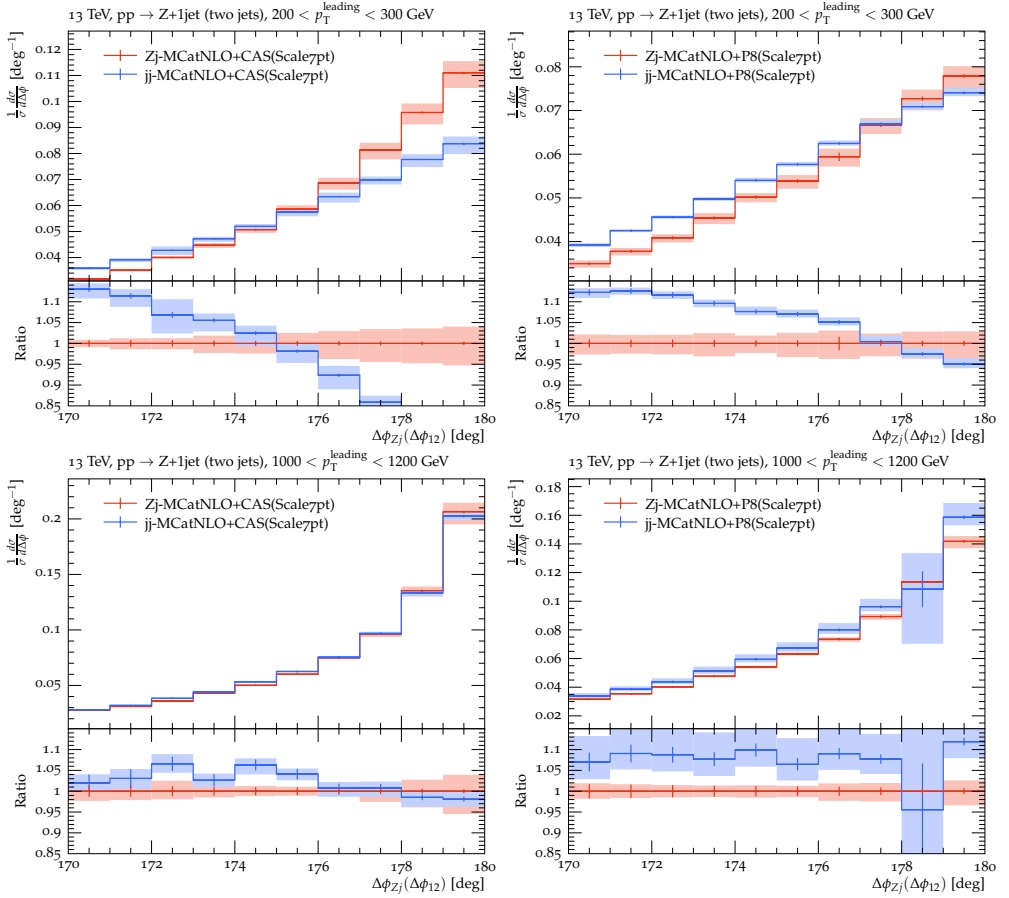

Figure 9.10: Predictions for the azimuthal correlation $\Delta\phi_{Zj}(\Delta\phi_{12})$ in the back-to-back region for Z+jet and di-jet production obtained with mc@nlo+CAS3 (left column) and mc@nlo+P8 (right column). Shown are different regions in $p_{T,j1} > 200$ GeV (upper row) and $p_{T,j1} > 1000$ GeV (lower row). The bands show the uncertainties obtained from scale variation.

The distributions in Fig. 9.10 of results from Cascade3 and Pythia8 differ due to different parton showers, but the ratio of the distributions for Z+jet and di-jet production are similar: Z+jet-production gives a steeper (more strongly correlated) distribution at low $p_{T,j1}$, while at high $p_{T,j1}$ the distributions become similar in shape. We conclude, that

the main effect of the $\Delta\phi$ decorrelation comes from initial state radiation, and the shape of the $\Delta\phi$ decorrelation in the back-to-back region becomes similar between Z+jet and di-jet processes at high $p_{T,j1}$ where similar initial partonic states are important.

9.4.3   Theoretical uncertainties from matching

The matching scale μ_M limits the hardness of parton-shower emissions, and is thus typically a non-negligible source of variation in matched calculations (see e.g. Ref. [283] for a detailed discussion). It is thus interesting to assess the robustness of the previous findings under variations of the matching scale. Assessing matching scale variations in both an angular-ordered shower – such as Cascade3 – and a p_T-ordered shower – such as Pythia8– additionally tests the interpretation and role of the matching scale. In transverse-momentum ordered showers, the matching scale sets the maximum transverse momentum of the first shower emission, while branchings beyond the first emission are not explicitly affected by the matching scale. In an angular-ordered shower, however, the matching scale is applied as "veto scale" to avoid larger transverse momenta for any branching, i.e. the matching scale directly affects all branchings. The result of changing the matching scale to half or twice the central value is shown in Fig. 9.11. As expected, the value of the matching scale has an impact on the prediction ($\sim 5\%$). This is particularly apparent when μ_M is used to set the maximal transverse momentum of the first emission in Pythia8. Overall, we find that interpreting the matching scale as veto scale in Cascade3 leads to apparently more robust predictions. Interestingly, the matching scale uncertainty becomes smaller for higher-$p_{T,j1}$ jet configurations in Cascade3. The size of the matching scale variation is comparable to scale variations, and should thus be carefully studied when designing uncertainty estimates.

In order to experimentally probe effects which could originate from factorization-breaking in the back-to-back region we propose to measure the ratio of distributions in $\Delta\phi_{Zj}$ for Z+jet and $\Delta\phi_{12}$ for di-jet production at low and very high $p_{T,j1}$, and compare the measurement with predictions assuming that factorization holds. The number of colored partons involved in Z+jet and di-jet events is different, and deviations from factorization will depend on the structure of the colored initial and final state. In order to minimize the effect of different initial state configurations, a measurement at high $p_{T,j1}$, hint more clearly at possible factorization-breaking effects.

9.5   Conclusion

We have investigated azimuthal correlations in Z+jet production and compared predictions with those for di-jet production in the same kinematic range. The predictions are based on PB-TMD distributions with NLO calculations via mc@nlo supplemented by PB-TMD parton showers via Cascade3. The azimuthal correlations $\Delta\phi_{Zj}$, obtained in Z+jet production are steeper compared to those in di-jet production ($\Delta\phi_{12}$) at transverse momenta $\mathcal{O}(100)$ GeV , while they become similar for very high transverse momenta, $\mathcal{O}(1000)$ GeV , which is a result of similar initial parton configuration of both processes.

In Z+jet production the color and spin structure of the partonic final state is different
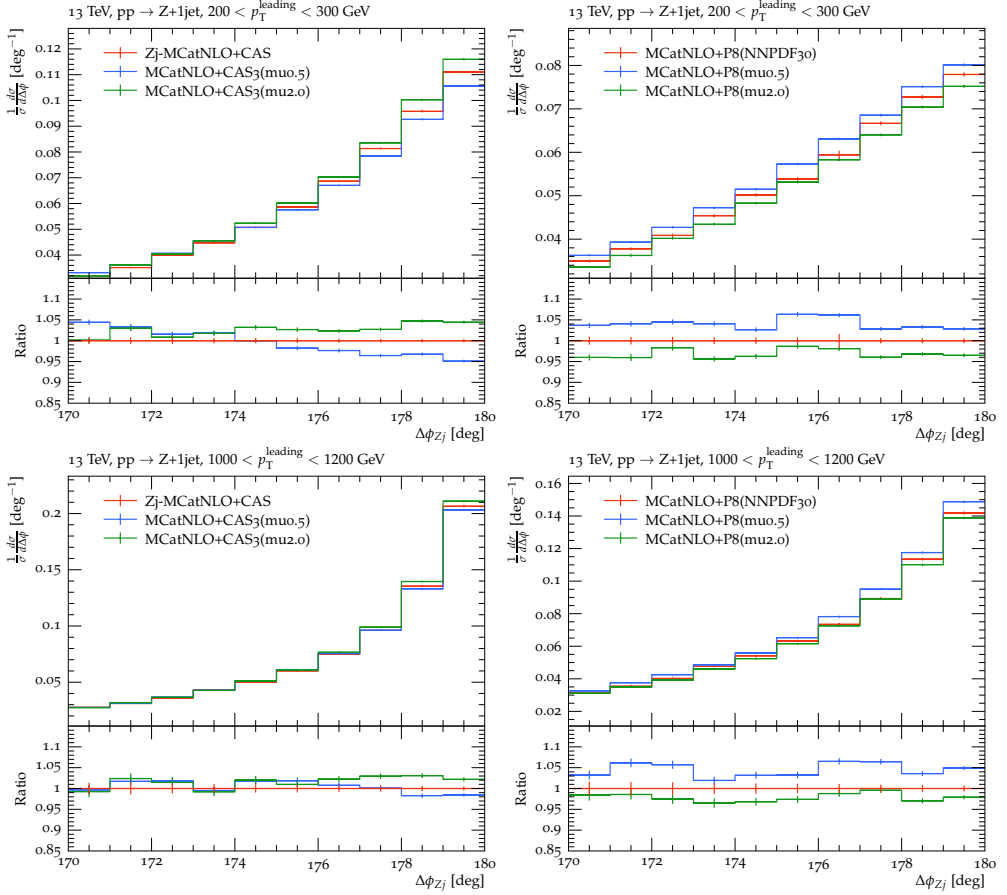
Figure 9.11: The dependence on the variation of the matching scale μ_m in predictions for the azimuthal correlation $\Delta\phi_{Zj}$ in the back-to-back region. Shown are predictions obtained with MC@NLO+CAS3 (left column) and MC@NLO+PYTHIA8 (right column) for $p_{T,j1} > 200$ GeV (upper row) and $p_{T,j1} > 1000$ GeV (lower row). The predictions with different matching scales μ_m varied by a factor of two up and down are shown.

compared to the one in di-jet production, and differences in the azimuthal correlation patterns can be used to search for potential factorization - breaking effects, involving initial and final state interferences. We cannot conclude about any violation of factorization since there are no experimental data to compare the predictions of Z+jet with. In order to experimentally investigate those effects, we propose to measure the ratio of the distributions in $\Delta\phi_{Zj}$ for Z+jet- and $\Delta\phi_{12}$ for di-jet production at low and at very high $p_{T,j1}$, and compare the measurements to predictions obtained assuming that factorization holds.

We have studied the matching scale dependence in the PB-TMD predictions and compared it with the case of NLO-matched calculations based on the PYTHIA8 shower. We find that variations of the matching scale lead to more stable predictions in the PB-TMD case, with the relative reduction of the matching scale theoretical uncertainty becoming more pronounced for increasing $p_{T,j1}$ transverse momenta.

TMD multi-jet merging: basic elements and Z + jets results

In Chapters 8 and 9 we have discussed applications of the "matching" approach to combining the PB TMD evolution, implemented in the CASCADE3 event generator described in Chapter 7, with finite-order perturbative matrix elements for hard scattering processes, such as di-jet and Z + jet production. In this chapter we begin the discussion of another approach, the "multi-jet merging" approach, to performing calculations for collider processes based on the PB TMD formalism.

The present chapter is devoted to briefly introduce the basic elements of the TMD multi-jet merging method, which has recently been proposed in the literature, and to illustrate it in the case of the first application which has been examined, the production of Z-boson + jets final states. The next two chapters will be devoted to two new studies of TMD merging, one on multi-jet production and event shapes and one on the merging scale dependence on the physical hard-scattering scale, which are based on original work that has been undertaken in this thesis.

The content of this chapter is as follows. In sections 10.1 and 10.2 we closely follow Refs. [58, 59, 284] to motivate and concisely describe TMD merging. In section 10.3 we present our own TMD-merged calculations for Z + jets production, which reproduce the results of Ref. [58]. In section 10.4 we give a summary.

10.1 Introduction

Final states with large multiplicities of jets constitute some of the most important production channels in high-energy collisions (at the LHC as well as at future colliders), and are used both in precision measurements within the Standard Model and in searches for possible physics signals beyond the Standard Model.

For the last twenty years, theoretical predictions for multi-jet observables have relied on "merging" algorithms to combine matrix-element and parton-shower event generators. Such algorithms have been developed and extensively used initially at LO [104–109, 285–287] and later at NLO [110–115]. A comparison of some of these algorithms can

be found in Ref. [288]. In a calculation based on merging, the matrix elements describe the underlying hard process with bare partons providing the primary sources for widely separated jets; the parton showers describe the evolution of partons by radiative processes predominantly at small angles; the two are sewn together via a "merging scheme" using a merging scale, to prevent double counting or exclusion of multi-jet phase space volumes.

Neither matrix element nor parton shower descriptions are exact: the merging scheme has the purpose of ensuring that, at any given point of phase space, the best possible approximation is used, i.e. either by matrix element or by parton shower contribution. The scheme and its parameters select the approximation to be used and correct the event weight accordingly[1]. The choice of the merging parameters introduces an important theoretical systematic uncertainty, which reflects the mismatch between the matrix-element and parton-shower weights assigned to a given final state. The larger the mismatch, the larger the uncertainty. The phase space regions that are most affected by this are those describing final states for which the jet multiplicity can vary under minor changes of the merging parameters. This mostly happens if a jet is soft or close to another hard jet. A better modeling of the emission probability for such jets by the parton shower evolution would reduce the difference with the weight assigned to these events by the matrix element description, reducing the mismatch and the relative systematic uncertainty.

This has been the motivation of Refs. [58, 59] to consider the TMD Parton Branching method [38, 39] and the associated parton shower [51] (described in Chapters 3 and 7) to devise a TMD multi-jet merging algorithm based on this. The main idea is that, compared to standard collinear merging algorithms, a better treatment of the transverse momentum recoils, that are taken into account by the TMD shower, can influence the theoretical uncertainty associated with merging matrix-element and parton-shower contributions. This method then leads to a reduction of the systematics associated with the dependence of multi-jet cross sections on the merging scale. In the next section a concise description of the method [58, 59] is given.

10.2   Basic elements of the TMD merging method

10.2.1   General concepts

Following Ref. [58], we start by considering general multi-jet events. A matrix element calculation generates n-jet configurations where n represents the number of final state partons. The corresponding $(n+1)$-jet configuration can be generated by a parton shower emission. However, the corresponding accuracy is limited to emissions in the soft and collinear phase space regions. A hard, wide-angle emission from an n-jet configuration will be better described by an $(n+1)$-jet matrix element calculation. The naive sum of the n- and $(n+1)$-jet calculations would not be correct due to regions of the $(n+1)$-jet phase space which would be doubly populated, both by the $(n+1)$-jet matrix elements and by the parton shower emissions off the n-jet configuration. Furthermore the $(n+1)$-jet partial cross section would be unstable, with its value strongly depending on the phase space

---

[1]In some merging schemes, as e.g. the MLM approach, events are either accepted or rejected and event weights of accepted events remain unchanged.

cut which prevents the extra parton from approaching the divergent soft or collinear regions.

As discussed in Ref. [58], the goal of a jet merging algorithm is to enforce exclusivity of the $(n + m)$-jet matrix element calculations above a merging scale $E_{\perp,\text{clus}}$, except for the highest available multiplicity which will remain inclusive. For instance, if the n-jet matrix element configuration is made exclusive, double counting with the $(n + 1)$-jet matrix element configuration will be avoided. This can be achieved by means of the Sudakov form factor which will suppress emissions from the n-jet configuration. When properly applied to the $(n + 1)$-jet matrix element configuration, the Sudakov will also suppress the divergent phase space region, making the partial $(n + 1)$-jet cross section stable.

In order to construct a TMD jet merging algorithm, PB TMD Sudakov form factors (discussed in Chapters 3 and 6) can be used. The inclusion of TMD evolution effects in a merging algorithm is then performed according to the procedure given in the next subsection, which extends the standard MLM algorithm [104–106, 288].

10.2.2 TMD merging algorithm

The TMD merging procedure consists of the following items [58].

1. Generation of matrix elements σ_n with $n = 0, 1, .., N$ real emissions, and generation cut μ_c. The generation cut μ_c gives a lower limit to the emitted partons' transverse momentum. Parton samples are generated by matrix elements, with a probability proportional to the respective cross section.

2. Reweight the strong coupling in the matrix elements according to the values from the corresponding shower history, as prescribed in Ref. [107] and implemented in the MLM algorithm [288].

3. For each of the two initial state partons of a given event, extract values of $\boldsymbol{k}_{\perp,i}$ $(i = 1, 2)$ distributed according to the PB TMD evolution equation, setting the factorization scale to the hard scale of the event. If $\boldsymbol{k}_{\perp,i}^2 \geq \mu_{min}^2$ for any $i = 1, 2$, the event is rejected, and its contribution to the sample cross section is subtracted. μ_{min}^2 corresponds to the minimum energy scale for the event, defined by $\mu_{min}^2 = \min\{q_{\perp,i}^2, q_{\perp,ij}^2\}$ where $i, j = 1, \ldots, n$, $q_{\perp,i}$ is the transverse momentum of parton i, and $q_{\perp,ij}^2$ $(i \neq j)$ is a measure of the relative transverse momentum between partons i, j. The overall kinematics of the final state is reconstructed by including the transverse boost induced by the transverse momentum $\boldsymbol{k} = \boldsymbol{k}_{\perp,1} + \boldsymbol{k}_{\perp,2}$.

4. Initial-state partons of the generated events are showered using the PB TMD backward shower evolution. Final-state partons are showered using the standard PYTHIA [117, 269] or HERWIG [118, 217] showers.

5. The MLM prescription [104, 288] is applied, comparing the jets in showered events to the jets in parton-level events after the $\boldsymbol{k}$ boost. This differs from the standard MLM procedure, where the final state of the parton-level event has no overall transverse momentum. The merging scale $E_{\perp,\text{clus}}$ is a fundamental parameter in

this step, that gives a maximum transverse energy for emitted partons within a jet. The strong condition $E_{\perp,\text{clus}} > \mu_c$ needs to be respected.

In MadGraph5_amc@nlo [55], the generation cut μ_c is set by the xqcut parameter. This defines a minimum in relative transverse momentum $q^2_{\perp,ij}$ between two final state partons i and j:

$$q^2_{\perp,ij} = 2\min\left(q^2_{\perp,i}, q^2_{\perp,j}\right)\left[\cosh(\eta_i - \eta_j) - \cos(\phi_i - \phi_j)\right]. \tag{10.1}$$

The same definition for relative transverse momentum is applied in step 3.

The LO method[2] described above is referred to as the "TMD merging method" [59]. This uses the MLM merging prescription. In the MLM style, the event weights are not changed by a suppression factor, as is done for example in CKKW by the Sudakov form factor. Instead, the parton shower is applied from the hard interaction scale of the event. A jet clustering algorithm (e.g. the anti-k_t algorithm [93]) constructs jets. Jets are defined by a cone size R_{clus}, a minimum transverse energy $E^{\text{clus}}_\perp$ and a maximum pseudo-rapidity $\eta^{\text{clus}}_{\text{max}}$. Partons are then iteratively "matched" onto the jets. If the distance in (η, ϕ) between the parton and the jet centroid is smaller than $c \times R_{\text{clus}}$ ($c = 1.5$ in TMD merging), the parton and the jet match. The event is fully matched if all partons match to jets. If events are not fully matched, they are rejected.

If the maximum jet multiplicity for which matrix elements are calculated is N_{max}, MLM merging requires that the total number of matched jets equals the number of partons for all n-parton samples up to $n = N_{max} - 1$ ("exclusive" multiplicity samples), while extra jets are allowed when $n = N_{max}$, provided they are softer than the jets matched to the original partons ("inclusive" multiplicity sample). If the number of matched jets in exclusive modes does not correspond to the jet multiplicity in the parton-level sample, the event is rejected.

In the next section, we will apply the TMD merging method to the case of Z + jets final states. We will start by analyzing differential jet rates (DJRs) in Z+jets final states. *A DJR is a distribution of the variable $d_{i,i+1}$ that is the square of the energy scale at which an i-jet event is resolved as an $(i + 1)$-jet event.* It requires an infrared safe definition of jets to calculate d_{ij}, which, in this work, is ensured by clustering the events with the k_t jet algorithm [90–92]. The DJR definition has a strong connection to the jet clustering algorithm. In sequential jet clustering like the k_t algorithm, partons are grouped together one-by-one based on a "distance" measure between two partons d_{ij} and one between a parton and the beam direction d_{iB}. Two partons are clustered if $d_{ij} < d_{iB}$, while they belong to different jets when $d_{ij} > d_{iB}$. In the k_t clustering algorithm, these measures are defined by:

$$d_{iB} = q^2_{\perp,i} \tag{10.2}$$

$$d_{ij} = \min(q^2_{\perp,i}, q^2_{\perp,j})\frac{R^2_{ij}}{R^2}, \tag{10.3}$$

where

$$R^2_{ij} = (\eta_i - \eta_j)^2 + (\phi_i - \phi_j)^2, \tag{10.4}$$

and R is the clustering radius. The differential jet rate is equal to d_{ij} in the case that there are $\max(i, j)$ clustered protojets in the event. The condition that all jets have $d_{ij} > d_{iB}$

---

[2]Virtual emissions are not yet included in the TMD merging algorithm.

does not necessarily have to be fulfilled. The DJR is therefore calculated within the jet clustering process.

DJRs have always been considered powerful means to test the consistency and systematic uncertainties of multi-jet merging algorithms [105]. Once DJRs are checked, we will examine jet multiplicity and transverse momentum distributions in Z+jets final states.

10.3 Application of the TMD merging method to Z+jets production

To illustrate the effectiveness of TMD merging, studies from [58] on Z+jets are reproduced which show clearly the effects of merging. Matrix elements containing $Z + 0j$, $1j$, $2j$ and $3j$ samples are generated in LHE format by MADGRAPH5_AMC@NLO [55]. The generation cut is $\mu_c = 16$ GeV, the maximum pseudo-rapidity $\eta_{max} = 5.0$ and a minimum di-lepton mass of $m_{ll}^{\min} = 40$ GeV ensures that most of the events have invariant masses around the Z mass. The collinear PDF for the hard scattering events is the default set provided by MADGRAPH5_AMC@NLO: NNPDF23_lo_as_0130_qed [289].

The transverse momentum from forward evolution is sampled from PB-TMD-set2. The factorization scale μ at which the TMD distribution is evaluated is equal to the center-of-mass energy for Born processes (Z+0j):

$$\mu^2 = \hat{s} = x_a x_b s \tag{10.5}$$

and equals the scalar sum of jet transverse momenta in the case of other matrix element samples (Z+1j, Z+2j, Z+3j):

$$\mu^2 = \frac{1}{2} \sum_{i=1}^{n_{\text{hard}}} q_{\perp,i}^2. \tag{10.6}$$

The LHC center-of-mass energy at time of writing is $\sqrt{s} = 14$ TeV. Analysed data and relevant analyses from earlier runs at lower energies are publicly available. Calculations of Z + jets with TMD merging are compared to measurements at $\sqrt{s} = 8$ and 13 TeV. Measurements of the Z boson transverse momentum spectrum at 8 TeV by ATLAS [290] and at 13 TeV by CMS [136] are compared to the analysed pseudo-data. The jet multiplicity spectra and jet transverse momentum spectra have been extracted from the generated and merged events and compared with measurements by ATLAS at 13 TeV [280]. First, we study differential jet rates in these cases.

10.3.1 Differential Jet Rates

Differential jet rates are calculated from the hard scattering samples of Z + jets at $\sqrt{s} = 13$ TeV. We apply TMD merging with a merging scale of $E_{\perp,\text{clus}} = 23$ GeV, cone radius $R_{\text{clus}} = 1.4$ and maximum pseudo-rapidity $\eta_{\text{clus}} = 5.0$. The results are shown in Fig. 10.1. Events originating from the different matrix element samples are shown in separate curves and the sum of all samples (labeled "TMD merging") is given by the red curve. The

exclusive mode is applied to all matrix element samples containing less than three final state partons. Three jet events are treated inclusively and are allowed by the algorithm to gain additional jets by parton showering. This enables the description of 4- and 5-jet events needed for d_{34} and d_{45}.

The normalized differential cross section is plotted against the logarithm of $\sqrt{d_{i,i+1}}$. The merging scale lies at $\log(\sqrt{d_{ij}}) = 1.36$. At this scale, the transition from parton shower contribution to matrix element contribution is strongly visible in the curves with a sample selection. Jet samples with less than $i + 1$ hard partons have $i + 1$ resolved jets only due to parton shower emissions below the merging scale. Soft emissions from the shower that have a transverse energy above the merging scale namely result in new jets. This generally results in rejection of the event. Hard emissions from the matrix element are limited by the generation cut and do not cause issues in the merging. By choosing too large merging scales, the parton shower will not be able to fill the region below and close to the merging scale properly causing a discontinuity in the sum of jet samples.

10.3.2   Jet multiplicity

The jet multiplicity is calculated according to the analysis of Ref. [280] where the physical jets are clustered with a clustering radius of 0.4, the transverse momentum of the jets is $p_T^j \geq 30$ GeV and the rapidity $|\eta| \leq 2.5$. Jet multiplicity spectra show the abundance of number of jets in the final state. Two resulting distributions are shown in Fig. 10.2 for DY production at $\sqrt{s} = 13$ TeV. The left plot shows the exclusive multiplicity distribution, where only events with exactly N_{jets} jets fill the distribution. The right plot shows the inclusive multiplicity distribution in which each bin is filled with events that at least have N_{jets} jets. In both scenarios, the TMD merging prediction falls within experimental uncertainties in all bins. The TMD merged calculation has no contributions from virtual diagrams, making a scaling factor necessary to normalize the overall distribution to the NNLO cross section. The Monte Carlo predictions are multiplied with a K factor (normalization factor, see Chapter 2) of 1.29 for a normalization to the theoretical NNLO cross Sec. [291].

It is remarkable that, with TMD showering and TMD merging, a maximum multiplicity of three jets in the hard scattering events, much higher jet multiplicities (at least up to seven accompanying jets) can be described accurately.

10.3.3 Z boson transverse momentum

Figure 10.3 shows the data from the ATLAS measurement and two theory calculations for the inclusive p_T spectrum of the di-lepton system at $\sqrt{s} = 8$ TeV. The MC calculations contain different approaches for combining higher order matrix elements with TMDs described in the following two paragraphs.

The blue curve is the result of matching PB-TMD-set2 to a next-to-leading order DY calculation with Herwig6 subtraction terms by MadGraph5_amc@nlo. The matrix elements are inclusive, parton showers and hadronization are not applied for this prediction. The

(a) d_{01}

(b) d_{12}

(c) d_{23}

(d) d_{34}

(e) d_{45}
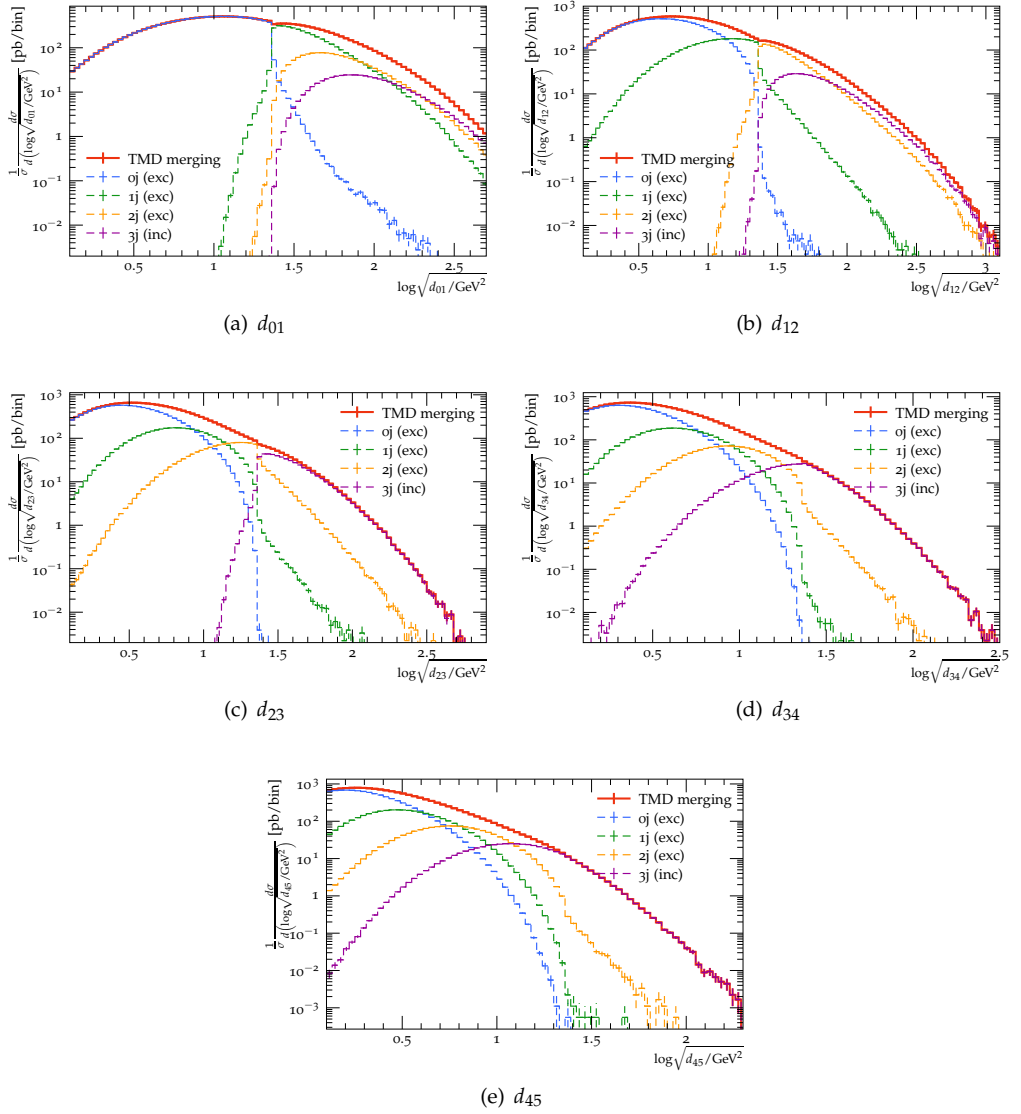
Figure 10.1: Differential jet rates from merging Z+jet samples at $\sqrt{s} = 13$ TeV with TMD and parton showers.
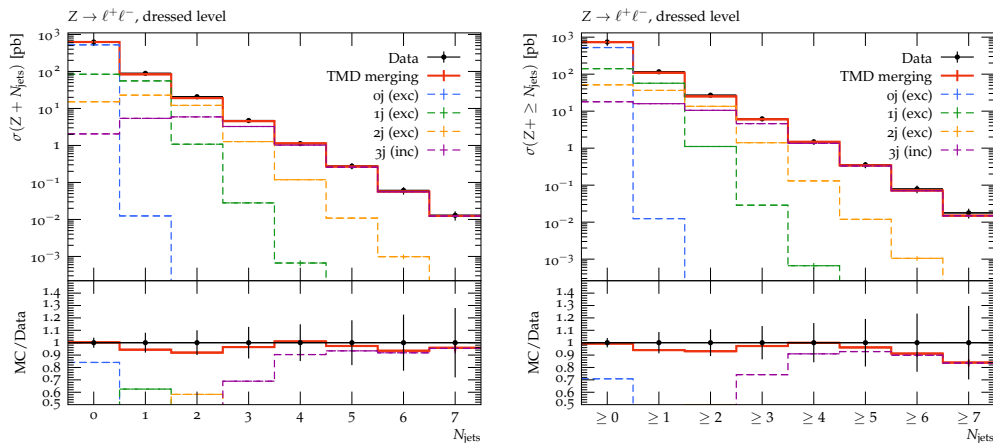
Figure 10.2: Jet multiplicity spectra for Z+jets at $\sqrt{s}$ = 13 TeV in comparison with ATLAS data [280]. Exclusive jet multiplicity is shown on the right plot and the inclusive jet multiplicity is shown on the left. This is a recalculation of results from [58].

matched calculation is performed in the same fashion as the calculations for azimuthal correlations described in Chapters 8 and 9.

The red curve shows the result of TMD merging PB-TMD-set2 to LO matrix elements containing higher jet multiplicities to sample events with DY + 0j, 1j, 2j or 3j. For this prediction, a generation cut μ_c = 16 GeV, merging scale $E_{\perp,\text{clus}}$ = 23 GeV and clustering radius R_{clus} = 1.4 have been applied. The error bars of the merged prediction (red) represent statistical uncertainties (Monte Carlo errors). The uncertainty band of the NLO matched prediction (blue) represents scale uncertainties that are calculated by varying the renormalization and factorization scales by a factor of 2 up and down. This cannot be done in a leading-order calculation because of the lack of $\alpha_s(\mu_R)$ in the matrix element calculation and the only scale in the hard event being the di-lepton mass m_{ll}. Systematic uncertainties due to TMD merging are estimated by varying the merging scale $E_{\perp,\text{clus}}$.

Matching the TMD evolution to fixed NLO cross sections as described in Ref. [36] and applied in Chapters 8 and 9 results in an accurate description of the low-p_T region (1 - 10 GeV) due to the soft-gluon resummation guaranteed by the TMD evolution. The intermediate-p_T region (between 10 and 40 GeV) is well-described due to all $O(\alpha_s)$ contributions in the matrix element and the rejection of double counted events by means of subtraction terms and the MC@NLO method. The high-p_T region cannot be described with an NLO calculation due to missing higher multiplicities of hard parton emissions. Figure 10.3(a) illustrates clearly that at high transverse momentum (p_T^{ll} > 200 GeV), the 2j and 3j samples that are not included at NLO give the largest contribution to the distribution. High precision at high transverse momentum can only be achieved by merging the soft calculation to higher order matrix element calculations. The result of TMD merging in Fig. 10.3(b) shows that the small and intermediate-p_T regions are still well described and that a good description of the high-p_T region is obtained.
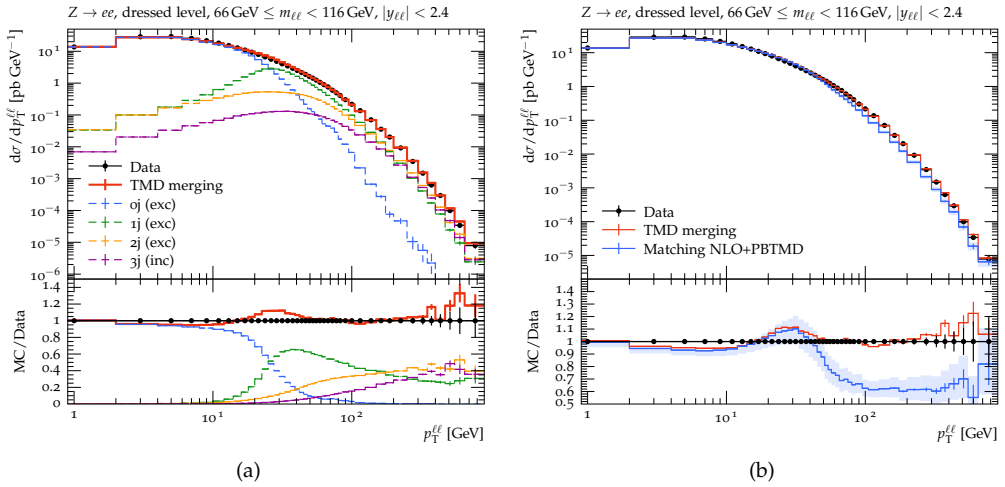
Figure 10.3: MC calculations of transverse momentum spectrum of the di-lepton system in DY production by pp collisions at $\sqrt{s} = 8$ TeV in comparison with ATLAS data [290]. The left plot (a) shows separate contributions of individual ME jet samples to the TMD merging sum (in red). The right plot (b) shows a comparison of TMD merging (red) with PB matching to NLO (blue).

10.3.4 Jet transverse momentum

The same set of TMD merged events are used to extract the transverse momentum of the leading, i.e. hardest, jet. Four jet transverse momentum distributions for different jet multiplicities are shown in Fig. 10.4. Small jet transverse momenta can only be described with the inclusion of resummation, in this case with the PB TMD, but also require inclusion of higher fixed orders in α_s. This is seen from the substantial contributions of multiple jet samples at low p_T^{jet}. A fixed-order calculation would not be sufficient to describe these observables.

10.4   Summary

In this chapter we have introduced the TMD jet merging method [59], and have reproduced the TMD merged results of [58] for Z + jets. The method complements standard algorithms, based on merging samples of different parton multiplicity showered through emissions in the collinear approximation, with the use of PB TMD evolution for the initial state. Compared to standard algorithms, it has been shown in [58] that the method leads to a reduced systematic uncertainty with respect to the merging parameters, and an improved description of high-order emissions, giving a better agreement with experimental measurements for final states with jet multiplicity larger than the largest multiplicity used in the generation of the matrix-element samples.

Having reproduced the results [58] for the case of Z + jets production, in the next chapter we turn to the application of TMD merging to a different process, the production of pure QCD multi-jets, and the computation of multi-jet event shapes.
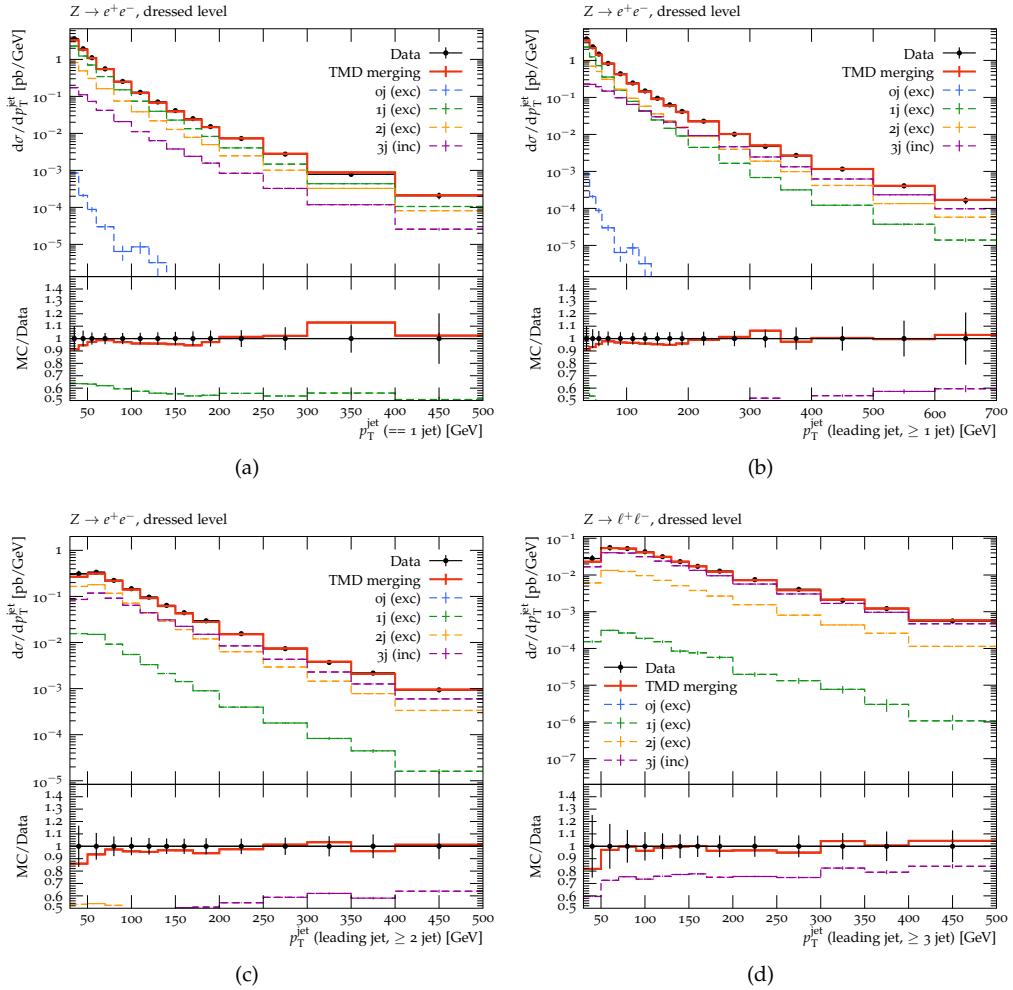
Figure 10.4: Differential cross section of the leading jet transverse momentum in different event selection scenarios in comparison with 13 TeV ATLAS data [280]. (a) exclusively Z plus 1 jet events, (b) Z plus at least one accompanying jet, (c) Z plus at least two accompanying jets, (d) Z plus at least three accompanying jets.

Multi-jet events at the Large Hadron Collider with TMD merging

The case of exclusive Drell-Yan production in the accompaniment of jets has been studied in detail in Ref. [58]. The results have been reproduced and reported in chapter 10. In the DY case, jets are initiated solely by initial-state radiation and there are no color charges in the final state of the leading-order process (i.e., at LO, there are no powers of α_s), which is a great simplification of a fully inclusive description of pp collisions. In practice at hadron colliders, a large fraction of the events have final states consisting purely of hadronic matter only. A substantial fraction of these final states are produced by strong interactions alone. It is this category of processes that is of interest in this chapter.

The leading order process with two incoming and two outgoing partons, called the "Born level" process, is the di-jet scenario. One of the possible Feynman diagrams of this leading order hard scattering process is shown in Fig. 11.1 where two quarks annihilate and produce a new quark-antiquark pair that radiates and hadronizes into jets. For the first time, the PB TMD evolution is studied at the multi-jet level. We have calculated jet multiplicity spectra and jet transverse momenta as well as event shapes; distributions that describe the energy flow of the jets in the final state. These studies are important because of their high frequency at hadron colliders and the need for more precision.
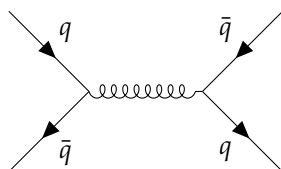
Figure 11.1: Leading order diagram of di-jet production from quark-antiquark annihilation.

In this chapter[1] we present original TMD merging results for pure QCD multi-jet events at the LHC. The structure in which this is presented is as follows. Section 11.1 describes the setup of the calculations performed. As a cross-check and validation of the method,

---

[1]This work is based on a paper in preparation A. Bermudez Martinez, F. Hautmann, A. M. van Kampen, *"Multi-jets from TMD merging"* [60]

we show in Sec. 11.2 extracted differential jet rates for two investigated scenarios. Sections 11.3 and 11.4 concern multi-jet processes at $\sqrt{s}$ = 7 TeV, while section 11.5 focuses only on multi-jet production at $\sqrt{s}$ = 13 TeV. Important standard multi-jet observables include jet multiplicities and transverse momenta, which are presented in Sec. 11.3. This section also includes a study of the TMD merging systematic uncertainties in the description of multi-jet production as well. Section 11.4 elaborates on a comparison of the obtained TMD merging calculations with results that are obtained by the MLM merging algorithm that is implemented in Pythia8 [116, 117] . Studies with Pythia8 have allowed studies of the effect of the underlying event in these processes, which are also presented in this section. We have calculated and studied hadronic event shapes at the LHC at $\sqrt{s}$ = 13 TeV with TMD merging for the first time. These results are given in Sec. 11.5. Finally, conclusions are given in Sec. 11.6.

11.1   Technical setup of the calculations

In Refs. [292] and [293] multi-jet events at the ATLAS detector were studied at center-of-mass energies of $\sqrt{s}$ = 7 TeV and $\sqrt{s}$ = 13 TeV, respectively.

The 7 TeV studies select events where the physically measured jets have transverse momenta $p_{\perp,j} \geq 60.0$ GeV, the leading jets have $p_{\perp,j1} \geq 80.0$ GeV and the rapidity of the jets is $|\eta| < 2.8$.

At 13 TeV, all jets are required to have transverse momenta $p_{\perp,j} \geq 100.0$ GeV. Furthermore, only events with leading jet transverse momenta of $p_{\perp,j1} \geq 460.0$ GeV are selected and the scalar sum of the transverse momenta of the two leading jets, $H_{T2} = |\vec{p}_{\perp,j1}| + |\vec{p}_{\perp,j2}|$, must be $H_{T2} \geq 1000.0$ GeV. Here the rapidity of the jets is $|\eta| < 2.4$.

These kinematical cuts in the measurement are crucial for the generation parameters and the merging scales.

11.1.1   Matrix elements

Calculations of jet observables with TMD merging require the generation of on-shell, leading-order matrix elements. Hard scattering multi-jet events are produced with Mad-Graph5_amc@nlo [55] in LHE format. In these processes, partons from each incoming proton interact through the strong interaction to form at least two jets in the final state:

$$p_1 + p_2 \rightarrow j + j + X, \tag{11.1}$$

with X representing zero, one or two hard, real parton emissions. The 4-jet samples are treated inclusively. Real higher order emissions are generated by initial state radiation, final state radiation or a combination of both.

To compare predictions with measurements at both center-of-mass energies, two sets of hard scattering events are required. The generation parameters, which that allow to fill the whole measured phase space, are as follows:

- **Di-jets + 0, 1, 2 jets at $\sqrt{s} = 7.0$ TeV**

    - Generation cut: $\mu_c = 20.0$ GeV
    - Jet transverse momenta: $p_{\perp,j} \geq 20.0$ GeV
    - Leading jet transverse momentum: $p_{\perp,j1} \geq 70.0$ GeV
    - Second leading jet transverse momentum: $p_{\perp,j2} \geq 50.0$ GeV
    - Maximum jet rapidity $|\eta_{\max}| = 3.2$
    - PDF: NNPDF2.3_LO_as0130

- **Di-jets + 0, 1, 2 jets at $\sqrt{s} = 13.0$ TeV**

    - Generation cut: $\mu_c = 50.0$ GeV
    - Jet transverse momenta: $p_{\perp,j} \geq 50.0$ GeV
    - Sum of transverse momenta of two leading jets: $H_{T2} \geq 800.0$ GeV
    - Maximum jet rapidity $|\eta_{\max}| = 2.8$
    - PDF: NNPDF3.1_NLO_as0118

The generation cuts are large compared to the Z+jets situation because the physically measured jets in the current measurements have larger transverse momenta compared to the physical jets in the DY case described in Chapter 10.

We have observed that the generation cut `xqcut` in MadGraph5_amc@nlo is a matrix element cut that was not applied by the original MLM merging approach. This parameter sets a lower bound on the relative transverse momentum $k_{\perp,ij}$ given in Eq. (10.1), which combines the absolute parton momenta and the angular distance. The combination of this generation cut and the merging parameters could lead to gaps in the phase space or to false rejections of events. We have tested the differences between applying `xqcut` and the original MLM parameters $p_T^{\min}$ and $R_{\min}$ and found that the differences are negligible.

11.1.2 TMD merging of multi-jet events

The procedure of Cascade3 to treat the multi-jet hard scattering events differs from that of the Z+jets scenario as described in section 10.3. In the multi-jet scenario, the factorization scale μ^2 at which PB-TMD-NLO-HERAI+II-2018-set2 (PB-TMD-Set2) is probed is equal to the scalar sum of the transverse momenta of the final state partons i:

$$\mu^2 = \frac{1}{2} \sum_{i=1}^{n} q_{\perp,i}^2. \tag{11.2}$$

Initial state and final state radiation are applied by the PB TMD initial state backward evolution described in Chapter 7 and the PYTHIA6 final state shower, respectively. In addition to these parton showers, time-like initial state splittings are applied. The effect of this type of splittings is smaller than the statistical uncertainties.

The merging parameters that work well for the multi-jet events are the following:

- **Di-jets + 0, 1, 2 jets at $\sqrt{s} = 7$ TeV**

  – Merging scale $E_{\perp,\mathrm{clus}} = 35.0$ GeV

  – Clustering radius $R_{\mathrm{clus}} = 0.7$

  – Maximum pseudorapidity $\eta_{\mathrm{clus,max}} = 3.2$

- **Di-jets + 0, 1, 2 jets at $\sqrt{s} = 13$ TeV**

  – Merging scale $E_{\perp,\mathrm{clus}} = 65.0$ GeV

  – Clustering radius $R_{\mathrm{clus}} = 0.7$

  – Maximum pseudorapidity $\eta_{\mathrm{clus,max}} = 2.8$

The merging scales are larger than those in the Z+jets scenario because of the larger generation cuts μ_c (and the condition $E_{\perp,\mathrm{clus}} > \mu_c$). Note also that the clustering radius in these pure jet scenarios is half of the clustering radius used for the Z+jets scenario. The merging of multi-jet events with high-$p_\perp$ jets is most effective when jets are required to be narrower than in the DY case.

After showering and merging, Cascade3 hadronizes the remaining events for color-neutral and observable final states.

11.1.3 Analyses

Showered and merged events in HEPMC format [81] are analyzed with Rivet3 [82, 83] identical to the analyses of data from ATLAS measurements at $\sqrt{s} = 7$ TeV [292] and $\sqrt{s} = 13$ TeV [293]. For the analyses, the jets in the showered, merged and hadronized events are clustered with the anti-k_t jet clustering algorithm [93] in FastJet [270] with a jet cone resolution parameter $R = 0.4$. The analyses have identical kinematic boundaries to the measurement cuts.

11.2 Differential Jet Rates

A crucial check on the reliability of merged events is to calculate DJRs (described in Sec. 10.2). Discontinuities in these distributions could indicate missing phase space or the double population of phase space regions. The results in this section are obtained at partonic level; no hadronization has been applied to the HEPMC events for the purpose of calculating DJRs. FastJet clusters showered events into jets using the k_t jet clustering algorithm [91, 92] with a jet cone radius of $R = 0.6$.

11.2.1 DJRs at $\sqrt{s} = 7$ TeV

Three differential jet rate distributions of the multi-jet events at $\sqrt{s} = 7$ TeV are shown in Fig. 11.2 together with the contributions from all matrix element samples. The two

leading jets are part of the Born level process causing d_{01} and d_{12} not to be relevant for observing merging effects.

With the merging parameters from Sec. 11.1.2, no discontinuities are observed in the relevant DJRs d_{23}, d_{34} and d_{45}. The dominant contributions of parton shower emissions and matrix element emissions are visible in Figs. 11.2(a) and 11.2(b).

(a) (b)

(c)

Figure 11.2: Differential jet rates of TMD merged multi-jet samples at $\sqrt{s} = 7$ TeV, with a generation cut at $\mu_c = 20$ GeV and a merging scale at $\log(E_{\perp,\text{clus}}/\text{GeV}) = \log(35) = 1.54$.

11.2.1.1 Systematic uncertainties

Systematic uncertainties can be estimated by varying the merging scale. In the logarithmic scale of the horizontal axis, the three merging scales have $\log(E_{\perp,\text{clus}}/\text{GeV})$ values of 1.48, 1.54, and 1.60. In Fig. 11.3 we show the effect of varying the merging scale by 5 GeV up and down (corresponding to a variation of more than 10%) on the distributions. The results show that varying the merging scale leads to small differences that are localized near the merging scale region itself. The fluctuations in the outer regions of the DJRs are due to low statistics in these phase-space regions. The statistical errors generally overlap in these regions.
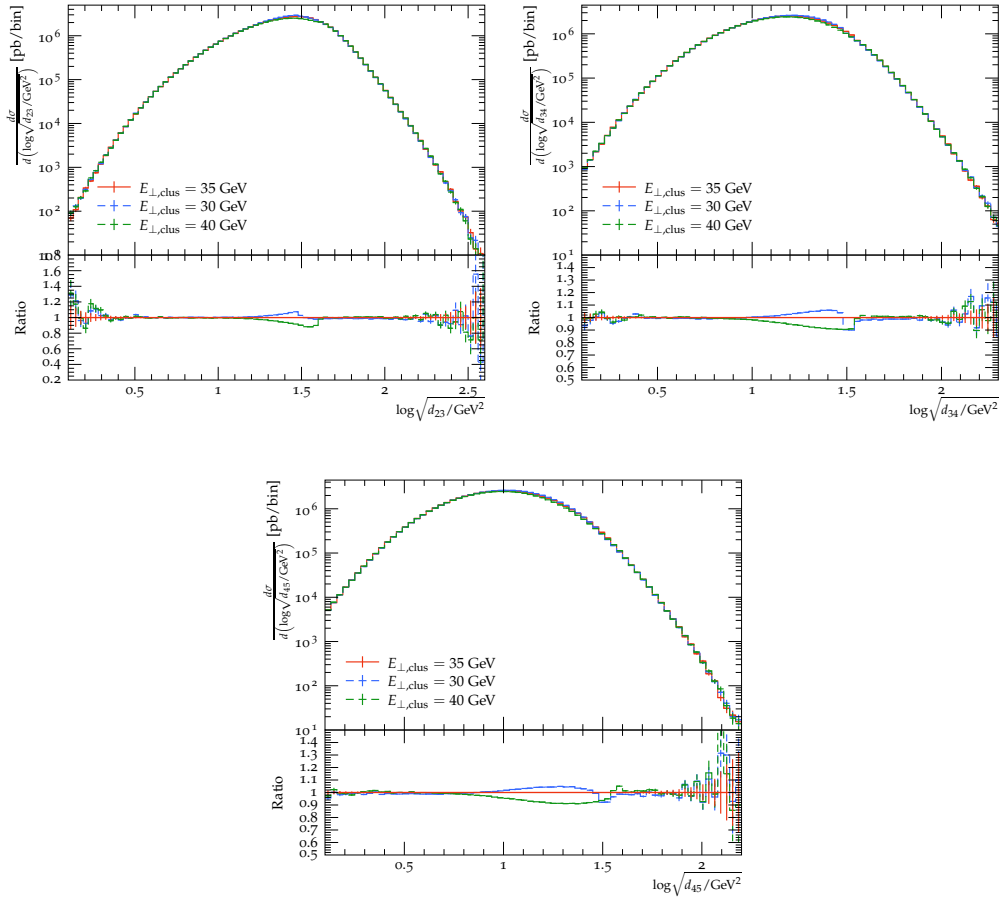
Figure 11.3: Differential jet rates with three merging scales for TMD merging of multi-jet samples at $\sqrt{s}$ = 7 TeV.

11.2.2   DJRs at $\sqrt{s}$ = 13 TeV

Fig. 11.4 shows d_{23}, d_{34} and d_{45} from TMD merging of the second set of hard scattering events at $\sqrt{s}$ = 13 TeV (described in Sec. 11.1). The DJRs are smooth, but a little kink is observed near the merging scale. Clearly, the merging of these highly energetic jets to TMDs and TMD parton showers is not trivial. Other merging scales around the current value have been tested and show similar behavior in the DJRs. The overall shape of the DJRs is effectively not disrupted by this.

11.3   **Jet-multiplicities and jet transverse momenta**

Pure multi-jet events are complex event types that involve many different scales. In DY events, some observables are well understood, such as the invariant di-lepton mass
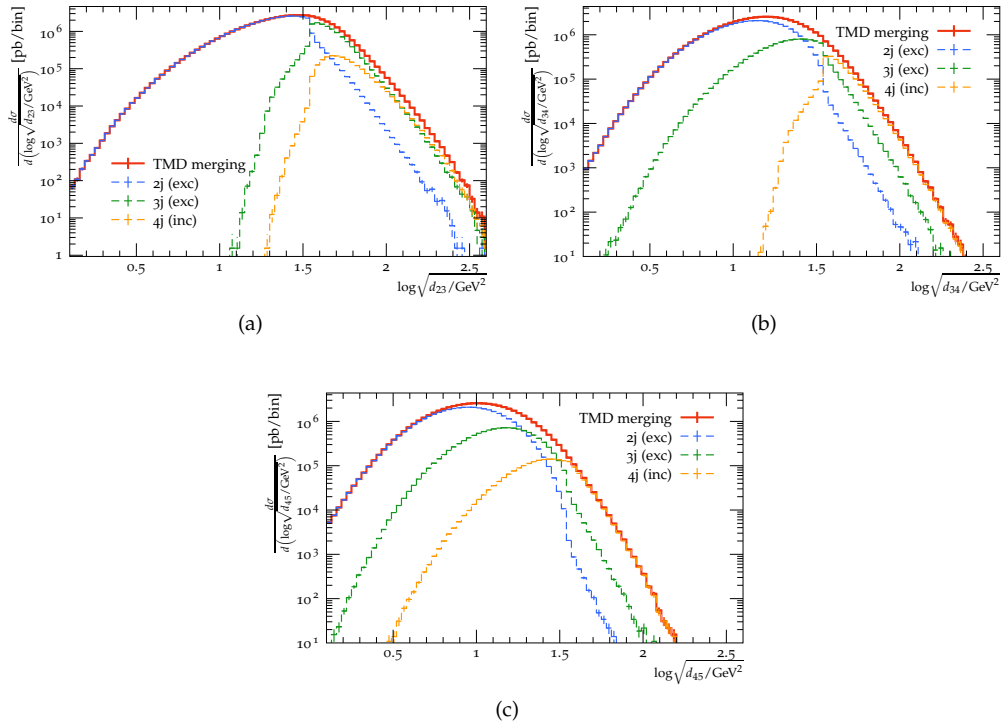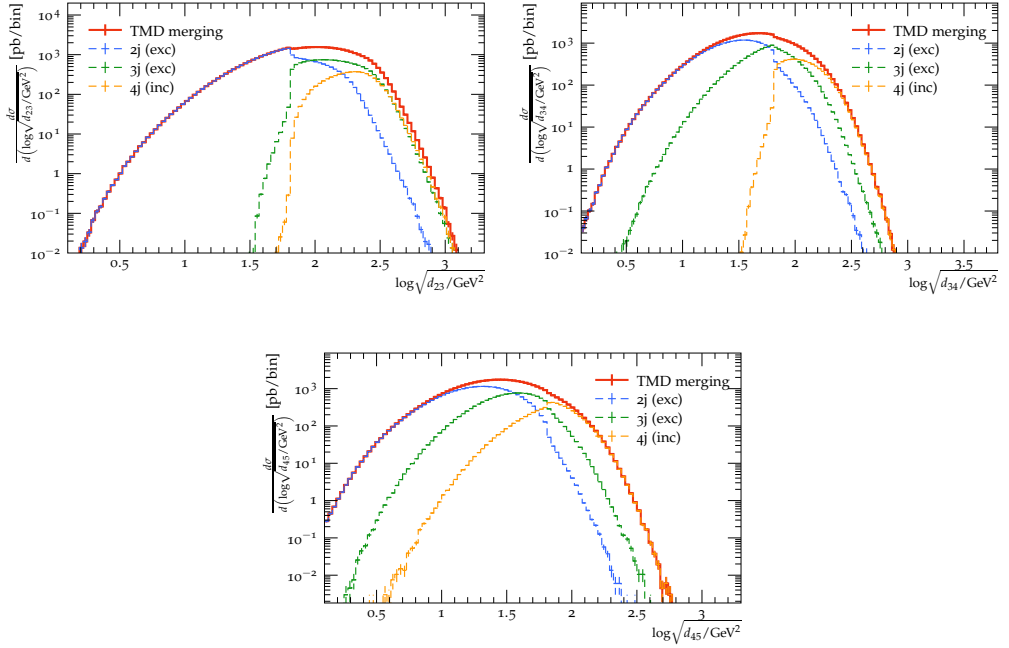
Figure 11.4: Differential jet rates of TMD merged multi-jet samples at $\sqrt{s}$ = 13 TeV, with a generation cut μ_c = 50 GeV and a merging scale $\log(E_{\perp,\text{clus}}/\text{GeV}) = \log(65) = 1.81$.

distribution m_{ll} and the transverse momentum p_T^{ll}. In multi-jet events, analogues of these quantities would be jet masses m_j, jet transverse momenta $p_{\perp,j}$, or scalar sums of jet transverse momenta H_T. However, since jets are bunches of hadrons formed by soft and collinear colored radiation, the predictability of such observables is much lower than for clean signal events such as resonance decays into leptons.

In this section we present calculations with TMD merging of jet multiplicity and jet transverse momentum spectra. With the change in cross sections due to merging scale variations, we show that TMD merging gives reasonably small systematic uncertainties.

11.3.1 Jet-multiplicity spectrum

Calculations of the jet multiplicity spectra at both center-of-mass energies and comparisons with data provide a second solid check of the TMD merging method. Of particular interest is the calculation of jet multiplicities beyond the inclusive multiplicity of the matrix element N_{max}. In both sets of multi-jet hard scattering events, $N_{max} = 4$.

Figure 11.5 shows jet multiplicity spectra calculated with TMD merging. Since TMD merging is applied at LO, total cross section scaling (K) factors are required. In the $\sqrt{s}$ = 7 TeV scenario the scaling factor is 1.28, for $\sqrt{s}$ = 13 TeV the scaling factor is 1.53.

The sum of all samples in red describes the data well for all jet multiplicities up to $N_{\text{jet}} = 6$.
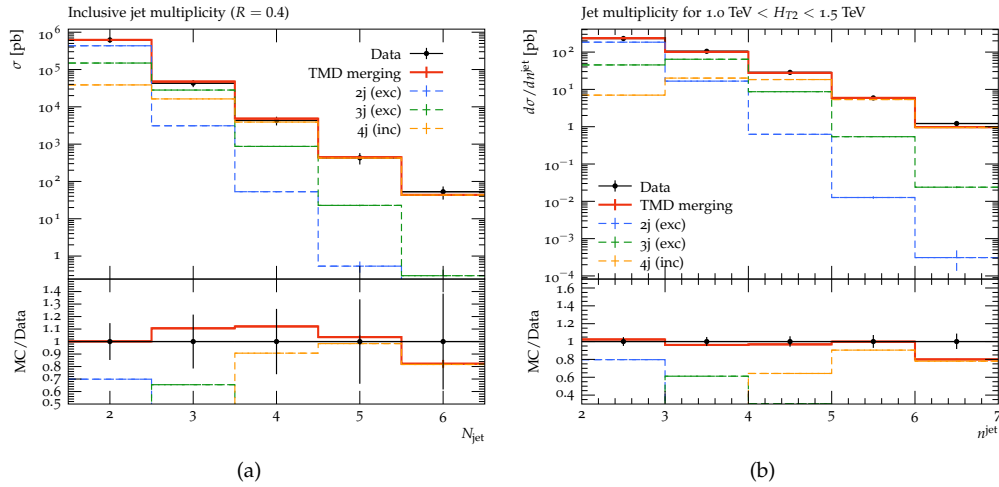
Figure 11.5: Jet multiplicity spectra for multi-jet events merged with TMD merging for different kinematic regimes. (a) $\sqrt{s}$ = 7 TeV, data and analysis from [292], (b) $\sqrt{s}$ = 13 TeV, data and analysis from [293].

11.3.2   Jet transverse momentum spectra

Individual jet transverse momenta $p_{\perp,j} = \sqrt{\vec{p}_{\perp,j}^2}$ are formed primarily by hard parton emissions in the matrix element. This observable is closely related to the branching scale of the partons, similar to the association of the evolution scale with the emitted transverse momentum of the partons via the angular ordering condition. Transverse momentum recoils and radiation of wide angle parton emissions can cause this initial transverse momentum to change in the shower process.

The transverse momentum distributions of the four hardest jets are calculated from the events at $\sqrt{s}$ = 7 TeV and the results are shown in Fig. 11.6. Although the four hardest emissions are included in the matrix elements, the final jet transverse momentum is influenced by the transverse TMD boost, which implements soft and collinear parton emission recoils. Parton showers follow the dynamics of the TMD and generate the explicit soft parton radiation within the jet cones.

Since the leading and subleading jets come from the Born level process ($qq \rightarrow g \rightarrow jj$), only the TMD boost and the final state shower affect their $p_\perp$ distributions. The third and fourth jets come from higher order emissions from any leg. The analysis and data from ATLAS require that all jets have $p_{\perp,j} \geq 60$ GeV. In addition, only events where the leading jet has a transverse momentum $p_{\perp,j1} \geq 80$ GeV are selected. Because of these analysis selection criteria, it is valid to have matrix elements with $p_{\perp,j1} \geq 70$ GeV and $p_{\perp,j2} \geq 50$ GeV. The lower value of the transverse momentum in all plots of Fig. 11.6 corresponds to that of the analysis cuts.

The result of the third jet $p_\perp$ fluctuates the most and statistical uncertainties are not as large as the observed fluctuations. This observable is complicated because it is the first higher order contribution to the Born process. Shower contributions to the third leading

jet occur at large scales. Relatively hard, wide-angle emissions would quickly lead to additional jets in the analysis where $R = 0.4$. Predictions fall within the experimental uncertainties in nearly all bins.

(a) Leading jet $p_\perp$

(b) Subleading jet $p_\perp$

(c) Third jet $p_\perp$

(d) Fourth jet $p_\perp$
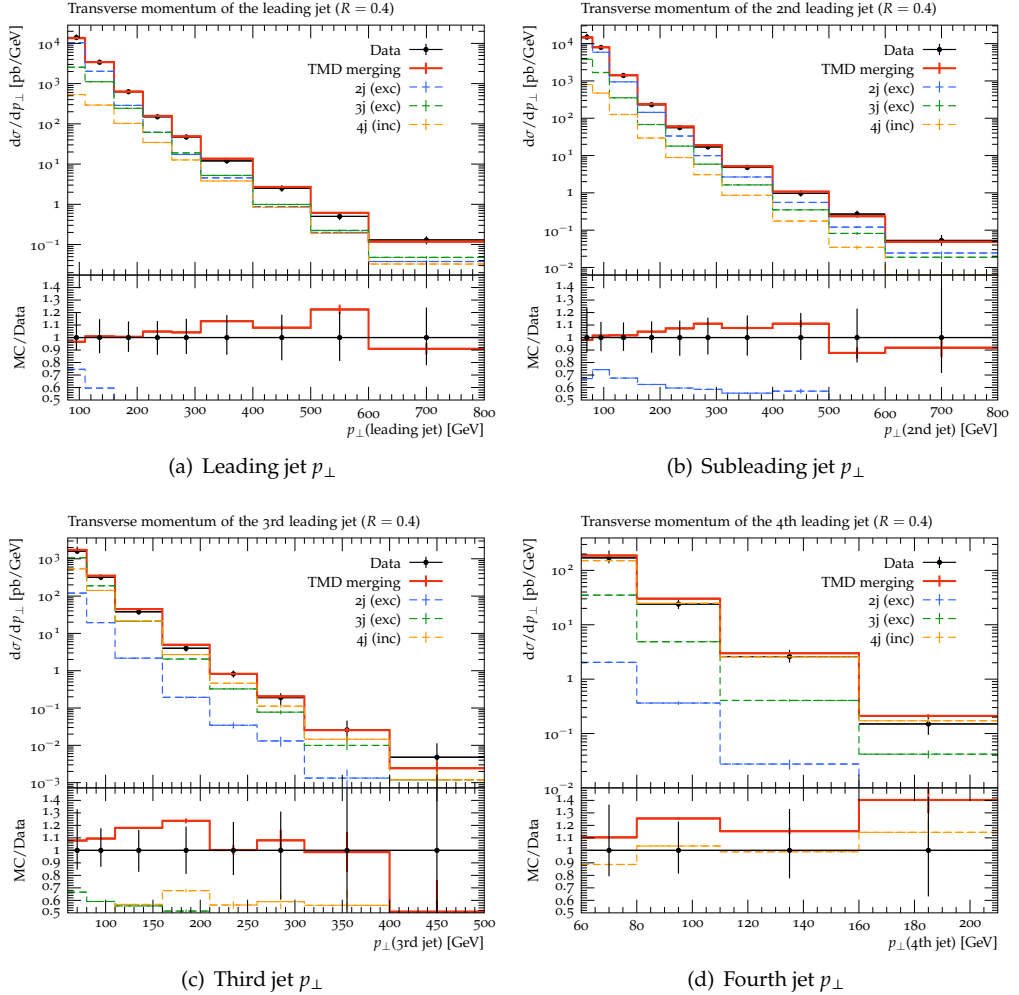
Figure 11.6: Transverse momentum spectra of four leading jets in pure jet events at $\sqrt{s} = 7$ TeV merged with TMD merging. Comparison to data from [292].

11.3.3 TMD merging systematics

As mentioned in Chapter 10, transverse momentum recoils in parton evolution affect the theoretical systematics. Here we show that the systematic uncertainties arising from TMD merging in the case of multi-jet events are small (in Ref. [59] it was already shown that the systematics of TMD merging in Z+jets are small).

Varying the merging scale gives a reliable estimate of the uncertainties arising from merging (in the same way as varying the factorization and renormalization scales gives

estimates of the systematics). Variations of 5 GeV up and down are performed with
respect to the previously applied value of $E_{\perp,\mathrm{clus}} = 35$ GeV. The systematic uncertainty is
then represented by the relative difference between the values of the cross section as:

$$\text{Syst. unc.} = \frac{\left| \sigma(E_{\perp,\mathrm{clus}}^{(-)}) - \sigma(E_{\perp,\mathrm{clus}}^{(+)}) \right|}{\frac{1}{2} \left(\sigma(E_{\perp,\mathrm{clus}}^{(-)}) + \sigma(E_{\perp,\mathrm{clus}}^{(+)}) \right)} \ , \tag{11.3}$$

where $E_{\perp,\mathrm{clus}}^{(\pm)}$ represents the upward (+) and downward (-) variations of the merging
scale. The cross sections for four inclusive jet multiplicities at a center-of-mass energy
of $\sqrt{s} = 7$ TeV are given in Tab. 11.1 for the two variations of the merging scale. The
systematic uncertainties given in the bottom row are less than 2%.

Merging scale [GeV]	$\sigma[\text{tot}]$ [nb]	$\sigma[\geq 3 \text{ jet}]$ [nb]	$\sigma[\geq 4 \text{ jet}]$ [nb]	$\sigma[\geq 5 \text{ jet}]$ [nb]	$\sigma[\geq 6 \text{ jet}]$ [nb]
30.0	519.0	40.24	4.115	0.381	0.031
40.0	517.6	40.76	4.100	0.381	0.030
Syst. unc. (%)	0.28	1.30	0.38	0.09	4.04

Table 11.1: Inclusive cross sections of pure jets events at 7 TeV with TMD merging. The clustering
radius is fixed at $R_{\mathrm{clus}} = 0.7$.

The result of varying the merging scale on the jet transverse momentum spectra is shown
in Fig. 11.7. The Monte Carlo errors that are shown in this figure overlap, indicating that
the systematic uncertainty is smaller than the statistical uncertainty. No K factors have
been applied to these curves.
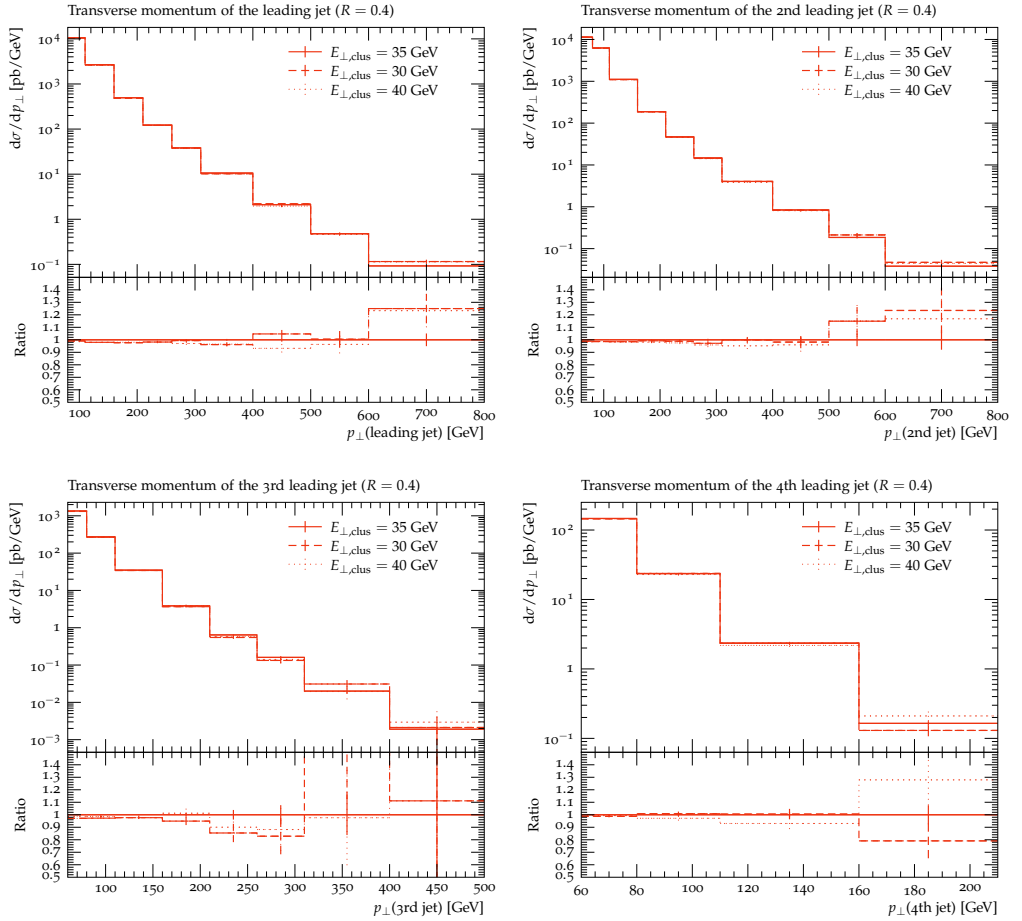
Figure 11.7: Estimation of TMD merging systematics by varying the merging scale in jet transverse momenta. The solid curve is the main TMD merging result presented before. The dashed and dotted curves are obtained by variations of the merging scale.

11.4   Comparison of TMD merging with collinear merging

We compare the results of TMD merging of multi-jet events with the results of collinear MLM merging [104–106, 288]. For this purpose, Pythia8 [116, 117] is used for MLM merging. Hard scattering events generated for TMD merging (with the generation cuts given in Sec. 11.1) are also used for showering and MLM merging with Pythia8. The merging parameters are kept the same (as in Sec. 11.1.2), the merging scale is $E_{\perp,\text{clus}} = 35$ GeV. Since the MLM merging calculation also deals with the LO matrix elements, a scaling factor is calculated according to the total cross section with respect to the data. This results in a scaling factor of 1.38 for MLM merging predictions and 1.28 for TMD merging predictions.

Figure 11.8 shows the inclusive jet multiplicity spectrum N_{jet}. Since this observable is not sensitive to TMD effects, it serves well as a cross check for both merging methods. The first bin represents the total cross section (hence both predictions fall exactly together with the data point due to the scaling factors applied).
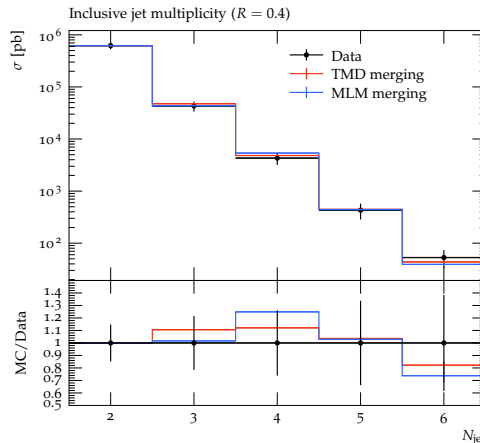
Figure 11.8: Inclusive jet-multiplicity calculated with TMD merging (in Cascade3) and MLM merging (in Pythia8).

Figure 11.9 shows curves for jet transverse momenta by TMD merging in red and curves from MLM merging in blue. These comparisons are made without simulating multiple partonic interactions (MPI). Both predictions describe the data quite well and are within experimental uncertainties for the vast majority of transverse momenta. It is noteworthy that the shape of the MLM prediction is slightly more off than the shape of the TMD merging. The statistical errors of the MLM prediction are generally larger than those of the TMD merging calculations. This could be the result of more event rejections in the merging algorithm.

The differences cannot be attributed to TMD effects alone, since both the initial and final parton showers of Pythia8 differ from those of Cascade3. The showers differ in the ordering of the branching scales: the applied parton showers of Pythia8 are p_T-ordered dipole showers.
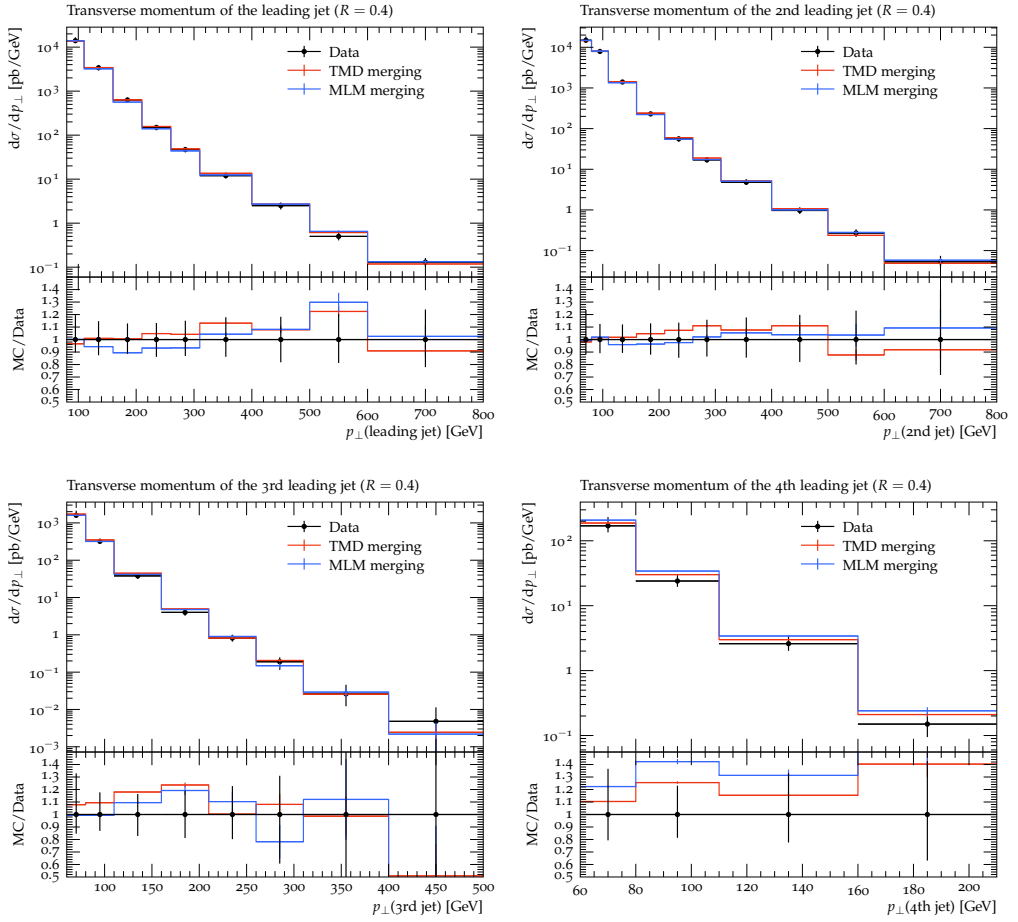
Figure 11.9: Jet transverse momenta at $\sqrt{s}$ = 7 TeV with TMD merging (by Cascade3) and MLM merging (by Pythia8).

11.4.1 Systematics

It is of interest to compare the systematics of TMD merging with that of collinear merging. For this purpose, the merging scale was varied in the MLM calculation and the systematic uncertainty was calculated as in Eq. (11.3). The results of the inclusive jet cross sections and systematic uncertainties are given in Tab. 11.2. The total cross section differs by more than 10%, while the uncertainty on the total cross section with TMD merging is less than 1%. Inclusive cross sections from MLM at a selection of higher jet multiplicities have larger systematic uncertainties compared to TMD merging.

To compare the systematics of MLM merging and TMD merging, a comparison of the subfigures 11.10(a) and 11.10(b) shows the systematics in the jet multiplicity spectrum. This is done by comparing the tables 11.1 and 11.2. We also consider systematics in the jet $p_\perp$-spectra by comparing Fig. 11.11 with Fig. 11.7. The systematics of MLM merging in the $p_\perp$-spectra are smaller than 10% in most bins. Strikingly, at low $p_\perp$ the curves differ

Merging scale [GeV]	σ[tot] [nb]	$\sigma[\geq 3$ jet] [nb]	$\sigma[\geq 4$ jet] [nb]	$\sigma[\geq 5$ jet] [nb]	$\sigma[\geq 6$ jet] [nb]
30.0	443.8	34.10	4.202	0.357	0.030
40.0	512.7	37.48	4.263	0.362	0.031
Syst. unc. (%)	14.41	9.46	1.45	1.26	2.28

Table 11.2: Inclusive cross sections of pure jets events at 7 TeV with MLM merging. The clustering radius is fixed at $R_{\text{clus}} = 0.7$.

(a) TMD merging
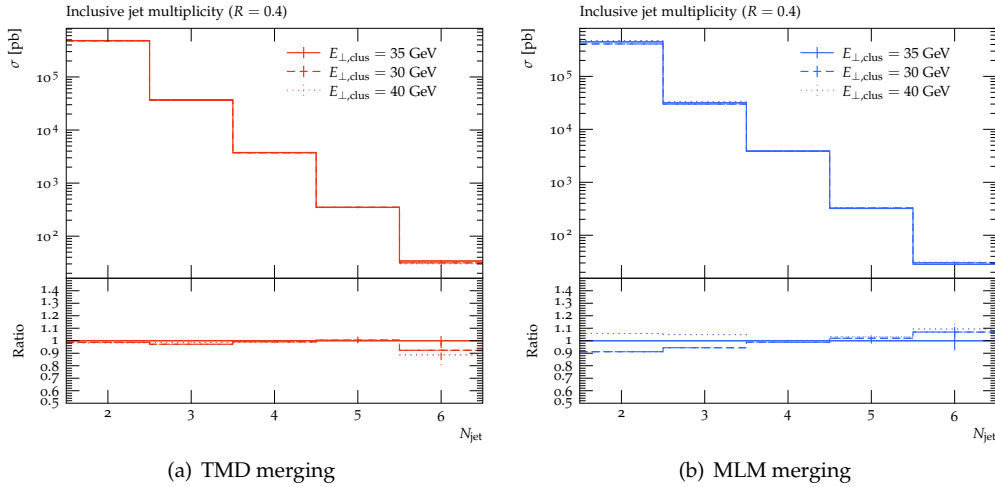
(b) MLM merging

Figure 11.10: Systematics of TMD merging and MLM merging in the inclusive jet-multiplicity spectrum with $R_{\text{clus}} = 0.7$.

most and statistical errors do not overlap. This effect is not seen in the TMD merging (Fig. 11.7), where at small $p_\perp$ the different curves are very similar.

11.4.2   Effect of the underlying event

In PYTHIA8 it is possible to include effects of the underlying event by modeling multiple parton interactions (MPI). We have investigated whether this significantly affects the result by MLM merging as shown in Fig. 11.9. Figure 11.12 shows the jet momentum spectra with MLM merging calculations with and without the MPI model from PYTHIA8. Note that MPI in PYTHIA8 is interleaved (i.e. run in parallel) with ISR and FSR, which can influence the merging procedure. The merging parameters in both calculations are the same, so the blue curves correspond to the blue curves in Fig. 11.9. No significant difference due to MPI is observed, since the statistical errors of the two results generally overlap.
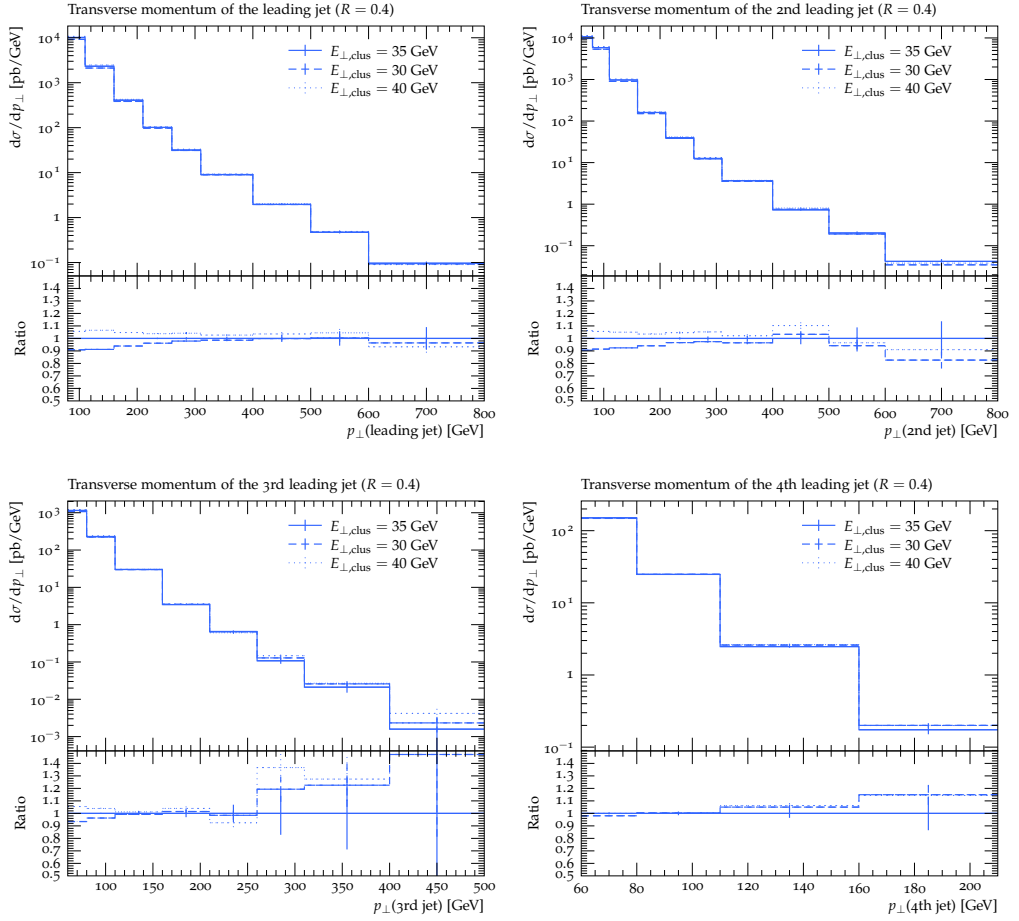
Figure 11.11: Systematics of MLM merging with Pythia8 in jet transverse momentum spectra with $R_{\text{clus}} = 0.7$.
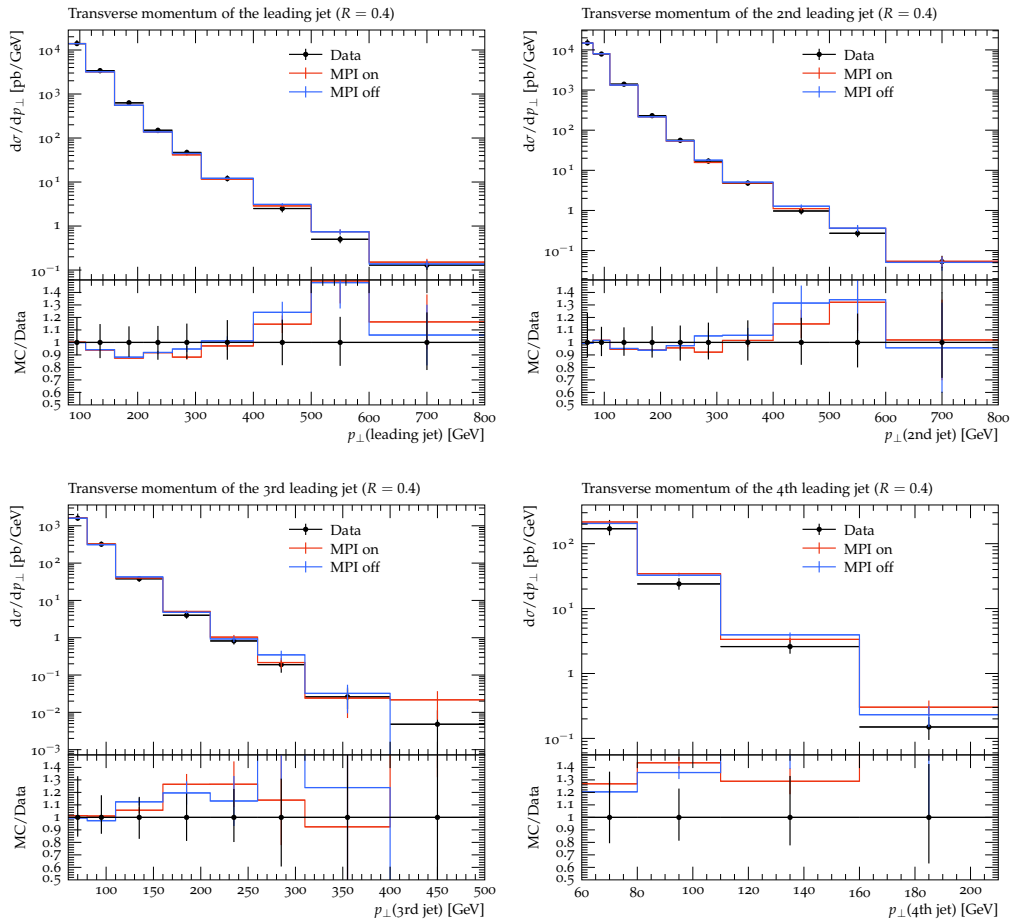
Figure 11.12: Effect of MPI in combination with MLM merging with PYTHIA8 for jet transverse momentum spectra.

11.5 Multi-jet event shapes

Event shapes are observables that represent the spatial distributions of jet energies in an event, sensitive to all final state particles of an event. Event shapes are infrared and collinear safe and should therefore be computable using Monte Carlo event generator techniques. Both hard emissions and multiple soft-gluon emissions are crucial for a complete description of the event shapes. Reliable predictions require a proper merging procedure of matrix element calculations and parton showers. In general, low values of event shapes correspond to di-jet-like configurations. In these regions, collinear and soft radiation need to be resummed. Large values of the event shapes are dominated by hard, well-separated jets [294] and can be described by fixed-order calculations.

The event shape distributions are defined only for a fixed jet multiplicity, since the shapes change greatly with the number of jets in an event. All event shapes vanish in the di-jet scenario due to the back-to-back configuration. Therefore, only events with three or more jets are of interest[2].

Recently, event shapes from pp collisions at $\sqrt{s} = 13$ TeV have been measured by ATLAS and the results presented in Ref. [293]. Six event shapes were measured in three different regions of H_{T2} (the scalar sum of the transverse momentum of two leading jets). This section is devoted to studies of the application of PB and TMD merging and the extraction of event shapes from multi-jet events. Forward evolution with PB-TMD-Set2 and backward evolution with showers from Cascade3 have been combined with the multi-jet matrix elements at 13 TeV (described in Sec. 11.1) by TMD merging with $E_{\perp,\text{clus}} = 65$ GeV. The event shapes are then extracted from the analyses in Ref. [293] using their Rivet plugin.

In this section, we show results of event shape calculations with TMD merging and for comparison we also insert the figures with results from general purpose Monte Carlo (GPMC) event generators given in [293]. A selection criterion to the phase space based on the scalar sum of leading jet transverse momenta is given by 1 TeV $< H_{T2} < 1.5$ TeV. With a lower cut on H_{T2} of 800 GeV in the generation of hard scattering events, there is a margin to avoid cutting in the analyzed phase space region.

11.5.1 Transverse thrust and thrust minor

The first type of event shape examined is that of projections of parton transverse momenta $\vec{q}_{\perp,i}$ onto the thrust axis. The thrust axis $\hat{n}_T$ is a unit vector in the direction for which the projections of all jet momenta are maximized. Two observables are constructed with the thrust axis: (i) the transverse thrust $\tau_\perp = 1 - T_\perp$ by a scalar product of parton momenta with the thrust axis and (ii) the thrust minor T_m by a cross product of parton momenta with the thrust axis:

$$\tau_\perp = 1 - T_\perp = 1 - \frac{\sum_i |\vec{q}_{\perp,i} \cdot \hat{n}_T|}{\sum_i |\vec{q}_{\perp,i}|} \qquad (11.4)$$

$$T_m = \frac{\sum_i |\vec{q}_{\perp,i} \times \hat{n}_T|}{\sum_i |\vec{q}_{\perp,i}|}, \qquad (11.5)$$

---

[2]This concerns showered events; the Born level events with two hard emissions can still contribute at higher multiplicities.

with the summation over all n final state partons. These observables provide information about the distribution of the jets in space. The transverse thrust $\tau_\perp$ becomes large (the maximum value is $1 - 2/\pi$ [293]) when the energy flow orthogonal to $\hat{n}_T$ increases and is small (with a minimum value of 0) when the shape is close to that of a back-to-back configuration (i.e., all jets are close to $\hat{n}_T$). The thrust minor provides information about the energy flow with respect to the plane that is formed by the thrust axis and the beam axis, known as the *event plane*. Large values of T_m indicate a large energy flow outside the event plane (with a maximum value of $2/\pi$) and $T_m = 0$ indicates that all energy flows within this plane. The transverse thrust and the thrust minor will therefore always be zero for two-jet configurations.

Results of $\tau_\perp$ and T_m with TMD merging are shown in Figs. 11.13 and 11.15. Different jet-multiplicity samples from the matrix element are shown in dotted lines. Low $\tau_\perp$ and T_m are the most non-trivial regions to describe because there jets are very close to each other. It is noteworthy that in the $n^{\text{jet}} = 4$ panels, the 3-jet samples contribute more to the event shape at the lowest values of $\tau_\perp$ and T_m than the 4-jet samples do. Possibly this is the effect of jet merging with a larger cone radius than the cone radius that is used for clustering in the analysis of the final events. In the lowest bins, deviations from the data up to 20% are observed. For most observables the deviation is only 10%. The predictions agree very well with the data even for the highest jet multiplicities ($n^{\text{jet}} = 5$ and $n^{\text{jet}} = 6$).

For comparison, we show figures of both event shapes calculated with GPMC event generators from Ref. [293]. The transverse thrust GPMC results are given in Fig. 11.14 and those of the thrust minor are given in Fig. 11.16.
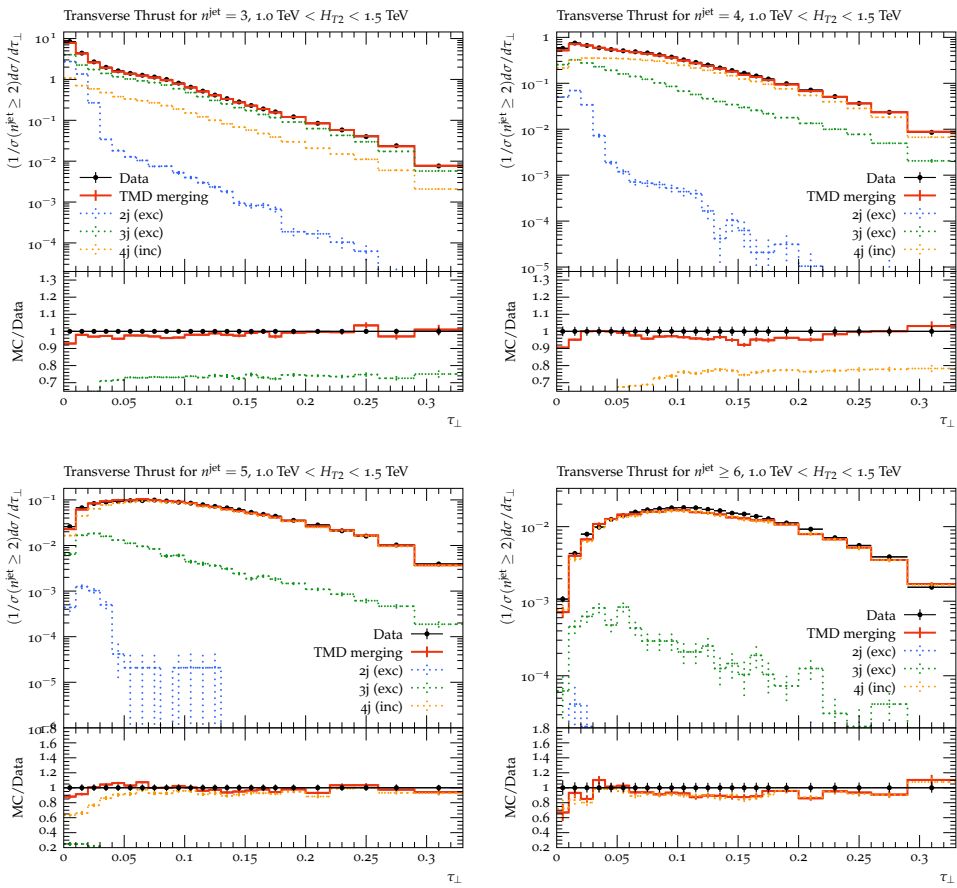
Figure 11.13: Transverse thrust $\tau_\perp$ with TMD merging (red) in comparison with ATLAS data (black).

Figure 11.14: Figure from [293]. Transverse thrust $\tau_\perp$ with general purpose Monte Carlo event generators and ATLAS data (black).

Figure 11.15: Thrust minor T_m with TMD merging (red) in comparison with ATLAS data.
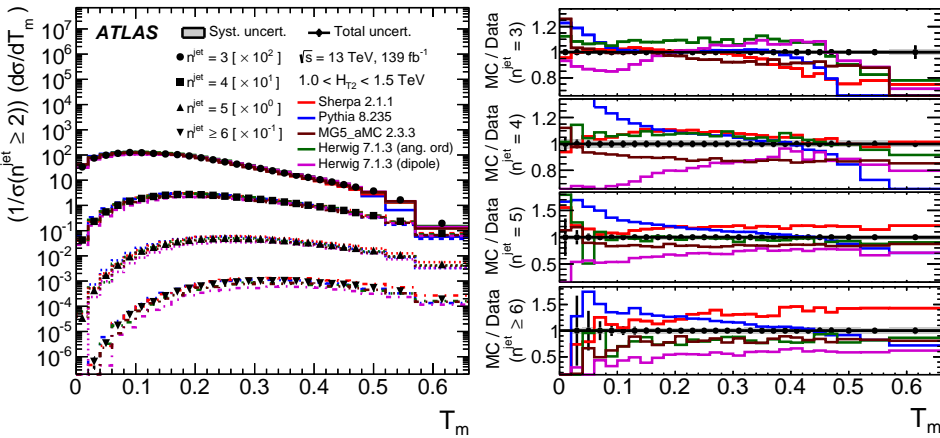
Figure 11.16: Figure from [293].   Thrust minor T_m with general purpose Monte Carlo event generators and ATLAS data (black).

11.5.2 Sphericity and aplanarity

The sphericity S is constructed from the eigenvalues λ_i of the sphericity tensor (a 3x3 matrix):

$$\Theta_{\alpha\beta} = \frac{1}{\sum_{i=1}^{n} |\vec{q}_i|} \sum_{i=1}^{n} \frac{\vec{q}_{i\alpha}\vec{q}_{i\beta}}{|\vec{q}_i|}, \tag{11.6}$$

where α and β are the spatial coordinates. The three eigenvalues λ_k of this matrix are normalized so that $\sum_{k=1}^{3} \lambda_k = 1$. If two eigenvalues are zero, all jet momenta are collinear and the event has a back-to-back configuration (that of di-jets). If only one eigenvalue is zero, the event has three jets lying in one plane. If all eigenvalues have the same value $(1/3)$, the event is as spherical as possible. [295]

With $\lambda_1 \geq \lambda_2 \geq \lambda_3$ the sphericity $(0 \leq S \leq 1)$ is defined for each jet multiplicity as follows

$$S = \frac{3}{2}(\lambda_2 + \lambda_3), \tag{11.7}$$

such that fully spherical events have $S = 1$ and di-jet-like events have $S = 0$. The transverse sphericity $S_\perp$ $(0 \leq S_\perp \leq 1)$ - extracted by the ATLAS measurement - is computed from the transverse component of the sphericity tensor (a 2x2 matrix), which has eigenvalues μ_1 and μ_2 $(\mu_1 > \mu_2)$:

$$S_\perp = \frac{2\mu_2}{\mu_1 + \mu_2}. \tag{11.8}$$

Fully spherical (in the transverse plane) jet energies have $\mu_1 = \mu_2 = 1/2$ and contrary back-to-back jets have $\mu_2 = 0$ and $\mu_1 = 1$.

Numerical results of the transverse sphericity with TMD merging are shown in Fig. 11.17. Results with general purpose Monte Carlo event generators are shown in Fig. 11.18.

The aplanarity $(0 \leq A \leq 1/2)$ is defined as

$$A = \frac{3}{2}\lambda_3, \tag{11.9}$$

such that planar events have $A = 0$, and the larger A, the more the jets are outside a common plane.

A proper calculation of the aplanarity requires a rescaling of the final result (according to the erratum in [293]) due to an error in the original Rivet analysis and the plugin that is used. With a scaling factor of 1.376, the TMD merging calculation shown in Fig. 11.19 results in properly normalized cross sections.
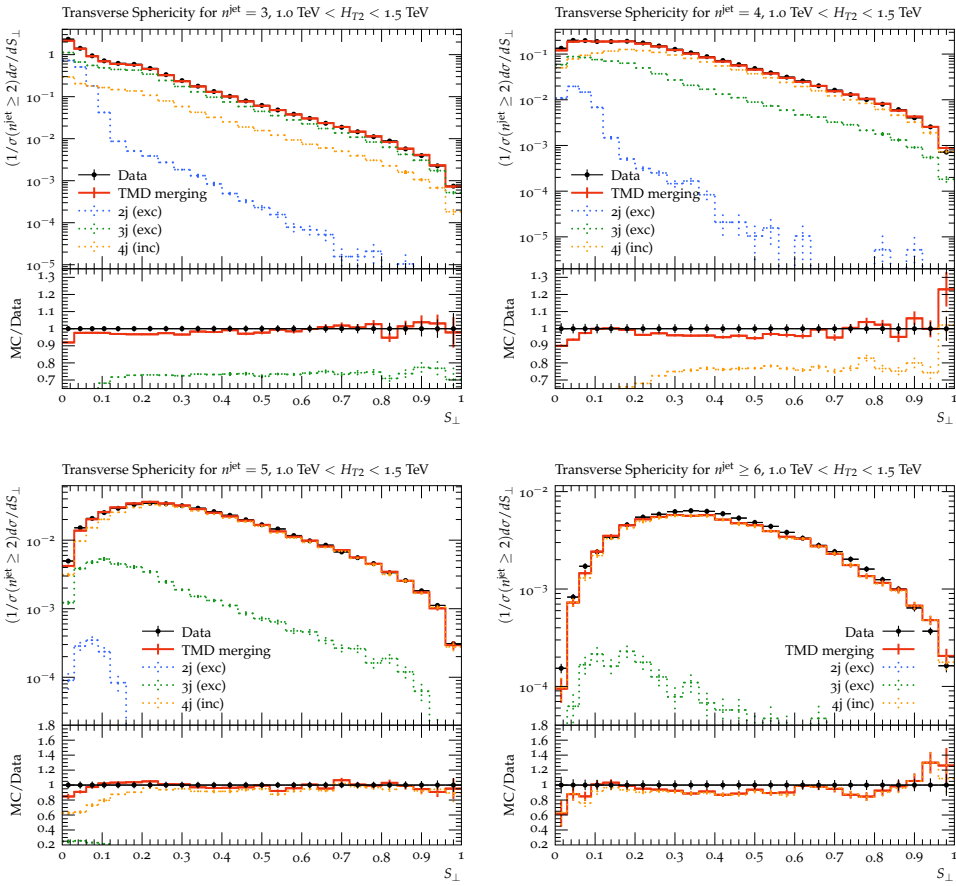
Figure 11.17: Transverse sphericity $S_\perp$ from TMD merging in comparison with data from ATLAS.
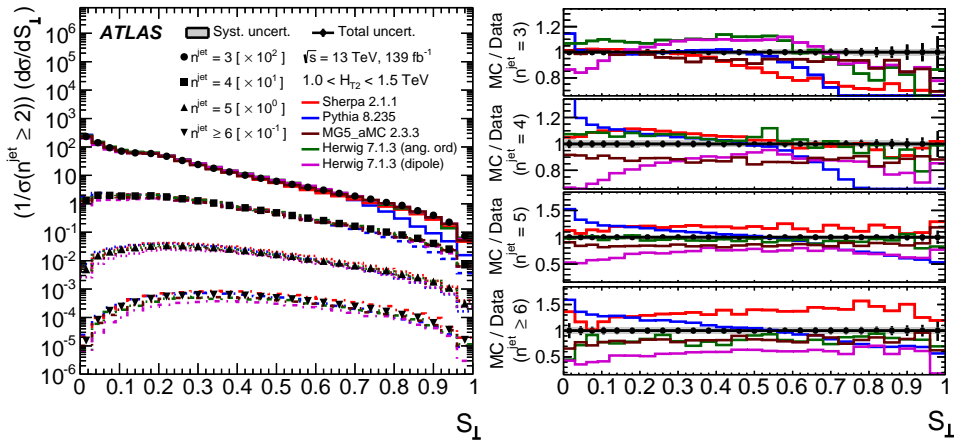
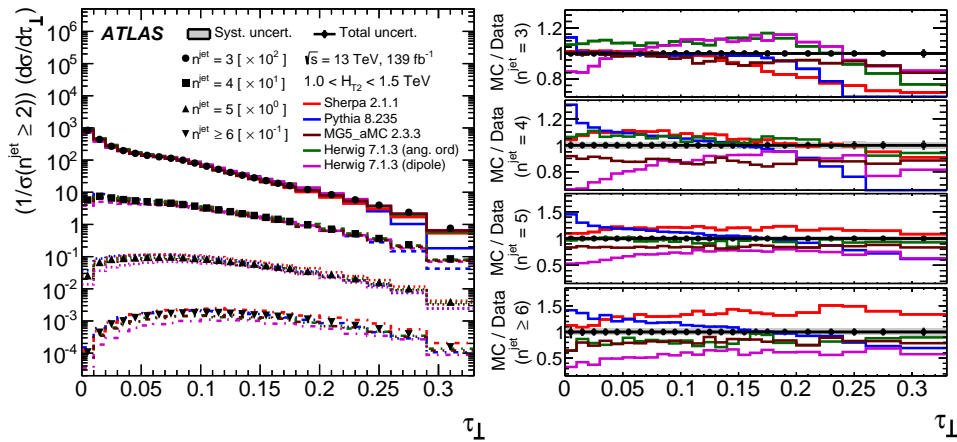*Figure 11.18:* Figure from [293]. Transverse sphericity $S_\perp$ with general purpose Monte Carlo event generators and ATLAS data (black).
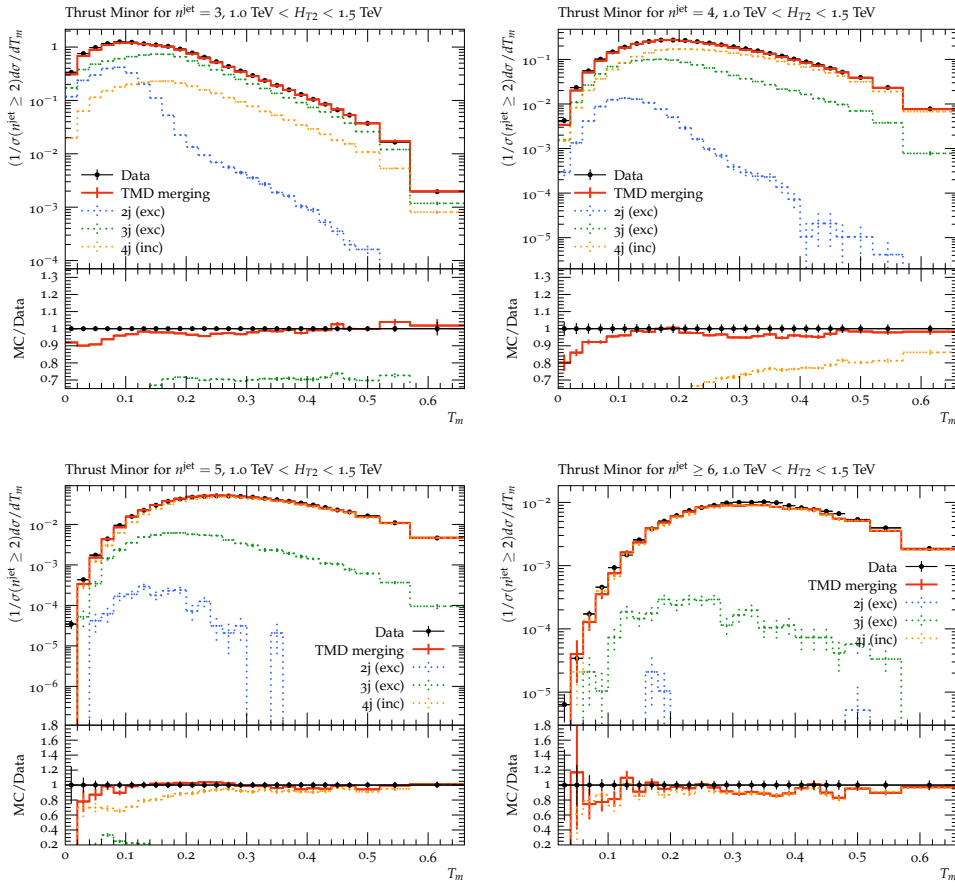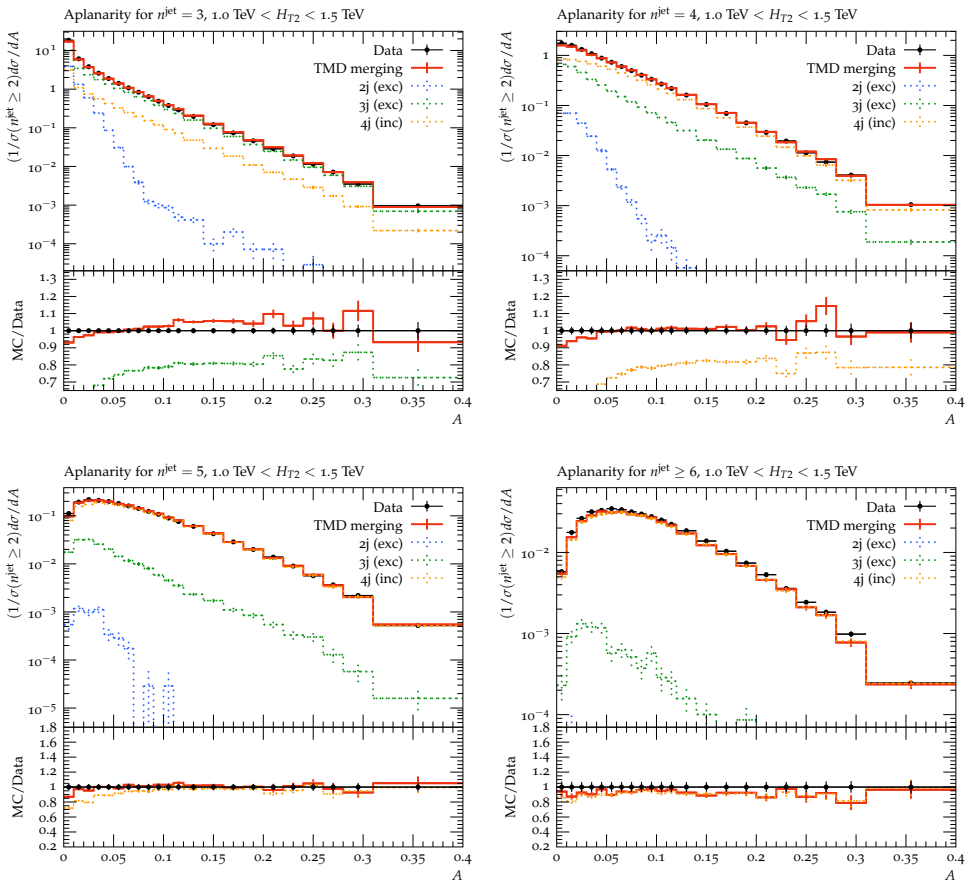
*Figure 11.19:* Aplanarity with TMD merging in comparison with ATLAS data.

Figure 11.20: Figure from [293]. Aplanarity A with general purpose Monte Carlo event generators and ATLAS data (black).

11.5.3 C and D parameters

Event shapes C and D have been studied in great detail in e^+e^- processes in Refs. [296–298]. They can be calculated in the same way for pp collision processes. The distributions of both parameters provide information about the fixed-order calculation, the resummation and the non-perturbative physics within the jet events.

C was originally defined in [296] as the rotationally invariant observable H_2 by using the spherical harmonics Y_2^m and all parton three-momenta $\vec{q}_i$.

$$C = \frac{4\pi}{5} \sum_{m=-2}^{2} \left| \sum_i Y_2^m(\Omega_i) \frac{|\vec{q}_i|}{\sqrt{s}} \right|^2. \tag{11.10}$$

Angles of momenta with respect to fixed axes are contained in Ω_i. Eq. (11.10) can be rewritten as:

$$C = \frac{3}{s} \sum_{i<j} |\vec{q}_i| |\vec{q}_j| \sin^2 \theta_{ij}, \tag{11.11}$$

where θ_{ij} is the relative angle between particles i and j. The nominator of Eq. (11.11) is similar to the relative transverse momentum used in jet clustering algorithms. Wider spread jets or many jets lead to larger C values. Narrower jets or fewer jets result in small C.

D was originally defined in [296] as H_3 and equal to:

$$D = \frac{4\pi}{7} \sum_{m=-3}^{3} \left| \sum_i Y_3^m(\Omega_i) \frac{|\vec{q}_i|}{\sqrt{s}} \right|^2. \tag{11.12}$$

It can also be written as in [298]:

$$D = \frac{27}{s^{3/2}} \sum_{i<j<k} \frac{|\vec{q}_i \cdot (\vec{q}_j \times \vec{q}_k)|^2}{|\vec{q}_i|}. \tag{11.13}$$

Both C and D can be written as projections of parton momenta as in Eqs. (11.11) and (11.13), like the thrust parameters. In contrast to thrust, no extremization is required, as it is only needed for the thrust axis, which is not used for calculating C and D. Instead, there is a double (for C) or triple (for D) summation over the parton momenta.

The eigenvalues of the sphericity tensor contain all the information needed for both the C and D parameters. They are easily computed as

$$C = 3(\lambda_1\lambda_2 + \lambda_2\lambda_3 + \lambda_1\lambda_3), \tag{11.14}$$
$$D = 27\lambda_1\lambda_2\lambda_3, \tag{11.15}$$

which are identical to the definitions above. The numerical integer factors are inserted to enforce a range of values between 0 and 1.

The C parameter takes values larger than 0.75 only in the case of 3 or more jets and aplanar configurations. It is zero for back-to-back di-jets and it is exactly equal to 0.75

for three jets in a plane. The $C = 0.75$ is a so-called "integrable singularity" and shows a slight discontinuity at all jet multiplicities as can be seen in Fig. 11.21. This observable is very non-trivial to describe, as can be seen from the results of general-purpose Monte Carlo generators shown in [293]. Results from SHERPA, HERWIG, MG5_aMC and PYTHIA8 that apply collinear jet merging do not accurately describe data of this event shape, see Fig. 11.22.

C is very sensitive to the value of α_s (hence it is well suited to determine the strong coupling), to non-perturbative power corrections and to large double Sudakov logarithms. The $C > 0.75$ region is dominated by the matrix element, as can be seen from the 3-jet sample contribution in Fig. 11.21(a) and the 4-jet sample contribution in Fig. 11.21(b). The intermediate C region ($3\pi\Lambda_{QCD} \ll C < 0.75$) is dominated by resummation and the low C region is described by non-perturbative physics [297]. The intermediate and large C regions are described quite accurately. However, the non-perturbative region shows some discrepancies. Here the deviations from the data are of the order of 10% in the case of $n^{jet} = 3$, 20 % in the case of $n^{jet} = 4$ and for $n^{jet} = 5$ and 6 the first bin is not filled at all.
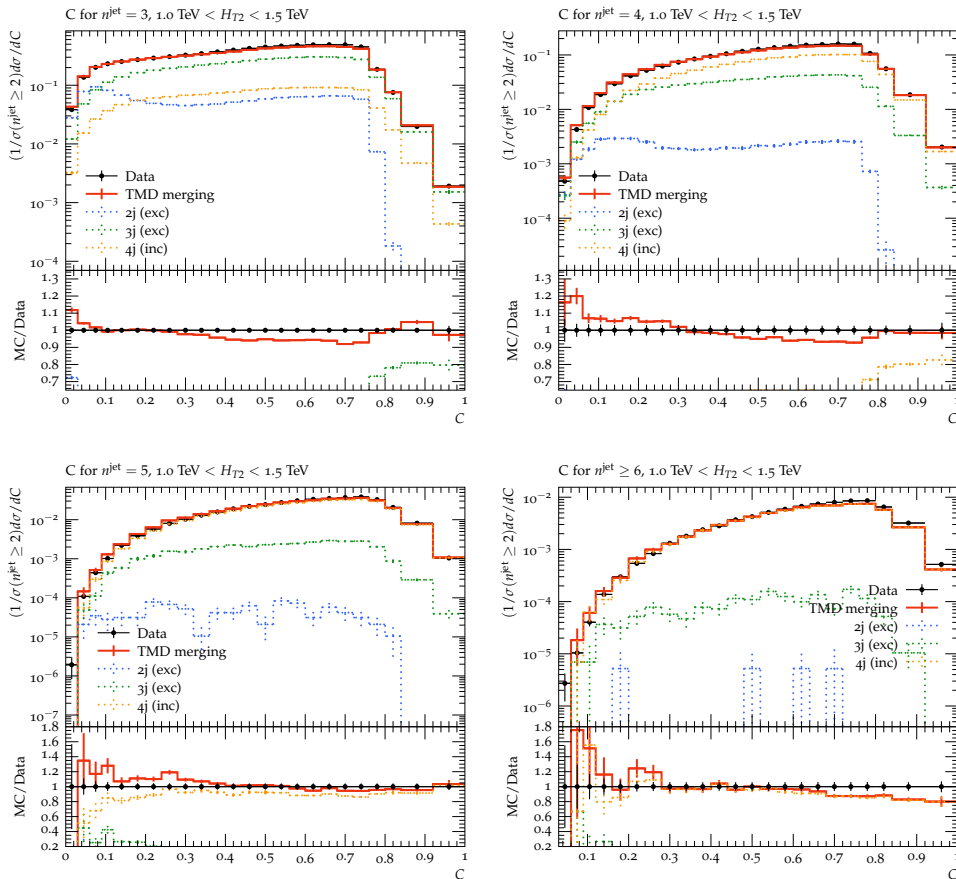
Figure 11.21: C parameter with TMD merging in comparison with ATLAS data.
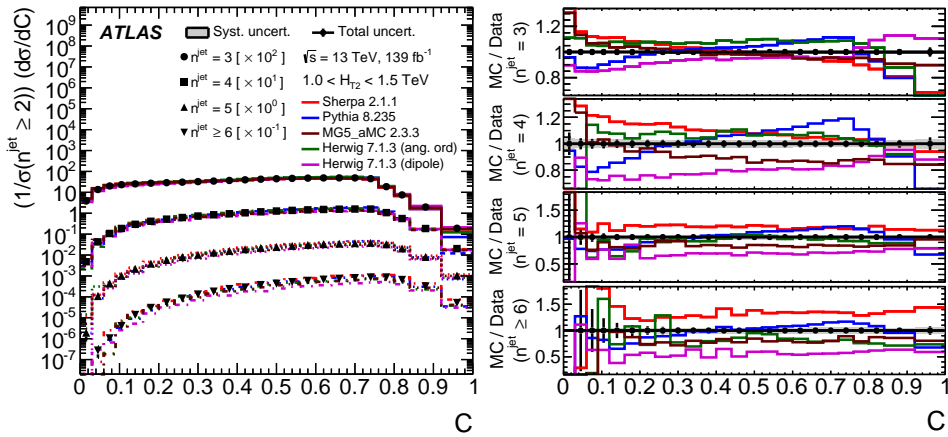
Figure 11.22: Figure from [293]. *C* parameter with general purpose Monte Carlo event generators and ATLAS data (black).

Results of predictions for the *D* parameter with TMD merging are shown in Fig. 11.23[3]. These agree very well with the data for all jet multiplicity bins over the entire range of *D*.

[3]The same rescaling factor is used as for aplanarity.
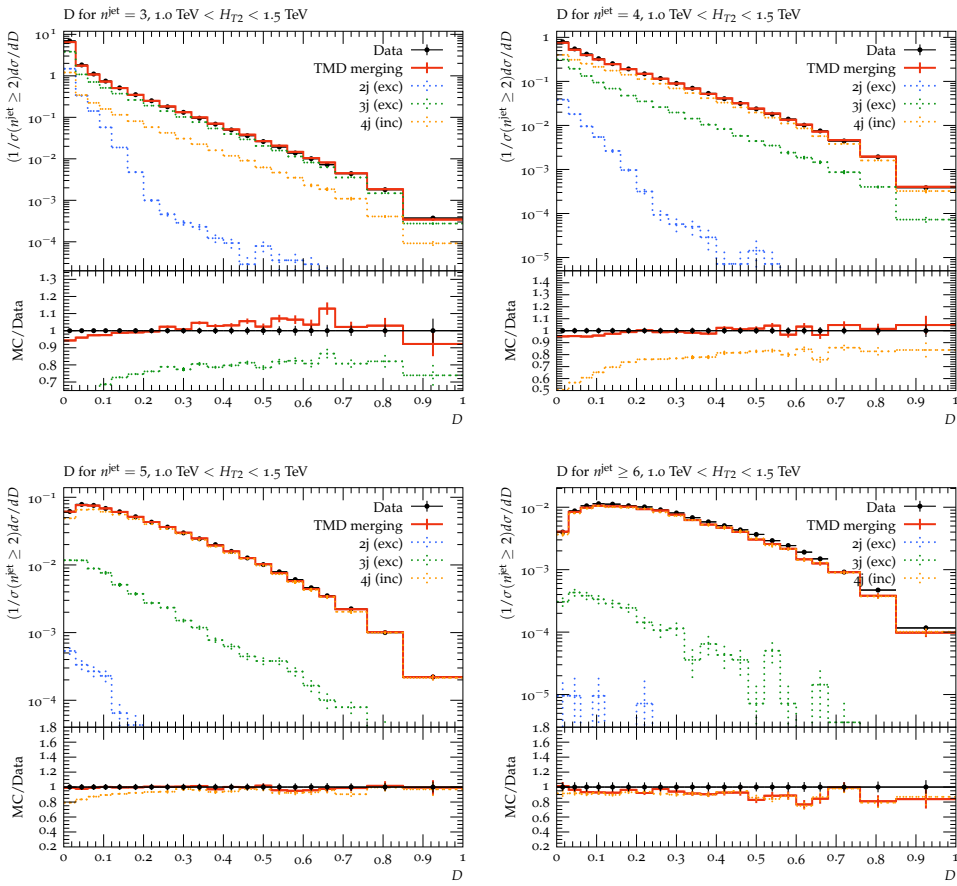
Figure 11.23: D parameter with TMD merging in comparison with ATLAS data.

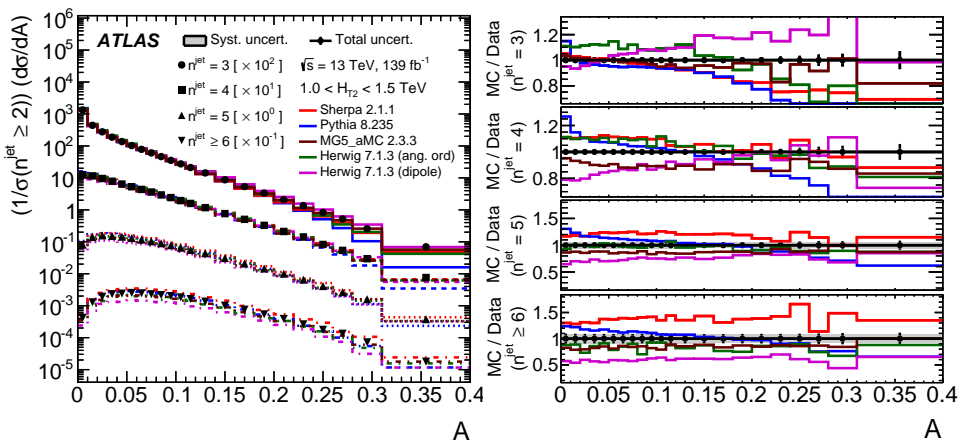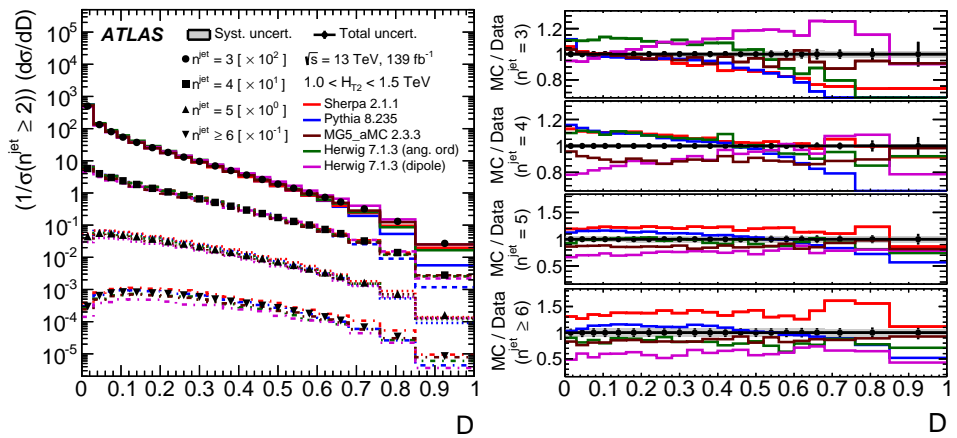*Figure 11.24:* Figure from [293]. D parameter with general purpose Monte Carlo event generators and ATLAS data (black).

11.5.4   Non-perturbative input in matrix elements

The sensitivity to the non-perturbative input and the value of the strong coupling in the matrix element is tested by varying the collinear PDF input. Two sets of multi-jet hard scattering samples that differ in the PDF input have been merged by TMD merging and the results for the event shapes are compared. The first set has an LO PDF (NNPDF2.3_as0130) with one-loop α_s ($\alpha_s(m_Z)$ = 0.130) and the second set has an NLO PDF (NNPDF3.1_as0118) with two-loop α_s ($\alpha_s(m_Z)$ = 0.118). Other generation parameters and the merging parameters are identical to those given in Sec. 11.1. Fig. 11.25 shows the results for the transverse thrust and the C parameter for $n^{\text{jet}} = 3$ and $n^{\text{jet}} = 4$ with the two PDFs. Results for higher jet multiplicities show the same behavior but with larger statistical errors.

(a) $\tau_\perp, n^{\text{jet}} = 3$

(b) $\tau_\perp, n^{\text{jet}} = 4$

(c) $C, n^{\text{jet}} = 3$

(d) $C, n^{\text{jet}} = 4$
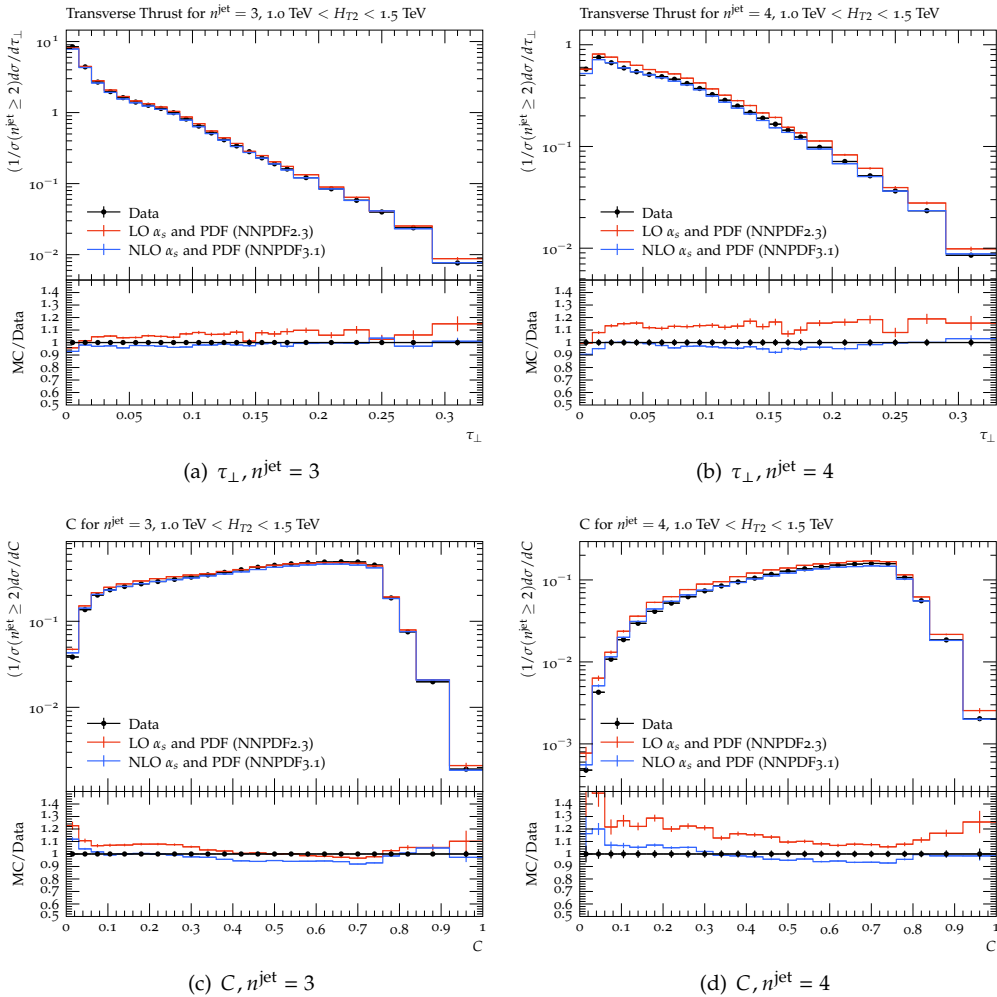
Figure 11.25: $\tau_\perp$ and C parameter from two sets of matrix elements merged identically with TMD merging. 1.0 TeV < H_{T2} < 1.5 TeV.

The choice of PDF in the matrix element has a rather large influence on the result. The

statistical errors do not overlap. Primarily it is the overall normalization that improves by going from LO to NLO for both the transverse thrust and the *C* parameter.

11.5.5 Effect of the underlying event

The dependence of event shapes on the underlying event is investigated. Cascade3 does not have any underlying event implementation. We ask ourselves whether the underlying event influences the results significantly. For answering this, the event shapes are computed with collinear, MLM merging in Pythia8. The merging calculation with matrix elements from Sec. 11.1 is done twice: once with MPI and once without MPI. The merging parameters are the same as for TMD merging: $E_{\perp,\text{clus}} = 65$ GeV and $R_{\text{clus}} = 0.7$.
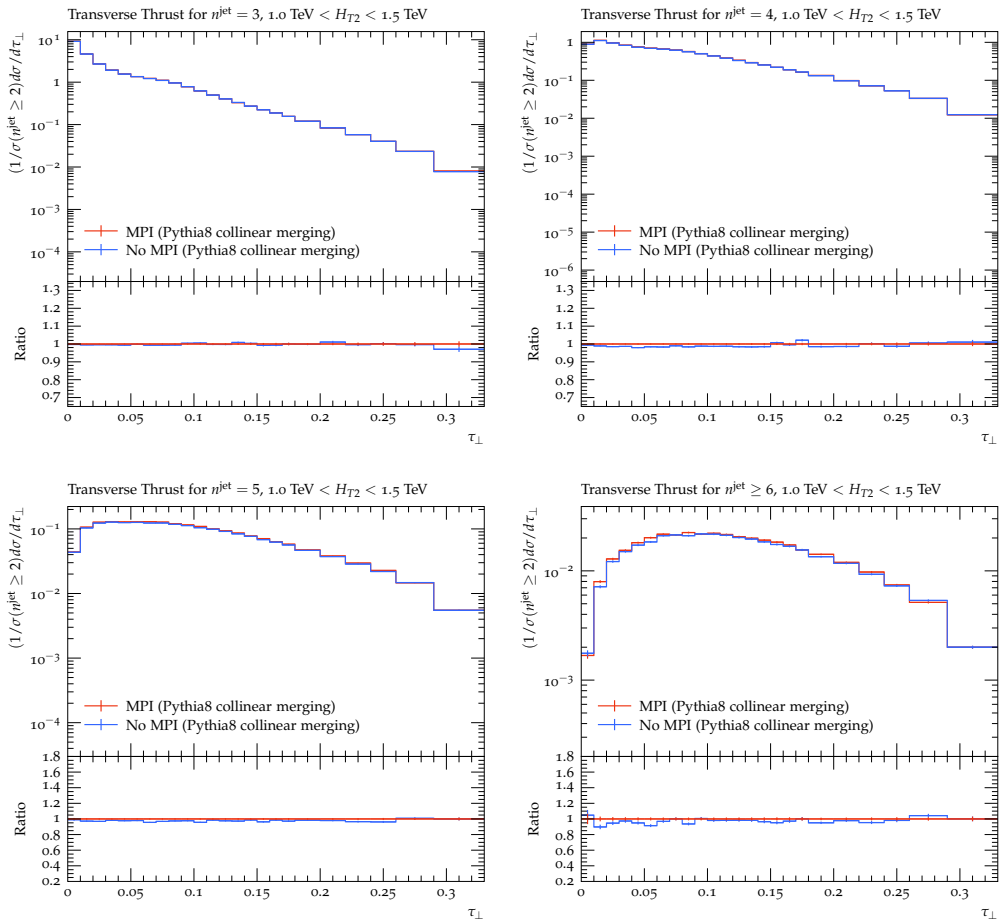
Figure 11.26: Effect of MPI modelling on the transverse thrust event shape $\tau_\perp$ for jet multiplicities $n^{\text{jet}} = 3$ up to $n^{\text{jet}} \geq 6$. Results are obtained with MLM merging in Pythia8 with MPI switched on and off. The di-jet transverse momentum selection criterium is: 1.0 TeV $< H_{T2} < 1.5$ TeV.

The results in Figs. 11.26 and 11.27 show that the event shapes are not sensitive to multi-parton interactions in these kinematic regions of the phase space. Regions of the event
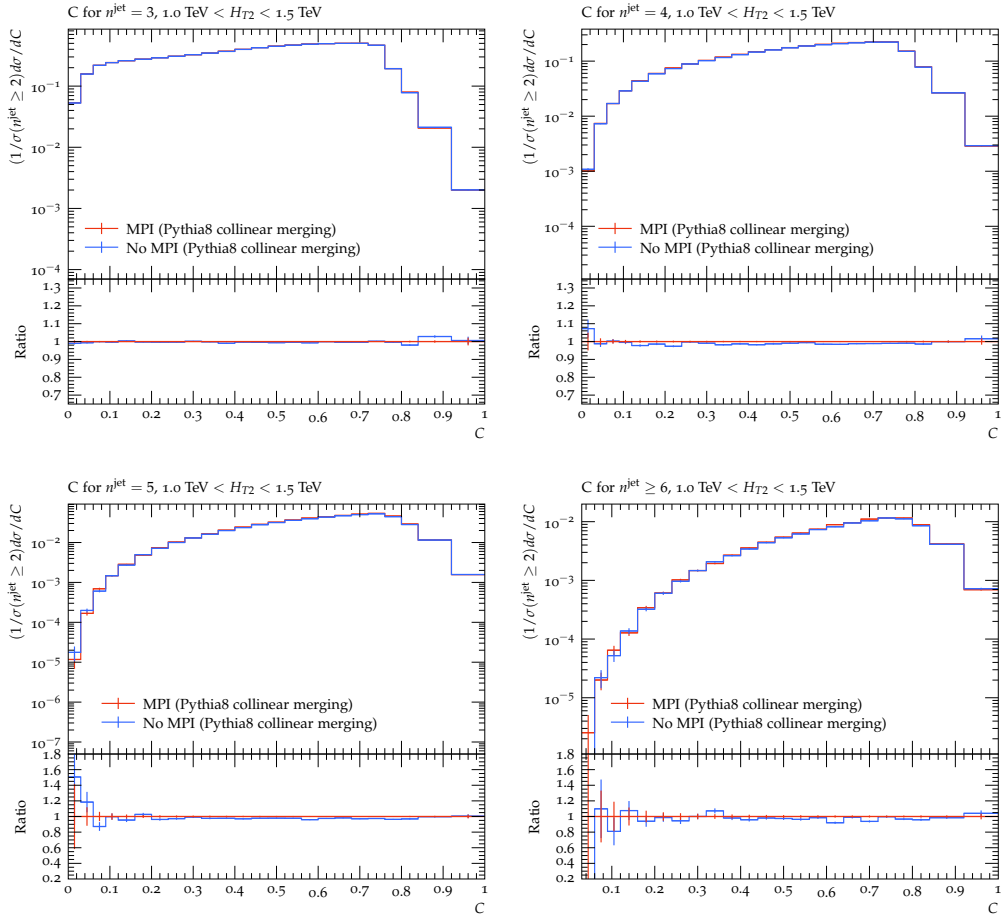
Figure 11.27: Effect of MPI modelling on the C event shape for jet multiplicities $n^{\text{jet}} = 3$ up to $n^{\text{jet}} \geq 6$. Results are obtained with MLM merging in Pʏᴛʜɪᴀ8 with MPI switched on and off. The di-jet transverse momentum selection criterium is: $1.0 \text{ TeV} < H_{T2} < 1.5 \text{ TeV}$.

shapes that are not accurately described are unlikely to be improved by implementing MPI effects in Cᴀsᴄᴀᴅᴇ3. Although the non-perturbative regions require improvement, due to an overestimation of the low C region, MPI will not provide the necessary correction.

11.6   Conclusion

The results presented in this chapter are new and very promising. With the generation of matrix elements up to four hard partons in the final state, complicated multi-jet event structures can be accurately described using forwardly evolved TMDs, (TMD) parton showers, a hadronization model, and TMD merging to avoid double counting in the resummation region. Jet multiplicity spectra are accurately described beyond the multiplicity of the matrix elements. Predictions for jet transverse momentum spectra

are also accurate. We have shown that even more complicated and global observables describing the overall event shape of QCD jets in the final state are accurately described with this method.

The general purpose Monte Carlo event generators that were applied for predictions by the experimental groups require input parameters additional to the merging parameters which are needed for the tuning of non-perturbative models to the perturbative (parton shower) calculations. The PB method and its implementation in CASCADE3 does not require such tuning to obtain similar or higher accuracy.

The matrix elements that are used for the studies at 7 TeV from [292] contain higher order emissions than used in our presented results by TMD merging. In [292] the jet-multiplicity in hard scattering events goes up to $n_{hard} = 6$, while in TMD merging $n_{hard} = 4$ is treated inclusively. Nevertheless, the jet multiplicity spectrum is accurately described at least up to $n^{jet} = 6$.

We have shown that TMD merging is very well suited to calculate event shapes. The results presented are increasingly more accurate than the predictions from the general purpose Monte Carlo programs. It is particularly interesting to compare the results of TMD merging with those of MG5_aMC, since the same matrix element generator is used with the same number of hard final state partons, also with NNPDF3.0_NLO and $\alpha_s(m_Z) = 0.118$. In [293], MG5_aMC matrix elements are showered by PYTHIA8 and merged according to the CKKW-L prescription. Deviations in the jet multiplicity spectra with the MG5_aMC+PYTHIA8 prediction appear already at $n^{jet} = 4$, while the TMD merging results show discrepancies only at $n^{jet} \geq 6$.

Large values of transverse thrust and thrust minor are largely underestimated by collinear factorization-based Monte Carlo programs, while they are generally well described by TMD merging (with only small deviations in a few bins). The shape of these distributions is better described by TMD merging than by any of the results given in [293]. The conclusion in Ref. [293] on event shape studies with general purpose (collinear) Monte Carlo event generators is that "none of the MC predictions investigated provide a good description of the data in all regions of the phase space". In this chapter we have shown that TMD merging improves the accuracy and shape of event shape distributions and is highly suitable for experimental studies.

A sliding merging scale

This chapter focuses on analyzing the merging scale's correlation with the hard scale of the process. Phenomenological studies and measurements of extremely hard interactions that are accompanied by soft jets are common more and more nowadays, eg. Ref. [299]. This is made possible by accurate jet clustering algorithms and sophisticated triggering systems at increasingly precise detectors. These studies are important for an increase in the accuracy and precision of parton branching methods, not only at the level of TMD merging, but also in the case of collinear event generators. To comprehend these physics, it is crucial to conduct accurate theoretical predictions.

In these multi-jet processes where typical scales differ by several orders of magnitude, precise calculations require merging of higher order matrix elements with parton showers. The merging scale is a key factor in accomplishing this level of accuracy. Chapters 10 and 11 demonstrate that variations of the merging scale provide insight into the systematic uncertainty of the merging procedure. In this chapter, we present a study to determine the appropriate central value for the merging scale. We developed a method to quantitatively analyze the merging algorithm and merging scale dependence on typical event scales in DY plus jets production.

This chapter[1] aims to guide the reader through the process of formalizing an appropriate merging scale. First, we present the situation and technical setup in section 12.1. Then, in section 12.2 we explain the method we constructed to quantify the impact of the merging scale value. Results from multiple scenarios are presented in sections 12.2.2 and 12.4.2. Eventually, section 12.5 summarizes the conclusions.

12.1 Introduction

The merging scale, similar to the factorization scale, is regarded as an arbitrary scale and is, therefore, not an observable quantity. Although associated to transverse energy, it acts as a separation between hard matrix element and soft parton shower contributions. The merging scale is denoted as

$$\mu_m \equiv E_{\perp,\text{clus}} \ . \tag{12.1}$$

A poorly selected merging scale can result in inaccurately filled phase spaces due to double counting events or missing events. According to Ref. [288], the first rigorous criterion for the merging scale given is that it should not be smaller than the generation cut μ_c to prevent exclusion of phase space regions. A rough guideline for determining a suitable merging scale in the MLM procedure was given in Ref. [288] by

$$\mu_m = \mu_c + \max(5\,\text{GeV}, 0.2 \cdot \mu_c) \,. \tag{12.2}$$

Following this guideline, the minimum merging scale should be $1.2 \cdot \mu_c$.

Possible relations of the merging scale to hard scales of processes remain an unexplored subject. The authors of MG5_aMC provide a rough estimate on the merging scale: "This value should be related to the hard scale (e.g. the mass of produced particle, H_T cut, or similar) in the process, and set to ~(1/6-1/3 x hard scale)."[2]. This problem concerns the definition of softness of jets. The merging scale distinguishes between soft and hard emissions. As the hard interaction scale Q^2 shifts, there is a need for a corresponding shift in the definition of hard and soft jets. This study hypothesizes that the merging scale μ_m is dependent on Q. For this study, we investigate differential jet rates (DJRs) at different hard interaction scales in Drell-Yan processes and different merging scale values.

To establish the connection between the merging scale and the hard scale, we merge Z + jets events at various di-lepton masses using TMD merging. These merged events are then utilized for in-depth studies on the merging scale variations. We conduct these studies on DY events as the hard scale in this process is equivalent to the mass of the di-lepton system:

$$Q^2 = m_{ll}^2 \,. \tag{12.3}$$

An increase in the hard scale Q is achieved through the application of a large lower limit on the di-lepton mass $m_{ll}^{\min} \gg m_Z$ during the generation of hard scattering events. The DY mass spectrum rapidly decreases (approximately as $1/m_{ll}^4$) in these high mass regions, indicating that the majority of the events have masses close to the lower limit. As a result, no upper limit on the mass has been imposed. These studies also incorporate the effect of a decreasing hard scale. In this scenario, it is necessary to establish an upper mass limit to prevent the occurrence of a large spread of hard scales in a single set of hard scattering events. However, the use of a merging procedure at lower energies may not be required.

High-mass DY events have been repeatedly merged using the TMD merging technique with varying merging scales. An algorithm has been developed to analyze the DJRs in order to identify the most appropriate merging scale. To achieve this, Cascade3 [51] is utilized to apply TMD merging to DY events that are generated with MG5_aMC, with hadronization being turned off since it does not affect DJRs and only impacts jet substructure. Transverse momentum is added according to PB-TMD-NLO-HERAI+II-2018-set2 [38] from TMDLib [40]. The calculation of the DJRs, which are analyzed, is performed using Rivet3 [82, 83]. Jet clustering is performed at the partonic level during the merging process with the anti-kt algorithm and at the analysis level using the kt algorithm, both within `FastJet` [270].

---

[2]Citation from the MG5_aMCwiki page: https://cp3.irmp.ucl.ac.be/projects/madgraph/wiki/Matching

12.2 Differential jet rates and the merging scale

In this section, we will explain the step-by-step procedure for quantifying the effectiveness of the merging process and the merging scale. We will illustrate our results using the scenario of $Q = m_{ll}^{\min} = 800$ GeV.

12.2.1 Measure of discontinuity

Double counting of events (overpopulation of the phase space) or missing events (leaving gaps in filling of the phase space) due to a misplaced merging scale can cause discontinuous DJRs. A discontinuity in the DJR manifests close to the merging scale. As shown in Chapter 10, when the di-lepton mass is close to the Z boson mass, $m_{ll} \simeq m_Z$, and the merging scale is $\mu_m = 23$ GeV, there are no significant discontinuities in the DJRs of Z + jets events from TMD merging (cf. Fig. 10.1). By applying this procedure to events with higher DY masses, discontinuities are observed in the region of this merging scale. Fig. 12.1 illustrates this, with all generating and merging parameters being identical to the examples in Chapter 10, except that the di-lepton mass of the generated events is increased to $m_{ll}^{\min} = 800$ GeV. A merging scale of $\mu_m = 23$ GeV is no longer sufficient for merging these events to TMD PDFs and TMD shower. A distinct discontinuity is visible near this merging scale.
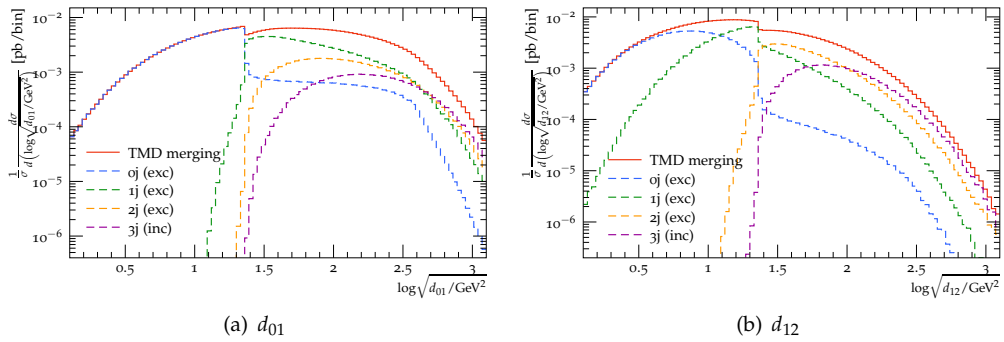
Figure 12.1: DJRs of TMD merged Z+jet events at masses $m_{ll}^{\min} = 800$ GeV with a merging scale of $\mu_m = 23$ GeV (located at $\log(23) \approx 1.36$).

We associate the magnitude of the discontinuity with the inadequacy of the merging procedure and quantify the level of "non-smoothness" of a DJR by a parameter D. Our goal is to identify the minimum value of this discontinuity, which is associated with an "optimal" merging scale.

The discontinuity quantity has been constructed by taking into account both the 0th- and 1st-order discontinuities to eliminate influences of the shape of the DJR near the discontinuity. A priori it is unknown what type of discontinuity occurs in the DJRs due to the finite bin size. Two conceivable types are: 1) a removable discontinuity or 2) a jump discontinuity. Due to the discretisation of the DJR distributions, it is preferable to consider a removable discontinuity. In order to calculate it correctly, limits should

be taken towards the discontinuity at the merging scale μ_m from both the left and right sides:

$$D(Q, \mu_m) = \lim_{\mu \to \mu_m^-} \left[\frac{1}{\sigma} \frac{d\sigma}{d\left(\log(\mu/\text{GeV})\right)} \right] - \lim_{\mu \to \mu_m^+} \left[\frac{1}{\sigma} \frac{d\sigma}{d\left(\log(\mu/\text{GeV})\right)} \right] , \tag{12.4}$$

with $\mu = \sqrt{d_{ij}}$.

In practice, an interpolation of the DJR is necessary due to the binned results. Tangent lines, denoted as $l(\mu)$, are fitted on both sides of the discontinuity based on either two or four data points of d_{ij} depending on the bin size (see section 12.3).

$$l(\mu) = a \log(\mu) + b . \tag{12.5}$$

The absolute difference at the merging scale between the fits on the left and right side of the discontinuity, denoted as $|l_{\text{left}}(\mu_m) - l_{\text{right}}(\mu_m)|$, is a zeroth order effect. The difference in the slope is a first order effect and is accounted for by shifting one bin width, represented as $\delta = \Delta \log(\mu)$: $|a_{\text{left}} \cdot \Delta - a_{\text{right}} \cdot \Delta|$. An object L_i is defined as:

$$L_i(\mu) = l_i(\mu) + a_i \cdot \delta , \tag{12.6}$$

which consists of a tangent fit l on either the left ($i = l$) or right ($i = r$) side of the merging scale, along with the first order correction. The difference between L_r and L_l serves as reasonable estimation of the discontinuity. Normalizing the quantity D is achieved through dividing it by the average:

$$D(Q, \mu_m) = \frac{|L_l(\mu_m) - L_r(\mu_m)|}{(L_l(\mu_m) + L_r(\mu_m))/2} . \tag{12.7}$$

Illustrative plots of the determination of discontinuities from d_{01} using multiple merging scales ($\mu_m = \{40, 70, 100, 150\}$ GeV) are shown in Fig. 12.2. To increase efficiency and reduce higher order effects, we have only included $Z+0j$ and $Z+1j$ samples in the DJRs. The discontinuity values are provided in the legends.

A set of discontinuities for a fixed hard scale can be plotted against the merging scale value. Figure 12.3 shows the discontinuities for twelve distinctive merging scale values.

12.2.2   Determination of the merging scale

The optimal merging scale is the one that minimizes the discontinuity distribution D and produces the smoothest DJR. By minimizing D at a fixed hard scale Q, the optimal merging scale $\mu_m^{(0)}(Q)$ can be determined. The distribution $D(800, \mu_m)$, shown in Fig. 12.3, in both linear scale (left) and logarithmic scale (right), provides visual evidence of a minimum near $\mu_m \simeq 75$ GeV. As the merging scale increases, the discontinuity distribution starts to fluctuate more, but a general upward trend is apparent.

To determine the minimum value, a polynomial fit through the data in logarithmic scale is performed. A second order polynomial is adequate for this fit using a set of points near the minimum:

$$D_{\text{fit}}(Q, x) = ax^2 + bx + c , \tag{12.8}$$
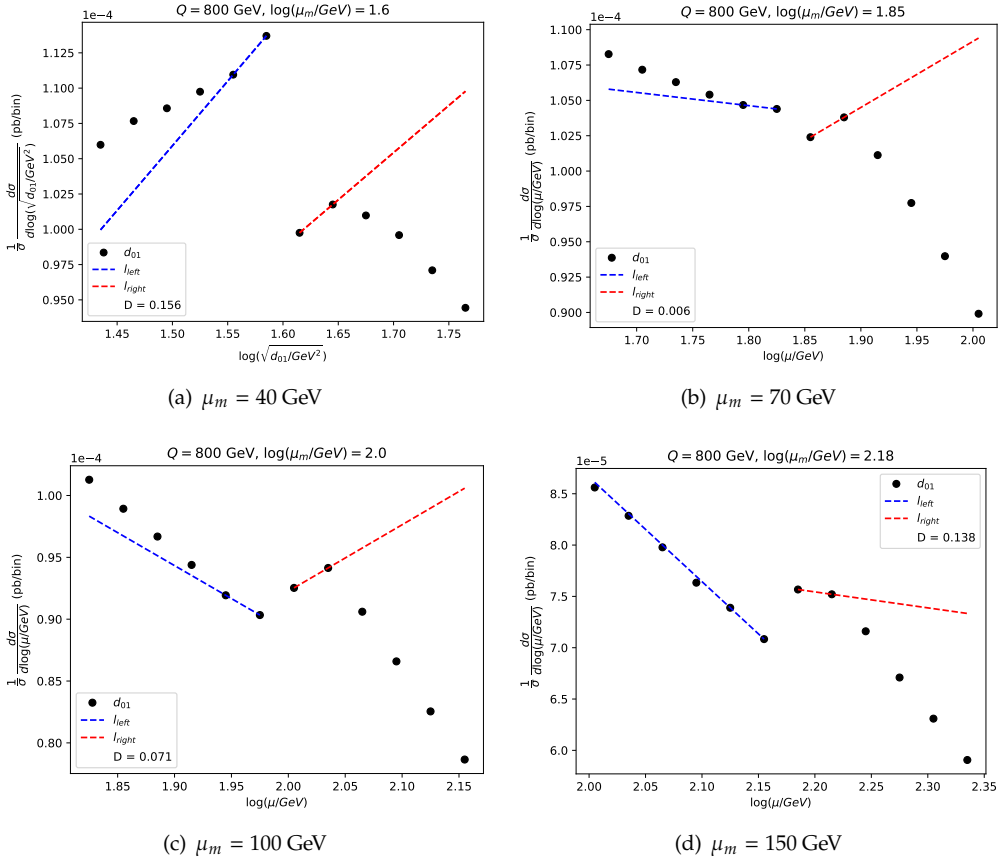
Figure 12.2: A close-up view of d_{01} with $Q = 800$ GeV, $\mu_c = 16$ GeV and $\eta^{\max} = 2.7$. A clustering radius of $R_{\mathrm{clus}} = 1.4$ is utilized for merging and the results are shown on four panels for different merging scales μ_m. The bin width is set at $\delta = 0.03$. The tangent line fits through two points next to the discontinuity are shown in blue (left) and red (right).

with $x = \log(\mu_m)$. To achieve a proper fit, at minimum, three data points near the minimum are necessary. The selection of data points is based on the χ^2-value of the fit, and we aim to utilize more than three points for all scenarios. Selections in which χ^2 is close to 1 are employed to determine $\mu_m^{(0)}$. Figure 12.4 shows the parabolic fits through the discontinuity distributions in the analyses of d_{01} and d_{12} with a hard scale of $Q = 800$ GeV.

12.3 Theoretical uncertainties

The calculation of the discontinuity must consider theoretical uncertainties.

Systematic uncertainties arise from the bin size δ used in the calculation of the DJR. Additionally, statistical uncertainties were computed in the analysis, although they seem

(a)   (b)
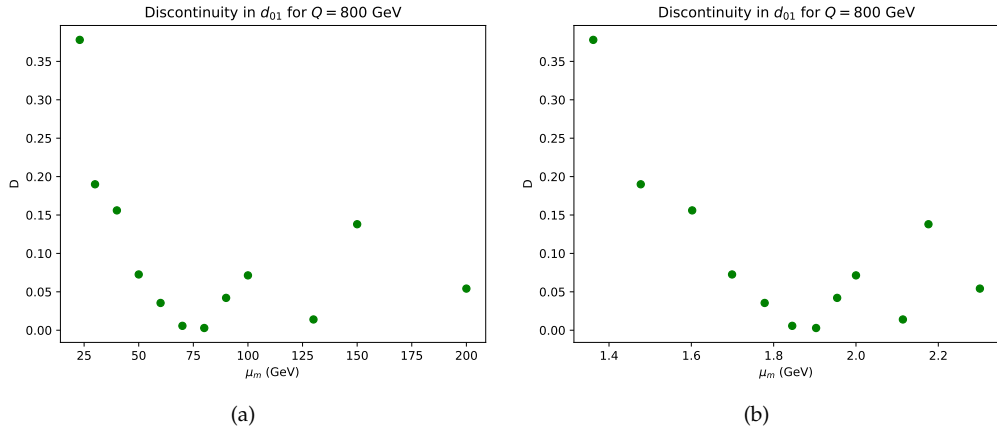
Figure 12.3: Discontinuity in d_{01} with a bin width of $\delta = 0.03$ obtained from merging Z + jets events with $Q = 800$ GeV, $\mu_c = 16$ GeV, $\eta^{\mathrm{max}} = 2.7$. Merging parameters used were $R_{\mathrm{clus}} = 1.4$, $\eta^{\mathrm{max}}_{\mathrm{clus}} = 2.7$ and $\mu_m \in \{23, 30, 40, 50, 60, 70, 80, 90, 100, 130, 150, 200\}$ GeV.

(a) $\mu_m^{(0)}$ from d_{01} (b) $\mu_m^{(0)}$ from d_{12}
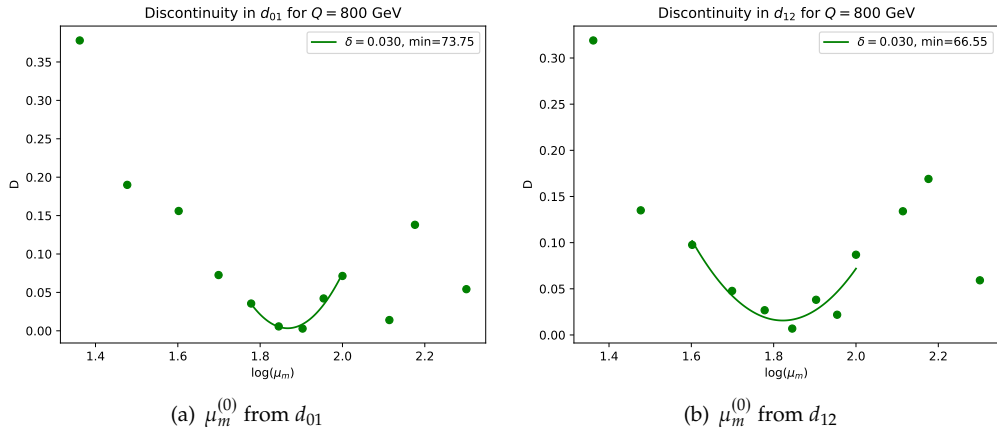
Figure 12.4: Fits to discontinuity distributions for $Q = 800$ GeV.

considerably smaller than the variation in uncertainty due to different bin sizes for all di-lepton masses under consideration.

12.3.1   Bin size uncertainty

The default calculation is performed in a domain $0.1 < \log(\sqrt{d_{ij}/\mathrm{GeV}^2}) < 3.1$, which is homogeneously divided into 100 bins. Each bin has a width $\delta \equiv \Delta(\log(\mu)) = 0.030$. The merging scale, where the discontinuity occurs, typically falls within a single bin. The degree of smoothing increases with the distance of the merging scale from the nearest bin border. Increasing bin sizes tend to reduce discontinuities and decrease the value of D. However, minimizing the bin size is also not optimal. Because of numerical effects

and impurities in the merging algorithm, the DJR becomes blurred around the merging scale and starts to become significant at smaller bin sizes.

To estimate the uncertainty caused by the bin size, we varied the bin size by ±0.015. This produced three data sets with bin widths $\delta \in \{0.015, 0.030, 0.045\}$. We recalculated DJR discontinuities following the above procedure. For $\delta = 0.015$, we fitted tangent lines l_i through four data points, and for $\delta = 0.030$ and $\delta = 0.045$, we fitted l_i lines through two data points.

Figure 12.5 shows the d_{01} distribution in four scenarios that differ in bin size (including $k = 4$, which was not used in further calculations). The analysis was performed with $Q = 800$ GeV and a merging scale of $\mu_m = 40$ GeV. Each scenario's discontinuity D is calculated using Eq. (12.7) and shown in the legend. The results for the three smallest bin sizes ($k \in \{1, 2, 3\}$) are $D_k(40 \text{ GeV}) = \{0.155, 0.156, 0.124\}$.

(a) $\delta = 0.015$ (b) $\delta = 0.030$

(c) $\delta = 0.045$ (d) $\delta = 0.060$
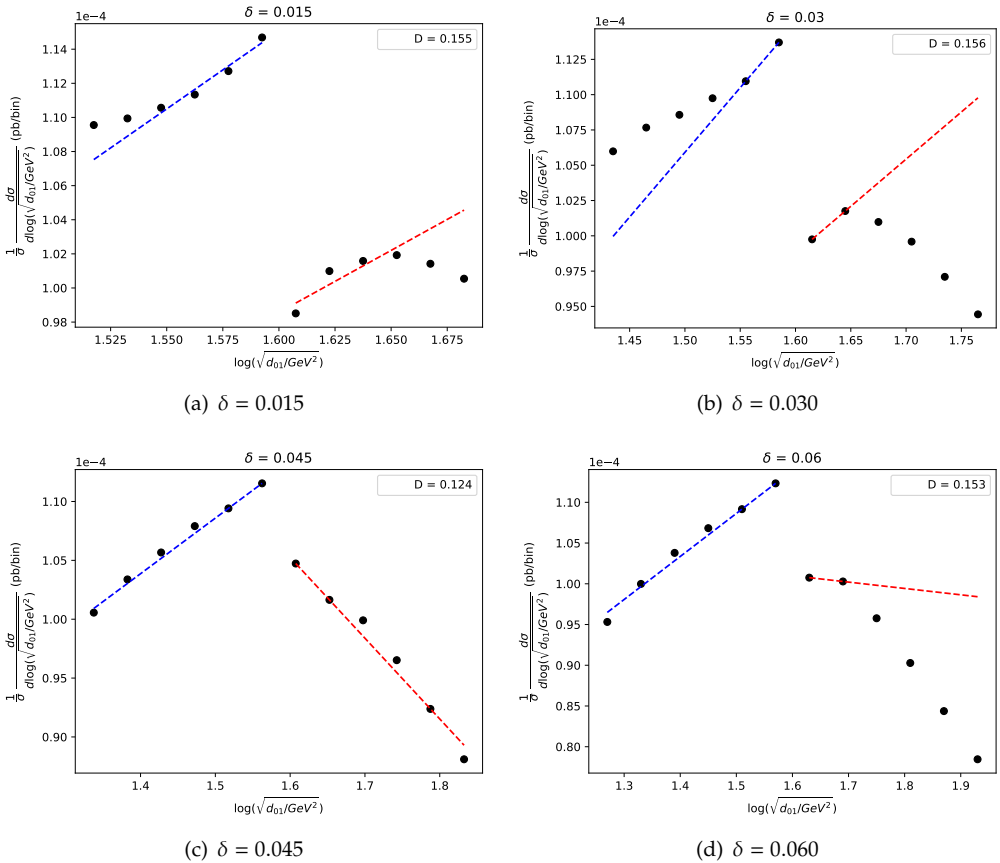
Figure 12.5: d_{01} with different bin sizes δ at a hard scale $Q = 800$ GeV and merging scale $\mu_m = 40$ GeV.

Various distributions $D_k(\mu_m)$ are calculated for each hard scale, which differ based on the bin width of the DJRs used to calculate the discontinuities. Figure 12.6 shows the discontinuities from d_{01} (left) and d_{12} (right), plotted against the merging scale (in log scale). The data from different bin sizes are represented by different colors. These

distributions are obtained with the method described in section 12.2.2. From three results, we derive the average optimal merging scale $\langle \mu_m^{(0)} \rangle$ and the associated systematic bin uncertainty σ_{bin} obtained by:

$$\langle \mu_m^{(0)} \rangle(Q) \pm \sigma_{\text{bin}}(Q) = \frac{1}{n} \sum_{k=1}^{n} \mu_{m,k}^{(0)}(Q) \pm \frac{1}{2} \left(\max_k \mu_{m,k}^{(0)} - \min_k \mu_{m,k}^{(0)} \right) , \qquad (12.9)$$

with $n = 3$.

Results of the optimal merging scale $\mu_m^{(0)}$ at 800 GeV for three bin sizes using d_{01} are $\mu_{m,k}^{(0)} = \{74.14, 73.75, 65.16\}$ GeV and using d_{12} these are $\mu_{m,k}^{(0)} = \{61.23, 66.55, 70.35\}$ GeV. These yield a final, ideal merging scale of:

$$\langle \mu_m^{(0)} \rangle(800\text{GeV}) \pm \sigma_{\text{bin}} = 71.0 \pm 4.5 \text{ GeV} , \qquad (12.10)$$

from calculations with d_{01} and

$$\langle \mu_m^{(0)} \rangle(800\text{GeV}) \pm \sigma_{\text{bin}} = 66.0 \pm 4.6 \text{ GeV} , \qquad (12.11)$$

from calculations with d_{12}.

12.3.2   Statistical uncertainty

A limited number of events in each bin of the DJR causes an uncertainty on the result for $\mu_m^{(0)}$. The statistical error $\sigma_{\text{stat.}}$ is calculated by altering the DJR values near the merging scale, following a Gaussian distribution with a standard deviation equal to the Monte Carlo error $\sigma_{MC} = \frac{1}{\sqrt{N}}$, with N being the number of events in that bin. The DJR value $d_{ij}(Q, \mu_m)$ is varied based on σ_{MC} by selecting a random number R uniformly from the range $[0, 1]$ and using it to determine $x(R)$:

$$R = \int_{-\infty}^{x(R)} dx \exp \left\{ \frac{(x - d_{ij}(Q, \mu_m))^2}{2\sigma_{MC}^2} \right\} . \qquad (12.12)$$

The DJR is randomly varied n times using a random number R. For each variation, we calculate the discontinuity D according to Eq. (12.7). We obtain $n = 100$ distributions of $D(\mu_m)$, from which we compute the minima $\mu_m^{(0)}$. Although this symmetric statistical variation has no effect on the average merging scale result given by Eq. (12.9), it does introduce an additional uncertainty $\sigma_{\text{stat.}}$ associated with the final outcome:

$$\sigma_{\text{stat.}}(Q) = \frac{1}{n} \sqrt{\sum_{i=1}^{n} \left(\mu_{m,i}^{(0)}(Q) - \langle \mu_m^{(0)}(Q) \rangle \right)^2} . \qquad (12.13)$$

12.3.3   Total theoretical uncertainty

The total uncertainty on the result of an optimal merging scale is determined by calculating the sum of squares:

$$\sigma_{\text{tot.}}(Q) = \sqrt{\sigma_{\text{stat.}}^2(Q) + \sigma_{\text{bin}}^2(Q)} . \qquad (12.14)$$
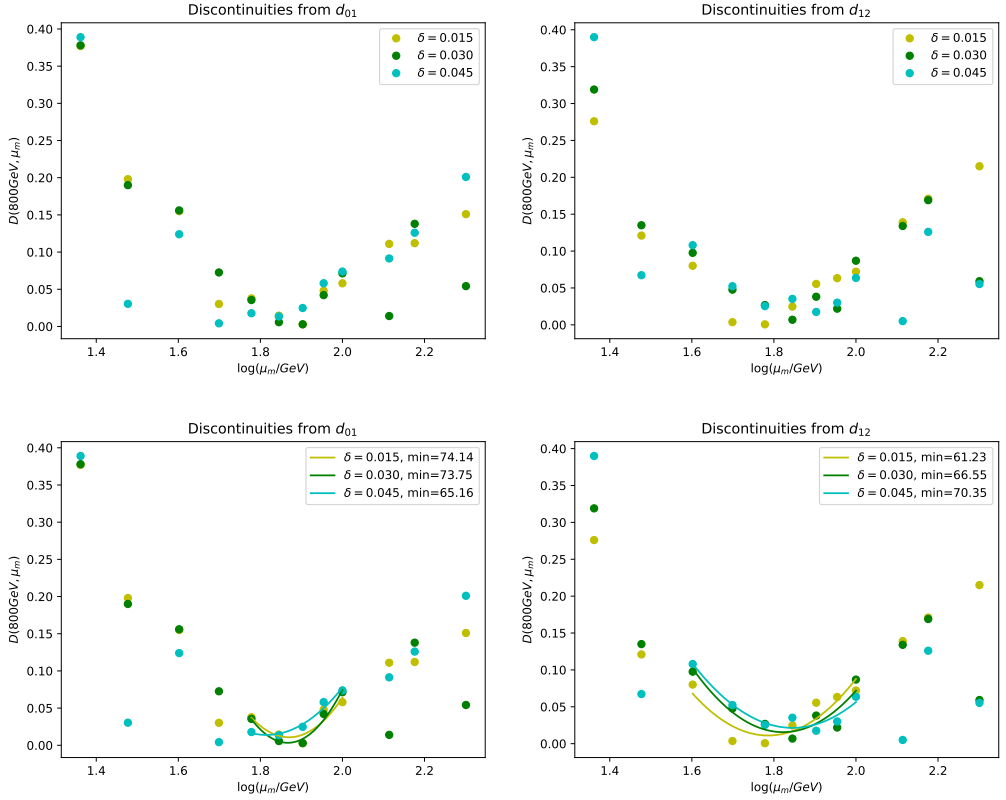
Figure 12.6: Discontinuity distributions from different bin sizes δ, with a hard scale of $Q = 800$ GeV. The results of all tested merging scales μ_m are shown. Parabolic fits are shown in the lower plots together with the merging scale values at the minima in the legends.

12.4 Multi-jet merging for DY+jets with varying masses

12.4.1 Jets associated with DY from 60 to 800 GeV

We have generated six sets of hard scattering Drell-Yan events in LHE format using MadGraph5_aMC@nlo [55]. These sets differ in the invariant mass of the di-lepton pairs which allows us to determine the relation between the optimal merging scale and the hard scale of the process.

The hard scattering events with a Z boson that decays to two leptons along with 0, 1, 2 or 3 jets are generated at a center-of-mass energy of $\sqrt{s} = 13$ TeV. A generation cut of $\mu_c = 16$ GeV is applied and the pseudorapidity of the leptons is limited to $\eta_l^{\max} = 2.7$. The default PDF used by MG5_aMC for generating momentum fractions and selecting parton flavours is NNPDF23_nlo_as_0119, which is globally fitted and has $\alpha_s(m_Z) = 0.119$.

Each set of LHE files contains $10^3 \times 10^5$ events, differing solely in the selection of hard scales Q, achieved by applying selection limits on the invariant di-lepton mass m_{ll}. With a

small lower limit $m_{ll}^{\min} = 40$ GeV, the majority of the events have a di-lepton invariant mass close to the resonance (Z boson) mass, $m_{ll} \simeq m_Z = 91.2$ GeV. For hard scale selections that are significantly larger than the mass of the Z boson, there is no need for an upper limit. This is due to the rapid fall-off of the mass distribution $(1/m_{ll}^4)$ such that the majority of events occur at masses close to the lower limit. However, for hard scale selections below the Z boson mass, both lower and upper limits on m_{ll} are necessary.

The following six large-scale scenarios are generated and analyzed in accordance with the previous subsections:

Q = 60 GeV.   At this scale, the DY mass distribution is relatively uniform. The generation of di-lepton masses near this value is only assured by imposing both lower and upper limits that are close to Q. We confine the di-lepton invariant mass between $m_{ll}^{\min} = 58$ GeV and $m_{ll}^{\max} = 62$ GeV. The generation cut is decreased to $\mu_c = 10$ GeV to enable us to lower the merging scale down to 16 GeV in this scenario.

Q = m$_{\mathbf{Z}}$ = 91.2 GeV.   With a lower di-lepton mass limit smaller than m_Z and no upper mass limit, inclusion of the resonance peak automatically guarantees that the majority of the events have $m_{ll} \simeq 91.2$ GeV. To avoid generating numerous hard virtual photons, a lower mass limit of $m_{ll}^{\min} = 40$ GeV is used.

Q = 250 GeV, Q = 400 GeV, Q = 600 GeV and Q = 800 GeV.   These hard scattering events were achieved through lower mass limits of $m_{ll}^{\min} = 250$ GeV, $m_{ll}^{\min} = 600$ GeV and $m_{ll}^{\min} = 800$ GeV, respectively.

Transverse momentum boosting, showering, and TMD merging are performed by CAS-CADE3 with PB-TMD-Set2 and merging parameters of $R_{\text{clus}} = 1.4$ and $\eta_{\text{clus}}^{max} = 5.0$. We performed this calculation multiple times with different merging scales within a wide range of values from 16 GeV up to 200 GeV.

DJRs are calculated for all six sets and applying the algorithm described in section 12.1 yields three sets of discontinuities for each hard scale. The differential cross sections $d\sigma/d\log(\sqrt{d_{i,(i+1)}/\text{GeV}^2})$ only include data from the i-jet and $(i+1)$-jet samples. Parabolic curves are fitted near the minimum of these distributions to determine a merging scale $\mu_{m,k}^{(0)}$. We calculated the bin size uncertainty using the formula presented in Eq. 12.9. Additionally, we performed statistical variations to determine statistical errors. The figures illustrating the results can be found in Fig. 12.7. Tabulated presentations of the results are detailed in Tab. 12.1 from the d_{01} analysis and in Tab. 12.2 from the analysis of d_{12}.

Overestimation of the merging scale appears to be less harmful than an underestimation of the merging scale because the discontinuity distribution has a less steep slope towards higher scales on the right of the minimum compared to the slope on the left. However, in logarithmic scale (as shown in Figs. 12.4 and 12.6), this picture gets shifted and the curve becomes more symmetric. At hard scales below and near the Z boson mass, specifically $Q = 60$ GeV and $Q = 91.2$ GeV, a large merging scale is unfavorable due to large discontinuities.
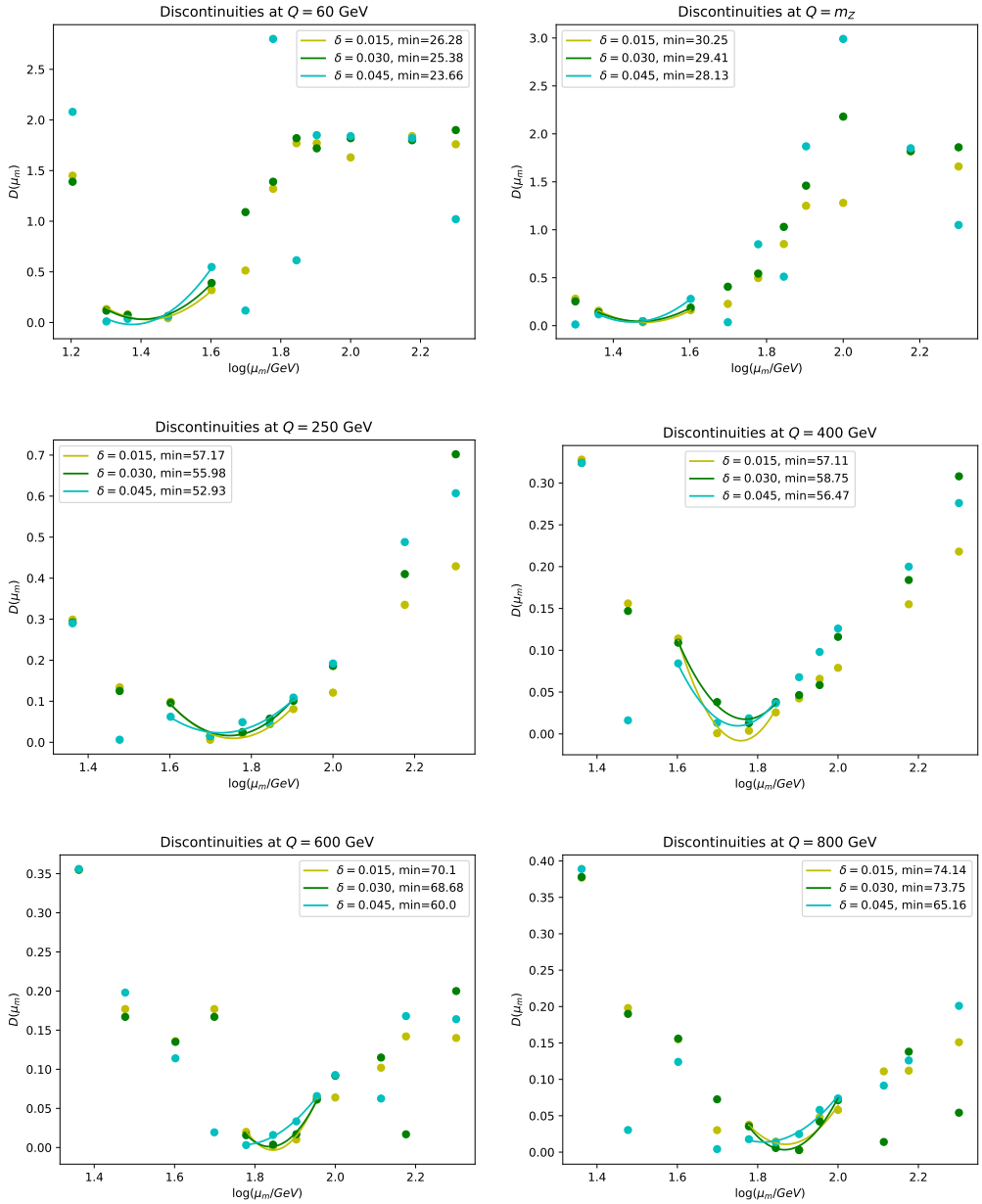
Figure 12.7: Discontinuity in d_{01} for samples of merging scales and a quadratic fit through points near the minimum.

The statistical uncertainty is small due to the large number of events in the DJRs d_{01} and d_{12}. The decision to use these DJRs was made to minimize the uncertainty and to eliminate additional dependence on the parton shower. The uncertainties associated with the bin size are large compared to the statistical fluctuations. On average, the uncertainty resulting from bin size variation is 3.4% for d_{01} and 2.7% for d_{12}.

Q (GeV)	$\Delta \log\left(\sqrt{d_{01}/\text{GeV}^2}\right)$			$\sigma_{bin.}$	$\sigma_{stat.}$	$\langle\mu_m^{(0)}\rangle \pm \sigma_{\mu_m}$ (GeV)
	0.015	0.030	0.045			
60.0	26.28	25.38	23.66	1.31	0.01	25.1 ± 1.4
91.2	30.25	29.41	28.13	1.06	0.03	29.3 ± 1.1
250.0	57.17	55.98	52.93	2.12	0.31	55.4 ± 2.2
400.0	57.11	58.75	56.47	1.14	0.28	57.4 ± 1.2
600.0	70.10	68.68	60.00	5.05	0.55	66.3 ± 5.1
800.0	74.14	73.75	65.16	4.49	0.34	71.0 ± 4.5

Table 12.1: Results of $\mu_m^{(0)}$ for different bin sizes within d_{01} distributions. The final central value $\langle\mu_m^{(0)}\rangle$ is obtained by averaging results from different bin sizes. The total uncertainty is given by σ_{μ_m}.

Q (GeV)	$\langle\mu_m^{(0)}\rangle \pm \sigma_{\mu_m}$ (GeV)
60.0	20.1 ± 1.4
91.2	26.2 ± 1.0
250.0	43.6 ± 2.0
400.0	58.4 ± 6.4
600.0	62.7 ± 4.4
800.0	66.0 ± 4.6

Table 12.2: Results of $\langle\mu_m^{(0)}\rangle$ obtained from d_{12} distributions. The total uncertainty is given by σ_{μ_m} including bin size uncertainties and statistical uncertainties.

12.4.2   Mass dependence of the merging scale

The results for $\langle\mu_m^{(0)}\rangle$ at various hard scales yield distributions $\mu_m^{(0)}(Q)$ that are shown in Fig. 12.8. Our analysis shows that the merging scale results are non-linearly dependent on the hard scale, which contradicts the ansatz given in Sec. 12.1, stating that the merging scale should be between one-sixth and one-third of the hard scale. A suppression of the merging scale towards large Q is observed. Thus, we propose a new ansatz that depends on the di-lepton mass as follows:

$$\mu_m^{(0)}(m_{ll}) = m_Z \left(a + b \ln\left(\frac{m_{ll}}{m_Z}\right)\right) \tag{12.15}$$

where the Z boson mass serves as a regulator to fix the units.

Fitting the functional form presented in Eq. (12.15) to the data yields values for a and b. When applied to the data from d_{01}, the fit produces:

$$\mu_m^{(0)}(m_{ll}) = m_Z \left(0.34 + 0.20 \ln\left(\frac{m_{ll}}{m_Z}\right)\right) . \tag{12.16}$$

A fit to the data from d_{12} results in:

$$\mu_m^{(0)}(m_{ll}) = m_Z \left(0.29 + 0.20 \ln\left(\frac{m_{ll}}{m_Z}\right)\right) . \tag{12.17}$$

The formulae (12.16) and (12.17) possess multiple characteristics, which we outline here.
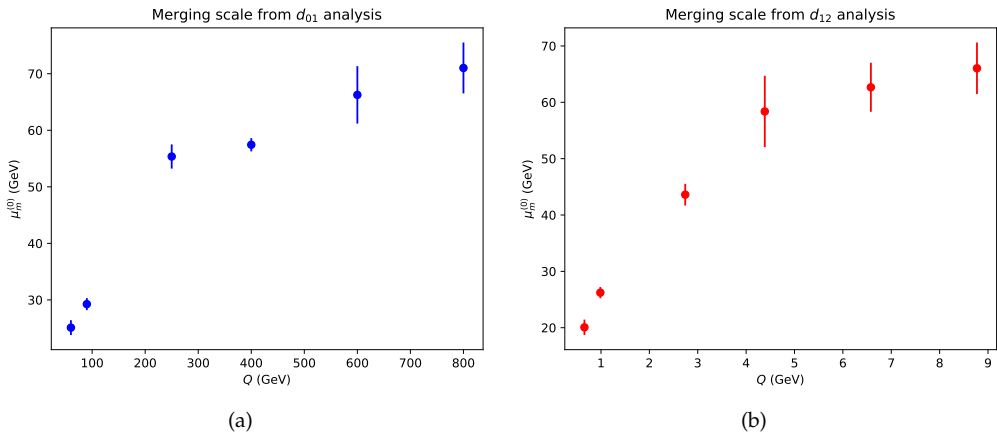
Figure 12.8: Data of ideal merging scales $\mu_m^{(0)}$ against the hard scale Q obtained from minimum discontinuities in d_{01} (left) and d_{12} (right).

- In the limit of Q approaching m_Z, the merging scale is approximately 30 GeV, which is equivalent to one-third of the Z boson's mass. This aligns with the merging scale that has been used in earlier studies where the Z boson's mass was included in the phase space. In this scenario, there is no logarithmic correction. It is crucial to note that these results serve as guidelines for the merging scale, and a slight variance should not significantly impact the outcome.

- When the hard scale reaches 20 GeV, the merging scale becomes zero and interaction energies below 20 GeV would imply negative merging scales. At these energies, calculating DY cross sections using multi-jet merging is not considered appropriate.

- There is a singularity present at the value of $Q = 0$. This is an unphysical hard scale, i.e. no interaction takes place at 0 GeV, let alone an interaction including jets.

These are all limits and properties that confirm the accuracy of the obtained relations. Figure 12.9 shows the data points and results from Eqs. (12.16) and (12.17) together.
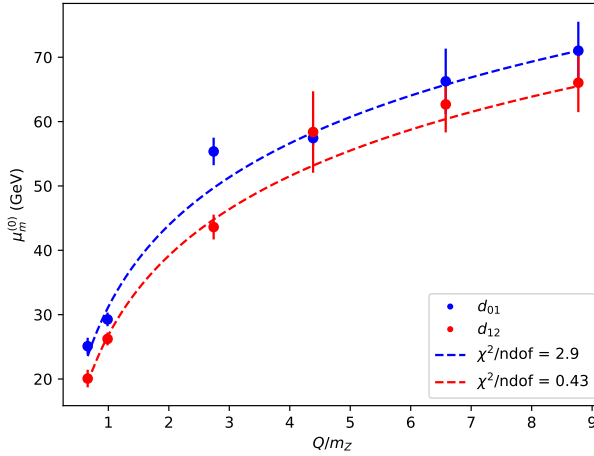
Figure 12.9: Merging scale distribution versus the hard scale.

12.5   Conclusion

For the first time, a method has been developed to quantify the discontinuity in differential jet rates. This is a means to study the effect of the merging scale in extreme kinematic configurations in the LO TMD merging approach that is partially based on MLM. Other effects that might cause discontinuities in DJRs, such as the mismatch of parton shower resolution scales and matrix element generation cuts causing gaps in the phase space that can be overcome by applying truncated showers [108], have not been addressed in this study and are assumed to be uncorrelated to the dependence of the merging scale on the hard scale.

The studies presented in this chapter have been performed in the Drell-Yan framework, where the hard scale is equivalent to the di-lepton invariant mass. Multiple hard scales, as in the case of pure QCD multi-jet events, increase the complexity of the issue. Similar examinations may be carried out on pure multi-jet events. However, identification of the hard scale becomes more challenging. It is unclear what the characteristic scale is, or whether multiple scales must be accounted for in these situations. A possible factor to consider would be the scalar sum of transverse momenta of the leading di-jet system.

High mass DY events indicate that a merging scale that is logarithmically dependent on the di-lepton mass is consistent. This yields fits with Chi-squared values that are near 1, and the fits resulting from analyses of d_{01} and d_{12} are highly similar.

We conclude that for DY events, the merging scale depends logarithmically on the di-lepton mass, or equivalently, on the process's hard scale.

Conclusions

In this thesis we have explored several strands of research into the Parton Branching approach to TMD dynamics at high energy colliders, and obtained new results which advance significantly the accuracy of transverse momentum dependent parton branching methods and their applications.

After the first three introductory review chapters (Chapters 1, 2 and 3), the thesis' key achievements have been the following.

i) The study of phase-space constraints from soft-gluon angular ordering in PB TMD evolution equations in Chapter 5, particularly concerning the soft-gluon resolution scale [42], has allowed us to establish the relationship of PB TMD results with results from two widely-used approaches, the coherent-branching CMW approach and the single-emission KMRW approach. Furthermore, this study has allowed us to decompose the PB TMD Sudakov form factor [48] into perturbative and non-perturbative components, which we have analyzed in Chapter 6. Perturbatively, we have advanced the Sudakov logarithmic accuracy of the PB TMD method to NNLL level, by exploiting the physical soft-gluon coupling and its relationship with the collinear anomaly, on one hand, and with the Collins-Soper kernel, on the other hand. Non-perturbatively, we have performed the numerical determination of the large-distance, non-perturbative Sudakov effects embodied in the Collins-Soper kernel, based on the PB TMD evaluation of DY cross sections at small transverse momenta and varying masses.

A software tool providing a collection of fits and parameterizations of non-perturbative TMD distributions, TMDLib2 [40], has been presented in Chapter 4.

ii) A parton shower MC event generator, Cascade3 [51], has been presented in Chapter 7, based on the PB TMD approach investigated in the previous chapters. Here the Sudakov form factor for backward initial-state showering is given, dependent on TMD distributions. This is the key ingredient to construct the TMD parton shower. The Cascade3 MC is a full hadron-level generator, including final-state showering, hadronization, and options for interfacing the showers with hard scattering matrix elements, such as "matching" and "merging" algorithms. Both such algorithms have been used to compute PB TMD predictions for LHC processes.

iii) NLO "matched" predictions have been obtained for azimuthal $\Delta\phi$ correlations of di-jet and Z+jet final states in Chapters 8 and 9, respectively, focusing on TMD effects near the back-to-back region across a broad kinematic range in the leading transverse momentum. Experimental measurements of nearly back-to-back di-jets at the LHC have been shown to be described well by theoretical predictions in which the form of the QCD running coupling dictated by soft-gluon angular ordering is used [56].

Possible factorization-breaking effects have long been conjectured to arise in the back-to-

back region due to soft-gluon interactions between initial and final states. It has been proposed that the combined analysis of $\Delta\phi$ correlations in di-jet and Z+jet events can afford further insight into this, by exploiting the fact that at low p_T the boson-jet state is more strongly correlated azimuthally than the jet-jet state, while for p_T far above the electroweak scale the behaviors become more similar, and performing systematic measurements for the cases of strong and weak azimuthal correlations [57].

iv) TMD "merging" has been applied to multi-jet final states in Chapter 11 and to Z+jets final states in Chapter 12 (after a brief introduction of the method in Chapter 10). In Chapter 11, merged predictions have been computed for several observables in multi-jet production at the LHC: jet transverse momenta, multiplicities and event shapes, including thrust, sphericity, aplanarity, C- and D-parameters. A phenomenological comparison has been carried out with measurements performed by LHC experiments. This illustrates that, by incorporating TMD evolution, the TMD merging approach is able to capture detailed features of multi-jet events also at high multiplicities, well beyond the number of partons generated in the fixed-order matrix element samples [60]. In Chapter 12 an investigation has been performed into the dependence of merged predictions on the hard scale of the underlying hard scattering process, using the example of Z+jets production with varying vector-boson invariant mass, from below the Z mass up to 800 GeV. The main finding has been the determination of a "sliding", i.e. hard scale dependent, merging scale [61]. By a thorough analysis of the differential jet rates associated with Z production across the examined mass range, we have determined a logarithmic increase in the merging scale with invariant mass.

Coefficients of perturbative functions of the DGLAP splitting functions

In this appendix we denote the perturbative coefficients of the virtual terms of the DGLAP splitting functions and the cusp anomalous dimension which are used throughout this work. These are taken from the literature [38, 208, 300] and determined with identical conventions. We use an expansion in powers of $\alpha_s/2\pi$ whereas in the literature, expansions in $\alpha_s/4\pi$ or α_s/π are also commonly used.

The splitting functions P_{ab} were subdivided in three functions that can be written as series expansions in the running coupling α_s:

$$d_a(\alpha_s) = \sum_{n=1}^{\infty} \left(\frac{\alpha_s}{2\pi}\right)^n d_a^{(n-1)}, \qquad k_a(\alpha_s) = \sum_{n=1}^{\infty} \left(\frac{\alpha_s}{2\pi}\right)^n k_a^{(n-1)}, \tag{A.1}$$

$$R_{ab}(\alpha_s, z) = \sum_{n=1}^{\infty} \left(\frac{\alpha_s}{2\pi}\right)^n R_{ab}^{(n-1)}(z), \tag{A.2}$$

where a and b are flavor indices for either quarks $a = q$, antiquarks $a = \bar{q}$ or gluons $a = g$.

The cusp anomalous dimension, as defined in the CSS2 formalism, has the following perturbative expansion

$$\gamma_K^{\mathrm{cusp}}(\alpha_s) = \sum_{n=1}^{\infty} \left(\frac{\alpha_s}{2\pi}\right)^n \gamma_K^{(n-1)}. \tag{A.3}$$

The leading order coefficients of the DGLAP splitting functions for both quark and gluon

splittings are given by

$$k_{q_i}^{(0)} = 2C_F = \gamma_K^{(0)}/2, \qquad\qquad\qquad k_g^{(0)} = 2C_A, \qquad\qquad\qquad \text{(A.4)}$$

$$d_{q_i}^{(0)} = \frac{3}{2}C_F, \qquad\qquad\qquad\qquad d_g^{(0)} = \frac{11}{6}C_A - \frac{2}{3}T_F N_f, \qquad \text{(A.5)}$$

$$R_{gg}^{(0)}(z) = 2C_A \left(\frac{1-z}{z} + z(1-z) - 1 \right), \qquad\qquad\qquad\qquad\quad \text{(A.6)}$$

$$R_{gq_i}^{(0)}(z) = R_{g\bar{q}_i}^{(0)}(z) = C_F \frac{1 + (1-z)^2}{z}, \qquad\qquad\qquad\qquad\quad \text{(A.7)}$$

$$R_{q_i g}^{(0)}(z) = R_{\bar{q}_i g}^{(0)}(z) = T_R \left(z^2 + (1-z)^2 \right), \qquad\qquad\qquad\qquad \text{(A.8)}$$

$$R_{q_i q_j}^{(0)}(z) = R_{\bar{q}_i \bar{q}_j}^{(0)}(z) = -C_F(1+z)\delta_{ij}, \qquad R_{\bar{q}_i q_j}^{(0)} = R_{q_i \bar{q}_j}^{(0)} = 0, \qquad \text{(A.9)}$$

with the quark color factor $C_F = \frac{N_c^2 - 1}{2N_c} = 3/2$, gluon color factor $C_A = 3$ and trace invariant $T_F = 1/2$.

At next-to-leading order (NLO), the coefficients of $k_a(\alpha_s)$ and $d_a(\alpha_s)$ are given by

$$k_q^{(1)} = 2C_F\gamma_K^{(1)} = 2C_F C_A \left(\frac{67}{18} - \frac{\pi^2}{6} \right) - \frac{20}{9}C_F T_R N_f, \qquad\qquad \text{(A.10)}$$

$$k_g^{(1)} = 2C_A\gamma_K^{(1)} = 2C_A^2 \left(\frac{67}{18} - \frac{\pi^2}{6} \right) - \frac{20}{9}C_A T_R N_f, \qquad\qquad \text{(A.11)}$$

$$d_q^{(1)} = C_F^2 \left(\frac{3}{8} - \frac{\pi^2}{2} + 6\zeta(3) \right) + C_F C_A \left(\frac{17}{24} + \frac{11}{18}\pi^2 - 3\zeta(3) \right) - C_F T_R N_f \left(\frac{1}{6} + \frac{2}{9}\pi^2 \right), \quad \text{(A.12)}$$

$$d_g^{(1)} = C_A^2 \left(\frac{8}{3} + 3\zeta(3) \right) - \frac{4}{3}C_A T_R N_f - C_F T_R N_f. \qquad\qquad\qquad \text{(A.13)}$$

The two-loop contributions $R_{ab}^{(1)}$ are given for quark-gluon and gluon-gluon cases by

$$
\begin{aligned}
R_{gq}^{(1)}(z) \;=\; & C_F^2 \Big[-\frac{5}{2} - \frac{7}{2}z + \left(2 + \frac{7}{2}z \right)\ln z + \left(\frac{1}{2}z - 1 \right)\ln^2 z - 2z\ln(1-z) \\
& -\; \left(3\ln(1-z) + \ln^2(1-z) \right)p_{gq}(z) \Big] + C_F C_A \Big[\frac{28}{9} + \frac{65}{18}z + \frac{44}{9}z^2 \\
& +\; \left(-12 - 5z - \frac{8}{3}z^2 \right)\ln z + (4+z)\ln^2 z + 2z\ln(1-z) + p_{gq}(z) \\
& \times\; \left(-2\ln z\ln(1-z) + \frac{1}{2}\ln^2 z + \frac{11}{3}\ln(1-z) + \ln^2(1-z) - \frac{\pi^2}{6} + \frac{1}{2} \right) \\
& +\; p_{gq}(-z)S_2(z) \Big] + C_F T_R N_f \Big[-\frac{4}{3}z - \left(\frac{20}{9} + \frac{4}{3}\ln(1-z) \right)p_{gq}(z) \Big], \qquad \text{(A.14)}
\end{aligned}
$$

$$
\begin{aligned}
R_{qg}^{(1)}(z) &= \frac{1}{2}C_F T_R\Big[4 - 9z + (-1 + 4z)\ln z + (-1 + 2z)\ln^2 z + 4\ln(1 - z)\\
&+ \Big(-4\ln z\ln(1 - z) + 4\ln z + 2\ln^2 z - 4\ln(1 - z) + 2\ln^2(1 - z)\\
&- \frac{2}{3}\pi^2 + 10\Big)p_{qg}(z)\Big] + \frac{1}{2}C_A T_R\Big[\frac{182}{9} + \frac{14}{9}z + \frac{40}{9z} + \Big(\frac{136}{3}z - \frac{38}{3}\Big)\ln z\\
&- 4\ln(1 - z) - (2 + 8z)\ln^2 z + \Big(-\ln^2 z + \frac{44}{3}\ln z - 2\ln^2(1 - z)\\
&+ 4\ln(1 - z) + \frac{\pi^2}{3} - \frac{218}{9}\Big)p_{qg}(z) + 2p_{qg}(-z)S_2(z)\Big]
\end{aligned}
\tag{A.15}
$$

and

$$
\begin{aligned}
R_{gg}^{(1)}(z) &= C_F T_R N_f\Big[-16 + 8z + \frac{20}{3}z^2 + \frac{4}{3z} + (-6 - 10z)\ln z + (-2 - 2z)\ln^2 z\Big]\\
&+ C_A T_R N_f\Big[2 - 2z + \frac{26}{9}z^2 - \frac{26}{9z} - \frac{4}{3}(1 + z)\ln z - \frac{20}{9}\Big(\frac{1}{z} - 2 + z - z^2\Big)\Big]\\
&+ C_A^2\Big[\frac{27}{2}(1 - z) + \frac{67}{9}\Big(z^2 - \frac{1}{z}\Big) + \Big(-\frac{25}{3} + \frac{11}{3}z - \frac{44}{3}z^2\Big)\ln z\\
&+ 4(1 + z)\ln^2 z + 2p_{gg}(-z)S_2(z) + \Big(-4\ln z\ln(1 - z) + \ln^2 z\Big)p_{gg}(z)\\
&+ \Big(\frac{67}{9} - \frac{\pi^2}{3}\Big)\Big(\frac{1}{z} - 2 + z - z^2\Big)\Big].
\end{aligned}
\tag{A.16}
$$

$$
\begin{aligned}
R_{qq}^{(1)}(z) &= C_F^2\Big[-1 + z + \Big(\frac{1}{2} - \frac{3}{2}z\Big)\ln z - \frac{1}{2}\Big(1 + z\Big)\ln^2 z + 2p_{qq}(-z)S_2(z)\\
&- \Big(\frac{3}{2}\ln z + 2\ln z\ln(1 - z)\Big)p_{qq}(z)\Big]\\
&+ C_F C_A\Big[\frac{14}{3}(1 - z) - p_{qq}(-z)S_2(z) + \Big(\frac{11}{6}\ln z + \frac{1}{2}\ln^2 z\Big)p_{qq}(z)\\
&- (z + 1)\Big(\frac{67}{18} - \frac{\pi^2}{6}\Big)\Big] + C_F T_R N_f\Big[-\frac{16}{3} + \frac{40}{3}z + \Big(10z + \frac{16}{3}z^2 + 2\Big)\\
&\times \ln z - \frac{112}{9}z^2 + \frac{40}{9z} - 2(1 + z)\ln^2 z - \frac{2}{3}\ln z p_{qq}(z) + \frac{10}{9}(z + 1)\Big].
\end{aligned}
\tag{A.17}
$$

The next-to-next-to-leading order (NNLO) coefficients $k_a^{(2)}$ are related to the cusp-anomalous dimension and given by [300]

$$
\begin{aligned}
k_q^{(2)} = 2C_F\gamma_K^{(2)} = 2C_F\Big[&C_A^2\Big(\frac{245}{24} - \frac{67}{54}\pi^2 + \frac{11}{6}\zeta(3) + \frac{11}{180}\pi^4\Big) - C_F N_f\Big(\frac{55}{24} - 2\zeta(3)\Big) +\\
&+ C_A N_f\Big(-\frac{209}{108} + \frac{10}{54}\pi^2 - \frac{7}{3}\zeta(3)\Big) - \frac{1}{27}N_f^2\Big]
\end{aligned}
\tag{A.18}
$$

and

$$k_g^{(2)} = 2C_A \left[C_A^2 \left(\frac{245}{24} - \frac{67}{54}\pi^2 + \frac{11}{6}\zeta(3) + \frac{11}{180}\pi^4 \right) - C_F N_f \left(\frac{55}{24} - 2\zeta(3) \right) + \right.$$

$$\left. + C_A N_f \left(-\frac{209}{108} + \frac{10}{54}\pi^2 - \frac{7}{3}\zeta(3) \right) - \frac{1}{27}N_f^2 \right] \qquad\qquad \text{(A.19)}$$

Coefficients of perturbative functions of the CSS Sudakov form factor

The CSS coefficients are taken from [207]. To make the comparison with Appendix A easier, we redefine them slightly by using the following definition of the perturbative functions:

$$
A_a(\alpha_s) = \sum_{n=1}^{\infty} \left(\frac{\alpha_s}{2\pi} \right)^n A_a^{(n)}, \qquad B_a(\alpha_s) = \sum_{n=1}^{\infty} \left(\frac{\alpha_s}{2\pi} \right)^n B_a^{(n)}, \tag{B.1}
$$

instead of the originally [207] used $A_a(\alpha_s) = \sum_{n=1}^{\infty} \left(\frac{\alpha_s}{\pi} \right)^n A_a^{(n)}$ (and analogous for B_a).

The LO coefficients of these functions are:

$$
A_q^{(1)} = 2C_F, \qquad\qquad A_g^{(1)} = 2C_A \tag{B.2}
$$

$$
B_q^{(1)} = -3C_F, \qquad\qquad B_g^{(1)} = -\frac{1}{3}(11C_A - 2N_f). \tag{B.3}
$$

The NLO coefficients are:

$$
A_a^{(2)} = 2C_a C_A \left(\frac{67}{18} - \frac{\pi^2}{6} \right) - \frac{20}{9} C_a N_f T_R, \tag{B.4}
$$

$$
B_q^{(2)} = C_F^2 \left(\pi^2 - \frac{3}{4} - 12\zeta(3) \right) + C_F C_A \left(\frac{11}{9}\pi^2 - \frac{193}{12} + 6\zeta(3) \right) + C_F T_R N_f \left(\frac{17}{3} - \frac{4}{9}\pi^2 \right). \tag{B.5}
$$

$$
B_g^{(2)} = C_A^2 \left(\frac{23}{6} + \frac{22}{9}\pi^2 - 6\zeta(3) \right) + 2C_F N_f - C_A N_f \left(\frac{1}{3} + \frac{4}{9}\pi^2 \right) - \frac{11}{2} C_F C_A \tag{B.6}
$$

where the $B_a^{(2)}$ coefficients are given in DY resummation scheme [207]. The color index $a = \{q, g\}$ indicates that for quarks $a = q$, the colour factor is C_F and for gluons $a = g$, the colour factor is C_A.

The NNLO coefficient of $A_q(\alpha_s)$ is

$$
A_q^{(3)} = C_A^2 \left(\frac{245}{24} - \frac{67}{9}\zeta_2 + \frac{11}{6}\zeta_3 + \frac{11}{5}\zeta_2^2 \right) + C_F N_f \left(-\frac{55}{24} + 2\zeta_3 \right) \tag{B.7}
$$

$$
+ C_A N_f \left(-\frac{209}{108} + \frac{10}{9}\zeta_2 - \frac{7}{3}\zeta_3 \right) - \frac{1}{27}N_f^2 + \frac{\pi\beta_0}{2} \left(C_A \left(\frac{808}{27} - 28\zeta_3 \right) - \frac{224}{54}N_f \right).
$$

CASCADE3 **documentation**

In CASCADE3 all variables are declared as `Double Precision`. With CASCADE3 the source of PYTHIA6.428 is included to avoid difficulties in linking.

Random Numbers

CASCADE3 uses the `RANLUX` [301] random number generator, with luxory level `LUX = 4`. The random number seed can be set via the environment variable `CASEED`, the default value is `CASEED=12345`.

Event Output

When `HEPMC` is included, generated events are written out in HEPMC [81] format for further processing. The environment variable `HEPMCOUT` is used to specify the file name, by default this variable is set to `HEPMCOUT=/dev/null`.

The HEPMC events can be further processed, for example with RIVET [83].

Input parameters

The input parameters are steered via steering files. The new format of steering is discussed in the next subsection and should be used when reading LHE files, while the other format, which is appropriate for the internal off-shell processes, is discussed in the subsection after that.

Examples for steering files are under `$install_path/share/cascade/LHE`.

Steering file

```
&CASCADE_input
NrEvents = -1              ! Nr of events to process
Process_Id = -1            ! Read LHE file
Hadronisation = 0          ! Hadronisation (on =1, off = 0)
SpaceShower = 1            ! Space-like Parton Shower
SpaceShowerOrderAlphas=2   ! Order alphas in Space Shower
TimeShower = 1            ! Time-like Parton Shower
ScaleTimeShower = 4        ! Scale choice for Time-like Shower
!                               1: 2(m^2_1t+m^2_2t)
!                               2: shat
!                               3: 2(m^2_1+m^2_2)
!                               4: 2*scalup (from lhe file)
!ScaleFactorFinalShower = 1.   ! scale factor for Final State Parton Shower
PartonEvolution = 2            ! type of parton evolution in Space-like Shower
!                               1: CCFM
!                               2: full all flavor TMD evolution
! EnergyShareRemnant = 4       ! energy sharing in proton remnant
!                               1: (a+1)(1-z)**a, <z>=1/(a+2)=1/3
!                               2: (a+1)(1-z)**a, <z>=1/(a+2)=mq/(mq+mQ
!                               3: N/(z(1-1/z-c/(1-z))**2), c=(mq/mQ)**2
!                               4: PYZDIS: KFL1=1
! Remnant = 0                  ! =0 no remnant treatment
PartonDensity = 102200        ! use TMDlib: PB-TMDNLO-set2
! PartonDensity = 102100       ! use TMDlib: PB-TMDNLO-set1
! TMDDensityPath= './share'    ! Path to TMD density for internal files
Uncertainty_TMD = 0                      ! calculate and store uncertainty TMD pdfs
lheInput='MCatNLO-example.lhe' ! LHE input file
lheHasOnShellPartons = 1       ! = 0 LHE file has off-shell parton configuration
lheReweightTMD = 0             ! Reweight with new TMD  given in PartonDensity
lheScale = 2                  ! Scale defintion for TMD
!                               0: use scalup
!                               1: use shat
!                               2: use 1/2 Sum pt^2 of final parton/particles
!                               3: use shat for Born and 1/2 Sum pt^2 of final parton(particle)
!                               4: use shat for Born and max pt of most forward/backward
!                                  parton(particle)
lheNBornpart = 2              ! Nr of hard partons (particles) (Born process)
ScaleFactorMatchingScale = 2. ! Scale factor for matching scale when including TMDs
&End


&PYTHIA6_input
P6_Itune = 370               ! Retune of Perugia 2011 w CTEQ6L1 (Oct 2012)
! P6_MSTJ(41) = 1            ! (D = 2) type of branchings allowed in shower.
!                               1: only QCD
!                               2: QCD and photons off quarks and leptons
P6_MSTJ(45) = 4             ! Nr of flavors in final state shower: g->qqbar
P6_PMAS(4,1)= 1.6           ! charm mass
P6_PMAS(5,1)= 4.75          ! bottom mass
P6_MSTJ(48) =  1            ! (D=0), 0=no max. angle, 1=max angle def. in PARJ(85)
! P6_MSTU(111) = 1          ! = 0 : alpha_s is fixed, =1 first order; =2 2nd order;
! P6_PARU(112) = 0.2        ! lambda QCD
P6_MSTU(112)=   4          ! nr of flavours wrt lambda_QCD
P6_MSTU(113)=             ! min nr of flavours for alphas
P6_MSTU(114)=   5          ! max nr of flavours for alphas
&End
```

Program Summary

Title of Program: Cascade3.1.0

Computer for which the program is designed and others on which it is operable: any with standard Fortran77 (gfortran)

Programming Language used: FORTRAN77

High-speed storage required: No

Keywords: QCD, TMD parton distributions.

Method of solution: Since measurements involve complex cuts and multi-particle final states, the ideal tool for any theoretical description of the data is a Monte Carlo event generator which generates initial state parton showers according to Transverse Momentum Dependent (TMD) parton densities, in a backward evolution, which follows the evolution equation as used for the determination of the TMD.

Restrictions on the complexity of the problem: Any LHE file (with on-shell or off-shell) initial state partons can be processed.

Other Program used: Pythia (*version > 6.4*) for final state parton shower and hadronization, Bases/Spring 5.1 for integration (both supplied with the program package), TMDlib as a library for TMD parton densities.

Bibliography

[1] Simone Alioli et al. "Monte Carlo event generators for high energy particle physics event simulation". In: (Feb. 2019). Ed. by Andy Buckley et al. arXiv: `1902.01674` `[hep-ph]`.

[2] P. Azzi et al. "Report from Working Group 1: Standard Model Physics at the HL-LHC and HE-LHC". In: *CERN Yellow Rep. Monogr.* 7 (2019). Ed. by Andrea Dainese et al., pp. 1–220. DOI: `10.23731/CYRM-2019-007.1`. arXiv: `1902.04070` `[hep-ph]`.

[3] Jonathan L. Feng et al. "The Forward Physics Facility at the High-Luminosity LHC". In: *J. Phys. G* 50.3 (2023), p. 030501. DOI: `10.1088/1361-6471/ac865e`. arXiv: `2203.05090` `[hep-ex]`.

[4] P. Agostini et al. "The Large Hadron–Electron Collider at the HL-LHC". In: *J. Phys. G* 48.11 (2021), p. 110501. DOI: `10.1088/1361-6471/abf3ba`. arXiv: `2007.14491` `[hep-ex]`.

[5] *Proceedings, Probing Nucleons and Nuclei in High Energy Collisions: Dedicated to the Physics of the Electron Ion Collider: Seattle (WA), United States, October 1 - November 16, 2018*. WSP, Feb. 2020. DOI: `10.1142/11684`. arXiv: `2002.12333` `[hep-ph]`.

[6] M. L. Mangano et al. "Physics at a 100 TeV pp Collider: Standard Model Processes". In: (July 2016). DOI: `10.23731/CYRM-2017-003.1`. arXiv: `1607.01831` `[hep-ph]`.

[7] R.K.Ellis, W.J.Stirling, and B.R.Webber. *QCD and Collider Physics*. Cambridge University Press, 2003.

[8] G. Dissertori, I. G. Knowles, and M. Schmelling. *High energy experiments and theory*. 2003.

[9] John Campbell, Joey Huston, and Frank Krauss. *The Black Book of Quantum Chromodynamics : a Primer for the LHC Era*. Oxford University Press, 2018. ISBN: 978-0-19-965274-7. DOI: `10.1093/oso/9780199652747.001.0001`.

[10] G. Marchesini and B. R. Webber. "Monte Carlo Simulation of General Hard Processes with Coherent QCD Radiation". In: *Nucl. Phys.* B310 (1988), pp. 461–526. DOI: `10.1016/0550-3213(88)90089-2`.

[11] B. R. Webber. "Monte Carlo Simulation of Hard Hadronic Processes". In: *Ann. Rev. Nucl. Part. Sci.* 36 (1986), pp. 253–286. DOI: `10.1146/annurev.ns.36.120186.001345`.

[12] G. Marchesini and B. R. Webber. "Simulation of QCD Jets Including Soft Gluon Interference". In: *Nucl. Phys.* B238 (1984), pp. 1–29. DOI: `10.1016/0550-3213(84)90463-2`.

[13] Hans-Uno Bengtsson and Torbjorn Sjostrand. "The Lund Monte Carlo for Hadronic Processes: Pythia Version 4.8". In: *Comput. Phys. Commun.* 46 (1987), p. 43. DOI: `10.1016/0010-4655(87)90036-1`.

[14] Torbjorn Sjostrand and Mats Bengtsson. "The Lund Monte Carlo for Jet Fragmentation and e+ e- Physics. Jetset Version 6.3: An Update". In: *Comput. Phys. Commun.* 43 (1987), p. 367. DOI: `10.1016/0010-4655(87)90054-3`.

[15] Bo Andersson et al. "Parton Fragmentation and String Dynamics". In: *Phys. Rept.* 97 (1983), pp. 31–145. DOI: `10.1016/0370-1573(83)90080-7`.

[16] Gavin Bewick et al. "Logarithmic accuracy of angular-ordered parton showers". In: *JHEP* 04 (2020), p. 019. DOI: `10.1007/JHEP04(2020)019`. arXiv: `1904.11866` `[hep-ph]`.

[17] Florian Herren et al. "A new approach to color-coherent parton evolution". In: (Aug. 2022). arXiv: `2208.06057` `[hep-ph]`.

[18] Leif Gellersen, Stefan Höche, and Stefan Prestel. "Disentangling soft and collinear effects in QCD parton showers". In: *Phys. Rev. D* 105.11 (2022), p. 114012. DOI: `10.1103/PhysRevD.105.114012`. arXiv: `2110.05964` `[hep-ph]`.

[19] Zoltán Nagy and Davison E. Soper. "Summations of large logarithms by parton showers". In: *Phys. Rev. D* 104.5 (2021), p. 054049. DOI: `10.1103/PhysRevD.104.054049`. arXiv: `2011.04773` `[hep-ph]`.

[20] Zoltán Nagy and Davison E. Soper. "Summations by parton showers of large logarithms in electron-positron annihilation". In: (Nov. 2020). arXiv: `2011.04777` `[hep-ph]`.

[21] Jeffrey R. Forshaw, Jack Holguin, and Simon Plätzer. "Building a consistent parton shower". In: *JHEP* 09 (2020), p. 014. DOI: `10.1007/JHEP09(2020)014`. arXiv: `2003.06400` `[hep-ph]`.

[22] Jack Holguin, Jeffrey R. Forshaw, and Simon Plätzer. "Improvements on dipole shower colour". In: *Eur. Phys. J. C* 81.4 (2021), p. 364. DOI: `10.1140/epjc/s10052-021-09145-1`. arXiv: `2011.15087` `[hep-ph]`.

[23] Silvia Ferrario Ravasio et al. "A parton shower with higher-logarithmic accuracy for soft emissions". In: (July 2023). arXiv: `2307.11142` `[hep-ph]`.

[24] Melissa van Beekveld et al. "PanScales parton showers for hadron collisions: formulation and fixed-order studies". In: *JHEP* 11 (2022), p. 019. DOI: `10.1007/JHEP11(2022)019`. arXiv: `2205.02237` `[hep-ph]`.

[25] Keith Hamilton et al. "Colour and logarithmic accuracy in final-state parton showers". In: *JHEP* 03.041 (2021), p. 041. DOI: `10.1007/JHEP03(2021)041`. arXiv: `2011.10054` `[hep-ph]`.

[26] Mrinal Dasgupta et al. "Parton showers beyond leading logarithmic accuracy". In: *Phys. Rev. Lett.* 125.5 (2020), p. 052002. DOI: `10.1103/PhysRevLett.125.052002`. arXiv: `2002.11114` `[hep-ph]`.

[27] John C. Collins and F. Hautmann. "Soft gluons and gauge invariant subtractions in NLO parton shower Monte Carlo event generators". In: *JHEP* 03 (2001), p. 016. DOI: `10.1088/1126-6708/2001/03/016`. arXiv: `hep-ph/0009286`.

[28] John C. Collins and Xiaomin Zu. "Initial state parton showers beyond leading order". In: *JHEP* 03 (2005), p. 059. DOI: `10.1088/1126-6708/2005/03/059`. arXiv: `hep-ph/0411332`.

[29] F. Hautmann and H. Jung. "Collinearity approximations and kinematic shifts in partonic shower algorithms". In: *Eur. Phys. J. C*72 (2012), p. 2254. DOI: `10.1140/epjc/s10052-012-2254-0`. arXiv: `1209.6549` `[hep-ph]`.

[30] S. Dooling et al. "Longitudinal momentum shifts, showering, and nonperturbative corrections in matched next-to-leading-order shower event generators". In: *Phys. Rev.* D87.9 (2013), p. 094009. DOI: `10.1103/PhysRevD.87.094009`. arXiv: `1212.6164` `[hep-ph]`.

[31] F. Hautmann. "Hadron structure and parton branching beyond collinear approximations". In: *Probing Nucleons and Nuclei in High Energy Collisions: Dedicated to the Physics of the Electron Ion Collider*. 2020, pp. 229–233. DOI: `10.1142/9789811214950_0047`. arXiv: `1912.13397` `[hep-ph]`.

[32] Marcello Ciafaloni. "Coherence Effects in Initial Jets at Small q**2 / s". In: *Nucl. Phys.* B296 (1988), pp. 49–74. DOI: `10.1016/0550-3213(88)90380-X`.

[33] S. Catani, M. Ciafaloni, and F. Hautmann. "High-energy factorization and small x heavy flavor production". In: *Nucl. Phys.* B366 (1991), pp. 135–188. DOI: `10.1016/0550-3213(91)90055-3`.

[34] R. Angeles-Martinez et al. "Transverse Momentum Dependent (TMD) parton distribution functions: status and prospects". In: *Acta Phys. Polon.* B46.12 (2015), pp. 2501–2534. DOI: `10.5506/APhysPolB.46.2501`. arXiv: `1507.05267` `[hep-ph]`.

[35] Renaud Boussarie et al. "TMD Handbook". In: (Apr. 2023). arXiv: `2304.03302` `[hep-ph]`.

[36] A. Bermudez Martinez et al. "Production of Z-bosons in the parton branching method". In: *Phys. Rev. D* 100.7 (2019), p. 074027. DOI: `10.1103/PhysRevD.100.074027`. arXiv: `1906.00919` `[hep-ph]`.

[37] A. Bermudez Martinez et al. "Collinear and TMD parton densities from fits to precision DIS measurements in the parton branching method". In: *Phys. Rev. D* 99.7 (2019), p. 074008. DOI: `10.1103/PhysRevD.99.074008`. arXiv: `1804.11152` `[hep-ph]`.

[38] F. Hautmann et al. "Collinear and TMD Quark and Gluon Densities from Parton Branching Solution of QCD Evolution Equations". In: *JHEP* 01 (2018), p. 070. DOI: `10.1007/JHEP01(2018)070`. arXiv: `1708.03279` `[hep-ph]`.

[39] F. Hautmann et al. "Soft-gluon resolution scale in QCD evolution equations". In: *Phys. Lett.* B772 (2017), pp. 446–451. DOI: `10.1016/j.physletb.2017.07.005`. arXiv: `1704.01757` `[hep-ph]`.

[40] N. A. Abdulov et al. "TMDlib2 and TMDplotter: a platform for 3D hadron structure studies". In: *Eur. Phys. J. C* 81.8 (2021), p. 752. DOI: `10.1140/epjc/s10052-021-09508-8`. arXiv: `2103.09741` `[hep-ph]`.

[41] F. Hautmann et al. "TMDlib and TMDplotter: library and plotting tools for transverse-momentum-dependent parton distributions". In: *Eur. Phys. J.* C74 (2014), p. 3220. DOI: `10.1140/epjc/s10052-014-3220-9`. arXiv: `1408.3015` `[hep-ph]`.

[42] F. Hautmann et al. "Dynamical resolution scale in transverse momentum distributions at the LHC". In: *Nucl. Phys. B* 949 (2019), p. 114795. DOI: `10.1016/j.nuclphysb.2019.114795`. arXiv: `1908.08524` `[hep-ph]`.

[43] S. Catani, B. R. Webber, and G. Marchesini. "QCD coherent branching and semi-inclusive processes at large x". In: *Nucl. Phys.* B349 (1991), pp. 635–654. DOI: `10.1016/0550-3213(91)90390-J`.

[44] M. A. Kimber, Alan D. Martin, and M. G. Ryskin. "Unintegrated parton distributions and prompt photon hadroproduction". In: *Eur. Phys. J.* C12 (2000), pp. 655–661. DOI: 10.1007/s100520000326. arXiv: hep-ph/9911379 [hep-ph].

[45] M. A. Kimber, Alan D. Martin, and M. G. Ryskin. "Unintegrated parton distributions". In: *Phys. Rev.* D63 (2001), p. 114027. DOI: 10.1103/PhysRevD.63.114027. arXiv: hep-ph/0101348 [hep-ph].

[46] G. Watt, A. D. Martin, and M. G. Ryskin. "Unintegrated parton distributions and inclusive jet production at HERA". In: *Eur. Phys. J.* C31 (2003), pp. 73–89. DOI: 10.1140/epjc/s2003-01320-4. arXiv: hep-ph/0306169 [hep-ph].

[47] A. D. Martin, M. G. Ryskin, and G. Watt. "NLO prescription for unintegrated parton distributions". In: *Eur. Phys. J.* C66 (2010), pp. 163–172. DOI: 10.1140/epjc/s10052-010-1242-5. arXiv: 0909.5529 [hep-ph].

[48] A. Bermudez Martinez et al. "The TMD Parton Branching Sudakov form factor and its relation to that of CSS". In: (). arXiv: inpreparation [hep-ph].

[49] John C. Collins, Davison E. Soper, and George F. Sterman. "Transverse Momentum Distribution in Drell-Yan Pair and W and Z Boson Production". In: *Nucl. Phys. B* 250 (1985), pp. 199–224. DOI: 10.1016/0550-3213(85)90479-1.

[50] John Collins. *Foundations of perturbative QCD*. Vol. 32. Cambridge University Press, Nov. 2013. ISBN: 978-1-107-64525-7, 978-1-107-64525-7, 978-0-521-85533-4, 978-1-139-09782-6.

[51] S. Baranov et al. "CASCADE3 A Monte Carlo event generator based on TMDs". In: *Eur. Phys. J. C* 81.5 (2021), p. 425. DOI: 10.1140/epjc/s10052-021-09203-8. arXiv: 2101.10221 [hep-ph].

[52] H. Jung et al. "The CCFM Monte Carlo generator CASCADE version 2.2.03". In: *Eur. Phys. J.* C70 (2010), pp. 1237–1249. DOI: 10.1140/epjc/s10052-010-1507-z. arXiv: 1008.0152 [hep-ph].

[53] H. Jung. "The CCFM Monte Carlo generator CASCADE". In: *Comput. Phys. Commun.* 143 (2002), pp. 100–111. DOI: 10.1016/S0010-4655(01)00438-6. arXiv: hep-ph/0109102 [hep-ph].

[54] H. Jung and G. P. Salam. "Hadronic final state predictions from CCFM: The Hadron level Monte Carlo generator CASCADE". In: *Eur. Phys. J.* C19 (2001), pp. 351–360. DOI: 10.1007/s100520100604. arXiv: hep-ph/0012143 [hep-ph].

[55] J. Alwall et al. "The automated computation of tree-level and next-to-leading order differential cross sections, and their matching to parton shower simulations". In: *JHEP* 07 (2014), p. 079. DOI: 10.1007/JHEP07(2014)079. arXiv: 1405.0301 [hep-ph].

[56] M. I. Abdulhamid et al. "Azimuthal correlations of high transverse momentum jets at next-to-leading order in the parton branching method". In: *Eur. Phys. J. C* 82.1 (2022), p. 36. DOI: 10.1140/epjc/s10052-022-09997-1. arXiv: 2112.10465 [hep-ph].

[57] H. Yang et al. "Back-to-back azimuthal correlations in Z+jet events at high transverse momentum in the TMD parton branching method at next-to-leading order". In: *Eur. Phys. J. C* 82.8 (2022), p. 755. DOI: 10.1140/epjc/s10052-022-10715-0. arXiv: 2204.01528 [hep-ph].

[58] A. Bermudez Martinez, F. Hautmann, and M. L. Mangano. "Multi-jet merging with TMD parton branching". In: *JHEP* 09 (2022), p. 060. DOI: `10.1007/JHEP09(2022)060`. arXiv: `2208.02276 [hep-ph]`.

[59] A. Bermudez Martinez, F. Hautmann, and M. L. Mangano. "TMD evolution and multi-jet merging". In: *Phys. Lett. B* 822 (2021), p. 136700. DOI: `10.1016/j.physletb.2021.136700`. arXiv: `2107.01224 [hep-ph]`.

[60] Armando Bermudez Martinez, Francesco Hautmann, and Aron Mees van Kampen. "Multi-jets from TMD merging". In: (). arXiv: `inpreparation [hep-ph]`.

[61] Aron Mees van Kampen, Armando Bermudez Martinez, and Francesco Hautmann. "Merging scale in Z + multi-jet events for varying masses". In: (). arXiv: `inpreparation [hep-ph]`.

[62] Franz Mandl and Graham Shaw. *QUANTUM FIELD THEORY*. 1985. URL: `http://eu.wiley.com/WileyCDA/WileyTitle/productCd-0471496839.html`.

[63] M. E. Peskin and D. V. Schroeder. *"An Introduction to quantum field theory"*. Ed. by Inspire HEP. Addison-Wesley Publishing Company, 1995.

[64] L. D. Faddeev and V. N. Popov. "Feynman Diagrams for the Yang-Mills Field". In: *Phys. Lett.* B25 (1967). [,325(1967)], pp. 29–30. DOI: `10.1016/0370-2693(67)90067-6`.

[65] Gerard 't Hooft. "Dimensional regularization and the renormalization group". In: *Nucl. Phys.* B61 (1973), pp. 455–468. DOI: `10.1016/0550-3213(73)90376-3`.

[66] F. Hautmann. "An Introduction to QED QCD". In: (2012). Lectures presented at the RAL High Energy Physics Summer School. URL: `https://www.ppd.stfc.ac.uk/Pages/2012-RAL-HEP-School.aspx`.

[67] R. D. Field. "Applications of Perturbative QCD". In: *Front. Phys.* 77 (1989), pp. 1–366.

[68] R. L. Workman et al. "Review of Particle Physics". In: *PTEP* 2022 (2022), p. 083C01. DOI: `10.1093/ptep/ptac097`.

[69] R. Hofstadter and R. W. McAllister. "Electron Scattering From the Proton". In: *Phys. Rev.* 98 (1955), pp. 217–218. DOI: `10.1103/PhysRev.98.217`.

[70] Serguei Chatrchyan et al. "Observation of a New Boson at a Mass of 125 GeV with the CMS Experiment at the LHC". In: *Phys. Lett. B* 716 (2012), pp. 30–61. DOI: `10.1016/j.physletb.2012.08.021`. arXiv: `1207.7235 [hep-ex]`.

[71] Georges Aad et al. "Observation of a new particle in the search for the Standard Model Higgs boson with the ATLAS detector at the LHC". In: *Phys. Lett. B* 716 (2012), pp. 1–29. DOI: `10.1016/j.physletb.2012.08.020`. arXiv: `1207.7214 [hep-ex]`.

[72] J. D. Bjorken and Emmanuel A. Paschos. "Inelastic Electron Proton and gamma Proton Scattering, and the Structure of the Nucleon". In: *Phys. Rev.* 185 (1969), pp. 1975–1982. DOI: `10.1103/PhysRev.185.1975`.

[73] Richard P. Feynman. "Very high-energy collisions of hadrons". In: *Phys. Rev. Lett.* 23 (1969), pp. 1415–1417. DOI: `10.1103/PhysRevLett.23.1415`.

[74] J. Ovarlez J. Bertrand P. Bertrand. *The Mellin Transform*. CRC Press LLC, 2000.

[75] Guido Altarelli and G. Parisi. "Asymptotic Freedom in Parton Language". In: *Nucl. Phys.* B126 (1977), pp. 298–318. DOI: `10.1016/0550-3213(77)90384-4`.

[76] A. Vogt et al. "Anomalous dimensions and splitting functions beyond the next-to-next-to-leading order". In: *PoS* LL2018 (2018), p. 050. DOI: `10.22323/1.303.0050`. arXiv: `1808.08981 [hep-ph]`.

[77] V. N. Gribov and L. N. Lipatov. "Deep inelastic e p scattering in perturbation theory". In: *Sov. J. Nucl. Phys.* 15 (1972). [Yad. Fiz.15,781(1972)], pp. 438–450.

[78] Yuri L. Dokshitzer. "Calculation of the Structure Functions for Deep Inelastic Scattering and e+ e- Annihilation by Perturbation Theory in Quantum Chromodynamics." In: *Sov. Phys. JETP* 46 (1977). [Zh. Eksp. Teor. Fiz.73,1216(1977)], pp. 641–653.

[79] Andy Buckley et al. "General-purpose event generators for LHC physics". In: *Phys. Rept.* 504 (2011), pp. 145–233. DOI: `10.1016/j.physrep.2011.03.005`. arXiv: `1101.2599 [hep-ph]`.

[80] F. James. "Monte Carlo Theory and Practice". In: *Rept. Prog. Phys.* 43 (1980), p. 1145. DOI: `10.1088/0034-4885/43/9/002`.

[81] Matt Dobbs and Jorgen Beck Hansen. "The HepMC C++ Monte Carlo event record for High Energy Physics". In: *Comput. Phys. Commun.* 134 (2001), pp. 41–46. DOI: `10.1016/S0010-4655(00)00189-2`.

[82] Christian Bierlich et al. "Robust Independent Validation of Experiment and Theory: Rivet version 3". In: *SciPost Phys.* 8 (2020), p. 026. DOI: `10.21468/SciPostPhys.8.2.026`. arXiv: `1912.05451 [hep-ph]`.

[83] Andy Buckley et al. "Rivet user manual". In: *Comput. Phys. Commun.* 184 (2013), pp. 2803–2819. DOI: `10.1016/j.cpc.2013.05.021`. arXiv: `1003.0694 [hep-ph]`.

[84] F. Bloch and A. Nordsieck. "Note on the Radiation Field of the electron". In: *Phys. Rev.* 52 (1937), pp. 54–59. DOI: `10.1103/PhysRev.52.54`.

[85] T. Kinoshita. "Mass singularities of Feynman amplitudes". In: *J. Math. Phys.* 3 (1962), pp. 650–677. DOI: `10.1063/1.1724268`.

[86] T. D. Lee and M. Nauenberg. "Degenerate Systems and Mass Singularities". In: *Phys. Rev.* 133 (1964). Ed. by G. Feinberg, B1549–B1562. DOI: `10.1103/PhysRev.133.B1549`.

[87] K. Konishi, A. Ukawa, and G. Veneziano. "Jet Calculus: A Simple Algorithm for Resolving QCD Jets". In: *Nucl. Phys.* B157 (1979), pp. 45–107. DOI: `10.1016/0550-3213(79)90053-1`.

[88] A. Bassetto, M. Ciafaloni, and G. Marchesini. "Inelastic Distributions and Color Structure in Perturbative QCD". In: *Nucl. Phys.* B163 (1980), pp. 477–518. DOI: `10.1016/0550-3213(80)90413-7`.

[89] Gavin P. Salam. "Towards Jetography". In: *Eur. Phys. J. C* 67 (2010), pp. 637–686. DOI: `10.1140/epjc/s10052-010-1314-6`. arXiv: `0906.1833 [hep-ph]`.

[90] S. Catani et al. "New clustering algorithm for multi - jet cross-sections in e+ e- annihilation". In: *Phys. Lett. B* 269 (1991), pp. 432–438. DOI: `10.1016/0370-2693(91)90196-W`.

[91] S. Catani et al. "Longitudinally invariant K_t clustering algorithms for hadron hadron collisions". In: *Nucl. Phys. B* 406 (1993), pp. 187–224. DOI: `10.1016/0550-3213(93)90166-M`.

[92] Stephen D. Ellis and Davison E. Soper. "Successive combination jet algorithm for hadron collisions". In: *Phys. Rev. D* 48 (1993), pp. 3160–3166. DOI: 10.1103/PhysRevD.48.3160. arXiv: hep-ph/9305266.

[93] Matteo Cacciari, Gavin P. Salam, and Gregory Soyez. "The anti-k_t jet clustering algorithm". In: *JHEP* 04 (2008), p. 063. DOI: 10.1088/1126-6708/2008/04/063. arXiv: 0802.1189 [hep-ph].

[94] Torbjorn Sjostrand and Maria van Zijl. "A Multiple Interaction Model for the Event Structure in Hadron Collisions". In: *Phys. Rev. D* 36 (1987), p. 2019. DOI: 10.1103/PhysRevD.36.2019.

[95] Stafano Frixione and Bryan R. Webber. "The MC@NLO 3.3 Event Generator". In: (Dec. 2006). arXiv: hep-ph/0612272.

[96] Stefano Frixione, Paolo Nason, and Bryan R. Webber. "Matching NLO QCD and parton showers in heavy flavor production". In: *JHEP* 08 (2003), p. 007. DOI: 10.1088/1126-6708/2003/08/007. arXiv: hep-ph/0305252 [hep-ph].

[97] Stefano Frixione and Bryan R. Webber. "The MC@NLO event generator". In: (2002). arXiv: hep-ph/0207182 [hep-ph].

[98] Stefano Frixione and Bryan R. Webber. "Matching NLO QCD computations and parton shower simulations". In: *JHEP* 06 (2002), p. 029. DOI: 10.1088/1126-6708/2002/06/029. arXiv: hep-ph/0204244 [hep-ph].

[99] Simone Alioli et al. "Jet pair production in POWHEG". In: *JHEP* 04 (2011), p. 081. DOI: 10.1007/JHEP04(2011)081. arXiv: 1012.3380 [hep-ph].

[100] Stefano Frixione, Paolo Nason, and Carlo Oleari. "Matching NLO QCD computations with Parton Shower simulations: the POWHEG method". In: *JHEP* 11 (2007), p. 070. DOI: 10.1088/1126-6708/2007/11/070. arXiv: 0709.2092 [hep-ph].

[101] Kyle Cormier et al. "Parton showers and matching uncertainties in top quark pair production with Herwig 7". In: *Eur. Phys. J. C* 79.11 (2019), p. 915. DOI: 10.1140/epjc/s10052-019-7370-7. arXiv: 1810.06493 [hep-ph].

[102] Simon Platzer and Stefan Gieseke. "Dipole Showers and Automated NLO Matching in Herwig++". In: *Eur. Phys. J. C* 72 (2012), p. 2187. DOI: 10.1140/epjc/s10052-012-2187-7. arXiv: 1109.6256 [hep-ph].

[103] Stefan Hoeche et al. "A critical appraisal of NLO+PS matching methods". In: *JHEP* 09 (2012), p. 049. DOI: 10.1007/JHEP09(2012)049. arXiv: 1111.1220 [hep-ph].

[104] Michelangelo L. Mangano et al. "Matching matrix elements and shower evolution for top-quark production in hadronic collisions". In: *JHEP* 01 (2007), p. 013. DOI: 10.1088/1126-6708/2007/01/013. arXiv: hep-ph/0611129.

[105] Stephen Mrenna and Peter Richardson. "Matching matrix elements and parton showers with HERWIG and PYTHIA". In: *JHEP* 05 (2004), p. 040. DOI: 10.1088/1126-6708/2004/05/040. arXiv: hep-ph/0312274.

[106] Michelangelo L. Mangano, Mauro Moretti, and Roberto Pittau. "Multijet matrix elements and shower evolution in hadronic collisions: $Wb\bar{b} + n$ jets as a case study". In: *Nucl. Phys. B* 632 (2002), pp. 343–362. DOI: 10.1016/S0550-3213(02)00249-3. arXiv: hep-ph/0108069.

[107] S. Catani et al. "QCD matrix elements + parton showers". In: *JHEP* 11 (2001), p. 063. DOI: 10.1088/1126-6708/2001/11/063. arXiv: hep-ph/0109231.

[108]   Keith Hamilton, Peter Richardson, and Jon Tully. "A Modified CKKW matrix element merging approach to angular-ordered parton showers". In: *JHEP* 11 (2009), p. 038. DOI: 10.1088/1126-6708/2009/11/038. arXiv: 0905.3072 [hep-ph].

[109]   Stefan Hoeche et al. "QCD matrix elements and truncated showers". In: *JHEP* 05 (2009), p. 053. DOI: 10.1088/1126-6708/2009/05/053. arXiv: 0903.1219 [hep-ph].

[110]   Rikkert Frederix and Stefano Frixione. "Merging meets matching in MC@NLO". In: *JHEP* 12 (2012), p. 061. DOI: 10.1007/JHEP12(2012)061. arXiv: 1209.6215 [hep-ph].

[111]   Keith Hamilton, Paolo Nason, and Giulia Zanderighi. "MINLO: Multi-Scale Improved NLO". In: *JHEP* 10 (2012), p. 155. DOI: 10.1007/JHEP10(2012)155. arXiv: 1206.3572 [hep-ph].

[112]   Johannes Bellm, Stefan Gieseke, and Simon Plätzer. "Merging NLO Multi-jet Calculations with Improved Unitarization". In: *Eur. Phys. J. C* 78.3 (2018), p. 244. DOI: 10.1140/epjc/s10052-018-5723-2. arXiv: 1705.06700 [hep-ph].

[113]   Simon Plätzer. "Controlling inclusive cross sections in parton shower + matrix element merging". In: *JHEP* 08 (2013), p. 114. DOI: 10.1007/JHEP08(2013)114. arXiv: 1211.5467 [hep-ph].

[114]   Leif Lönnblad and Stefan Prestel. "Merging Multi-leg NLO Matrix Elements with Parton Showers". In: *JHEP* 03 (2013), p. 166. DOI: 10.1007/JHEP03(2013)166. arXiv: 1211.7278 [hep-ph].

[115]   Stefan Hoeche et al. "QCD matrix elements + parton showers: The NLO case". In: *JHEP* 04 (2013), p. 027. DOI: 10.1007/JHEP04(2013)027. arXiv: 1207.5030 [hep-ph].

[116]   Christian Bierlich et al. "A comprehensive guide to the physics and usage of PYTHIA 8.3". In: (Mar. 2022). DOI: 10.21468/SciPostPhysCodeb.8. arXiv: 2203.11601 [hep-ph].

[117]   Torbjrn Sjostrand et al. "An Introduction to PYTHIA 8.2". In: *Comput. Phys. Commun.* 191 (2015), pp. 159–177. DOI: 10.1016/j.cpc.2015.01.024. arXiv: 1410.3012 [hep-ph].

[118]   Johannes Bellm et al. "Herwig 7.0/Herwig++ 3.0 release note". In: *Eur. Phys. J. C* 76.4 (2016), p. 196. DOI: 10.1140/epjc/s10052-016-4018-8. arXiv: 1512.01178 [hep-ph].

[119]   M. Bahr et al. "Herwig++ Physics and Manual". In: *Eur. Phys. J. C* 58 (2008), pp. 639–707. DOI: 10.1140/epjc/s10052-008-0798-9. arXiv: 0803.0883 [hep-ph].

[120]   G. Corcella et al. "HERWIG 6: An Event generator for hadron emission reactions with interfering gluons (including supersymmetric processes)". In: *JHEP* 01 (2001), p. 010. DOI: 10.1088/1126-6708/2001/01/010. arXiv: hep-ph/0011363.

[121]   Enrico Bothmann et al. "Event Generation with Sherpa 2.2". In: *SciPost Phys.* 7.3 (2019), p. 034. DOI: 10.21468/SciPostPhys.7.3.034. arXiv: 1905.09127 [hep-ph].

[122]   T. Gleisberg et al. "Event generation with SHERPA 1.1". In: *JHEP* 02 (2009), p. 007. DOI: 10.1088/1126-6708/2009/02/007. arXiv: 0811.4622 [hep-ph].

[123] T. Stelzer and W. F. Long. "Automatic generation of tree level helicity amplitudes". In: *Comput. Phys. Commun.* 81 (1994), pp. 357–371. DOI: `10.1016/0010-4655(94)90084-1`. arXiv: `hep-ph/9401258`.

[124] F. Krauss, R. Kuhn, and G. Soff. "AMEGIC++ 1.0: A Matrix element generator in C++". In: *JHEP* 02 (2002), p. 044. DOI: `10.1088/1126-6708/2002/02/044`. arXiv: `hep-ph/0109036`.

[125] Johan Alwall et al. "A Standard format for Les Houches event files". In: *Comput. Phys. Commun.* 176 (2007), pp. 300–304. DOI: `10.1016/j.cpc.2006.11.010`. arXiv: `hep-ph/0609017 [hep-ph]`.

[126] S. D. Drell and Tung-Mow Yan. "Massive Lepton Pair Production in Hadron-Hadron Collisions at High-Energies". In: *Phys. Rev. Lett.* 25 (1970). [Erratum: Phys. Rev. Lett.25,902(1970)], pp. 316–320. DOI: `10.1103/PhysRevLett.25.316, 10.1103/PhysRevLett.25.902.2`.

[127] E. A. Kuraev, L. N. Lipatov, and Victor S. Fadin. "Multi - Reggeon Processes in the Yang-Mills Theory". In: *Sov. Phys. JETP* 44 (1976). [Zh. Eksp. Teor. Fiz.71,840(1976)], pp. 443–450.

[128] E. A. Kuraev, L. N. Lipatov, and Victor S. Fadin. "The Pomeranchuk Singularity in Nonabelian Gauge Theories". In: *Sov. Phys. JETP* 45 (1977). [Zh. Eksp. Teor. Fiz.72,377(1977)], pp. 199–204.

[129] S. Catani, F. Fiorani, and G. Marchesini. "Small x Behavior of Initial State Radiation in Perturbative QCD". In: *Nucl. Phys.* B336 (1990), pp. 18–85. DOI: `10.1016/0550-3213(90)90342-B`.

[130] Giuseppe Bozzi et al. "Transverse-momentum resummation and the spectrum of the Higgs boson at the LHC". In: *Nucl. Phys. B* 737 (2006), pp. 73–120. DOI: `10.1016/j.nuclphysb.2005.12.022`. arXiv: `hep-ph/0508068`.

[131] Georges Aad et al. "Measurement of the transverse momentum and ϕ_η^* distributions of Drell–Yan lepton pairs in proton–proton collisions at $\sqrt{s} = 8$ TeV with the ATLAS detector". In: *Eur. Phys. J.* C76.5 (2016), p. 291. DOI: `10.1140/epjc/s10052-016-4070-4`. arXiv: `1512.02192 [hep-ex]`.

[132] Georges Aad et al. "Measurement of the Z/γ^* boson transverse momentum distribution in pp collisions at $\sqrt{s} = 7$ TeV with the ATLAS detector". In: *JHEP* 09 (2014), p. 145. DOI: `10.1007/JHEP09(2014)145`. arXiv: `1406.3660 [hep-ex]`.

[133] Vardan Khachatryan et al. "Measurement of the transverse momentum spectra of weak vector bosons produced in proton-proton collisions at $\sqrt{s} = 8$ TeV". In: *JHEP* 02 (2017), p. 096. DOI: `10.1007/JHEP02(2017)096`. arXiv: `1606.05864 [hep-ex]`.

[134] Serguei Chatrchyan et al. "Measurement of the Rapidity and Transverse Momentum Distributions of Z Bosons in pp Collisions at $\sqrt{s} = 7$ TeV". In: *Phys. Rev.* D85 (2012), p. 032002. DOI: `10.1103/PhysRevD.85.032002`. arXiv: `1110.4973 [hep-ex]`.

[135] Georges Aad et al. "Measurement of the transverse momentum distribution of Drell–Yan lepton pairs in proton–proton collisions at $\sqrt{s} = 13$ TeV with the ATLAS detector". In: *Eur. Phys. J. C* 80.7 (2020), p. 616. DOI: `10.1140/epjc/s10052-020-8001-z`. arXiv: `1912.02844 [hep-ex]`.

[136] Albert M Sirunyan et al. "Measurements of differential Z boson production cross sections in proton-proton collisions at $\sqrt{s} = 13$ TeV". In: *JHEP* 12 (2019), p. 061. DOI: `10.1007/JHEP12(2019)061`. arXiv: `1909.04133 [hep-ex]`.

[137] John C. Collins, Davison E. Soper, and George F. Sterman. "Factorization of Hard
       Processes in QCD". In: *Adv. Ser. Direct. High Energy Phys.* 5 (1989), pp. 1–91. DOI:
       `10.1142/9789814503266_0001`. arXiv: `hep-ph/0409313 [hep-ph]`.

[138] Sonny Mantry and Frank Petriello. "Transverse Momentum Distributions from Ef-
       fective Field Theory with Numerical Results". In: *Phys. Rev.* D83 (2011), p. 053007.
       DOI: `10.1103/PhysRevD.83.053007`. arXiv: `1007.3773 [hep-ph]`.

[139] Gerhard Bohm and Günter Zech. *Introduction to Statistics and Data Analysis for
       Physicists*. Deutsches Elektronen-Synchrotron, 2010.

[140] Torbjorn Sjostrand. "A Model for Initial State Parton Showers". In: *Phys. Lett.* B157
       (1985), pp. 321–325. DOI: `10.1016/0370-2693(85)90674-4`.

[141] F. Hautmann et al. "A parton branching with transverse momentum dependent
       splitting functions". In: *Phys. Lett. B* 833 (2022), p. 137276. DOI: `10.1016/j.
       physletb.2022.137276`. arXiv: `2205.15873 [hep-ph]`.

[142] Aleksandra Lelek. "Determination of TMD parton densities from HERA data
       and application to pp processes". PhD thesis. Hamburg: Hamburg U., 2018. DOI:
       `10.3204/PUBDB-2018-02949`.

[143] A. Bassetto, M. Ciafaloni, and G. Marchesini. "Jet Structure and Infrared Sensitive
       Quantities in Perturbative QCD". In: *Phys. Rept.* 100 (1983), pp. 201–272. DOI:
       `10.1016/0370-1573(83)90083-2`.

[144] Yuri L. Dokshitzer et al. "QCD Coherence in High-Energy Reactions". In: *Rev.
       Mod. Phys.* 60 (1988), p. 373. DOI: `10.1103/RevModPhys.60.373`.

[145] S. Catani, F. Fiorani, and G. Marchesini. "QCD Coherence in Initial State Radia-
       tion". In: *Phys. Lett*. B234 (1990), pp. 339–345. DOI: `10.1016/0370-2693(90)91938-
       8`.

[146] A. E. Chudakov. In: *Izvestiya Akademii Nauk SSSR, Seriya Fizicheskaya 19 650* (1955).

[147] Giuseppe Marchesini. "QCD coherence in the structure function and associated
       distributions at small x". In: *Nucl. Phys.* B445 (1995), pp. 49–80. DOI: `10.1016/0550-
       3213(95)00149-M`. arXiv: `hep-ph/9412327 [hep-ph]`.

[148] D. Amati et al. "A Treatment of Hard Processes Sensitive to the Infrared Structure
       of QCD". In: *Nucl. Phys.* B173 (1980), pp. 429–455. DOI: `10.1016/0550-3213(80)
       90012-7`.

[149] F. Hautmann. "TMDs and Monte Carlo Event Generators". In: *23rd International
       Symposium on Spin Physics (SPIN 2018) Ferrara, Italy, September 10-14, 2018*. 2019.
       arXiv: `1907.03353 [hep-ph]`.

[150] John C. Collins and Davison E. Soper. "Back-To-Back Jets in QCD". In: *Nucl. Phys.*
       B193 (1981). [Erratum: Nucl. Phys.B213,545(1983)], p. 381. DOI: `10.1016/0550-
       3213(81)90339-4`.

[151] Xiang-dong Ji, Jian-ping Ma, and Feng Yuan. "QCD factorization for semi-
       inclusive deep-inelastic scattering at low transverse momentum". In: *Phys.
       Rev.* D71 (2005), p. 034005. DOI: `10.1103/PhysRevD.71.034005`. arXiv:
       `hep-ph/0404183 [hep-ph]`.

[152] Xiang-dong Ji, Jian-Ping Ma, and Feng Yuan. "QCD factorization for spin-
       dependent cross sections in DIS and Drell-Yan processes at low transverse
       momentum". In: *Phys. Lett.* B597 (2004), pp. 299–308. DOI: `10.1016/j.physletb.
       2004.07.026`. arXiv: `hep-ph/0405085 [hep-ph]`.

[153] Miguel G. Echevarria, Ahmad Idilbi, and Ignazio Scimemi. "Factorization Theorem For Drell-Yan At Low q_T And Transverse Momentum Distributions On-The-Light-Cone". In: *JHEP* 07 (2012), p. 002. DOI: 10.1007/JHEP07(2012)002. arXiv: 1111.4996 [hep-ph].

[154] Jui-yu Chiu et al. "The Rapidity Renormalization Group". In: *Phys. Rev. Lett.* 108 (2012), p. 151601. DOI: 10.1103/PhysRevLett.108.151601. arXiv: 1104.0881 [hep-ph].

[155] John C. Collins and Davison E. Soper. "Parton Distribution and Decay Functions". In: *Nucl. Phys.* B194 (1982), pp. 445–492. DOI: 10.1016/0550-3213(82)90021-9.

[156] John C. Collins, Davison E. Soper, and George F. Sterman. "Factorization for One Loop Corrections in the Drell-Yan Process". In: *Nucl. Phys. B* 223 (1983), pp. 381–421. DOI: 10.1016/0550-3213(83)90062-7.

[157] John C. Collins, Davison E. Soper, and George F. Sterman. "Does the Drell-Yan Cross-section Factorize?" In: *Phys. Lett.* 109B (1982), pp. 388–392. DOI: 10.1016/0370-2693(82)91097-8.

[158] Ruibin Meng, Fredrick I. Olness, and Davison E. Soper. "Semiinclusive deeply inelastic scattering at small q(T)". In: *Phys. Rev.* D54 (1996), pp. 1919–1935. DOI: 10.1103/PhysRevD.54.1919. arXiv: hep-ph/9511311 [hep-ph].

[159] Pavel M. Nadolsky, D. R. Stump, and C. P. Yuan. "Semiinclusive hadron production at HERA: The Effect of QCD gluon resummation". In: *Phys. Rev.* D61 (2000). [Erratum: Phys. Rev.D64,059903(2001)], p. 014003. DOI: 10.1103/PhysRevD.64.059903,10.1103/PhysRevD.61.014003. arXiv: hep-ph/9906280 [hep-ph].

[160] Pavel M. Nadolsky, D. R. Stump, and C. P. Yuan. "Phenomenology of multiple parton radiation in semiinclusive deep inelastic scattering". In: *Phys. Rev.* D64 (2001), p. 114011. DOI: 10.1103/PhysRevD.64.114011. arXiv: hep-ph/0012261 [hep-ph].

[161] S. Catani, M. Ciafaloni, and F. Hautmann. "GLUON CONTRIBUTIONS TO SMALL x HEAVY FLAVOR PRODUCTION". In: *Phys. Lett. B* 242 (1990), pp. 97–102. DOI: 10.1016/0370-2693(90)91601-7.

[162] E. M. Levin et al. "Heavy quark production in semihard nucleon interactions". In: *Sov. J. Nucl. Phys.* 53 (1991). [Yad. Fiz.53,1059(1991)], p. 657.

[163] John C. Collins and R. Keith Ellis. "Heavy quark production in very high-energy hadron collisions". In: *Nucl. Phys. B* 360 (1991), pp. 3–30. DOI: 10.1016/0550-3213(91)90288-9.

[164] S. Catani, M. Ciafaloni, and F. Hautmann. "High-energy factorization in QCD and minimal subtraction scheme". In: *Phys. Lett. B* 307 (1993), pp. 147–153. DOI: 10.1016/0370-2693(93)90204-U.

[165] S. Catani and F. Hautmann. "High-energy factorization and small x deep inelastic scattering beyond leading order". In: *Nucl. Phys.* B427 (1994), pp. 475–524. DOI: 10.1016/0550-3213(94)90636-X. arXiv: hep-ph/9405388 [hep-ph].

[166] F. Hautmann. "Heavy top limit and double logarithmic contributions to Higgs production at m(H)**2 / s much less than 1". In: *Phys. Lett.* B535 (2002), pp. 159–162. DOI: 10.1016/S0370-2693(02)01761-6. arXiv: hep-ph/0203140 [hep-ph].

[167] Emil Avsar. "TMD factorization and the gluon distribution in high energy QCD". In: (Mar. 2012). arXiv: 1203.1916 [hep-ph].

[168]   Emil Avsar. "On the Understanding and Use of 'Unintegrated' Parton Distributions in Small-x QCD". In: *Int. J. Mod. Phys. Conf. Ser.* 04 (2011). Ed. by Ian Balitsky, Alexei Prokudin, and Anatoly Radyushkin, pp. 74–84. DOI: `10.1142/S2010194511001589`. arXiv: `1108.1181 [hep-ph]`.

[169]   S. Jadach and M. Skrzypek. "QCD evolution in the fully unintegrated form". In: *Acta Phys. Polon. B* 40 (2009). Ed. by Krzysztof Golec-Biernat and Michal Praszalowicz, pp. 2071–2096. arXiv: `0905.1399 [hep-ph]`.

[170]   Fabio Dominguez. "Unintegrated Gluon Distributions at Small-x". PhD thesis. Columbia U., 2011.

[171]   Fabio Dominguez et al. "On the linearly polarized gluon distributions in the color dipole model". In: *Phys. Rev. D* 85 (2012), p. 045003. DOI: `10.1103/PhysRevD.85.045003`. arXiv: `1109.6293 [hep-ph]`.

[172]   Fabio Dominguez et al. "On the small-*x* evolution of the color quadrupole and the Weizsäcker–Williams gluon distribution". In: *Phys. Lett. B* 705 (2011), pp. 106–111. DOI: `10.1016/j.physletb.2011.09.104`. arXiv: `1108.1752 [hep-ph]`.

[173]   F. Hautmann. "Unintegrated parton distributions and applications to jet physics". In: *Acta Phys. Polon. B* 40 (2009). Ed. by Krzysztof Golec-Biernat and Michal Praszalowicz, pp. 2139–2163.

[174]   F. Hautmann, M. Hentschinski, and H. Jung. "TMD PDFs: A Monte Carlo implementation for the sea quark distribution". In: (2012). arXiv: `1205.6358 [hep-ph]`.

[175]   F. Hautmann and H. Jung. "Recent results on unintegrated parton distributions". In: *Nucl. Phys. B Proc. Suppl.* 184 (2008). Ed. by F. Kapusta, pp. 64–72. DOI: `10.1016/j.nuclphysbps.2008.09.139`. arXiv: `0712.0568 [hep-ph]`.

[176]   H. Plothow-Besch. "PDFLIB: A Library of all available parton density functions of the nucleon, the pion and the photon and the corresponding alpha-s calculations". In: *Comput. Phys. Commun.* 75 (1993). Ed. by K. Bos and B. van Eijk, pp. 396–416. DOI: `10.1016/0010-4655(93)90051-D`.

[177]   H. Plothow-Besch. "The Parton distribution function library". In: *Int. J. Mod. Phys. A* 10 (1995), pp. 2901–2920. DOI: `10.1142/S0217751X9500139X`.

[178]   Andy Buckley et al. "LHAPDF6: parton density access in the LHC precision era". In: *Eur. Phys. J. C* 75 (2015), p. 132. DOI: `10.1140/epjc/s10052-015-3318-8`. arXiv: `1412.7420 [hep-ph]`.

[179]   H. Abramowicz et al. "Combination of measurements of inclusive deep inelastic $e^{\pm}p$ scattering cross sections and QCD analysis of HERA data". In: *Eur. Phys. J. C* 75.12 (2015), p. 580. DOI: `10.1140/epjc/s10052-015-3710-4`. arXiv: `1506.06042 [hep-ex]`.

[180]   Alessandro Bacchetta et al. "Extraction of partonic transverse momentum distributions from semi-inclusive deep-inelastic scattering, Drell-Yan and Z-boson production". In: *JHEP* 06 (2017), p. 081. DOI: `10.1007/JHEP06(2017)081`. arXiv: `1703.10157 [hep-ph]`.

[181]   L. A. Harland-Lang et al. "Parton distributions in the LHC era: MMHT 2014 PDFs". In: *Eur. Phys. J. C* 75.5 (2015), p. 204. DOI: `10.1140/epjc/s10052-015-3397-6`. arXiv: `1412.3989 [hep-ph]`.

[182] G. Watt, A. D. Martin, and M. G. Ryskin. "Unintegrated parton distributions and electroweak boson production at hadron colliders". In: *Phys. Rev. D* 70 (2004). [Erratum: Phys.Rev.D 70, 079902 (2004)], p. 014012. DOI: 10.1103/PhysRevD.70.014012. arXiv: hep-ph/0309096.

[183] John Collins and Hannes Jung. "Need for fully unintegrated parton densities". In: *HERA and the LHC: A Workshop on the implications of HERA for LHC physics. Proceedings, Part B*. 2005. arXiv: hep-ph/0508280 [hep-ph].

[184] J. C. Collins, T. C. Rogers, and A. M. Stasto. "Fully unintegrated parton correlation functions and factorization in lowest-order hard scattering". In: *Phys. Rev. D* 77 (2008), p. 085009. DOI: 10.1103/PhysRevD.77.085009. arXiv: 0708.2833 [hep-ph].

[185] H. Abdolmaleki et al. "xFitter: An Open Source QCD Analysis Framework. A resource and reference document for the Snowmass study". In: June 2022. arXiv: 2206.12465 [hep-ph].

[186] S. Alekhin et al. "HERAFitter". In: *Eur. Phys. J.* C75.7 (2015), p. 304. DOI: 10.1140/epjc/s10052-015-3480-z. arXiv: 1410.4412 [hep-ph].

[187] J. Pumplin et al. "New generation of parton distributions with uncertainties from global QCD analysis". In: *JHEP* 07 (2002), p. 012. DOI: 10.1088/1126-6708/2002/07/012. arXiv: hep-ph/0201195.

[188] Walter T. Giele and Stephane Keller. "Implications of hadron collider observables on parton distribution function uncertainties". In: *Phys. Rev. D* 58 (1998), p. 094023. DOI: 10.1103/PhysRevD.58.094023. arXiv: hep-ph/9803393.

[189] Walter T. Giele, Stephane A. Keller, and David A. Kosower. "Parton Distribution Function Uncertainties". In: (Apr. 2001). arXiv: hep-ph/0104052.

[190] Gionata Luisoni and Simone Marzani. "QCD resummation for hadronic final states". In: *J. Phys.* G42.10 (2015), p. 103101. DOI: 10.1088/0954-3899/42/10/103101. arXiv: 1505.04084 [hep-ph].

[191] F. Hautmann. "Endpoint singularities in unintegrated parton distributions". In: *Phys. Lett.* B655 (2007), pp. 26–31. DOI: 10.1016/j.physletb.2007.08.081. arXiv: hep-ph/0702196 [HEP-PH].

[192] F. Hautmann, H. Jung, and S. Taheri Monfared. "The CCFM uPDF evolution uPDFevolv Version 1.0.00". In: *Eur. Phys. J.* C74 (2014), p. 3082. DOI: 10.1140/epjc/s10052-014-3082-1. arXiv: 1407.5935 [hep-ph].

[193] L. N. Lipatov. "The parton model and perturbation theory". In: *Sov. J. Nucl. Phys.* 20 (1975). [Yad. Fiz.20,181(1974)], pp. 94–102.

[194] M. Botje. "QCDNUM: Fast QCD Evolution and Convolution". In: *Comput. Phys. Commun.* 182 (2011), pp. 490–532. DOI: 10.1016/j.cpc.2010.10.020. arXiv: 1005.1481 [hep-ph].

[195] Krzysztof Golec-Biernat and Anna M. Stasto. "On the use of the KMR unintegrated parton distribution functions". In: *Phys. Lett.* B781 (2018), pp. 633–638. DOI: 10.1016/j.physletb.2018.04.061. arXiv: 1803.06246 [hep-ph].

[196] Georgios Billis, Frank J. Tackmann, and Jim Talbert. "Higher-Order Sudakov Resummation in Coupled Gauge Theories". In: *JHEP* 03 (2020), p. 182. DOI: 10.1007/JHEP03(2020)182. arXiv: 1907.02971 [hep-ph].

[197] Markus A. Ebert. "Analytic results for Sudakov form factors in QCD". In: *JHEP* 02 (2022), p. 136. DOI: 10.1007/JHEP02(2022)136. arXiv: 2110.11360 [hep-ph].

[198] Marcin Bury et al. "Calculations with off-shell matrix elements, TMD parton densities and TMD parton showers". In: *Eur. Phys. J.* C78.2 (2018), p. 137. DOI: 10.1140/epjc/s10052-018-5642-2. arXiv: 1712.05932 [hep-ph].

[199] Hung-Liang Lai et al. "New parton distributions for collider physics". In: *Phys. Rev.* D82 (2010), p. 074024. DOI: 10.1103/PhysRevD.82.074024. arXiv: 1007.2241 [hep-ph].

[200] Torbjorn Sjostrand, Stephen Mrenna, and Peter Z. Skands. "A Brief Introduction to PYTHIA 8.1". In: *Comput. Phys. Commun.* 178 (2008), pp. 852–867. DOI: 10.1016/j.cpc.2008.01.036. arXiv: 0710.3820 [hep-ph].

[201] A. Bermudez Martinez et al. "The Parton Branching Sudakov and its relation to CSS". In: *Proceedings of Science PoS (EPS-HEP2023)*. 2023.

[202] Andrea Banfi, Basem Kamal El-Menoufi, and Pier Francesco Monni. "The Sudakov radiator for jet observables and the soft physical coupling". In: *JHEP* 01 (2019), p. 083. DOI: 10.1007/JHEP01(2019)083. arXiv: 1807.11487 [hep-ph].

[203] Stefano Catani, Daniel De Florian, and Massimiliano Grazzini. "Soft-gluon effective coupling and cusp anomalous dimension". In: *Eur. Phys. J. C* 79.8 (2019), p. 685. DOI: 10.1140/epjc/s10052-019-7174-9. arXiv: 1904.10365 [hep-ph].

[204] John C. Collins and Davison E. Soper. "Back-To-Back Jets: Fourier Transform from B to K-Transverse". In: *Nucl. Phys. B* 197 (1982), pp. 446–476. DOI: 10.1016/0550-3213(82)90453-9.

[205] Armando Bermudez Martinez and Alexey Vladimirov. "Determination of the Collins-Soper kernel from cross-sections ratios". In: *Phys. Rev. D* 106.9 (2022), p. L091501. DOI: 10.1103/PhysRevD.106.L091501. arXiv: 2206.01105 [hep-ph].

[206] John Collins and Ted C. Rogers. "Connecting Different TMD Factorization Formalisms in QCD". In: *Phys. Rev. D* 96.5 (2017), p. 054011. DOI: 10.1103/PhysRevD.96.054011. arXiv: 1705.07167 [hep-ph].

[207] Stefano Catani, Daniel de Florian, and Massimiliano Grazzini. "Universality of nonleading logarithmic contributions in transverse momentum distributions". In: *Nucl. Phys. B* 596 (2001), pp. 299–312. DOI: 10.1016/S0550-3213(00)00617-9. arXiv: hep-ph/0008184.

[208] Thomas Becher and Matthias Neubert. "Drell-Yan Production at Small q_T, Transverse Parton Distributions and the Collinear Anomaly". In: *Eur. Phys. J. C* 71 (2011), p. 1665. DOI: 10.1140/epjc/s10052-011-1665-7. arXiv: 1007.4005 [hep-ph].

[209] Miguel G. Echevarria, Ahmad Idilbi, and Ignazio Scimemi. "Factorization Theorem For Drell-Yan At Low q_T And Transverse Momentum Distributions On-The-Light-Cone". In: *JHEP* 07 (2012), p. 002. DOI: 10.1007/JHEP07(2012)002. arXiv: 1111.4996 [hep-ph].

[210] Alexey Vladimirov. "Structure of rapidity divergences in multi-parton scattering soft factors". In: *JHEP* 04 (2018), p. 045. DOI: 10.1007/JHEP04(2018)045. arXiv: 1707.07606 [hep-ph].

[211] Alexey A. Vladimirov. "Self-contained definition of the Collins-Soper kernel". In: *Phys. Rev. Lett.* 125.19 (2020), p. 192002. DOI: 10.1103/PhysRevLett.125.192002. arXiv: 2003.02288 [hep-ph].

[212]   Ignazio Scimemi and Alexey Vladimirov. "Non-perturbative structure of semi-inclusive deep-inelastic and Drell-Yan scattering at small transverse momentum". In: *JHEP* 06 (2020), p. 137. DOI: `10.1007/JHEP06(2020)137`. arXiv: `1912.06532` `[hep-ph]`.

[213]   Valentin Moos et al. "Extraction of unpolarized transverse momentum distributions from fit of Drell-Yan data at N^{4}LL". In: (May 2023). arXiv: `2305.07473` `[hep-ph]`.

[214]   Min-Huan Chu et al. "Nonperturbative determination of the Collins-Soper kernel from quasitransverse-momentum-dependent wave functions". In: *Phys. Rev. D* 106.3 (2022), p. 034509. DOI: `10.1103/PhysRevD.106.034509`. arXiv: `2204.00200` `[hep-lat]`.

[215]   Maximilian Schlemmer et al. "Determination of the Collins-Soper Kernel from Lattice QCD". In: *JHEP* 08 (2021), p. 004. DOI: `10.1007/JHEP08(2021)004`. arXiv: `2103.16991` `[hep-lat]`.

[216]   Yuan Li et al. "Lattice QCD Study of Transverse-Momentum Dependent Soft Function". In: *Phys. Rev. Lett.* 128.6 (2022), p. 062002. DOI: `10.1103/PhysRevLett.128.062002`. arXiv: `2106.13027` `[hep-lat]`.

[217]   G. Corcella et al. "HERWIG 6.5 release note". In: (Oct. 2002). arXiv: `hep-ph/0210213`.

[218]   G. Marchesini et al. "HERWIG: A Monte Carlo event generator for simulating hadron emission reactions with interfering gluons. Version 5.1 - April 1991". In: *Comput. Phys. Commun.* 67 (1992), pp. 465–508. DOI: `10.1016/0010-4655(92)90055-4`.

[219]   Mats Bengtsson, Torbjorn Sjostrand, and Maria van Zijl. "Initial State Radiation Effects on *W* and Jet Production". In: *Z. Phys.* C32 (1986), p. 67. DOI: `10.1007/BF01441353`.

[220]   Zoltán Nagy and Davison E. Soper. "Evolution of parton showers and parton distribution functions". In: *Phys. Rev. D* 102.1 (2020), p. 014025. DOI: `10.1103/PhysRevD.102.014025`. arXiv: `2002.04125` `[hep-ph]`.

[221]   Leif Gellersen, David Napoletano, and Stefan Prestel. "Monte Carlo studies: Les Houches 2019: Standard Model Working Group Report, p.131". In: *11th Les Houches Workshop on Physics at TeV Colliders: PhysTeV Les Houches*. Mar. 2020. arXiv: `2003.01700` `[hep-ph]`.

[222]   Simon Platzer and Malin Sjodahl. "The Sudakov Veto Algorithm Reloaded". In: *Eur. Phys. J. Plus* 127 (2012), p. 26. DOI: `10.1140/epjp/i2012-12026-x`. arXiv: `1108.6180` `[hep-ph]`.

[223]   Georges Aad et al. "Measurement of Dijet Azimuthal Decorrelations in pp Collisions at $\sqrt{s} = 7$ TeV". In: *Phys. Rev. Lett.* 106 (2011), p. 172002. DOI: `10.1103/PhysRevLett.106.172002`. arXiv: `1102.2696` `[hep-ex]`.

[224]   Vardan Khachatryan et al. "Dijet Azimuthal Decorrelations in pp Collisions at $\sqrt{s} = 7\sim$TeV". In: *Phys. Rev. Lett.* 106 (2011), p. 122003. DOI: `10.1103/PhysRevLett.106.122003`. arXiv: `1101.5029` `[hep-ex]`.

[225]   Vardan Khachatryan et al. "Measurement of dijet azimuthal decorrelation in pp collisions at $\sqrt{s} = 8$ TeV". In: *Eur. Phys. J. C* 76.10 (2016), p. 536. DOI: `10.1140/epjc/s10052-016-4346-8`. arXiv: `1602.04384` `[hep-ex]`.

[226] Albert M Sirunyan et al. "Azimuthal correlations for inclusive 2-jet, 3-jet, and 4-jet events in pp collisions at $\sqrt{s}$ = 13 TeV". In: *Eur. Phys. J. C* 78.7 (2018), p. 566. DOI: 10.1140/epjc/s10052-018-6033-4. arXiv: 1712.05471 [hep-ex].

[227] Albert M Sirunyan et al. "Azimuthal separation in nearly back-to-back jet topologies in inclusive 2- and 3-jet events in pp collisions at $\sqrt{s}$ = 13 TeV". In: *Eur. Phys. J. C* 79.9 (2019), p. 773. DOI: 10.1140/epjc/s10052-019-7276-4. arXiv: 1902.04374 [hep-ex].

[228] Vardan Khachatryan et al. "Measurements of differential production cross sections for a Z boson in association with jets in pp collisions at $\sqrt{s}$ = 8 TeV". In: *JHEP* 04 (2017), p. 022. DOI: 10.1007/JHEP04(2017)022. arXiv: 1611.03844 [hep-ex].

[229] Albert M Sirunyan et al. "Measurement of differential cross sections for Z boson production in association with jets in proton-proton collisions at $\sqrt{s}$ = 13 TeV". In: *Eur. Phys. J. C* 78.11 (2018), p. 965. DOI: 10.1140/epjc/s10052-018-6373-0. arXiv: 1804.05252 [hep-ex].

[230] Peng Sun, C. -P. Yuan, and Feng Yuan. "Soft Gluon Resummations in Dijet Azimuthal Angular Correlations in Hadronic Collisions". In: *Phys. Rev. Lett.* 113.23 (2014), p. 232001. DOI: 10.1103/PhysRevLett.113.232001. arXiv: 1405.1105 [hep-ph].

[231] Peng Sun, C. -P. Yuan, and Feng Yuan. "Transverse Momentum Resummation for Dijet Correlation in Hadronic Collisions". In: *Phys. Rev. D* 92.9 (2015), p. 094007. DOI: 10.1103/PhysRevD.92.094007. arXiv: 1506.06170 [hep-ph].

[232] Yoshitaka Hatta et al. "Azimuthal angular asymmetry of soft gluon radiation in jet production". In: *Phys. Rev. D* 104.5 (2021), p. 054037. DOI: 10.1103/PhysRevD.104.054037. arXiv: 2106.05307 [hep-ph].

[233] Yoshitaka Hatta et al. "Anisotropy in Dijet Production in Exclusive and Inclusive Processes". In: *Phys. Rev. Lett.* 126.14 (2021), p. 142001. DOI: 10.1103/PhysRevLett.126.142001. arXiv: 2010.10774 [hep-ph].

[234] Hamza Bouaziz, Yazid Delenda, and Kamel Khelifa-Kerfa. "Azimuthal decorrelation between a jet and a Z boson at hadron colliders". In: *JHEP* 10 (2022), p. 006. DOI: 10.1007/JHEP10(2022)006. arXiv: 2207.10147 [hep-ph].

[235] Yang-Ting Chien et al. "Precision boson-jet azimuthal decorrelation at hadron colliders". In: *JHEP* 02 (2023), p. 256. DOI: 10.1007/JHEP02(2023)256. arXiv: 2205.05104 [hep-ph].

[236] Luca Buonocore et al. "Transverse-momentum resummation for boson plus jet production at hadron colliders". In: *Eur. Phys. J. C* 82.1 (2022), p. 27. DOI: 10.1140/epjc/s10052-021-09962-4. arXiv: 2110.06913 [hep-ph].

[237] Yang-Ting Chien et al. "Recoil-free azimuthal angle for precision boson-jet correlation". In: *Phys. Lett. B* 815 (2021), p. 136124. DOI: 10.1016/j.physletb.2021.136124. arXiv: 2005.12279 [hep-ph].

[238] Yang-Ting Chien, Ding Yu Shao, and Bin Wu. "Resummation of Boson-Jet Correlation at Hadron Colliders". In: *JHEP* 11 (2019), p. 025. DOI: 10.1007/JHEP11(2019)025. arXiv: 1905.01335 [hep-ph].

[239] Maarten G. A. Buffing et al. "A transverse momentum dependent framework for back-to-back photon+jet production". In: (Dec. 2018). arXiv: 1812.07549 [hep-ph].

[240] Peng Sun et al. "Resummation of High Order Corrections in *Z* Boson Plus Jet Production at the LHC". In: *Phys. Rev. D* 100.5 (2019), p. 054032. DOI: `10.1103/ PhysRevD.100.054032`. arXiv: `1810.03804` [`hep-ph`].

[241] Ted C. Rogers and Piet J. Mulders. "No Generalized TMD-Factorization in Hadro-Production of High Transverse Momentum Hadrons". In: *Phys. Rev. D* 81 (2010), p. 094006. DOI: `10.1103/PhysRevD.81.094006`. arXiv: `1001.2977` [`hep-ph`].

[242] Ted C. Rogers. "Extra spin asymmetries from the breakdown of transverse-momentum-dependent factorization in hadron-hadron collisions". In: *Phys. Rev. D* 88.1 (2013), p. 014002. DOI: `10.1103/PhysRevD.88.014002`. arXiv: `1304.4251` [`hep-ph`].

[243] John Collins and Jian-Wei Qiu. "k_T factorization is violated in production of high-transverse-momentum particles in hadron-hadron collisions". In: *Phys. Rev. D* 75 (2007), p. 114014. DOI: `10.1103/PhysRevD.75.114014`. arXiv: `0705.2141` [`hep-ph`].

[244] Werner Vogelsang and Feng Yuan. "Hadronic Dijet Imbalance and Transverse-Momentum Dependent Parton Distributions". In: *Phys. Rev. D* 76 (2007), p. 094013. DOI: `10.1103/PhysRevD.76.094013`. arXiv: `0708.4398` [`hep-ph`].

[245] Georges Aad et al. "Measurement of the inclusive jet cross section in pp collisions at sqrt(s)=2.76 TeV and comparison to the inclusive jet cross section at sqrt(s)=7 TeV using the ATLAS detector". In: *Eur. Phys. J. C* 73.8 (2013), p. 2509. DOI: `10.1140/epjc/s10052-013-2509-4`. arXiv: `1304.4739` [`hep-ex`].

[246] Shreyasi Acharya et al. "Measurements of inclusive jet spectra in pp and central Pb-Pb collisions at $\sqrt{s_{\mathrm{NN}}}$ = 5.02 TeV". In: *Phys. Rev. C* 101.3 (2020), p. 034911. DOI: `10.1103/PhysRevC.101.034911`. arXiv: `1909.09718` [`nucl-ex`].

[247] Georges Aad et al. "Measurement of inclusive jet and dijet production in *pp* collisions at $\sqrt{s}$ = 7 TeV using the ATLAS detector". In: *Phys. Rev. D* 86 (2012), p. 014022. DOI: `10.1103/PhysRevD.86.014022`. arXiv: `1112.6297` [`hep-ex`].

[248] G. Aad et al. "Measurement of Inclusive Jet and Dijet Cross Sections in Proton-Proton Collisions at 7 TeV Centre-of-Mass Energy with the ATLAS Detector". In: *Eur. Phys. J. C* 71 (2011), p. 1512. DOI: `10.1140/epjc/s10052-010-1512-2`. arXiv: `1009.5908` [`hep-ex`].

[249] Vardan Khachatryan et al. "Measurement of the inclusive jet cross section in pp collisions at $\sqrt{s}$ = 2.76 TeV". In: *Eur. Phys. J. C* 76.5 (2016), p. 265. DOI: `10.1140/ epjc/s10052-016-4083-z`. arXiv: `1512.06212` [`hep-ex`].

[250] Serguei Chatrchyan et al. "Measurements of Differential Jet Cross Sections in Proton-Proton Collisions at $\sqrt{s}$ = 7 TeV with the CMS Detector". In: *Phys. Rev. D* 87.11 (2013). [Erratum: Phys.Rev.D 87, 119902 (2013)], p. 112002. DOI: `10.1103/ PhysRevD.87.112002`. arXiv: `1212.6660` [`hep-ex`].

[251] Serguei Chatrchyan et al. "Measurement of the Ratio of Inclusive Jet Cross Sections using the Anti-k_T Algorithm with Radius Parameters R=0.5 and 0.7 in pp Collisions at $\sqrt{s}$ = 7 TeV". In: *Phys. Rev. D* 90.7 (2014), p. 072006. DOI: `10.1103/ PhysRevD.90.072006`. arXiv: `1406.0324` [`hep-ex`].

[252] Morad Aaboud et al. "Measurement of the inclusive jet cross-sections in proton-proton collisions at $\sqrt{s}$ = 8 TeV with the ATLAS detector". In: *JHEP* 09 (2017), p. 020. DOI: `10.1007/JHEP09(2017)020`. arXiv: `1706.03192` [`hep-ex`].

[253] Vardan Khachatryan et al. "Measurement and QCD analysis of double-differential inclusive jet cross sections in pp collisions at $\sqrt{s}$ = 8 TeV and cross section ratios to 2.76 and 7 TeV". In: *JHEP* 03 (2017), p. 156. DOI: `10.1007/JHEP03(2017)156`. arXiv: `1609.05331` [`hep-ex`].

[254] M. Aaboud et al. "Measurement of inclusive jet and dijet cross-sections in proton-proton collisions at $\sqrt{s}$ = 13 TeV with the ATLAS detector". In: *JHEP* 05 (2018), p. 195. DOI: `10.1007/JHEP05(2018)195`. arXiv: `1711.02692` [`hep-ex`].

[255] Vardan Khachatryan et al. "Measurement and QCD analysis of double-differential inclusive jet cross sections in pp collisions at $\sqrt{s}$ = 8 TeV and cross section ratios to 2.76 and 7 TeV". In: *JHEP* 03 (2017), p. 156. DOI: `10.1007/JHEP03(2017)156`. arXiv: `1609.05331` [`hep-ex`].

[256] Albert M Sirunyan et al. "Dependence of inclusive jet production on the anti-k_T distance parameter in pp collisions at $\sqrt{s}$ = 13 TeV". In: *JHEP* 12 (2020), p. 082. DOI: `10.1007/JHEP12(2020)082`. arXiv: `2005.05159` [`hep-ex`].

[257] Zoltan Nagy. "Three jet cross-sections in hadron hadron collisions at next-to-leading order". In: *Phys. Rev. Lett.* 88 (2002), p. 122003. DOI: `10.1103/PhysRevLett.88.122003`. arXiv: `hep-ph/0110315`.

[258] W. T. Giele, E. W. Nigel Glover, and David A. Kosower. "The Two-Jet Differential Cross Section at $O(\alpha_s^3)$ in Hadron Collisions". In: *Phys. Rev. Lett.* 73 (1994), pp. 2019–2022. DOI: `10.1103/PhysRevLett.73.2019`. arXiv: `hep-ph/9403347`.

[259] Stephen D. Ellis, Zoltan Kunszt, and Davison E. Soper. "Two jet production in hadron collisions at order alpha-s**3 in QCD". In: *Phys. Rev. Lett.* 69 (1992), pp. 1496–1499. DOI: `10.1103/PhysRevLett.69.1496`.

[260] Michał Czakon et al. "Single-jet inclusive rates with exact color at $O(\alpha_s^4)$". In: *JHEP* 10 (2019), p. 262. DOI: `10.1007/JHEP10(2019)262`. arXiv: `1907.12911` [`hep-ph`].

[261] A. Gehrmann-De Ridder et al. "Triple Differential Dijet Cross Section at the LHC". In: *Phys. Rev. Lett.* 123.10 (2019), p. 102001. DOI: `10.1103/PhysRevLett.123.102001`. arXiv: `1905.09047` [`hep-ph`].

[262] J Currie, E. W. N. Glover, and J Pires. "Next-to-Next-to Leading Order QCD Predictions for Single Jet Inclusive Production at the LHC". In: *Phys. Rev. Lett.* 118.7 (2017), p. 072002. DOI: `10.1103/PhysRevLett.118.072002`. arXiv: `1611.01460` [`hep-ph`].

[263] James Currie et al. "Single Jet Inclusive Production for the Individual Jet p_T Scale Choice at the LHC". In: *Acta Phys. Polon. B* 48 (2017), pp. 955–967. DOI: `10.5506/APhysPolB.48.955`. arXiv: `1704.00923` [`hep-ph`].

[264] V. M. Abazov et al. "Measurement of dijet azimuthal decorrelations at central rapidities in $p\bar{p}$ collisions at $\sqrt{s}$ = 1.96 TeV". In: *Phys. Rev. Lett.* 94 (2005), p. 221801. DOI: `10.1103/PhysRevLett.94.221801`. arXiv: `hep-ex/0409040`.

[265] Victor Mukhamedovich Abazov et al. "Measurement of the Combined Rapidity and p_T Dependence of Dijet Azimuthal Decorrelations in $p\bar{p}$ Collisions at $\sqrt{s}$ = 1.96 TeV". In: *Phys. Lett. B* 721 (2013), pp. 212–219. DOI: `10.1016/j.physletb.2013.03.029`. arXiv: `1212.1842` [`hep-ex`].

[266] Mees van Kampen et al. "Azimuthal correlations in high pT processes with the TMD parton branching method at NLO". In: *PoS* ICHEP2022 (2022), p. 830. DOI: `10.22323/1.414.0830`. arXiv: `2209.13945` [`hep-ph`].

[267] A. Bermudez Martinez and F. Hautmann. "Azimuthal di-jet correlations with parton branching TMD distributions". In: *29th International Workshop on Deep-Inelastic Scattering and Related Subjects*. Aug. 2022. arXiv: 2208.08446 [hep-ph].

[268] A. Bermudez Martinez et al. "The transverse momentum spectrum of low mass Drell–Yan production at next-to-leading order in the parton branching method". In: *Eur. Phys. J. C* 80.7 (2020), p. 598. DOI: 10.1140/epjc/s10052-020-8136-y. arXiv: 2001.06488 [hep-ph].

[269] Torbjorn Sjostrand, Stephen Mrenna, and Peter Z. Skands. "PYTHIA 6.4 Physics and Manual". In: *JHEP* 05 (2006), p. 026. DOI: 10.1088/1126-6708/2006/05/026. arXiv: hep-ph/0603175.

[270] Matteo Cacciari, Gavin P. Salam, and Gregory Soyez. "FastJet User Manual". In: *Eur. Phys. J. C* 72 (2012), p. 1896. DOI: 10.1140/epjc/s10052-012-1896-2. arXiv: 1111.6097 [hep-ph].

[271] Richard D. Ball et al. "Parton distributions for the LHC Run II". In: *JHEP* 04 (2015), p. 040. DOI: 10.1007/JHEP04(2015)040. arXiv: 1410.8849 [hep-ph].

[272] Vardan Khachatryan et al. "Event generator tunes obtained from underlying event and multiparton scattering measurements". In: *Eur. Phys. J. C* 76.3 (2016), p. 155. DOI: 10.1140/epjc/s10052-016-3988-x. arXiv: 1512.00815 [hep-ex].

[273] S. Mrenna and P. Skands. "Automated Parton-Shower Variations in Pythia 8". In: *Phys. Rev. D* 94.7 (2016), p. 074005. DOI: 10.1103/PhysRevD.94.074005. arXiv: 1605.08352 [hep-ph].

[274] Leif Gellersen and Stefan Prestel. "Scale and Scheme Variations in Unitarized NLO Merging". In: *Phys. Rev. D* 101.11 (2020), p. 114007. DOI: 10.1103/PhysRevD.101.114007. arXiv: 2001.10746 [hep-ph].

[275] T. Aaltonen et al. "Measurement of inclusive jet cross-sections in $Z/\gamma^* \rightarrow e^+e^- +$ jets production in $p\bar{p}$ collisions at $\sqrt{s}$ = 1.96-TeV". In: *Phys. Rev. Lett.* 100 (2008), p. 102001. DOI: 10.1103/PhysRevLett.100.102001. arXiv: 0711.3717 [hep-ex].

[276] V. M. Abazov et al. "Measurement of differential $Z/\gamma^* +$ jet + X cross sections in $p\bar{p}$ collisions at $\sqrt{s}$ = 1.96-TeV". In: *Phys. Lett. B* 669 (2008), pp. 278–286. DOI: 10.1016/j.physletb.2008.09.060. arXiv: 0808.1296 [hep-ex].

[277] Georges Aad et al. "Measurement of the production cross section of jets in association with a Z boson in pp collisions at $\sqrt{s}$ = 7 TeV with the ATLAS detector". In: *JHEP* 07 (2013), p. 032. DOI: 10.1007/JHEP07(2013)032. arXiv: 1304.7098 [hep-ex].

[278] Georges Aad et al. "Measurement of the production cross section for Z/gamma* in association with jets in pp collisions at $\sqrt{s}$ = 7 TeV with the ATLAS detector". In: *Phys. Rev. D* 85 (2012), p. 032009. DOI: 10.1103/PhysRevD.85.032009. arXiv: 1111.2690 [hep-ex].

[279] Vardan Khachatryan et al. "Measurements of jet multiplicity and differential production cross sections of Z+ jets events in proton-proton collisions at $\sqrt{s}$ = 7 TeV". In: *Phys. Rev. D* 91.5 (2015), p. 052008. DOI: 10.1103/PhysRevD.91.052008. arXiv: 1408.3104 [hep-ex].

[280] Morad Aaboud et al. "Measurements of the production cross section of a Z boson in association with jets in pp collisions at $\sqrt{s}$ = 13 TeV with the ATLAS detector". In: *Eur. Phys. J. C* 77.6 (2017), p. 361. DOI: 10.1140/epjc/s10052-017-4900-z. arXiv: 1702.05725 [hep-ex].

[281] S. Dooling, F. Hautmann, and H. Jung. "Hadroproduction of electroweak gauge boson plus jets and TMD parton density functions". In: *Phys. Lett. B* 736 (2014), pp. 293–298. DOI: `10.1016/j.physletb.2014.07.035`. arXiv: `1406.2994 [hep-ph]`.

[282] F. Hautmann and H. Jung. "Angular correlations in multi-jet final states from k-perpendicular - dependent parton showers". In: *JHEP* 10 (2008), p. 113. DOI: `10.1088/1126-6708/2008/10/113`. arXiv: `0805.1049 [hep-ph]`.

[283] Johannes Bellm et al. "Parton Shower Uncertainties with Herwig 7: Benchmarks at Leading Order". In: *Eur. Phys. J. C* 76.12 (2016), p. 665. DOI: `10.1140/epjc/s10052-016-4506-x`. arXiv: `1605.01338 [hep-ph]`.

[284] A. Bermudez Martinez, F. Hautmann, and M. L. Mangano. "Multi-jet physics at high-energy colliders and TMD parton evolution". In: Sept. 2021. arXiv: `2109.08173 [hep-ph]`.

[285] Leif Lonnblad. "Correcting the color dipole cascade model with fixed order matrix elements". In: *JHEP* 05 (2002), p. 046. DOI: `10.1088/1126-6708/2002/05/046`. arXiv: `hep-ph/0112284`.

[286] Nils Lavesson and Leif Lonnblad. "Extending CKKW-merging to One-Loop Matrix Elements". In: *JHEP* 12 (2008), p. 070. DOI: `10.1088/1126-6708/2008/12/070`. arXiv: `0811.2912 [hep-ph]`.

[287] Leif Lonnblad and Stefan Prestel. "Matching Tree-Level Matrix Elements with Interleaved Showers". In: *JHEP* 03 (2012), p. 019. DOI: `10.1007/JHEP03(2012)019`. arXiv: `1109.4829 [hep-ph]`.

[288] Johan Alwall et al. "Comparative study of various algorithms for the merging of parton showers and matrix elements in hadronic collisions". In: *Eur. Phys. J. C* 53 (2008), pp. 473–500. DOI: `10.1140/epjc/s10052-007-0490-5`. arXiv: `0706.2569 [hep-ph]`.

[289] Richard D. Ball et al. "Parton distributions with QED corrections". In: *Nucl. Phys. B* 877 (2013), pp. 290–320. DOI: `10.1016/j.nuclphysb.2013.10.010`. arXiv: `1308.0598 [hep-ph]`.

[290] Georges Aad et al. "Measurement of the transverse momentum and ϕ_η^* distributions of Drell–Yan lepton pairs in proton–proton collisions at $\sqrt{s} = 8$ TeV with the ATLAS detector". In: *Eur. Phys. J. C* 76.5 (2016), p. 291. DOI: `10.1140/epjc/s10052-016-4070-4`. arXiv: `1512.02192 [hep-ex]`.

[291] Ryan Gavin et al. "FEWZ 2.0: A code for hadronic Z production at next-to-next-to-leading order". In: *Comput. Phys. Commun.* 182 (2011), pp. 2388–2403. DOI: `10.1016/j.cpc.2011.06.008`. arXiv: `1011.3540 [hep-ph]`.

[292] Georges Aad et al. "Measurement of multi-jet cross sections in proton-proton collisions at a 7 TeV center-of-mass energy". In: *Eur. Phys. J. C* 71 (2011), p. 1763. DOI: `10.1140/epjc/s10052-011-1763-6`. arXiv: `1107.2092 [hep-ex]`.

[293] Georges Aad et al. "Measurement of hadronic event shapes in high-p_T multijet final states at $\sqrt{s} = 13$ TeV with the ATLAS detector". In: *JHEP* 01 (2021). [Erratum: JHEP 12, 053 (2021)], p. 188. DOI: `10.1007/JHEP01(2021)188`. arXiv: `2007.12600 [hep-ex]`.

[294] Andrea Banfi, Gavin P. Salam, and Giulia Zanderighi. "Phenomenology of event shapes at hadron colliders". In: *JHEP* 06 (2010), p. 038. DOI: `10.1007/JHEP06(2010)038`. arXiv: `1001.4082 [hep-ph]`.

[295] G. Parisi. "Super Inclusive Cross-Sections". In: *Phys. Lett. B* 74 (1978), pp. 65–67. DOI: `10.1016/0370-2693(78)90061-8`.

[296] Geoffrey C. Fox and Stephen Wolfram. "Observables for the Analysis of Event Shapes in e+ e- Annihilation and Other Processes". In: *Phys. Rev. Lett.* 41 (1978), p. 1581. DOI: `10.1103/PhysRevLett.41.1581`.

[297] André H. Hoang et al. "State-of-the-art predictions for C-parameter and a determination of α_s". In: *Nucl. Part. Phys. Proc.* 273-275 (2016). Ed. by M Aguilar-Benıtez et al., pp. 2015–2021. DOI: `10.1063/1.4938630`. arXiv: `1501.04753` [`hep-ph`].

[298] Andrew J. Larkoski and Aja Procita. "New Insights on an Old Problem: Resummation of the D-parameter". In: *JHEP* 02 (2019), p. 104. DOI: `10.1007/JHEP02(2019)104`. arXiv: `1810.06563` [`hep-ph`].

[299] Armen Tumasyan et al. "Measurement of the mass dependence of the transverse momentum of lepton pairs in Drell-Yan production in proton-proton collisions at $\sqrt{s}$ = 13 TeV". In: *Eur. Phys. J. C* 83.7 (2023), p. 628. DOI: `10.1140/epjc/s10052-023-11631-7`. arXiv: `2205.04897` [`hep-ex`].

[300] S. Moch, J. A. M. Vermaseren, and A. Vogt. "The Three loop splitting functions in QCD: The Nonsinglet case". In: *Nucl. Phys. B* 688 (2004), pp. 101–134. DOI: `10.1016/j.nuclphysb.2004.03.030`. arXiv: `hep-ph/0403192`.

[301] F. James. "RANLUX: A FORTRAN implementation of the high quality pseudo-random number generator of Luscher". In: *Comput. Phys. Commun.* 79 (1994). [Erratum: Comput.Phys.Commun. 97, 357 (1996)], pp. 111–114. DOI: `10.1016/0010-4655(94)90233-X`.